AD NUMBER
AD912109
LIMITATION CHANGES

TO:

Approved for public release; distribution is unlimited.

FROM:

Distribution authorized to U.S. Gov't. agencies only; Test and Evaluation; 28 NOV 1972. Other requests shall be referred to Air Force Flight Dynamics Laboratory, Wright-Patterson AFB. OH.

AUTHORITY

AFFDL per ltr, 27 Aug 1979

AFFDL-TR-72-138
Volume II

AD912109

AEROACOUSTIC LOADS ASSOCIATED WITH HIGH BETA RE-ENTRY VEHICLES

L. E. CHAUMP, A. MARTELLUCCI, A. MONFORT

GENERAL ELECTRIC COMPANY

TECHNICAL REPORT AFFDL-TR-72-138, VOLUME II

MAY 1973

AIR FORCE FLIGHT DYNAMICS LABORATORY
AIR FORCE SYSTEMS COMMAND
WRIGHT-PATTERSON AIR FORCE BASE, OHIO

NOTICE

When Government drawings, specifications, or other data are used for any purpose other than in connection with a definitely related Government procurement operation, the United States Government thereby incurs no responsibility nor any obligation whatsoever; and the fact that the government may have formulated, furnished, or in any way supplied the said drawings, specifications, or other data, is not to be regarded by implication or otherwise as in any manner licensing the holder or any other person or corporation, or conveying any rights or permission to manufacture, use, or sell any patented invention that may in any way be related thereto.

Copies of this report should not be returned unless return in required by security considerations, contractual obligations, or notice on a specific document.

AEROACOUSTIC LOADS ASSOCIATED WITH HIGH BETA RE-ENTRY VEHICLES

L. E. CHAUMP, A. MARTELLUCCI, A. MONFORT

GENERAL ELECTRIC COMPANY

FOREWORD

This report has been reviewed and is approved.

WALTER J. MYKYTOW
Asst. for Research & Technology
Vehicle Dynamics Division
AF Flight Dynamics Laboratory

ABSTRACT

A detailed description is presented defining the wind tunnel test facility, test model and associated instrumentation and recording system. Wind tunnel conditions including test model local flow properties are defined along with a discussion of acoustic data obtained for the various flow regimes of interest (transition, fully turbulent, base and separated flow). Finally, test data in the form of acoustic intensity distributions along the vehicle and third octave pressure spectrums are presented.

TABLE OF CONTENTS

LIST OF ILLUSTRATIONS

LIST OF ILLUSTRATIONS (Continued)

LIST OF TABLES

SECTION I

EXPERIMENTAL PROGRAM

An experimental ground test program was conducted at Arnold Engineering Development Center (AEDC) in the Von Karman Gas Dynamics Facilities Tunnels A, B, and C, [1] at Mach numbers of 4, 8, and 10, respectively. The objective of this test program was to obtain acoustic data which would be used to verify and/or redefine aeroacoustic prediction methods currently in use in the aerospace industry. This section describes the wind tunnels employed in this test program, the model and support details, and the instrumentation used to obtain these data.

1. TEST FACILITY DESCRIPTION

a. AEDC Tunnel A

Tunnel A is a 40 x 40 inch continuous flow, closed circuit, variable density, supersonic wind tunnel with a Mach number range 1.6 to 6. Continuous curvature nozzle contours are obtained by flexible top and bottom walls, mounted on electrically driven screw jacks. The side walls of the nozzle are plane and parallel. Operation of the nozzle-actuating jacks is completely automatic. Window panels which form the test section walls are available in three different window arrangements. Spark shadowgraph and Schlieren photography is available for flow visualization during tunnel operation. Models are generally supported from the rear by stings which attach to the roll sting hub, or adapter hub, mounted on the top of the single ended support strut. The model support is injected into the test section and translated upstream to the test area. In either the retracted or injected position, the model may be rolled ±180 degrees and pitched ±15-1/2 degrees while the center of rotation is in the downstream position. At the most forward position, the model pitch is limited to ±10 degrees. Figure 1 is a general assembly of Tunnel A which includes the performance capability.

b. AEDC Tunnel B

The Tunnel B facility is a continuous flow, hypersonic wind tunnel with a 50-inch diameter test section. Interchangeable axisymmetric contoured nozzles provide flow at either Mach 6 or 8. The tunnel is a closed circuit type which operates over a range of pressures with air supplied by a central compressor system. A model injection system provides the capability for quick model changes without interrupting tunnel operation. The tunnel flow conditions provide free stream Reynolds numbers from 0.30×10^6 to 3.8×10^6 per foot at Mach 8 with a total temperature of 1350°R. The tunnel layout and a summary chart of the performance characteristics of this facility are shown in Figure 2.

Model support and sting assemblies provide, in general, a 30-degree pitch range capability. Model support in the tunnel is positioned so that dual windows can provide flow visualization and photography. Each window is equipped with either a conventional single

1
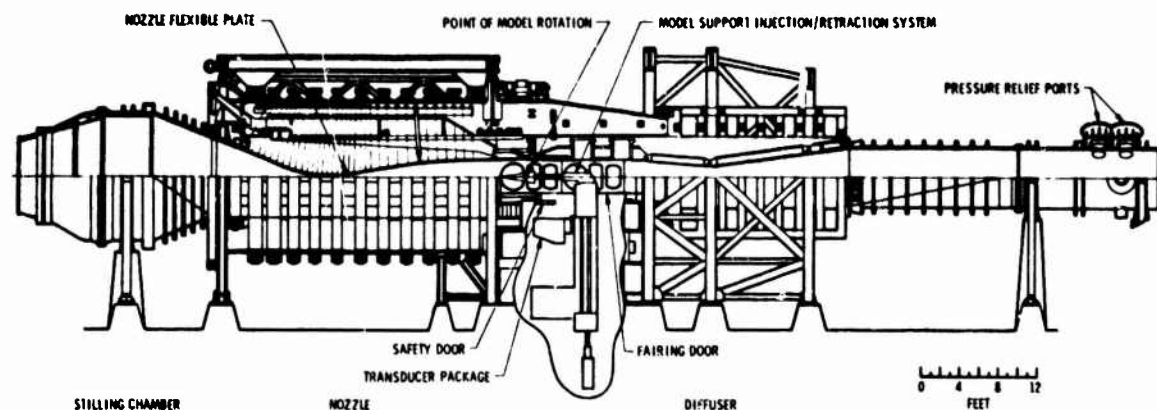
Tunnel A Assembly

Mach No.	Stages of Compression	P_0, psia		T_0, °F		q_∞, psia		Re/ft × 10^{-6}	
		Max	Min	Max	Min	Max	Min	Max	Min
1.50	Type B	29	1.5	105	70(1)	12.4	0.64	9.07(2)	0.41
1.75		30	2.0	105	70	12.1	0.81	8.72	0.53
2.00		35	3.0	105	70	12.5	1.07	9.16	0.72
1.50	2	15	1.5	180	70	6.4	0.64	4.69	0.36
1.75		17	1.5	180	70	6.8	0.60	4.94	0.34
2.00		21	1.5	190	70	7.5	0.54	5.54	0.30
2.25		26	1.7	190	70	8.0	0.52	6.11	0.30
2.50		33	2.0	190	70	8.5	0.51	6.85	0.31
2.75		41	2.5	190	70	8.6	0.53	7.50	0.34
3.00		51	3.2	220	70	8.7	0.55	8.18	0.35
3.00	3	37	2.7	220	70	6.3	0.46	5.93	0.30
3.25		45	3.2	220	70	6.3	0.44	6.38	0.31
3.50		57	3.5	220	70	6.4	0.39	7.03	0.30
3.75		65	4.2	220	70	5.9	0.38	7.04	0.32
4.00		73	4.6	240	70	5.4	0.34	6.95	0.29
4.00	4	50	4.6	180	70	3.7	0.34	4.75	0.33
4.50		115	7.2	195	70	5.6	0.35	8.16(2)	0.39
5.00		150	10.5	230	70	5.0	0.35	6.66	0.41
5.50		150	15.0	245	160	3.4	0.34	4.39	0.56
5.50	5	200	25.0	290	180	4.6	0.57	5.81	0.87
6.00		200	30.0	290	270	3.2	0.48	4.35	0.69

Tunnel A Performance

Figure 1. Tunnel A Assembly and Performance Characteristics

2

WINDOWS FOR MODEL INSPECTION
OR PHOTOGRAPHY

WINDOWS FOR SHADOWGRAPH
SCHLIEREN PHOTOGRAPHY

AIR DUCTS TO COOL
MODEL FOR HEAT-
TRANSFER TESTS OR
QUICK MODEL CHANGE

PRESSURE TRANSDUCERS
AND VALVES

NOZZLE

TANK ENTRANCE DOOR
FOR MODEL INSTALLATION
OR INSPECTION

MODEL INJECTION AND
PITCH MECHANISM
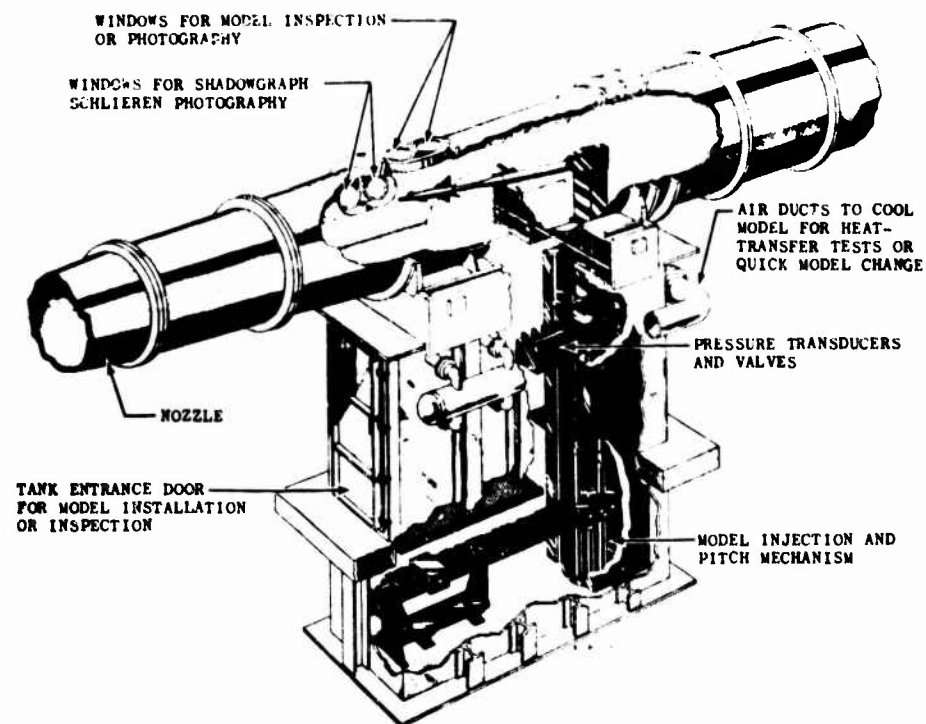
Tunnel B   Test Section

Nominal Mach Number	p_o, psia		T_o, °F	q_∞, psia		Re. ft x 10^{-6}	
	Min.	Max.	Max.	Min.	Max.	Min.	Max.
6	20	270 (1)	390 (3)	0.3	4.1	0.3	4.7
8	50	850 (2)	890	0.3	3.8	0.3	3.6

Screen Section — Nozzle Section — Test Section · Diffuser Section

Mach 6 or 8 Throat

Quartz Windows

Operating Floor

Tank to Tunnel Vent

Subsonic Diffuser

Atmosphere Vent

Tank Access Floor

Relief Valve

Ground Floor

Tank Entrance
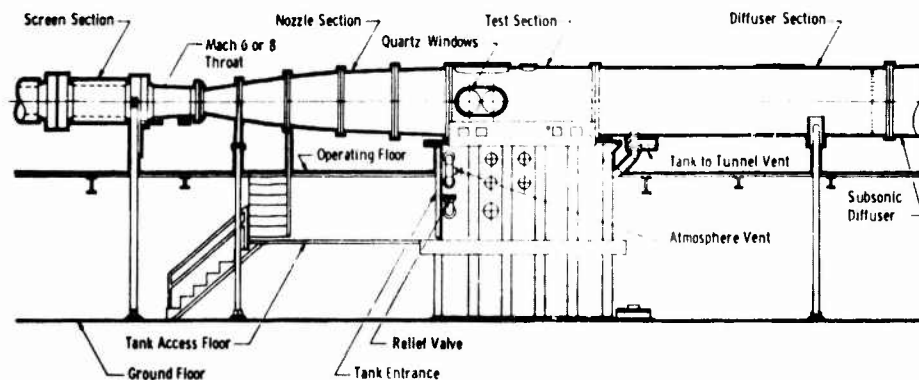
General Assembly, Tunnel B

Figure 2. Tunnel B Assembly and Performance Characteristics

3

pass Schlieren system or a parallel beam refocused shadowgraph system. Model attitude in the tunnel was measured by the data readout system and verified optically with a scope.

c. AEDC Tunnel C

Tunnel C is a continuous flow, hypersonic wind tunnel with a 50-inch diameter test section. Interchangeable axisymmetric contoured nozzles provide flow at either $M_\infty = 10$ or 12. A model injection system provides the capability for quick model changes without interrupting tunnel operation. The tunnel flow conditions provide free stream Reynolds numbers from 0.3 to 2.4 x 10^6 per foot at total temperatures up to 2000°F.

Model support and sting assemblies provide, in general, a 30-degree pitch range capability. Model support in the tunnel is positioned so that dual windows can provide complete flow visualization and photography. Each window is equipped with either a conventional single pass Schlieren system or a parallel beam refocused shadowgraph system. Tunnel layout and performance is shown in Figure 3.

2. TEST HARDWARE DESCRIPTION

a. Model

The model to be used in the current wind tunnel test is a heat transfer model which was used on the Air Force sponsored STREET-G Program[2]. The model is a 7.2 degree half angle cone with changeable noses with radii of 0, 0.055, and 0.110 inches and a base radius of 5.40 inches. The model is constructed of 0.050-inch thick series 400 stainless steel, and was instrumented with 32 high intensity microphones and 40 Chromel-Alumel thermocouples. A detailed drawing of the model defining the acoustic instrument locations is shown in Figure 4. A photograph of the strut mounted model shown in the Tunnel B vacuum tank below the test section is shown in Figure 5.

b. Model Support

The model support system that was used for this test program is a compression strut support system, which was designed and built by GE for use on the STREET-G Program, based on the concept of Reference 3. Figure 6 depicts the details of the support system including the method of attachment to the base of the cone. A photograph of the cone and the strut support system is shown in Figure 7. The four-strut support is mounted to the base plate of the model, and each leg is hollow to accommodate instrumentation access to the model. Basically, the struts are swept-back 60 degree, and their leading and trailing edges are wedge shaped with a 20 degree included angle measured normal to the edge. The unit was manufactured from series 400 stainless steel.

Since the struts support the vehicle from its base, they will not have any influence on the flow over the conical portion of the model. However, credence in the base pressure data is predicted on the minimal effect that the model support has on the wake structure. This has been assessed by comparing the base pressure of the supported model with

4

WINDOWS FOR MODEL INSPECTION
OR PHOTOGRAPHY

WINDOWS FOR SHADOWGRAPH/
SCHLIEREN PHOTOGRAPHY

AIR DUCTS TO COOL
MODEL FOR HEAT-
TRANSFER TESTS OR
QUICK MODEL CHANGE

NOZZLE

PRESSURE TRANSDUCERS
AND VALVES

TANK ENTRANCE DOOR
FOR MODEL INSTALLATION
OR INSPECTION

MODEL INJECTION AND
PITCH MECHANISM
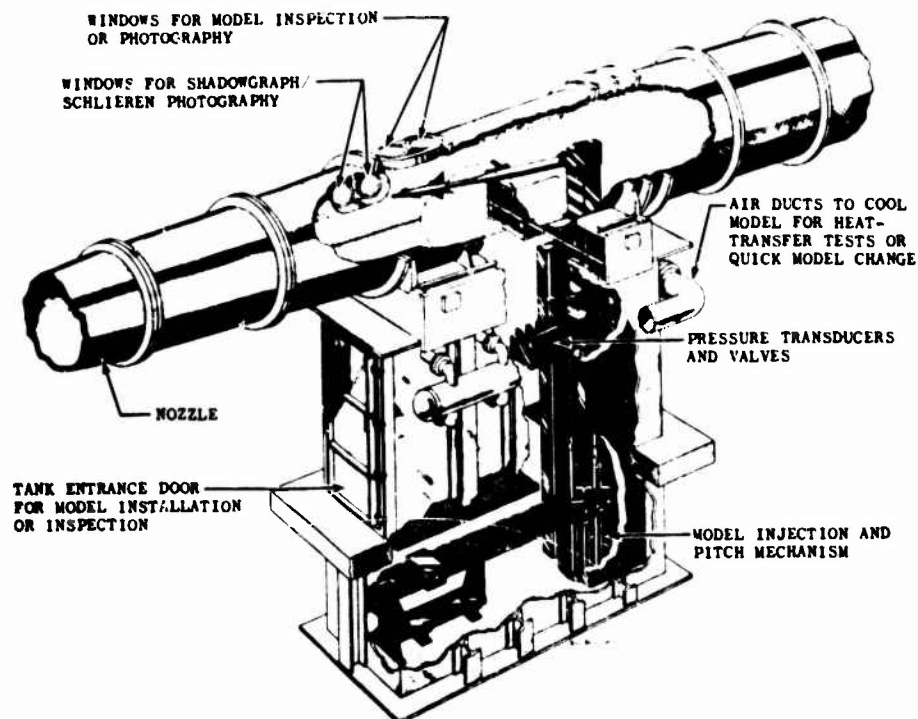
Tunnel C Test Section

Tunnel Performance

Tunnel	Nominal Mach Number	P_o, psia		T_o, °F	q', psia		R_e/ft x 10^{-6}		
		Min	Max	Max	Min	Max	Min	Max	
C	10	200	2000	1440	0.3	3.0	0.3	2.4	
	12	600	2400	1940	0.4	1.6	0.3	1.2	

TEST SECTION

INSTRUMENTATION RING

MODEL SUPPORT
INJECTION/RETRACTION
SYSTEM

MACH 10 OR 12
THROAT
SECTION

QUARTZ WINDOWS

SCREEN
SECTION

NOZZLE

SAFETY DOOR

DIFFUSER SECTION

TRANSITION
SECTION

FAIRING
DOOR

MODEL COOLING
AIR LINE

TANK
ENTRANCE
DOOR

PRESSURE TRANSDUCER
SYSTEM

OPERATION
FLOOR

MODEL COOLING
NOZZLES

TEST SECTION TANK

FEET
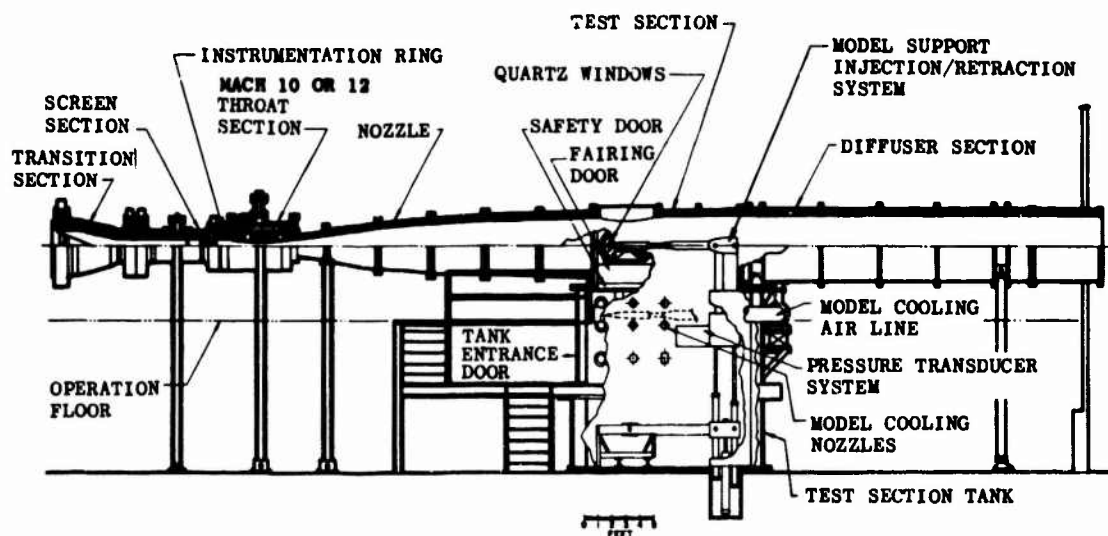
Tunnel C Assembly

Figure 3. Tunnel C Assembly

Figure 4. Test Vehicle

6
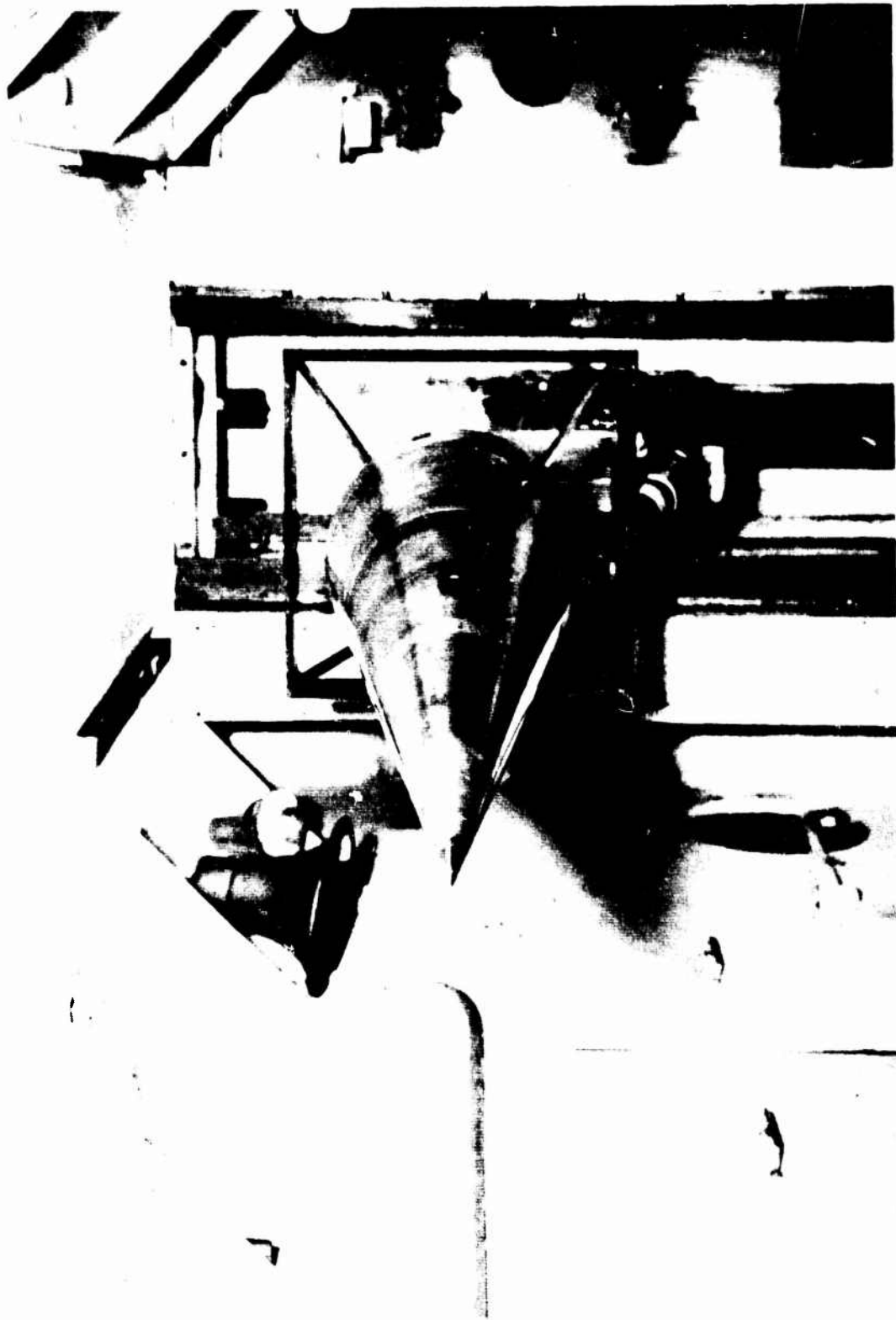
Figure 5. Strut Mounted Model in Tunnel B Vacuum Tank

7

Figure 6. Test Vehicle Support System

8
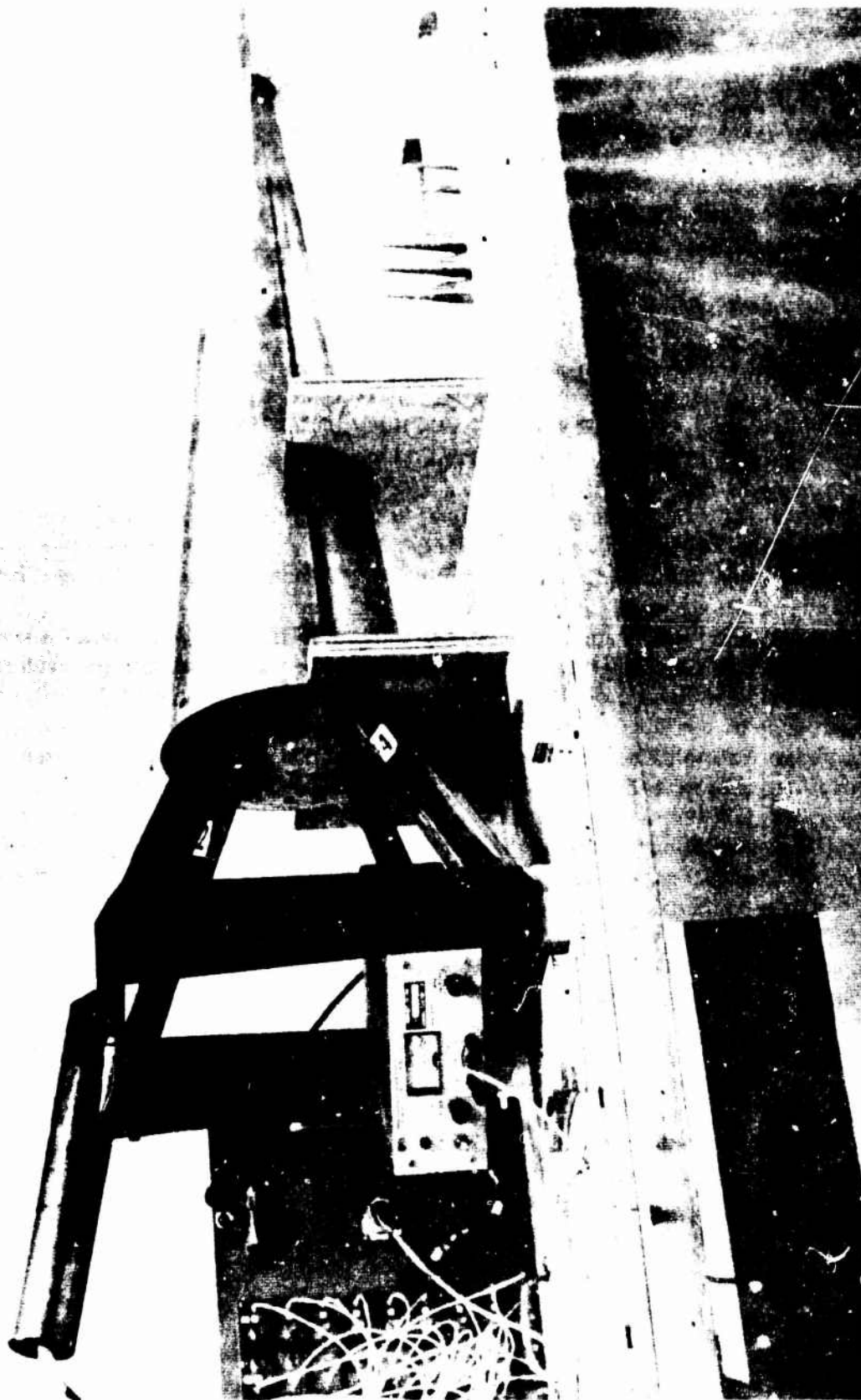
Figure 7. Cone and Strut Support System

9

free-flight data for the same flow conditions. The base pressure for the cone ($R_N/R_B = 0.02$) at Mach 8, 10, and 12.3 from Reference 3 are presented in Figure 8. Also shown in this figure are some free-flight ("drop-test") data[4], as well as the free-flight data of Reference 5, both obtained at AEDC. The agreement between the flight data and the supported model data is excellent for all Reynolds numbers. The Mach 12 data of Muntz and Softley et. al. [6] are also shown in Figure 8 and are in agreement with the Mach 12 results. It should be noted that the data presented in this figure are for different size models and that the base pressure apparently scales with Mach number and Reynolds number. It was further shown[3] that the near-wake properties as obtained using the strut support system were in excellent agreement with free-flight wake data as well as with some recently developed near-wake theories.

Thus, it can be concluded on the basis of the base pressure correlation and also the agreement with the near-wake properties at a station in the vicinity of the neck, that the compression strut system has a negligible effect on the wake structure and, consequently, should give meaningful base fluctuation measurements.

The use of sting mount was ruled out in favor of the compression strut supports on the basis of the following data. It has long been recognized that single sting supports have an influence on the base flow characteristics. From numerous investigations, it was concluded that if the ratio of sting diameter to base diameter of a cone is below 0.2, this effect is minimized. However, it was recently shown[7] that the inclusion of a hub or a supporting device to which the sting is attached influences the wake closure even though the hub may be some 3-4 base cone diameters downstream. An example of the influence that a sting-hub support could have on the base pressure of a slender cone is shown in Figure 9. The data shown were obtained in Tunnels A and B at AEDC for a sting-supported model versus data obtained using an AEDC-developed free-flight technique[5] [4]. For these free-flight tests, the model was injected into a continuous hypersonic stream, and a telemetering system was used to monitor the base pressure. The model attitude was monitored optically. Also shown on this figure are data obtained using a compression strut support system[3]. It is rather evident that the sting support affects the base static pressure; therefore, one would expect it to affect the fluctuating pressures as well. Consequently, the four-strut support which was shown to have a minimal effect on wake properties was chosen as the best design available.

The facilities at AEDC are of the continuous type, and the data are to be acquired by pulsing the model into the flow for a period of time which is compatible with that required to obtain the acoustic data. In Tunnel A, the stagnation temperature is sufficiently low so that the cone and strut system will not be exposed to any aerodynamic heating. In Tunnels B and C, the stagnation temperature is sufficiently high that some aerodynamic heating will occur. For the short exposure time to the flow (i.e., order of seconds) no appreciable model heating occurred.

c. Instrument Locations and Test Conditions

The free stream test conditions were selected, so that the location of transition was spatially fixed on the model surface. The Reynolds number was selected in each

10
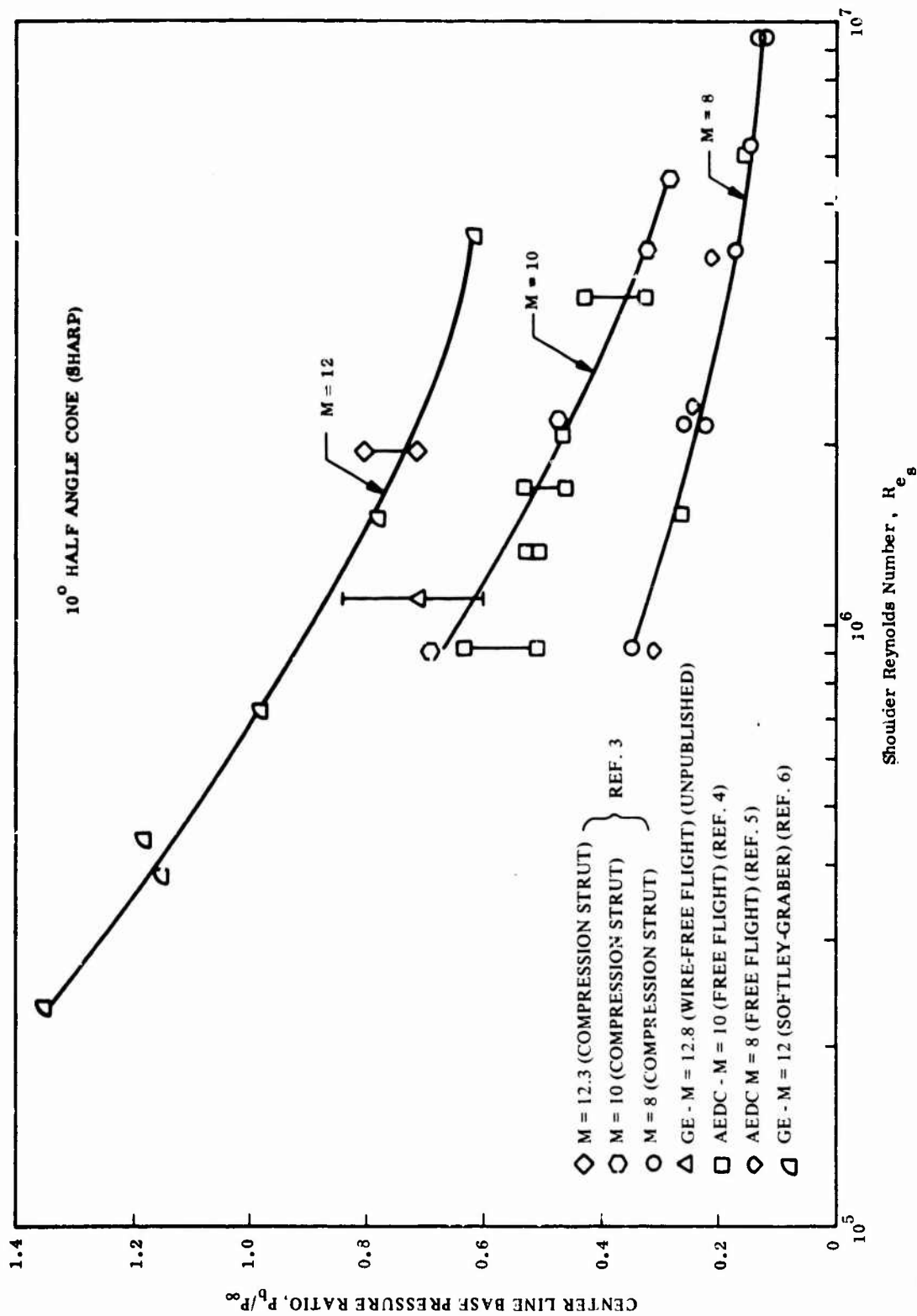
Figure 8. Comparison of Base Pressure Measurements for Various Support Systems

10° HALF ANGLE CONE (SHARP)

M = 12
M = 10
M = 8

CENTER LINE BASE PRESSURE RATIO, P_b/P_∞

Shoulder Reynolds Number, R_{e_s}

◇ M = 12.3 (COMPRESSION STRUT)
○ M = 10 (COMPRESSION STRUT) } REF. 3
○ M = 8 (COMPRESSION STRUT)
△ GE - M = 12.8 (WIRE-FREE FLIGHT) (UNPUBLISHED)
□ AEDC - M = 10 (FREE FLIGHT) (REF. 4)
◇ AEDC M = 8 (FREE FLIGHT) (REF. 5)
◁ GE - M = 12 (SOFTLEY-GRABER) (REF. 6)

11
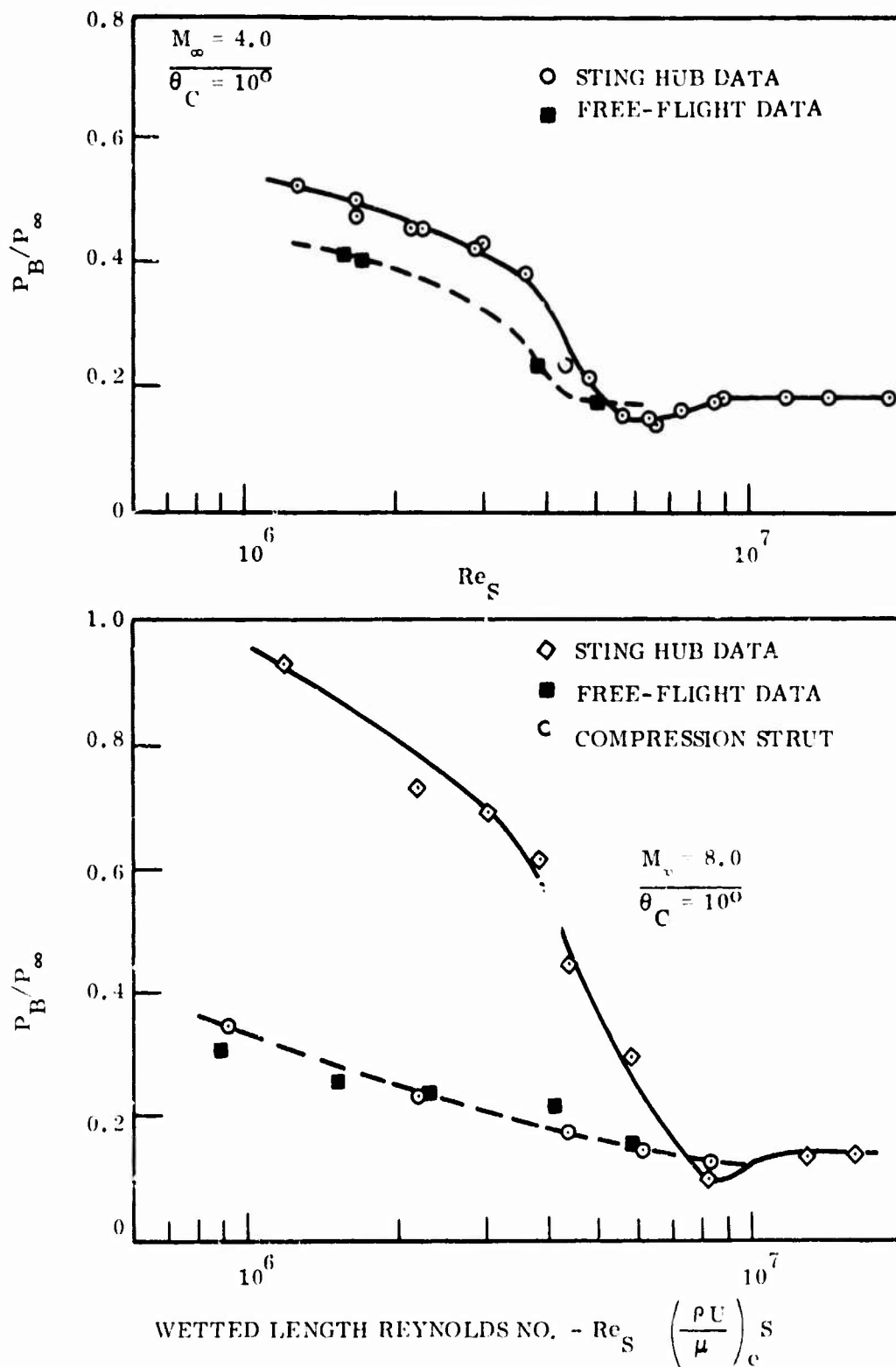
Figure 9. Sting-Hub Effects on Base Pressure

facility so that acoustic data were obtained at the beginning and end of transitional flow regions and also at several stations in the turbulent flow region.

In order to determine the spacing of the sensors on the cone, it was necessary to establish the location of the transitional boundary layer zone for each of the proposed test conditions. This required the correlation of available transition data for each of the three AEDC test facilities where tests were planned.

The largest single source of applicable transition data for the Mach 8 condition (Tunnel B) may be found in Reference 2. These data were obtained for the same cone and range of test conditions that was used in the current test series. The location of onset and end of transition was deduced from the heat transfer measurements. That is, the onset of transition was defined as the point where the heat transfer is a minimum, and the end of transition as the point where the heat transfer is locally a maximum. For these data the spatial distribution of the end of transition was deduced (from $\dot{q}_{max}$) ans some typical results are repeated here in Figure 10.

Available transition data for sharp cones in Tunnel A at Mach 4 and Tunnel C at Mach 10 may be found in References 8, 9, and 10. These data were used to establish the Mach number sensitivity of transition location with Reynolds number. The available data were for cone angles which were different than the 7.2 degree half-angle cone to be tested. The following procedure was used to establish the transition location on the test model for various free stream unit Reynolds numbers.

The local wetted length Reynolds number at transition, $R_{eST} = (\rho u/\mu)_{e\,ST}$ for the zero angle-of-attack case was computed for each data case. Where the value $(\rho u/\mu)_e$ is the local unit Reynolds number at the boundary layer edge, evaluated at the transition point (S_T). Then assuming that the same value of R_{eST} would prevail for the 7.2 degree half-angle cone, the corresponding free stream unit Reynolds number was determined. Transition location data thus obtained are presented in Figure 10. It is of interest to note that the available end-of-transition data for the sharp cones, collapses to a single line in this particular format. The sensor locations (single and arrays) were selected to be consistent with the test conditions shown in Figure 11 and Table I.

The only applicable transition data available to date for the blunt body case was from Reference 2 (i.e., for $M_\infty = 8$). The onset and end of transition data for $R_N = 0.055$ in. and $R_N = 0.110$ in. are presented in Figure 12. Based upon the sensor locations established for the sharp cone, the test conditions for the blunted cone were selected to provide a fixed location of transition as noted in Figure 12.

Because of the paucity of blunt cone transition data on cones at Mach 4 and 10, it was assumed that the Mach 8 data of Reference 2 are representative of the bluntness effect. The validity of this assumption was to be verified by the current tests.

13
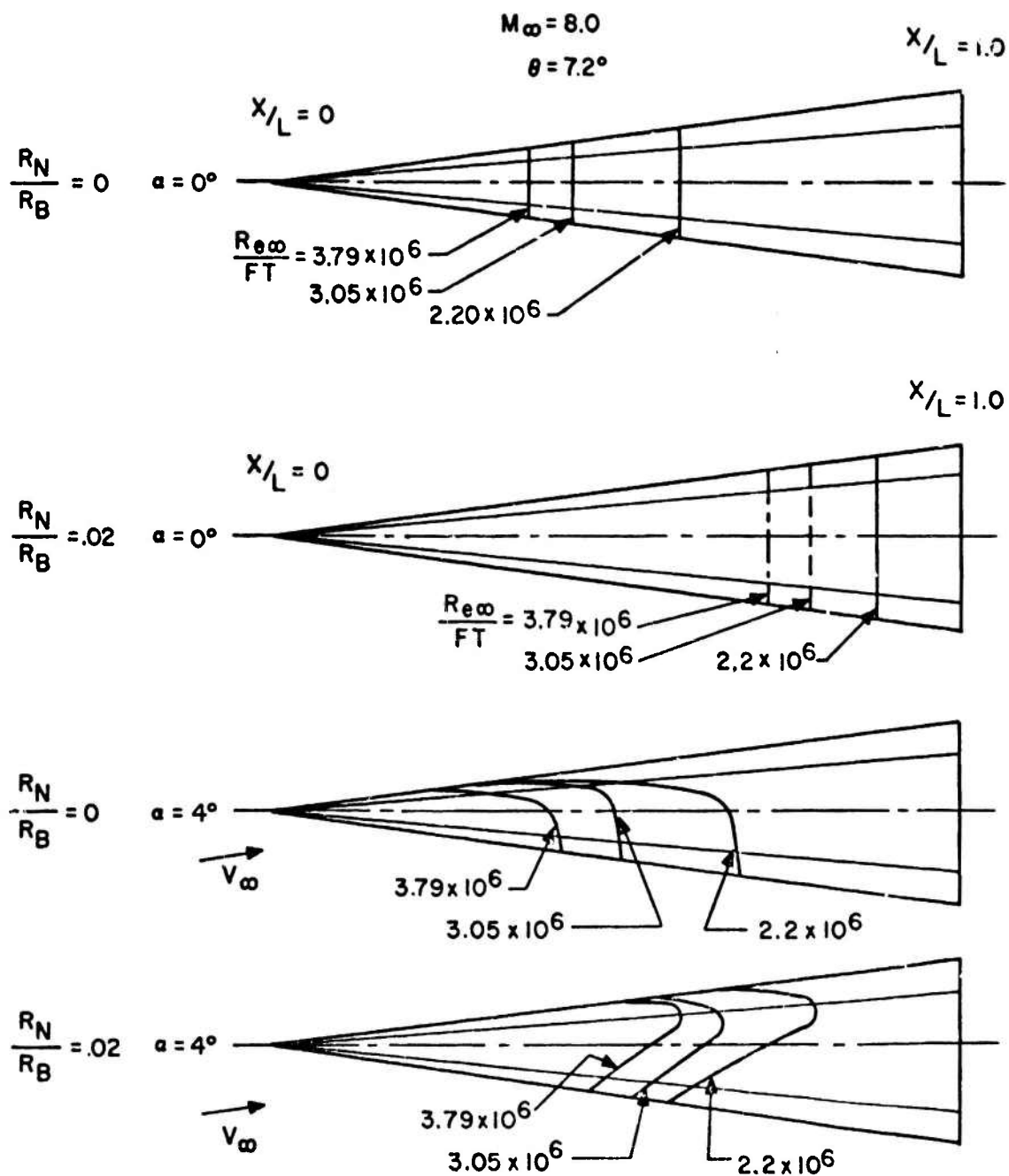
Figure 10. Spatial Distribution of End of Transition With
Reynolds Number and Angle-of-Attack Variation
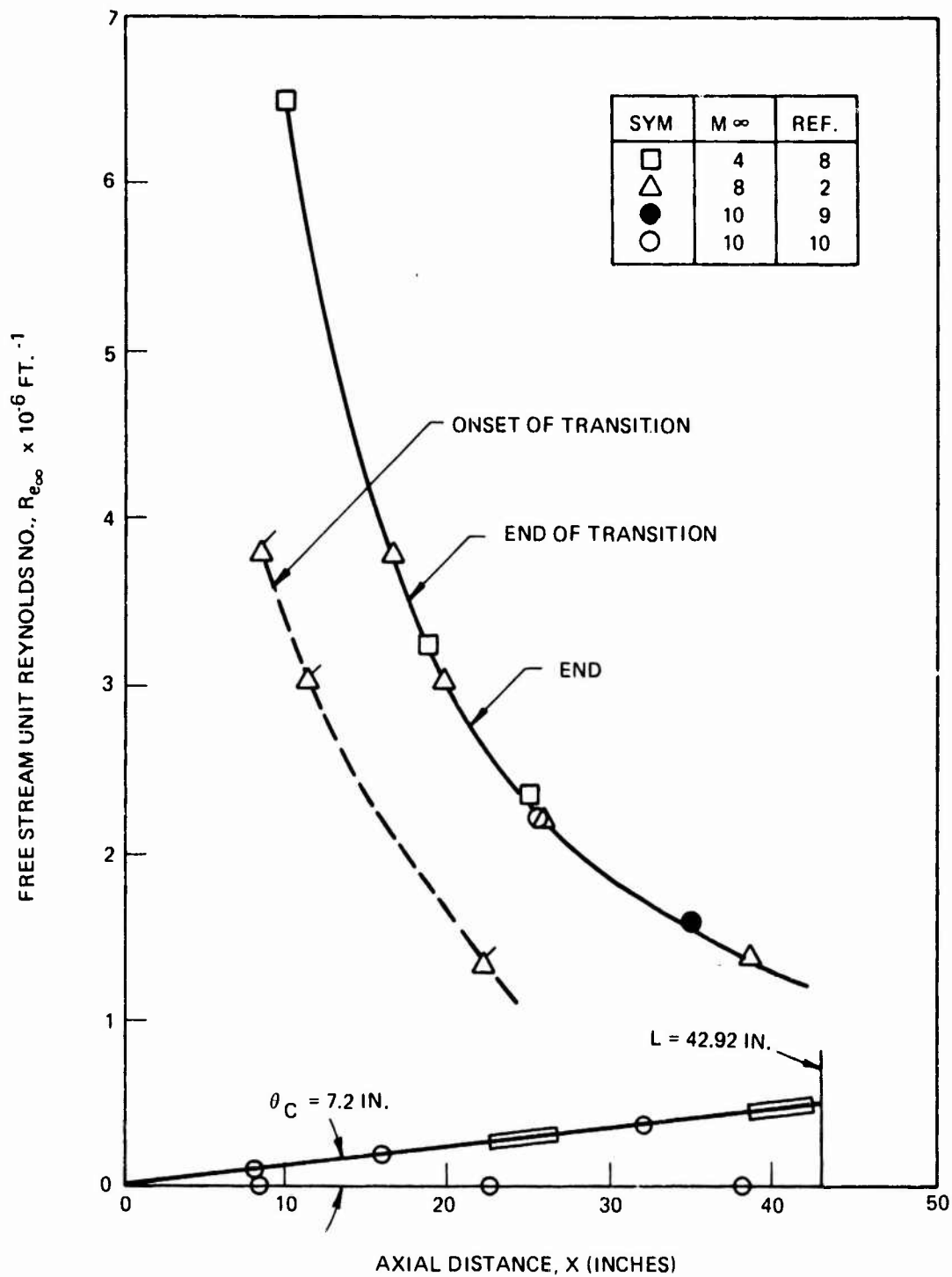
Figure 11. Correlation for the Location of the Boundary Layer
Transition Zone for the Sharp Cone ($\alpha = 0°$)

TABLE I. ACOUSTIC GAGE LOCATIONS

X Dim. From Point	Ray Location & Gage No.							
	0°	5.97°	10.08°	19.1°	32.25°	90°	180°	270°
8.00	1							
8.375						2		
16.00	3							
22.50	4		5		6	7	8	9
23.00	10							
23.60	11							
24.60	12							
25.90	13							
32.00	14							
38.00	15	16		17		18	19	
38.50	20							
39.10	21							
40.10	22							
41.40	23							
Radius								
0.00	24							
1.50	25							
3.00	26					28		
4.75						29	27	

Cone Surface

Cone Base

ARRAY #1

ARRAY #2

16
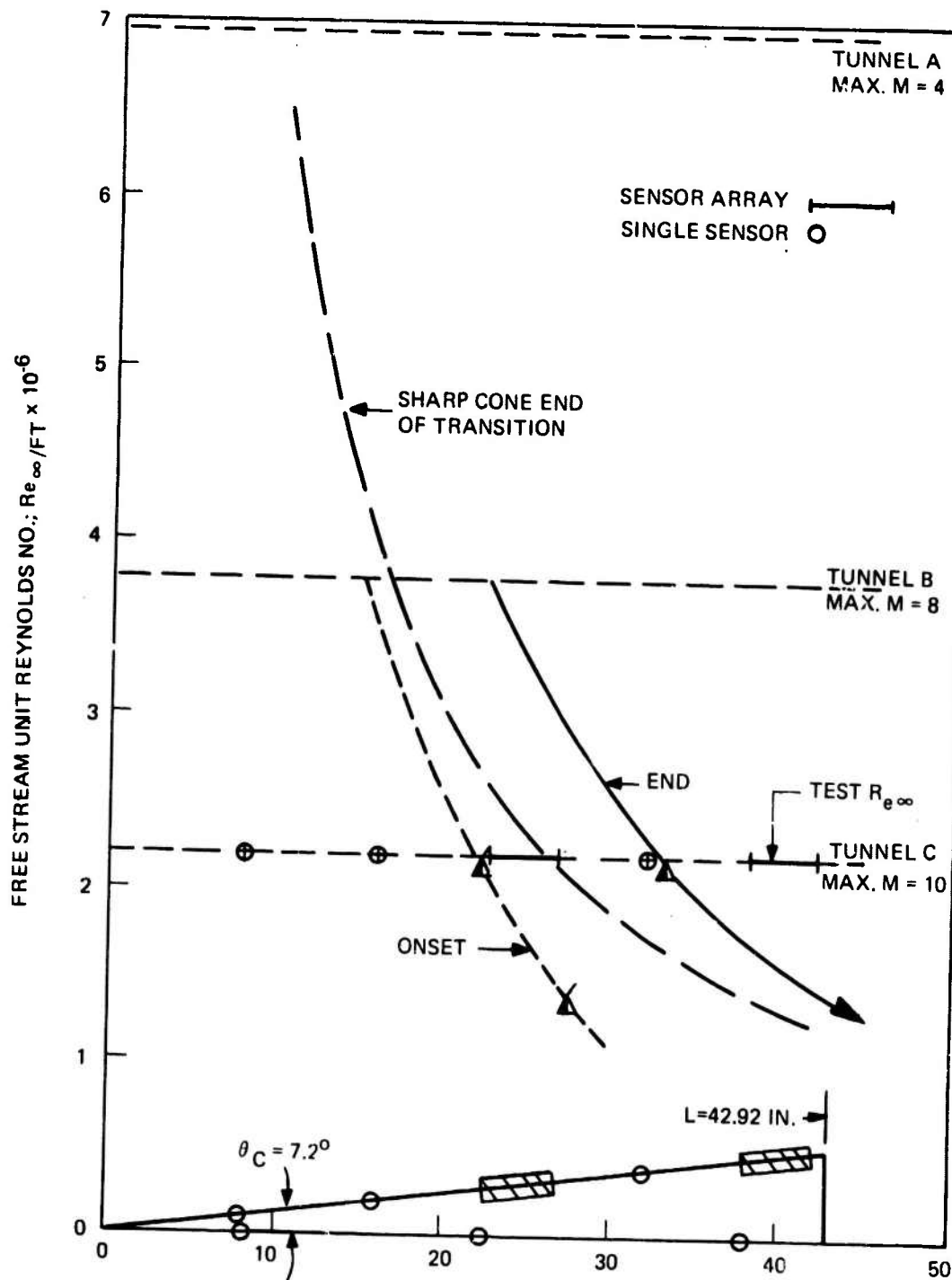
Figure 12. Location of the Boundary Layer
Transition Zone Blunt Cone ($R_N = 0.055$ in.)

17

d. Acoustic Sensors

The acoustic sensors selected for this program are high intensity piezo-electric crystal microphones manufactured by Gulton Industries. Twenty-three microphones were installed in an essentially flush-mounted configuration on the cone surface of the model and were subjected to a relatively high heating source during the Mach 8 and 10 tests in AEDC Tunnels B and C, respectively. Therefore, these sensors, Model MQA-2400, were of special high temperature construction, rated to maintain their calibrated sensitivity within ±2 db over a temperature range from 0 to 250°F and +2, -4 db from -65°F to +400°F. (Based on backface thermocouple measurements, it is estimated that the sensor temperature rise did not exceed about 150-200°F during the present testing). Of the six microphones mounted on the base of the model, one was a Model MQA-2400 and five were Model MVA-2400 which were essentially identical to the MQA-2400 except for an operating upper temperature limit of 250°F (survivable to 300°F). Two sensors were mounted in ported configurations on the cone surface in order to obtain frequency response characteristics in mounting configurations more representative of potential flight vehicle mountings.

Figure 4 shows the microphone locations and the details of the mounting. In order to obtain data to as high a frequency as possible, the flush configuration was chosen. Shock tube calibration testing showed that microphone response was down 3 db at about 10 kHz when the vendor supplied perforated protective cap was used, but was extended to at least 28 kHz with the cap removed. Application of a 3 to 5 mil layer of RTV-560 silicone rubber over the face of the sensor had no noticeable effect on frequency response and was essential in order to preserve the model contour and prevent any surface discontinuity from affecting the flow field. The thin layer of rubber also provided some physical protection for the very thin microphone diaphragm and a degree of filtering of any high frequency heat transfer to the ceramic elements of the sensor which might result in unwanted pyroelectric responses. Each microphone was screwed into a nylon holder which electrically isolated it from the model. The diaphragm was recessed about 3 to 5 mils below the surface of the model and the resultant cavity filled with RTV-560 rubber which had been vacuum pumped after mixing in order to eliminate trapped air bubbles. The silicon rubber was then smoothed to the surface contour of the model to provide a surface free of any discontinuities. Photographs of the model showing the acoustic gage installation and spatial arrangement may be found in Figures 13 and 14.

In order to obtain as high a signal-to-noise ratio as possible from the high impedance piezoelectric microphones, each gage was connected by a short length of subminiature low-noise coaxial cable to its own electrically isolated single-stage amplifier in an amplifier assembly in the rear section of the model. These amplifiers introduced a nominal voltage gain of five while also providing an impedance transformation from several megohms at the input to about 2200 Ω so that the signal could be coupled out through the model strut support via microminiature coaxial cable without concern over noise pickup due to cable vibration and signal cross-talk. Sixty cycle power line pickup was minimized by using individual isolated ground returns for each circuit which were connected to the building ground at a common point - at the power supply/junction box just outside the wind tunnel.
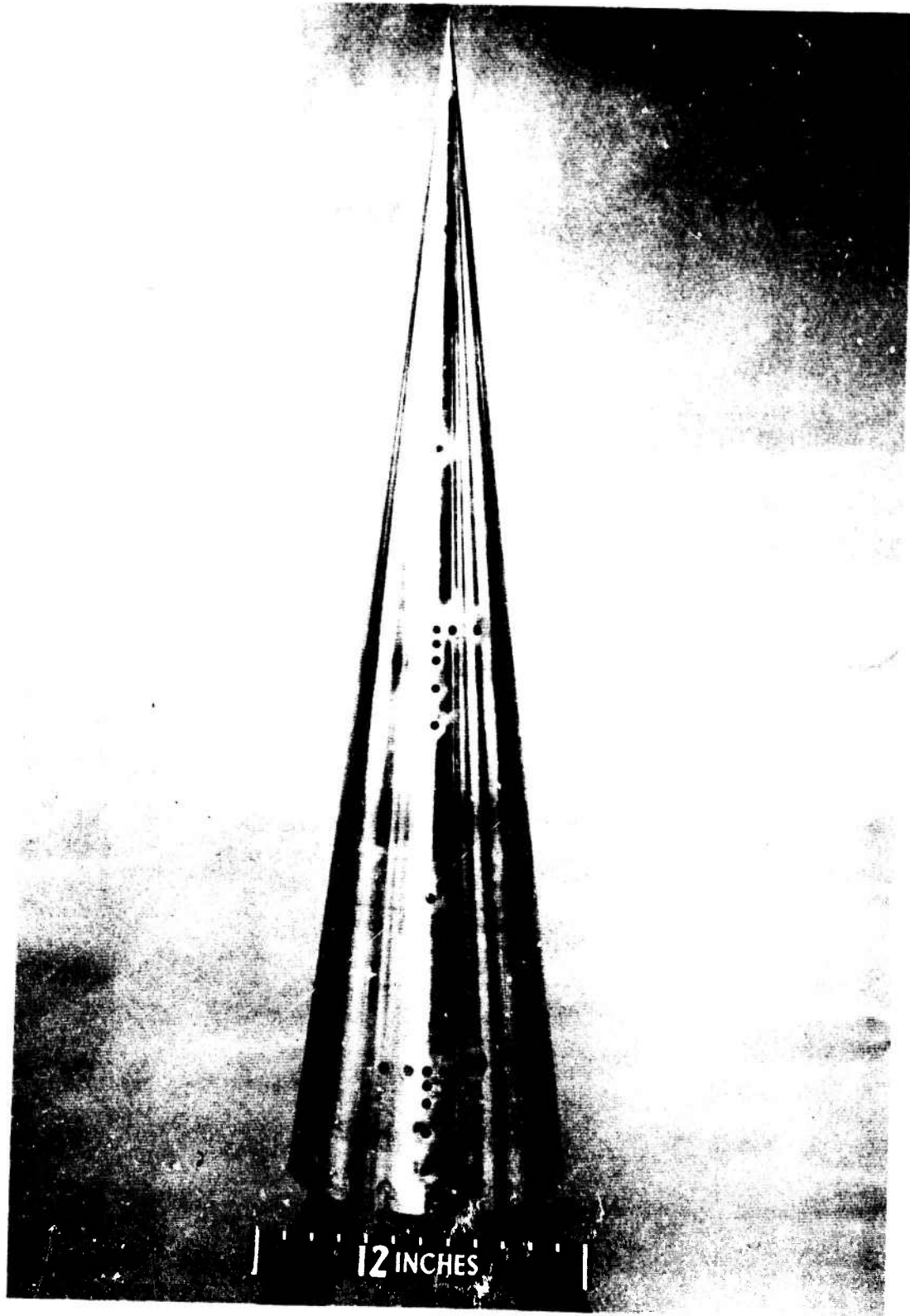
Figure 13. Acoustic Gage Installation

19
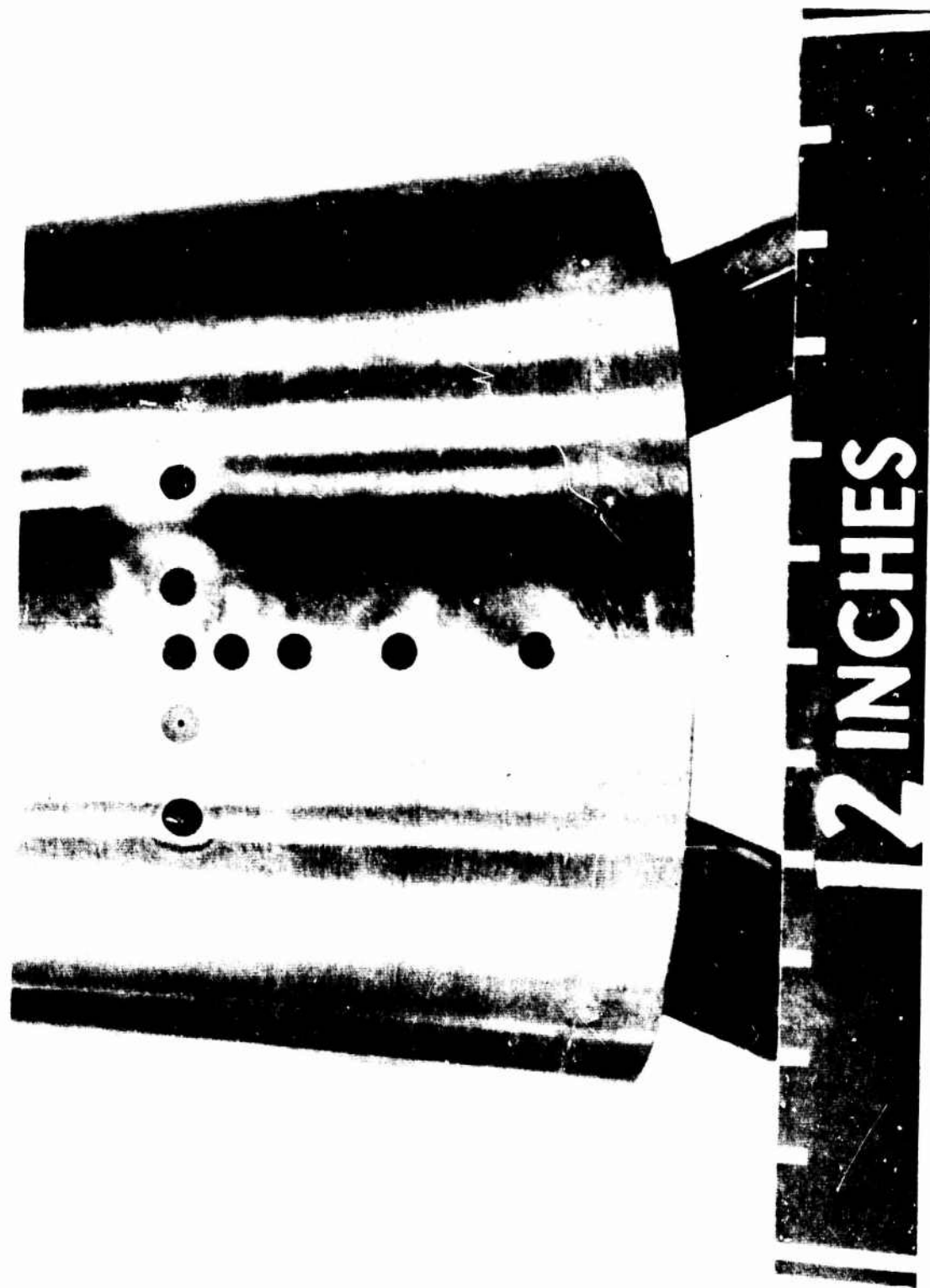
Figure 14. Aft Array Acoustic Gate Installation

A schematic diagram of the on-board amplifier system is shown in Figure 15. The amplifier input provides a low frequency cut-off at about 30 Hz (for a microphone and cable capacitance of 1000 pf. This prevents saturation of the amplifier due to the pyroelectric signal generated by the microphone when subjected to heating by the wind tunnel flow. The use of an unbypassed source resistor in the amplifier provides negative feedback to stabilize the circuit gain. Circuit noise measured at the output of the on-board amplifiers had a value equivalent to an input noise of about ten microvolts rms or, using a typical microphone sensitivity of 600 microvolts at 120 dB sound pressure level (SPL), an equivalent microphone system electrical noise of about 85 dB SPL.

The outputs of the on-board amplifiers were coupled through about thirty feet of microminiature coaxial cable to a junction box which contained the load resistor for each circuit, a common well-regulated low noise power supply and capacitive coupling to output BNC connectors for subsequent transmission of the signal via one hundred foot lengths of RG-58μ cable to the racks of Preston amplifiers (furnished by AEDC) where the final individual channel gains were set prior to recording of the signal or magnetic tape. By placing the on-board amplifier load resistors in the junction box, it was possible to maintain the very low output impedance of the common power supply and avoid the potential cross-talk inherent in carrying power supply leads into the model. The Preston amplifiers are direct-coupled, high input impedance amplifiers. Therefore, dc blocking capacitors were provided in the junction box (large enough to avoid signal attenuation) together with load resistors small enough to permit rapid recovery from any transient overloads without affecting the low frequency response set in by the on-board amplifier input circuit.

Each of the microphones was supplied with a vendor calibration which gave charge sensitivity at 120 dB SPL as a function of frequency over the range from 50 Hz to 15 kHz (10 kHz in the case of the MVA-2400 microphones) linearity from 110 to 160 dB at 1 kHz, internal capacitance and leakage resistance. The frequency response characteristic showed a consistent peak value at 10 kHz which was 20 to 40 percent higher than the 1 kHz value. In order to determine whether this was a real characteristic of this type of microphone or a result of the measurement technique and also to check the effect of an RTV rubber coating on microphone sensitivity and frequency response shock tube tests were run by General Electric.

Upon receipt from the supplier, the capacitance of each microphone and associated cable was checked using a General Radio Model 716-C Capacitance Bridge and the charge sensitivity was checked (at a nominal sound pressure level of 124 dB at 252 Hz) using a B&K Type 4220 Piston-phone Calibrator. Measured capacitance agreed quite well with the value stated by the vendor - there being less than four percent difference except for one sensor, MQA-2400, Serial No. 1026, whose measured capacitance of 832 pf was almost twice that quoted by the vendor (438 pf). This microphone reverted to the lower value of capacitance when mounted in the model - apparently as a result of a poor connection. When its data were corrected for this behavior, its results were in line with expected values.

21

Figure 15. Acoustic Sensor On-Board Amplifier Circuit Schematic

22

The pistonphone check on sensitivity was also in generally good agreement with the vendor's measurement - a difference of less than five percent for nineteen of the thirty-one gages and of between five and 10 percent for five others. However, the shock tube check gave values of charge sensitivity which were generally higher than the manufacturer's value, though more than half of the microphones used had shock tube derived sensitivities within 15 percent of the vendor's 1 kHz value. The reason for this discrepancy is not known, but may be related to the fact that the sensor's are sealed with one atmosphere pressure inside the case. When tested in the shock tube (and in the AEDC wind tunnels) the microphones are in a vacuum environment while the vendor calibration and the pistonphone check were made at one atmosphere ambient pressure. In any event, whichever sensitivity is used, the effect on the resultant data is less than ±2 dB, maximum.

In the shock tube calibration, the microphones under test (protective caps removed) were screwed into plexiglass holders to within a few mils of the front surface which was contoured to the curvature of the shock tube inside surface. Silicone rubber was then applied to the primed face of the sensor to make it flush with the face of the holder. After curing, the microphones were installed in the sidewall of the shock tube (two at a time, spaced six inches apart) and calibrated at ambient pressures over the range of 0.05 psia to about 0.58 psia, corresponding to the range encountered in the subsequent wind tunnel testing. The shock tube driver was evacuated to an initial pressure in the range from about 5.5 to about 10 psia and the mylar diaphragm separating the driver from the driven tube was pierced by a pneumatically actuated spear. The resultant shock wave travelled down the tube at velocities between Mach 1.5 and 2, traversing the microphone sensitive element in less than 10 microseconds with a resultant step in pressure of from 0.1 to 1.0 psi. The duration of the pressure step is of the order of 2 to 10 milliseconds and its precise value is given (for air) by:

$$\Delta P \approx 1.167 \ P_1 \ (M_s^2 - 1), \text{ where}$$

P_1 is the initial shock tube pressure and M_s is the shock Mach number. Both of these quantities were carefully measured. In addition, a reference dynamic pressure gage (Kistler Model 606A) was used to provide an indication of the quality of the flow and an independent measure of the pressure step.

Several things were apparent from the shock tube calibration. First, the response of the gage did not show any overshoot, but was essentially flat with time. Thus, the frequency response is flat for all practical purposes. Second, the rise time of the sensor output was in the order of 10 to 12 microseconds indicating high frequency cut-off (-3 dB) at about 25 to 30 kHz. Third, tests conducted using microphones without the RTV coating resulted in a rising output as a function of time except for tests at the lowest initial pressure. This behavior can be attributed to the pyroelectric sensitivity of these microphones and these tests clearly demonstrated the value of the rubber coating in inhibiting the effect. The tests without a RTV coating did, however, show that the RTV had a negligible effect on frequency response and no noticeable effect on sensitivity.

e. **Aerothermo Instrumentation**

The location of boundary layer transition was deduced from model surface heat transfer measurements. In tunnels B and C (Mach 8 and 10), where the stream total temperature is much greater than the model wall temperature, the heat transfer was deduced from back face thermocouples attached to the model skin. Using the transient one-dimensional heat conduction equation which is valid for the current thin walled model, one can express the heat transfer in the following form.

$$\dot{q} = \rho C p \tau \frac{dT}{d\tau}$$

where

ρ = Model material density

C_p = Coefficient of specific heat of the model material

τ = Material thickness at the thermocouple location: the slope of the temperature time history of the model wall as deduced from the thermocouple is $dT/d\tau$.

As the model is inserted into the wind tunnel, with an initially uniform ambient wall temperature, the model wall heats up. The surface heat transfer is deduced at several time steps when the model is on tunnel centerline. The Stanton number (i.e., $S_T = \dot{q}/ \left[(\rho u)_\infty (H_0 - h_w) \right]$) is deduced at several time increments and for the first 10 to 15 seconds the Stanton number is a constant. A typical axial distribution of Stanton number is shown in Figure 16. The location of transition was deduced from this axial distribution of the Stanton number where transition onset is defined as the point where the local heat transfer as a minimum and the end of transition is defined as the point where the local heat transfer is a maximum (see Figure 16).

At Mach 4 where the low stream total temperature (120°F) precluded the measurement of heat transfer with thermocouples, thermographic phosphorescent paint was used to establish the transition zone. For these measurements a thin coating of phosphor paint was sprayed on to a fiberglass shell which was fit over the basic steel model. The model with the fiberglass shell mounted to the strut system in the tunnel vacuum tank is shown in Figure 17. The phosphorescent paint technique[11] consists of photographing the painted model surface and measuring the optical density of the recorded image. The optical density of a photographic image is a function of the logarithm of the intensity of the exposure, for a given exposure time. If the exposure from the phosphorescent paint falls within the logarithmically linear region, the optical density will be a function of the ultraviolet (u-v) light intensity and the emitted light intensity of the paint. For these wind tunnel tests, the procedure was to take a photograph of the model before the tunnel run (i.e., a t.re) and then take another one during the run. It suffices to say that the incremental change in optical density is proportional to the surface heat transfer. In the present case we were not searching for the absolute level of the heat transfer but for those points where it reached a minimum (transition onset) or a maximum (transition end). Due to the limited region of photographic coverage, only the end of transition data were obtained.
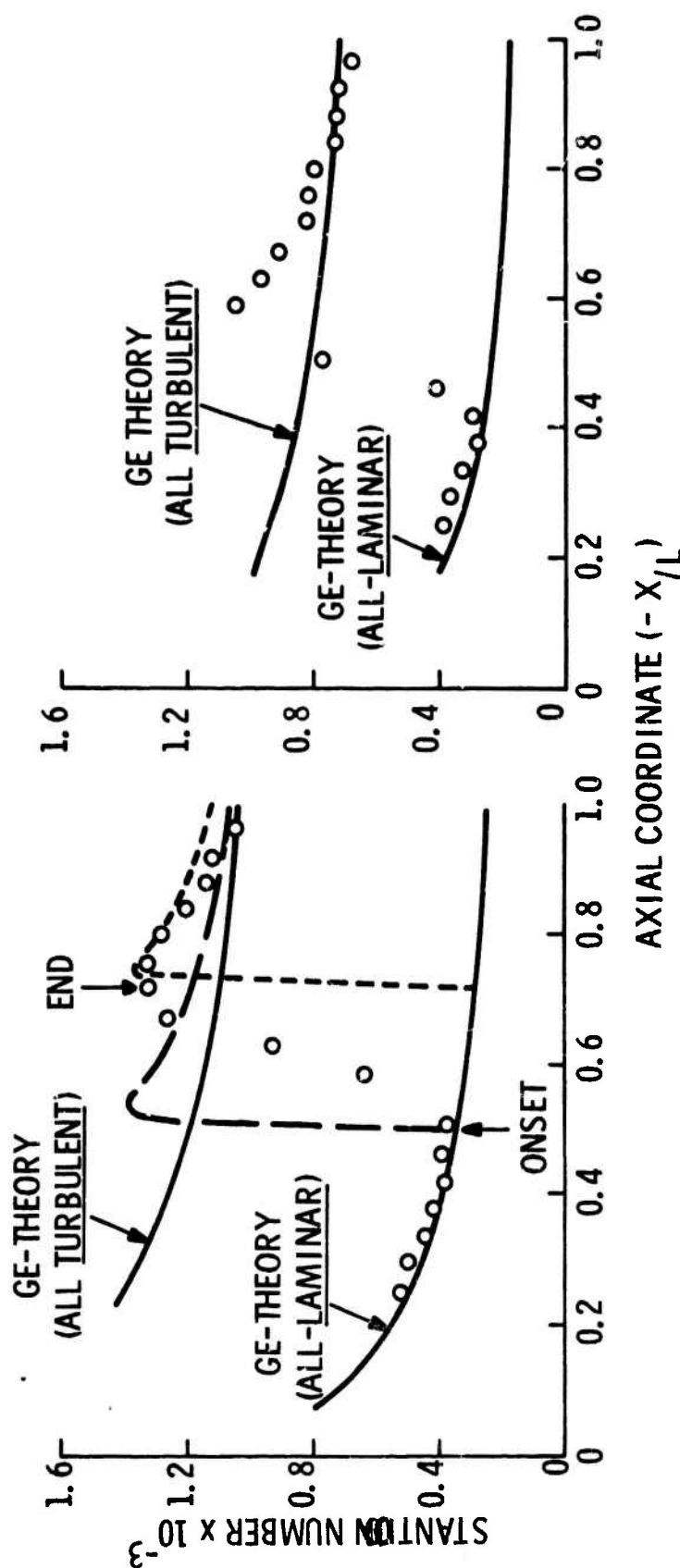
Figure 16. Heat Transfer Distribution on a Cone

25
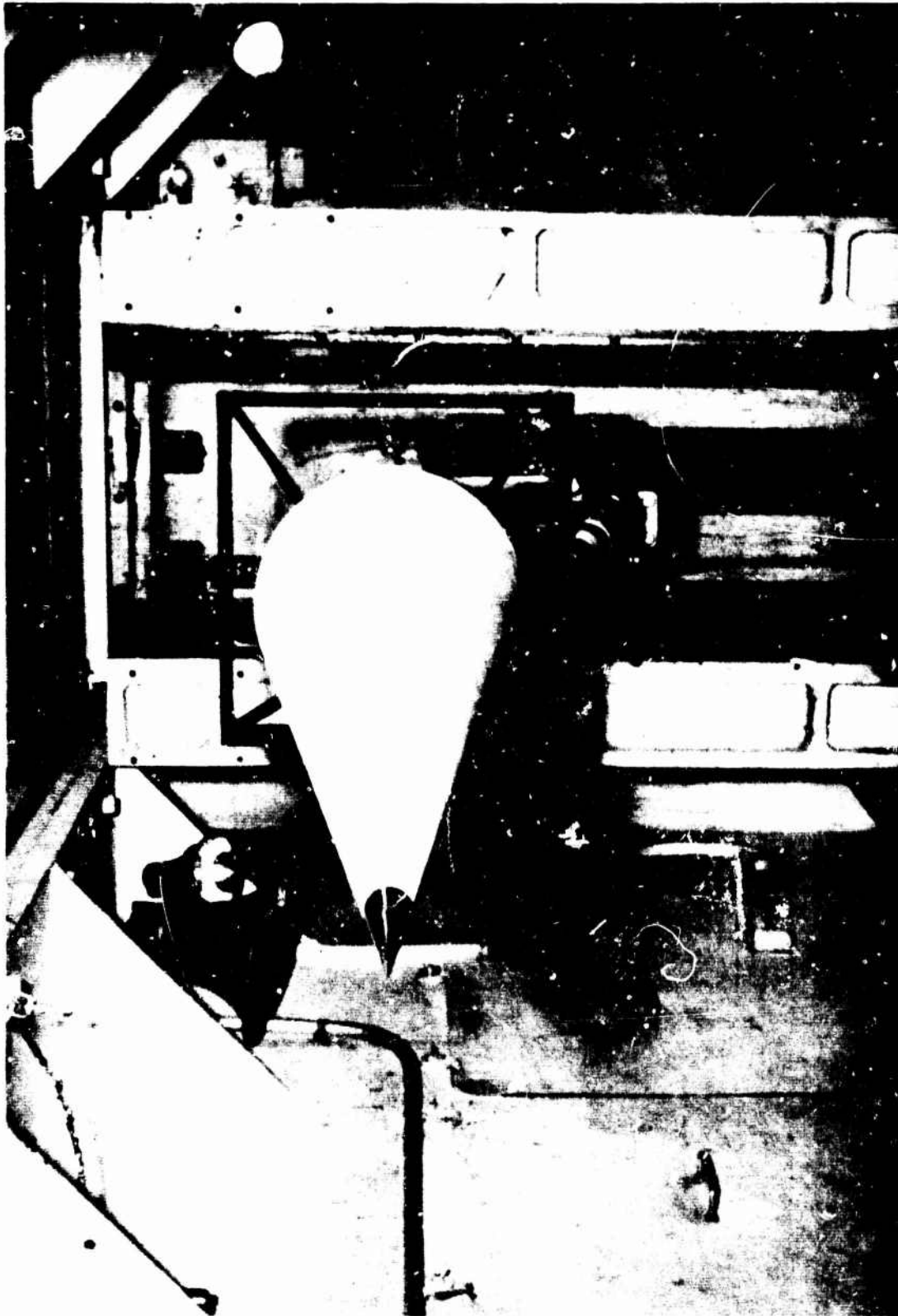
Figure 17. Model with Fiberglass Shell

f.   Test Procedure

The test procedures in terms of the sequence and cycling of data acquisition and screeing are presented with appropriate rationale in the following paragraphs for each of the tests in Tunnels A, B, andC.

The acoustic gages have a temperature limitation which could be exceeded in Tun-nels B and C of the test model remains in the flow for protracted periods. From a safety point of view it was decided to plan the test sequencing in order of increasing hazard. As mentioned before, the facilities at AEDC are of the continuous type, and in general, the data were acquired by pulsing the model into the flow for a time period which is compatible with that required to obtain the acoustic data. The low total temperatures required at low Mach numbers, as in the Tunnel A test, represented a case where the model could remain in the flow continuously without any hazard to the gages, therefore these tests were conducted first. The Tunnel B tests were then conducted next with the most hazardous test conducted last, (i.e., Tunnel C which has the highest total temperature of the three facilities).

Since valid boundary layer transition data, especially those with bluntness effects, were not generally available for the Tunnel A (Mach 4) conditions, these data were planned first. As such, the initial tunnel installation was with the fiberglass shell mounted over the basic steel model. Qualitative heating data were obtained at several test conditions (Reynolds numbers) for each of the three model noses. From these data, the end of transition was de-duced and compared to the pre-test predictions. These results will be discussed in Section II-1 of this report. Thus, with the location of transition determined, the fiberglass shell was removed and acoustic data were obtained. In the Tunnel B and C tests, the transfer data were acquired simultaneously with the acoustic data. Consequently a verification of the transition location (which actually was a re-verification of results acquired on earlier programs) was performed and was found to be in good agreement with the predictions.

Since the acquisition of "valid" acoustic noise data was the primary concern of the wind tunnel test program, considerable attention was paid to the methods of conditioning and recording these data, to providing adequate calibration of the data acquisition system and to screening of the recorded data to assure that the level of the recording was below saturation level but well above the tape recorded background noise.

All acoustic data within the frequency range from d-c to 20 kHz were recorded on magnetic tape using two fourteen channel Ampex FR-1300 portable recorders and one four-teen channel Bell & Howell VR-3360 recorder. All of the recording was done at a tape speed of 60 inches per second using FM record amplifiers whose center frequency was 108 kHz, and whose internal gain was set to give full-scale (±40%) deviation for one volt root-mean-square (rms) sinusoidal input.

To facilitate data reduction and minimize tape recorder/reproducer based phase errors in the data processing for cross-correlation functions, the tape recording format shown in Table II was used. This arrangement assured that all data from the microphones in a given array were recorded on the same machine. IRIG-B Time Code information was

TABLE II. ANALOG TAPE FORMAT

Track No.	Recorder No. 1 (Ampex FR-1300)	Recorder No. 2 (Ampex FR-1300)	Recorder No. 3 (CEC VR-3360)
1	A-4	A-15	A-24
2	A-7	A-14	A-1
3	A-5	A-16	A-35
4	A-8	A-18	A-28
5	A-6	A-17	A-26
6	A-9	A-19	A-3
7	A-10	A-20	A-27
8	A-2	V-3*	A-29
9	A-11	A-21	V-1*
10	Mod. Insert Sig.	Mod. Insert Sig.	Mod. Insert Sig.
11	A-12	A-22	V-2*
12	Tape Speed Ref.	Tape Speed Ref.	A-31 +
13	A-13	A-23	A-30+
14	Time Code/Voice	Time Code/Voise	Time Code/Voice

*V-1, V-2, and V-3 are tri-axial accelerometer signals used to give an indication of vibration on the roll, pitch and yaw axis, respectively.

+A-22 and A-23 were recorded in place of these ported sensor signals during some of the testing in Tunnel B.

recorded on all machines in order to permit time synchronization between machines to within about one millisecond. The "Mod Insert Sig." was a voltage signal placed on the tape when the model reached tunnel centerline after insertion (Tunnels B & C).

Each acoustic sensor signal--after amplification in the on-board amplifier and capacitive coupling in the power supply/junction box--was coupled to a Preston Model 8300XWB amplifier through a "Calibrate-Operate" switch which, in the "Calibrate" position, inserted the output of a sine wave generator into the inputs of all of the Preston amplifiers simultaneously. All amplifiers were set to a "fixed" gain of X100 and--with the output of the sine wave oscillator set to give 5 mv rms--frequencies of 20, 200, 2000 and 20,000 Hz were recorded at the beginning of each day's testing. Each new reel of tape had the 2 kHz signal recorded on it to permit standardization of the gain during data processing.

The Preston amplifier outputs were connected to the appropriate tape recorder input and to a multi-position switch so that any of the amplified signals could be measured or viewed on an oscilloscope. This feature permitted the "Variable" gain on each amplifier to be set such that a 120 dB sound pressure level would give the same output (0.5 V rms at a course gain setting of X100) from all of the Preston amplifiers, thus normalizing the gains and facilitating the "quick-look" data analysis. The output from each tape reproduce amplifier was connected to a selector switch so that the reproduced data from any channel could be selected for oscilloscope viewing or metering.

Data screening in tunnel A was greatly facilitated by the fact that the model could be left in the flow continuously. Thus, the Preston amplifier coarse gain could be set for optimum record level for each channel before actuating the tape recorders. In Tunnels B and C, a gain setting was chosen on the basis of predicted acoustic noise levels, the model was then inserted into the flow for a nominal ten seconds while recording data and then retracted. While air jets were cooling the model, the tape recorded data was played back and all channels observed visually to assess the amplitude. If the amplitude were judged to be either too low or too high, amplifier gain was reset to a more appropriate value and a repeat run made. Although this was a time-consuming procedure, it was felt to be the best method of assuring that useable data were obtained from all sensors at all test conditions.

During nose changes or Reynolds number changes, model inspections were conducted to assure that no significant deterioration of the surface smoothness had occurred which might interfere with natural boundary layer transition. The RTV coatings held up extremely well through the entire test series and no repairs were necessary.

The B&K Model 4220 Piston phone was fitted with a very short rubber tube adapter to permit it to be fitted tightly over each microphone in the model so that—with care— reasonably accurate (±10%) checks on each complete sensor channel performance could be made with the model installed in the tunnel. These checks were performed before and after each day's testing and provided valuable qualitative information on system behavior.

SECTION II

DISCUSSION OF RESULTS

1. AEROTHERMODYNAMIC DATA AND ANALYSES

Wind tunnel data were obtained in Tunnels A, B, and C at Mach numbers of 4, 8, and 10, respectively. Since the acoustic instrumentation was located predominately along one conical ray, data were obtained with this ray on both the leeward and windward sides of the model (i.e., for both ± angles of attack). Tables III and IV present free stream conditions for which data were obtained. The -α condition implies data on the windward ray.

a. Transition Shape Data

Heat transfer data defining the shape of the transition front were obtained at Mach 8 and 10 along three conical rays. As mentioned earlier, the location of transition onset was defined as that point where the heat transfer (i.e., Stanton number) is a minimum. The end of transition was defined as the point where the heat transfer is a maximum. For the zero angle of attack case, comparisons of these data with the "design correlation" is shown in Figures 18 and 19 for $R_N = 0$ and $R_N \neq 0$, respectively. Agreement was good for all cases except for the low Reynolds number test at Mach 10 where transition onset was 5 inches aft of the expected value. Location of the transition region was obtained using the phosphorescent paint technique. The end of transition results from the phosphorescent paint technique for the Mach 4 tests are also shown in Figures 18 and 19.

For the sharp cone excellent agreement is noted. For the blunted cone, the Mach 4 data indicate that the end of transition, for a given free stream Reynolds number, is further forward than for the comparable Mach 8, 10 case. Comparisons of the end of transition from heat transfer and phosphor paint were made at Mach 8 and the data indicate that the two are in excellent agreement.

b. Local Flow Properties

Local flow properties on the model, which are required for the correlation and analysis of acoustic data, were not measured during this test series. Predictions of the flow conditions that existed on the cone were made using proven analytic techniques summarized in Table V. The inviscid flow properties such as the surface pressure distribution, and bow shock shape are required inputs to the viscous flow analysis programs. Viscous flow properties such as the boundary layer thickness parameters δ, δ^*, and θ were determined with the aid of computer programs defined in Table V. Summarized in Table VI are local flow properties, as deduced from the VIZAAD program [14], that exist over the forward two sensors in each array (i.e., at $x = 22.5$ and 38.0 inches). Some question arises as to the validity of these computed values since they will be utilized to normalize and correlate the measured data. One must recognize that the viscous programs such as VIZAAD[14] and SCAAT[15] are engineering techniques which rely on empirical correlations based upon ground test data for better agreement. Over the past several years

TABLE III. SUMMARY OF NOMINAL TEST CONDITIONS

Facility	Mach Number	Reynolds Number (× 10⁻⁶ Ft⁻¹)	Stagnation Pressure (psia)	Stagnation Temperature (°F)	Nose Radius (in.)	Angle of Attack (Degrees)
A	4	1.4	18	140	0	0 ±1 ±2 -4 -7.2 -8.2
		2.2	28		0	0 ±1 ±2 -4 -7.2
		2.8	35.7		0	0 ±1 ±2 -4 -7.2
		2.2	28		0.055	0 ±1 ±2 -4 -7.2
		3.0	38.1		0.110	0 ±1 ±2 -4 -7.2
B	8	1.4*	285	785	0	0 ±1 ±2 ±4 ±7.2
		1.4	285	785	0	0 ±1 ±2 ±7.2
		2.2	475	833	0	0 ±1 ±2 ±4 ±7.2
		2.8	620	853	0	0 ±1 ±2 ±7.2
		2.2	475	833	0.055	0 ±1 ±2 ±4 ±7.2
		3.25	730	865	0.110	0 ±1 ±2 ±7.2
C	10	1.34	1080	1450	0	0, -0.5, ±1, ±2, -4, -7.2
		2.2	1810	1450	0	0, -0.5, ±1, ±2, -4, -7.2
		2.2	1810	1450	0.055	0 ±1 ±2 -4 -7.2
		2.2	1810	1450	0.110	0
		2.2	1810	1450	0	-0.5 (with trip)

*Tunnel doors open, remaining tests in Tunnel B with doors closed.

TABLE IV. SUMMARY OF FREE STREAM CONDITIONS

Facility	M_∞	Re_∞ ft ($\times 10^{-6}$)	P_0 (psia)	T_0 (°R)	U_∞ (fps)	q_∞ (fsia)	P_∞ (psia)	T_∞ (°R)	ρ_∞ (lbm/ft^3)
A	4	1.4	18.2	605	2352	1.348	0.120	144	1.28×10^{-6}
		2.2	28.4	602	2332	2.109	0.187	143	2.0×10^{-6}
		2.8	39.9	597	2332	2.651	0.236	142	2.56×10^{-6}
		3.0	38.3	603	2332	2.832	0.252	143	2.70×10^{-6}
B	8	1.4	286.2	1257	3742	1.351	0.0305	92.2	8.93×10^{-4}
		2.2	473.8	1297	3800	2.212	0.0497	94.7	1.41×10^{-3}
		2.8	620.9	1321	3836	2.866	0.0641	95.9	1.80×10^{-3}
		3.25	728.2	1320	3835	3.342	0.0745	95.7	2.10×10^{-3}
C	10	1.4	1081	1910	4793	1.717	0.0245	95.7	6.92×10^{-4}
		2.2	1811	1911	4804	2.755	0.0383	93.6	1.105×10^{-3}

there have been many ground test programs, the results of which were used to upgrade the prediction capabilities of these engineering techniques. Some examples of the current accuracy of the viscous predictions using VIZAAD and SCAAT programs can best be illustrated from comparisons with measured heat transfer and viscous layer thickness parameter data. The heat transfer deduced using the thin wall back-face thermocouple technique for the test model is shown in Figure 16, for both $\alpha = 0°$ and $\alpha = 4°$. Note that agreement between theory and data are good for both laminar and turbulent boundary layer flows. As is customary with boundary layer theory, one can utilize the Reynolds analogy to relate skin friction to heat transfer, i.e.,

$$\frac{C_f}{2} = S_T P_r^{2/3} \quad \frac{\dot{q}}{\rho_e U_e (h_r - h_w)} P_r^{2/3}$$

Thus, if good agreement between theory and experiment with $\dot{q}$ is achieved, one can speculate that C_f will also be in good agreement.

As part of an earlier SAMSO sponsored study on the GE STREET-G contract, boundary layer profile measurements were obtained on a 7.25 degree half-angle cone in Tunnel B at Mach 8 [17]. From these measurements, the viscous layer thickness measurements were deduced. Figure 20 gives comparisons of the VIZAAD program with the transitional-turbulent boundary layer data. It is observed from this figure that the program accurately predicts the data levels and trends. Therefore, although the local flow properties were not measured, in this acoustic loads investigation, the prediction methods for deducing the local flow properties proved to be adequate.
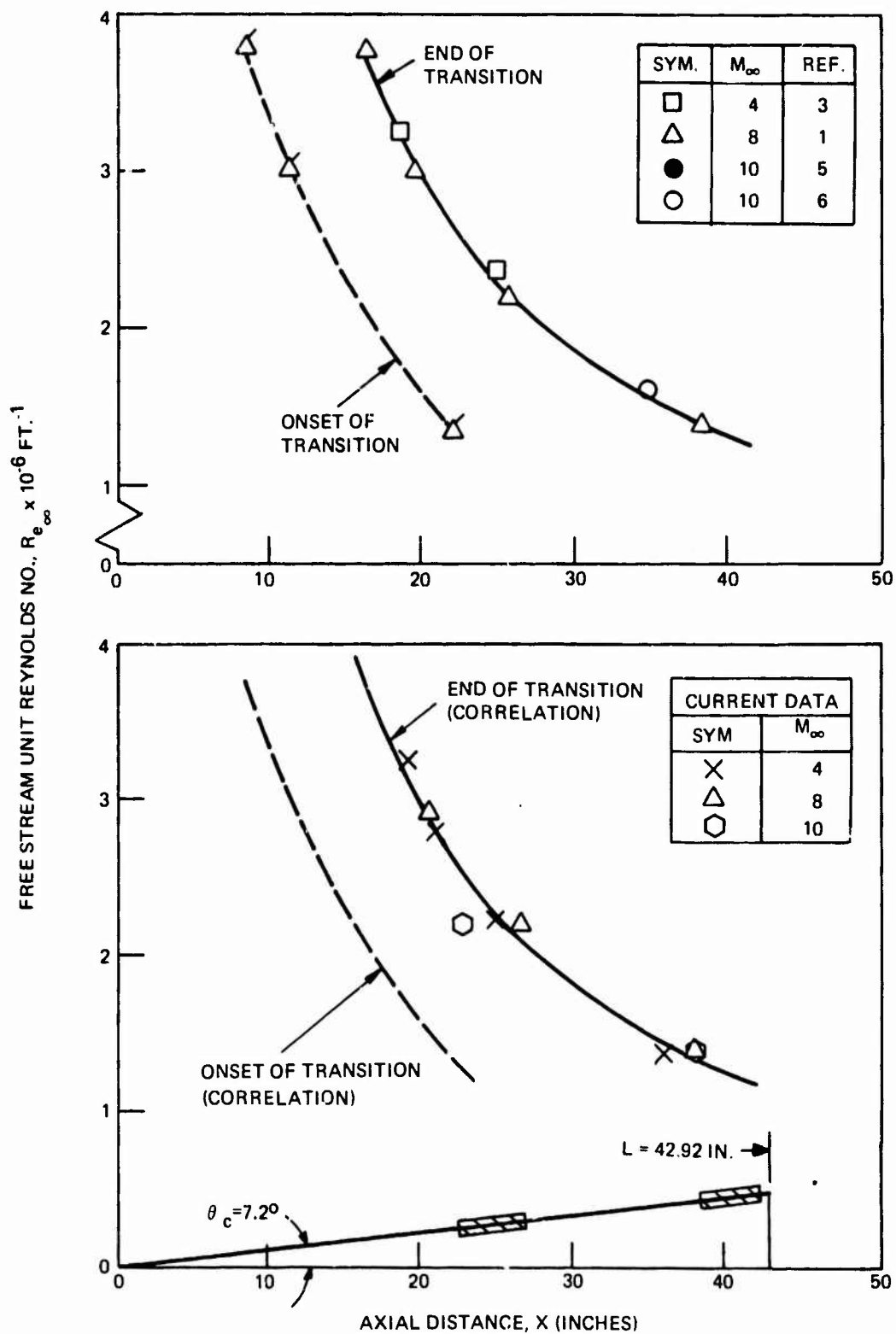
Figure 18. Correlation for the Location of the Boundary
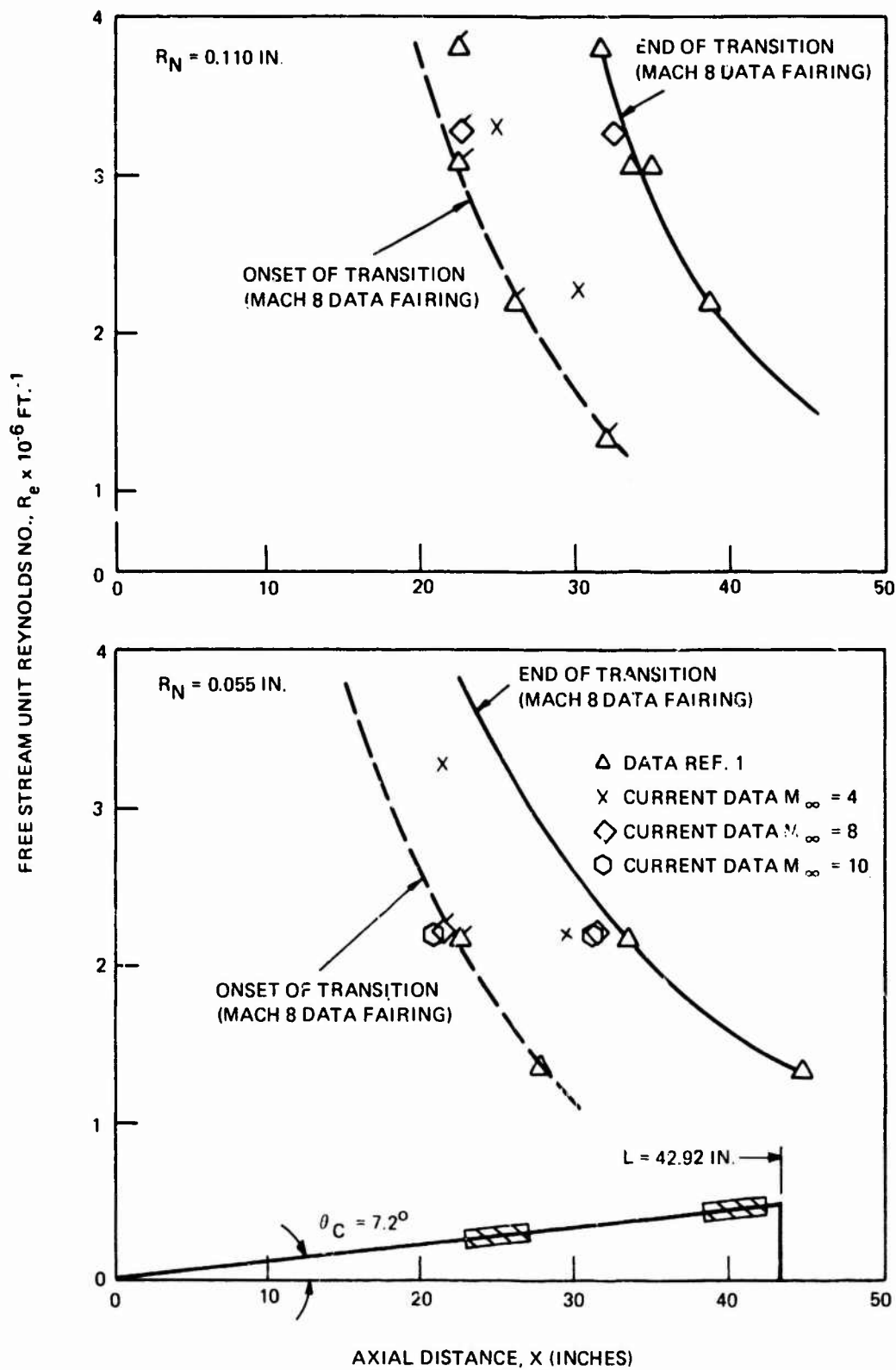Layer Transition Zone for Sharp Cones ($\alpha = 0°$)

Figure 19. Correlation for the Location of the Transition Boundary Layer Zone for Blunted Cones ($\alpha = 0°$)

TABLE V. AERODYNAMIC COMPUTER PROGRAMS

Programs	Program Capability	Vehicle Geometry	Theory	Program Function
Inviscid Real Gas Flow Field System(12)	Determines shock shape, complete flow properties in shock layer, static and dynamic force and moment coefficients, location and strength of embedded shocks	Two-dimensional or axisymmetric, sharp or blunt, expansion corners, flared bodies	Time-asymptotic Finite difference for blunt body solution, method of characteristics for locally supersonic flows, perturbation methods for dynamic analysis	Provides detailed solution for inviscid shock layer properties about given body; provides surface, pressures and shock shape for input to boundary layer calculations.
Inviscid Three-Dimensional Flow Field System (13)	Determines shock shape and complete inviscid flow properties about body at angle of attack	Nose: Arbitrary body of revolution Afterbody: Conical	Time-asymptotic finite difference solution over blunt nose; space-asymptotic solution for afterbody	Provides flow properties and shock shape for detailed analysis
Viscous Interaction Zero Angle of Attack Drag Program (VIZAAD)(14)	Determines boundary layer outer edge conditions, surface shear stress, induced pressure, and mass addition effects for laminar or turbulent flow	Two-dimensional or axisymmetric, sharp or blunt	Laminar: Modified Lees-Reference Enthalpy Turbulent: Walker-Reference Enthalpy Visc. Interaction: Lees and Probstein Mass Addition: Correlations	Rapid design tool for evaluation of enthalpy gradient, viscous interaction transverse curvature, and mass addition or vehicle drag

TABLE V. AERODYNAMIC COMPUTER PROGRAMS (Continued)

Programs	Program Capability	Vehicle Geometry	Theory	Program Function
Sphere-Cone Angle of Attack Program (SCAAT)[15]	Determines boundary layer outer edge conditions, surface shear stress, and aeroforce and moment coefficients due to viscous interacting trans. curvature, and mass addition	Spherically blunted cones	Laminar: Modified Lees-Reference Enthalpy Turbulent: Walker-Reference Enthalpy Viscous Interaction: Lees and Probstein Mass Addition: Correlations	Rapid design tool for evaluation of entropy gradient, viscous interaction, transverse curvature, and mass addition on vehicle force and moment coefficients.
Equilibrium Nonsimilar Boundary Layer Program (ENSBL)[16]	Determines detailed solution of laminar transitional, and turbulent boundary layer equation with mass addition and transverse curvature effects	Two-dimensional or axisymmetric, sharp or blunt	Finite-difference solution of boundary layer equations; eddy-viscousity model used for transitional and turbulent flows. Noble Program. Uses method of spalding and atanker to avoid numerical complexity near wall.	Provides detailed profiles of boundary layer properties and values of gross boundary layer parameters such as thickness, surface shear stress and heat transfer.

36

TABLE VI. LOCAL FLOW PROPERTIES
($\alpha = 0°$)

Facility	M_∞	Re_∞/ft ($\times 10^{-6}$)	R_N (in.)	M_e	q_e (psia)	P_e/P_∞	Forward Array, x = 22.5 in.					Aft Array, x = 38.0 in.				
							C_f ($\times 10^3$)	Re_s ($\times 10^{-6}$)	δ (in.)	δ^* (in.)	θ (in.) $\times 10^3$	C_f ($\times 10^3$)	Re_s ($\times 10^{-6}$)	δ (in.)	δ^* (in.)	θ (in.) $\times 10^3$
A	4	1.4	0	3.63	1.63	1.55	3.08	3.15	0.130	0.050	6.75	1.85	5.34	0.465	0.179	24.2
		2.2	0	3.68	2.59	1.56	1.98	5.05	0.236	0.091	9.13	1.63	8.20	0.473	0.182	24.6
		2.8	0	3.69	3.25	1.55	1.75	6.01	0.271	0.104	14.1	1.53	10.64	0.472	0.182	24.5
		2.2	0.055	3.70	2.55	1.51	2.80	4.89	0.114	0.043	5.77	1.68	8.31	0.422	0.163	21.7
		2.25	0.110	3.69	3.66	1.51	2.63	6.84	0.098	0.038	5.10	1.57	11.87	0.389	0.151	20.1
B	8	1.4	0	6.71	2.64	2.87	2.13	3.75	0.139	0.061	5.76	1.31	6.67	0.414	0.180	17.4
		2.2	0	6.72	4.39	2.84	1.41	6.26	0.212	0.092	8.99	1.16	10.45	0.419	0.182	17.7
		2.8	0	6.73	5.70	2.83	1.27	7.95	0.240	0.104	10.2	1.09	13.33	0.415	0.180	17.6
		2.2	0.055	6.71	4.27	2.83	1.96	6.02	0.114	0.050	4.76	1.21	10.22	0.378	0.164	16.0
		3.25	0.110	6.77	6.74	2.82	1.86	8.66	0.097	0.042	4.05	1.11	15.41	0.343	0.145	14.5
C	10	1.4	0	8.00	4.17	3.75	1.94	3.82	0.137	0.061	5.61	1.20	6.99	0.455	0.167	16.0
		2.2	0	8.02	7.05	3.74	1.27	7.12	0.193	0.084	8.06	1.04	11.88	0.382	0.167	15.9
		2.2	0.055	8.08	6.79	3.54	1.78	6.85	0.104	0.045	4.30	1.05	11.43	0.345	0.159	14.3

37
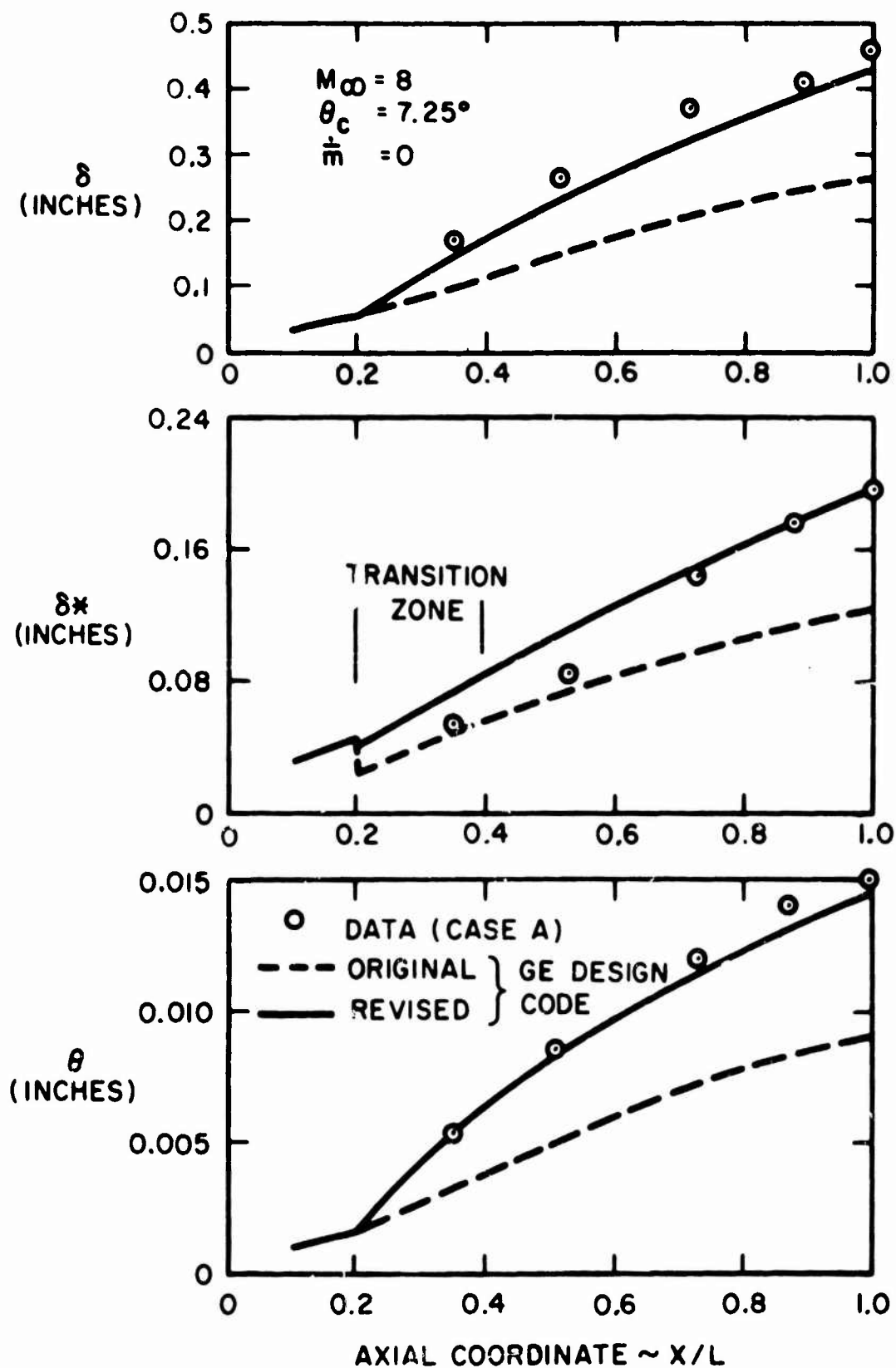
Figure 20. Comparison of Computed Boundary Layer Values to Test Data

c. Base Pressure Prediction

Analytic methods do not exist for the prediction of base pressures on slender cone configurations. As a result, one must resort to data correlations to obtain estimates of the base pressure for a prescribed cone and free stream conditions. Correlations have been developed for laminar-transitional flows [18] and for turbulent flows [19]. From these two sources, estimates of the mean flow centerline base pressure ratio, P_{bo}/P_∞ were obtained and are presented in Table VII. It was noted in Reference 18 that the base pressure, for laminar-transitional boundary layer flows, correlates with the value of the edge Mach number M_e, and wetted length Reynolds number at the cone shoulder. This implies that the value of P_{bo}/P_∞ is Reynolds number dependent. Implications from Reference 14 indicate that for turbulent flow this dependency is minimal. The results represented in Table VII reflect these observations.

2. ACOUSTIC DATA ANALYSIS

Fluctuating pressure data in transitional, fully turbulent, separated and base flow were obtained for selected angles of attack at three test Mach numbers and Reynolds number. Data was also obtained for various nose radii at selected tunnel conditions. Table VII defines the various tunnel conditions and model attitude for which data was obtained.

TABLE VII. BASE PRESSURE ESTIMATES – CENTERLINE OF SYMMETRY ($\alpha = 0^\circ$)

M_∞	Re_∞/ft $\times 10^{-6}$	M_e	Re_s $\times 10^{-6}$	P_{bo}/P_∞
4	1.4	3.7	6.05	0.13
	2.2		9.52	0.12
	2.8		12.11	0.12
8	1.4	6.8	7.85	0.20
	2.2		12.35	0.17
	2.8		15.7	0.16
10	1.4	8.1	8.64	0.57
	2.2		13.55	0.55

a. Acoustic Intensity

For screening purposes, the acoustic data were reduced using one-third octave band analysis to 20 kHz, which included the overall pressure level for this frequency range. Effects of angle of attack (windward ray) on the overall sound pressure level distribution at Mach 4 for three unit Reynolds numbers are shown in Figures 21, 22, and 23. As expected, the transition zone moves aft for negative angle of attack and decreasing Reynolds number.

Tunnel tare noise was obtained for each test from sensor 2, located in the laminar flow region. As the test Reynolds number (R_e) increased, tunnel tare noise also increased with a significant jump between $R_e = 1.4 \times 10^6$/ft and $R_e = 2.2 \times 10^6$/ft. This is believed due to additional compressor stages required to achieve desired operating conditions. Tunnel tare noise reached approximately 124 dB at Mach 8 and 127 dB at Mach 10, as indicated in Figure 24. This figure compares pressure distributions at low angle of attack for the three test Mach numbers and a given unit Reynolds number of 2.2×10^6. Fisher and Weinstein [20] noted that a region exists upstream of the classical point on the body surface where the heat transfer begins to rise, which was used in the present study to define transition onset. In this region the outer portions of the boundary layer are turbulent and the inner region is laminar. Hence, the critical disturbance begins at the outer upstream layer and spreads to the wall as one moves downstream. These authors determined that the spreading angle relative to the wall was in the range from 0.5 to 1.0 degree at local Mach numbers from 2.5 to 13.6. Thus a microphone located at a point upstream of the transition region (such as sensor 2 in this study) would indicate higher sound pressure levels than that associated with the free stream because of the turbulence that exists in the outer portions of the boundary layer. Tunnel tare noise levels thus measured actually are combined measurements depending upon the location of the transition zone.

Benefiting from the lower tunnel tare noise levels associated with tests conducted at $R_e = 1.4 \times 10^6$/ft, estimates of acoustic intensity were made. Figure 25 gives representative pressure distributions at this Reynolds number for the three test Mach numbers. Using data from Figure 25 in turbulent flow results in the following nondimensional acoustic intensity given in Table VIII.

TABLE VIII. ACOUSTIC INTENSITY FOR TURBULENT FLOW

| M_∞	Local Mach No.	P_{rms}/q_e (0 to 20 kHz)	
		Actual Data	Noise Eliminated
4	3.6	1.62×10^{-3}	1.31×10^{-3}
8	6.7	1.1×10^{-3}	0.58×10^{-3}
10	8	1.27×10^{-3}	0.67×10^{-3}
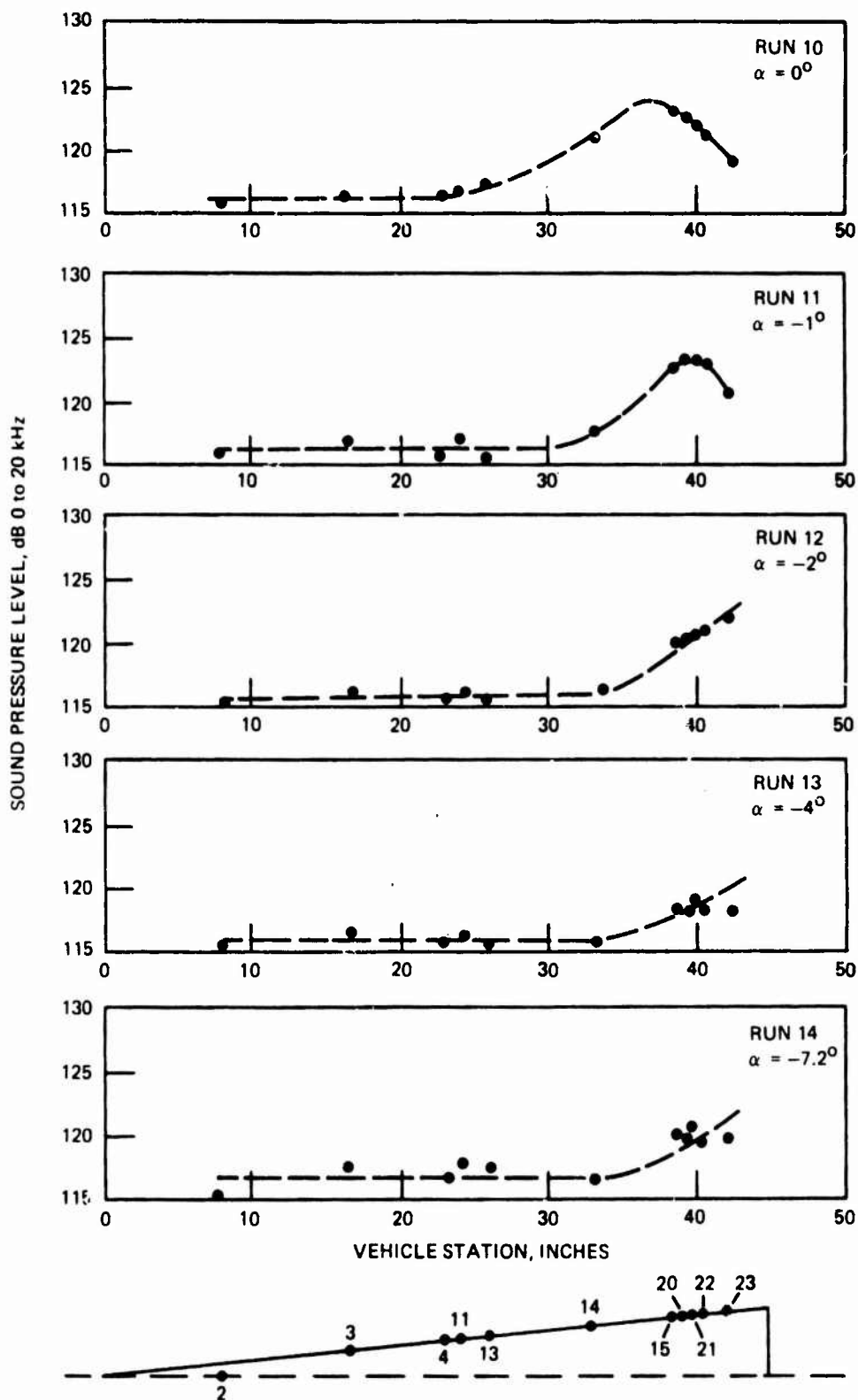
Figure 21. Fluctuating Pressure Distribution Tunnel Condition
$(R_{e_\infty} = 1.4 \times 10^6, \; M_\infty = 4.0, \; R_N = 0.0)$
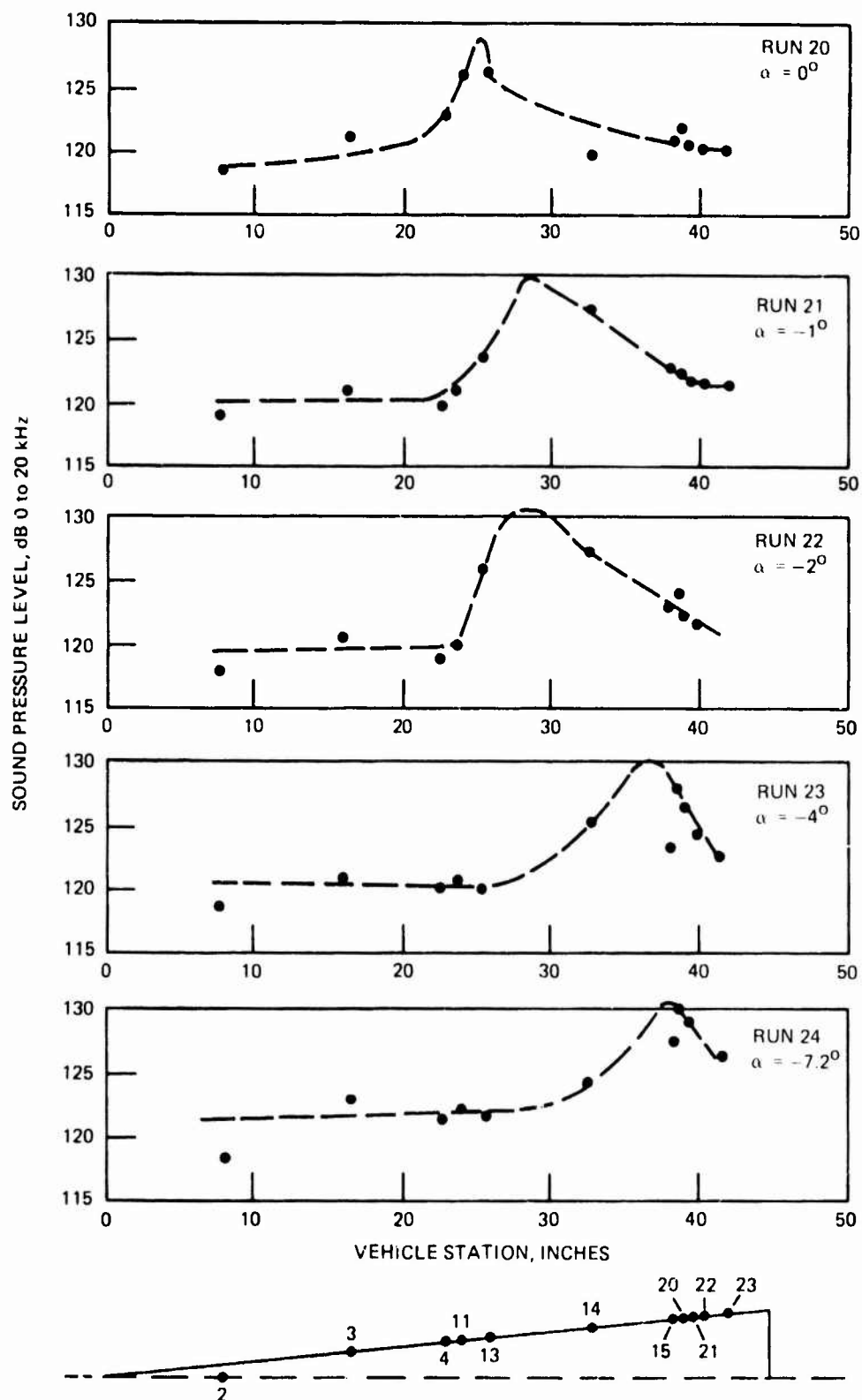
Figure 22.   Fluctuating Pressure Distribution Tunnel Condition
($Re_\infty = 2.2 \times 10^6$, $M_\infty = 4.0$, $R_N = 0.0$)
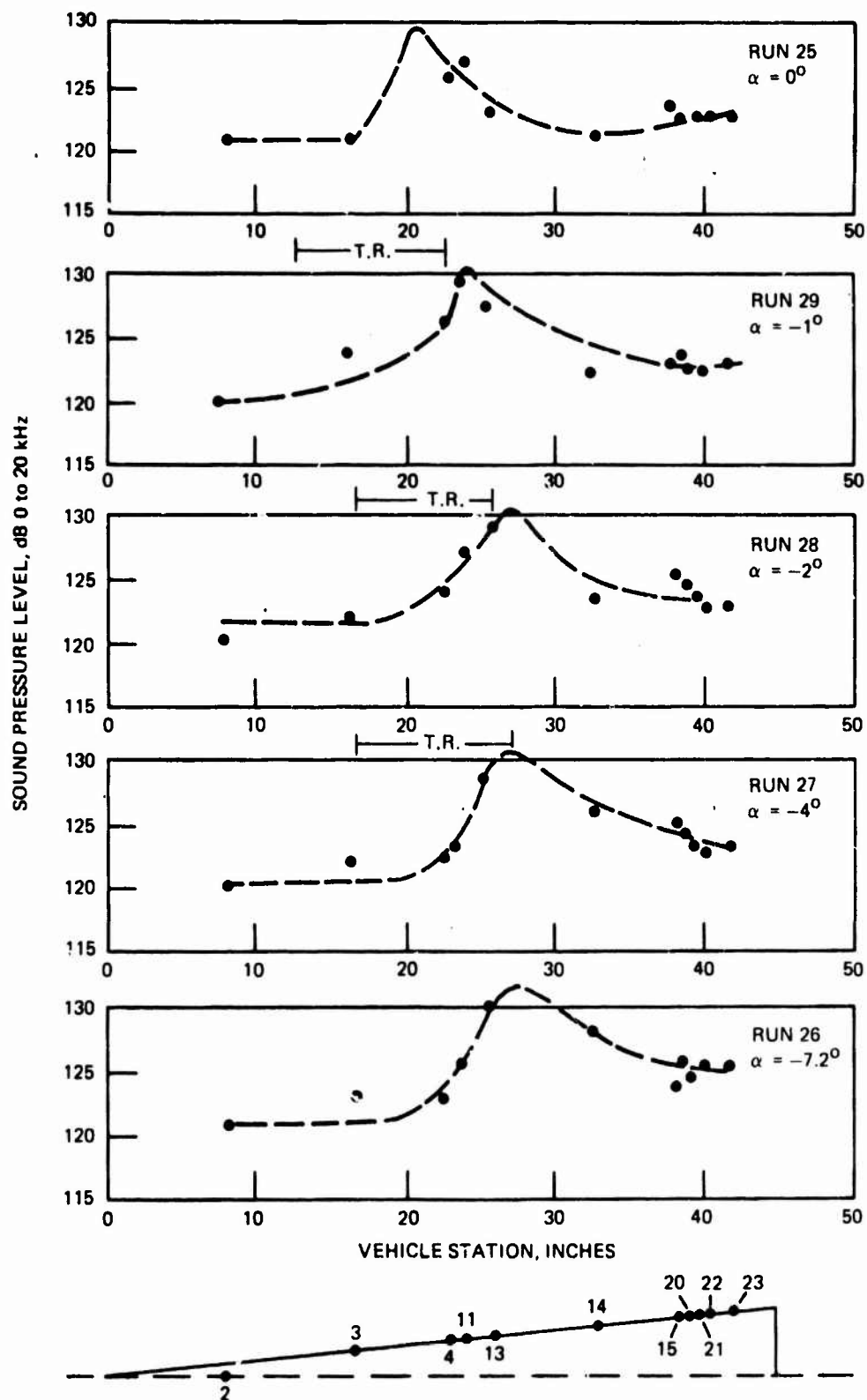
Figure 23. Fluctuating Pressure Distribution Tunnel Condition
$(Re_\infty = 2.8 \times 10^6, M_\infty = 4.0, R_N = 0.0)$
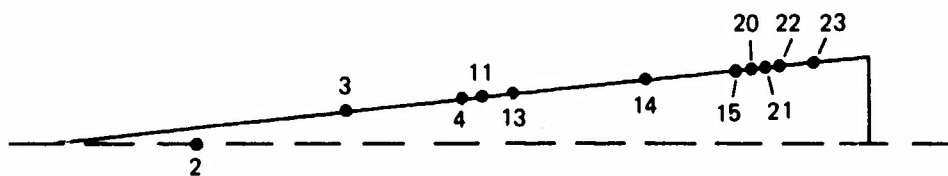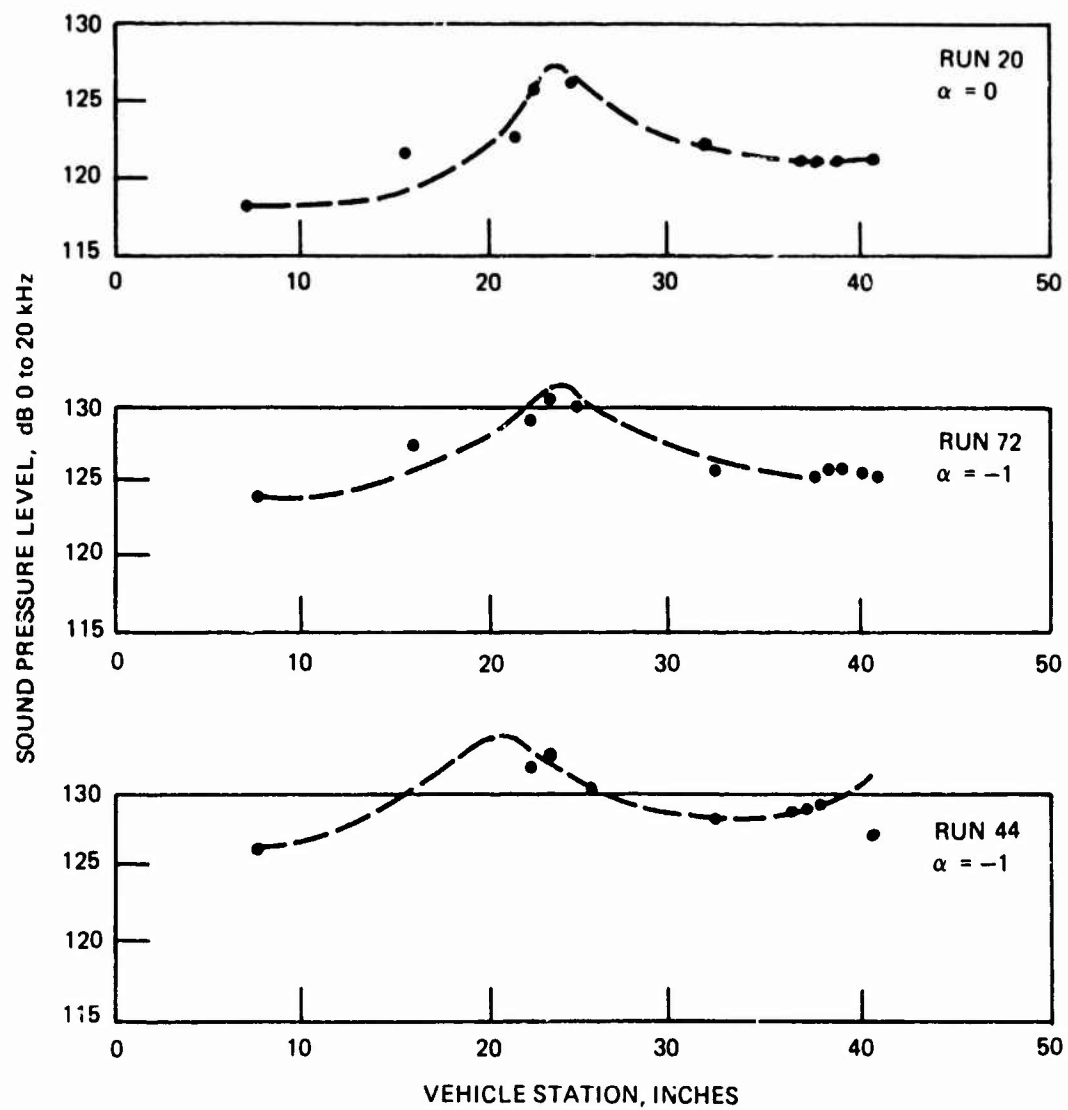
Figure 24. Fluctuating Pressure Distribution Tunnel Condition
$(R_{e_\infty} = 2.2 \times 10^6, \ M_\infty = 4.0, \ 8.0, \ 10.0, \ R_N = 0)$

It is apparent from Figure 25 that the tunnel tare noise level must be considered for data obtained at Mach 8 and 10, the degree is unknown. Hence, the data is presented as spread in data.

Table IX summarizes the peak normalized fluctuating pressures measured during transitional flow. The acoustic environment in the transition region is a gradual build up in fluctuating pressure reaching a maximum towards the end of the transition zone. Fully turbulent flow is achieved at distances downstream ranging from 10 to 100 boundary layer thicknesses. Pressure distributions in Figure 24 are representative of data obtained in the transition zone.

TABLE IX. PEAK ACOUSTIC INTENSITY IN TRANSITIONAL FLOW

M_∞	Local Mach No.	P_{rms}/q_e (0 to 20 kHz)
4	3.7	2.86/-3 - 3.16/-3
8	6.9	1.85/-3 - 2.70/-3
10	8.1	1.67/-3 - 1.96/-3

A 5 to 10 dB difference exists between tunnel tare noise and peak transitional data, therefore tunnel tare noise does not present a problem in data evaluation.

Several tests were conducted at a free stream Mach number of 8 at angles of attack of $\alpha \pm 7.2°$ (vehicle half cone angle) which resulted in separate flow on the leeward side of the vehicle. Though these high angles of attack are not representative of nominal ballastic flight, they are of interest in regards to advanced re-entry vehicle concepts. Figure 26 represents typical fluctuating pressure distributions measured at these high angles of attack. Of significance in these runs are the high fluctuating pressures on the windward side of the vehicle which remain high downstream from the transition region, and the low pressure levels on the leeward side of the vehicle in the separated flow region. Levels were observed to fall below tunnel tare noise levels indicating attenuation across the shock wave. The composite distribution results in a 15 dB circumferential variation in fluctuating pressures over a large portion of the vehicle. This could excite the higher shell harmonics, or "hoop modes", thereby inducing responses in the vehicle which should be considered.

Fluctuating pressure measurements were also made on the base of the test vehicle for all runs. Figure 27 represents typical distributions measured for three test Reynolds numbers at a free stream Mach number of 4.0. Data obtained at Mach 8 exhibited erratic spectral characteristics, which are discussed in Section II.2.b, such that this data was considered invalid. At a free stream Mach number of 10 only sensor 24 located at the center of the base provided well behaved spectra. Typical levels are also given in Figure 27. A slight increase in pressure levels is observed at 0.26 r_b, however sensors located

45
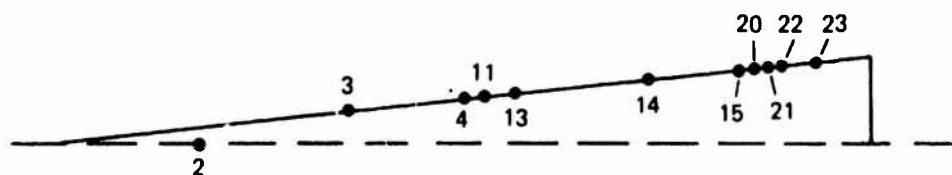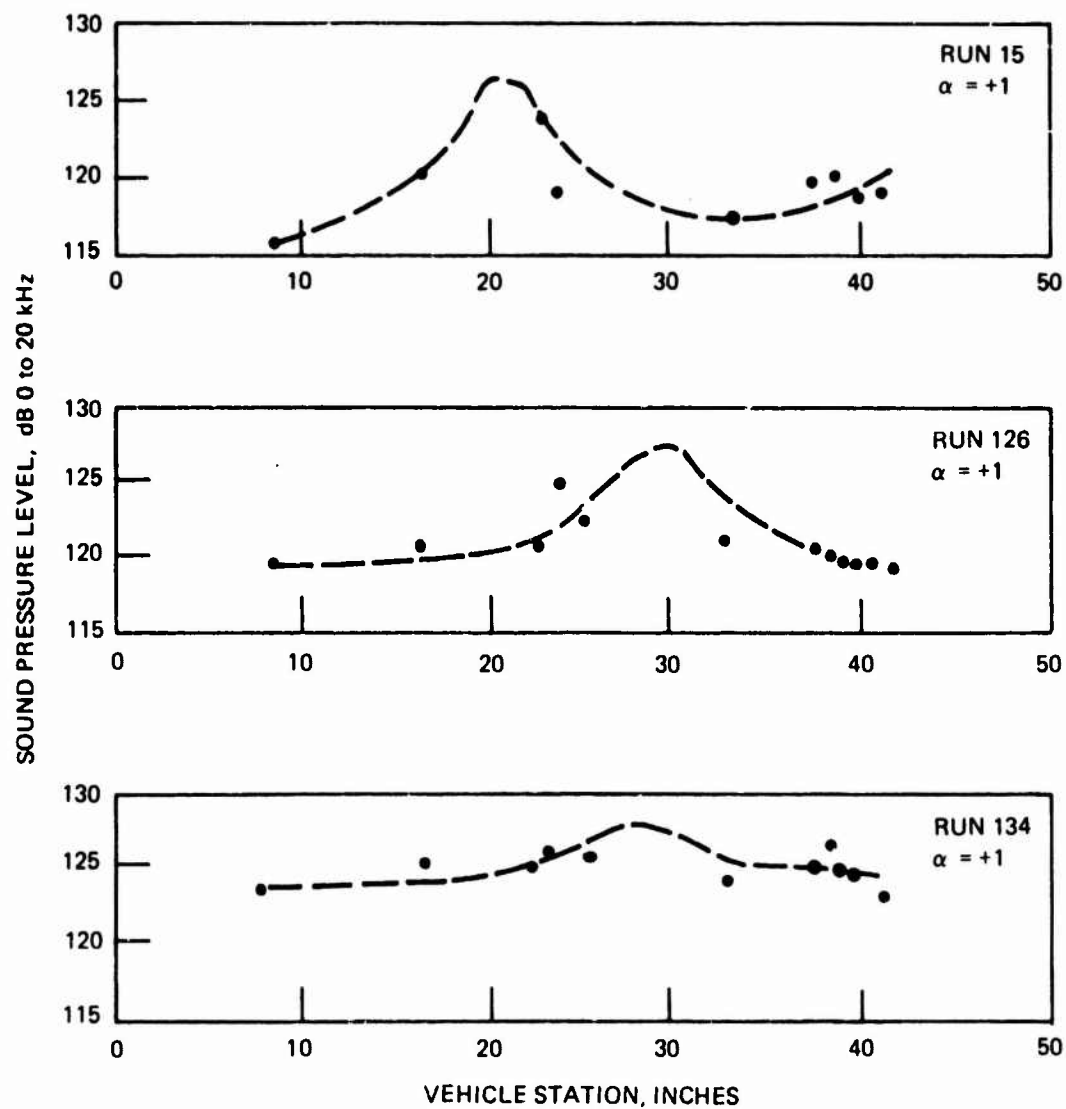
Figure 25. Fluctuating Pressure Distribution Tunnel Condition
$(R_{e_\infty} = 1.4 \times 10^6, \ M_\infty = 4.0, \ 8.0, \ 10.0, \ R_N = 0)$

(RUN − 116)

α = 7.2°

(RUN − 120)

(RUN − 107)

α ≈ 7.2°

(RUN − 110)
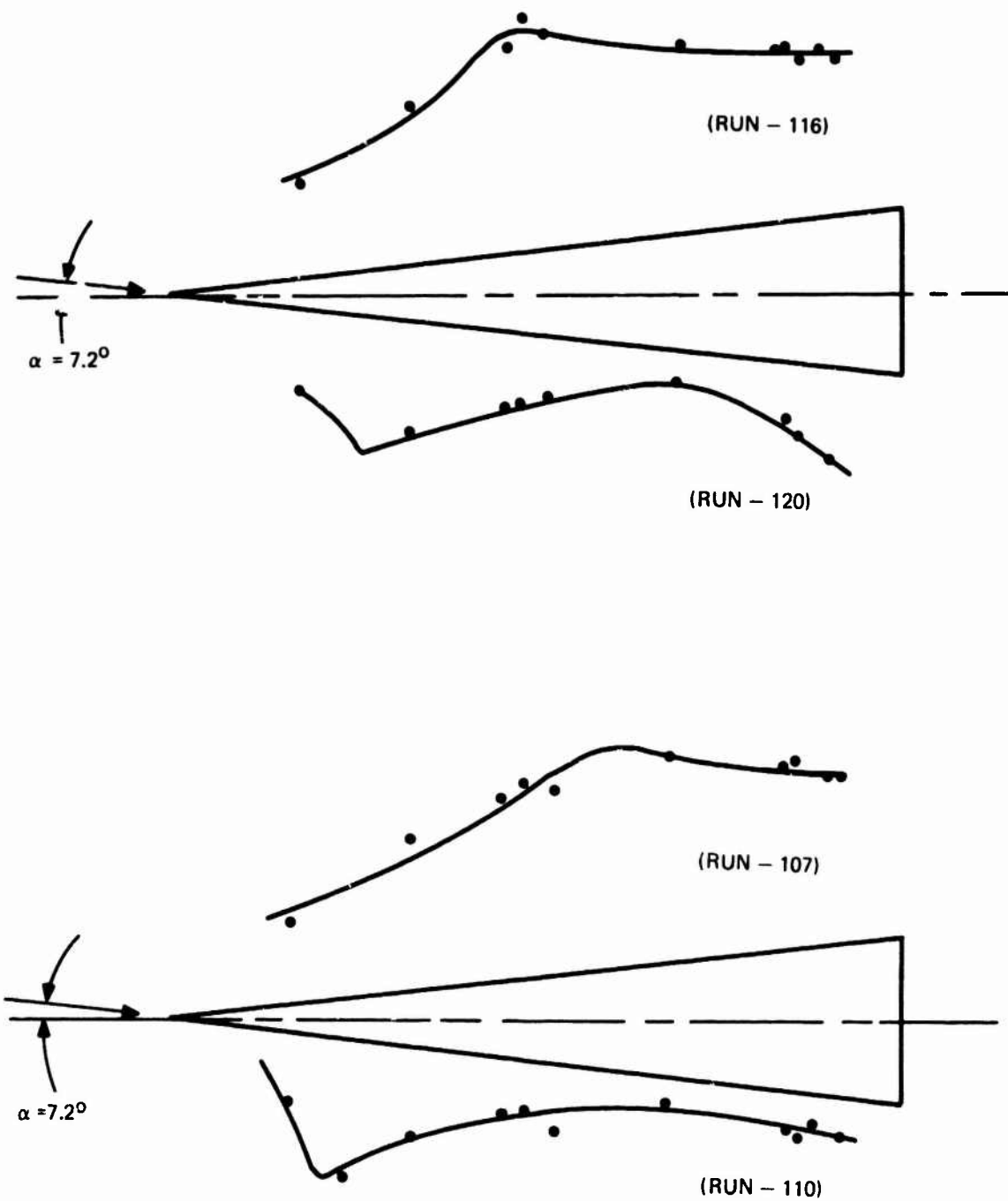
Figure 26. Acoustic Intensity Distribution (dB) at High α ($\pm 7.2°$)

47
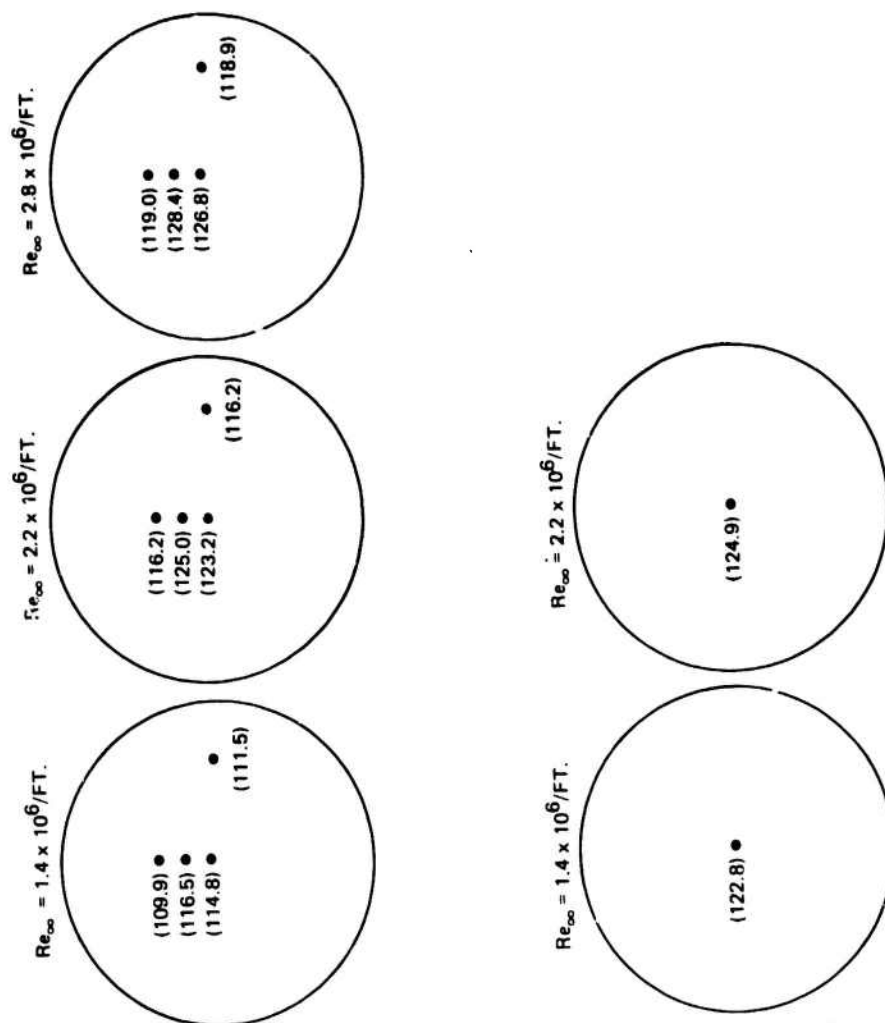
Figure 27. Base Acoustic Intensity Distribution (dB) at Various Reynolds Numbers and Mach Numbers (α = 0)

at 0.52 r_b (sensors 26 and 28,0 and 90° ray) show a consistent drop in fluctuating pressure levels. Figure 28 shows the variation in fluctuating pressure levels for various angles of attack measured at the center of the base for all three test conditions. In general, the highest pressure levels were observed at zero angle of attack. As the Reynolds number was increased, the fluctuating pressure also increased in a proportionate manner. Figure 29 shows the effect of bluntness on the overall sound pressure level at Mach 4. For this comparison, free stream conditions were selected so that the location is fixed on the model surface. It is evident from these results that over the range investigated, there is little effect of bluntness on the sound pressure level and distribution, (including base flow) although bluntness does have an effect on the location of transition on the body.

b. Power Spectral Density Distribution

Acoustic spectra are presented in the form of third octave pressure distributions and normalized spectra $\left[\dfrac{\phi(f) \, U_e}{q_e \delta^*} \right]$. Figure 30 presents as measured (no consideration given to noise) power spectral distribution for $R_{e_\infty} = 1.4 \times 10^6/$ ft at $M_\infty = 4$ along with the same data with tunnel tare noise eliminated. Figures 31 and 32 represent typical data obtained at the free stream Mach numbers of 8 and 10. For these Mach numbers, the degree to which tunnel tare noise affects the true levels is unobtainable. Therefore, the data as measured represents a conservative distribution.

Figures 33, 34 and 35 present normalized pressure sprectra (using local flow properties) of transitional flow. These spectra were obtained at the location where the fluctuating pressure was maximum in the transition zone. Transition spectra obtained on forward and aft arrays were similar with a tendency for measurements on the aft array to roll-off at a slightly higher Strouhal number. Figure 36 ($M_\infty = 4$, $R_{e_\infty} = 1.4 \times 10^6/$ft) shows the third octave pressure distributions at various points in the transition region. At peak transition it is noted that the pressure distribution across the frequency range is increased by 8 to 15 db. During transition decay (region between peak pressure levels and fully developed turbulent flow) the pressure in both the high and low frequency ranges drop equally; however, in the 1 kHz to 5 kHz range, fluctuating pressures remain high until further down stream, where all levels throughout the frequency range decrease to the turbulent flow level. Figures 37 and 38 are similar curves defining pressure spectra for various degrees of transitional flow. Similarly, in the transitional decay region, high frequency pressures are observed to attenuate more rapidly. Tunnel conditions for both figures are $M_\infty = 4$ and $R_{e_\infty} = 2.2 \times 10^6/$ft. It is also apparent from these figures that data obtained in the turbulent flow regime are masked by the tunnel tare noise. In Figure 36, however, good separation exists between tunnel tare noise and turbulent flow (tunnel conditions $M_\infty = 4$, $R_{e_\infty} = 1.4 \times 10^6/$ft. Figures 39 and 40 define the pressure distribution for various stages of transitional flow at Mach 8. Similar characteristics to those observed at Mach 4 are evident.

At an angle of attack equal to the half cone angle of the test vehicle separated flow occurs on the leeward side of the vehicle. The effects on the fluctuating pressure levels were significant in that extreme low pressures ($P_{rms} \approx 117$ dB) were observed

49
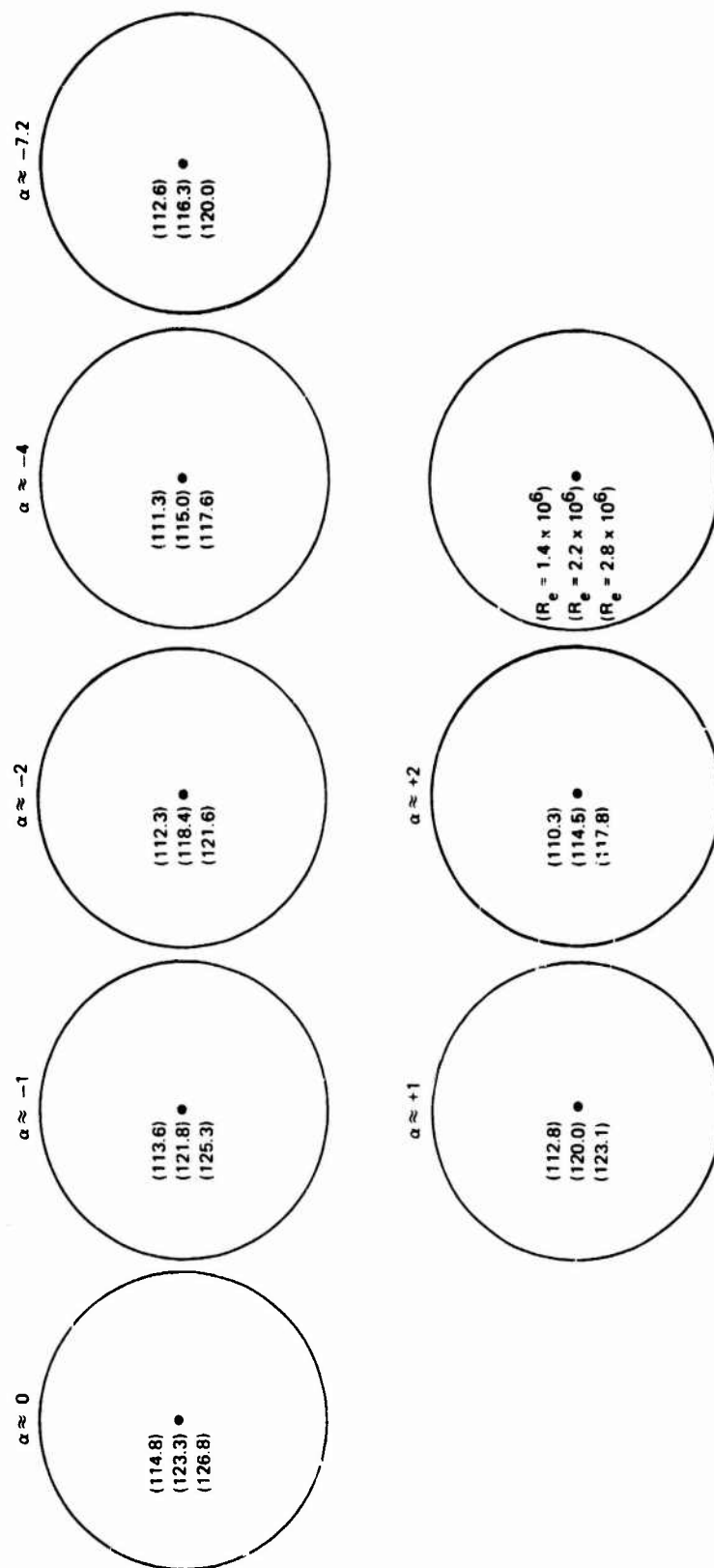
Figure 28. Base Acoustic Intensity Distribution (dB) at Various Reynolds Number Angles of Attack ($M_\infty = 4.0$)
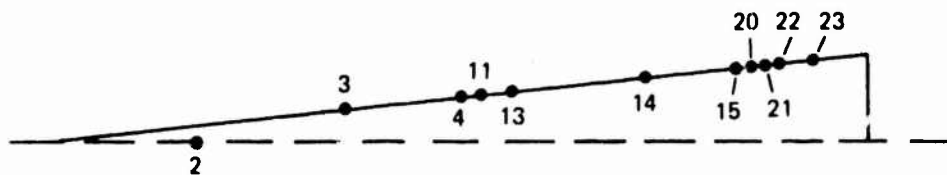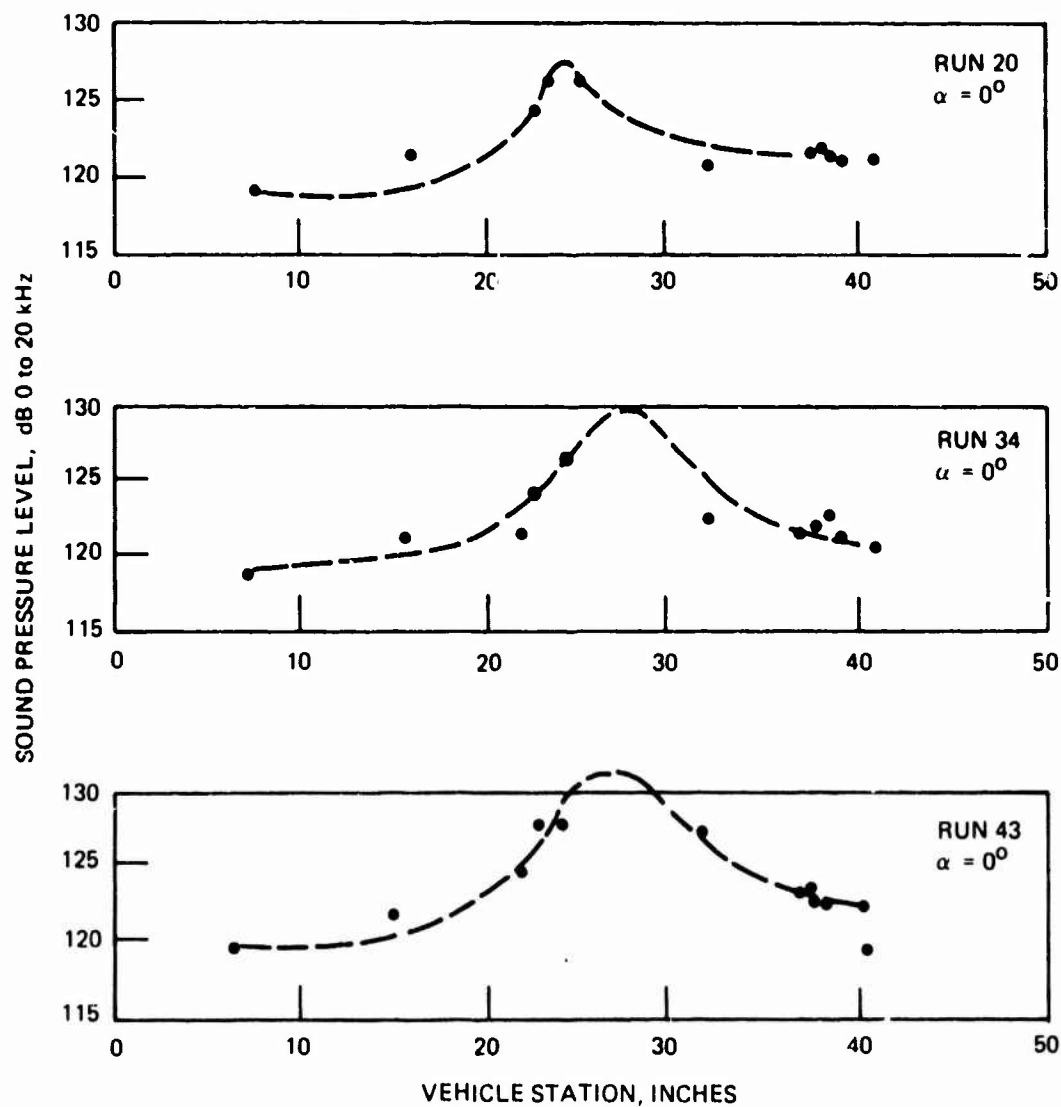
Figure 29. Fluctuating Pressure Distribution Tunnel Condition
$(R_{e_\infty} = 2.2 \times 10^6,\ M_\infty = 4.0,\ R_\infty = 0.0,\ 0.055,\ 0.110)$

51
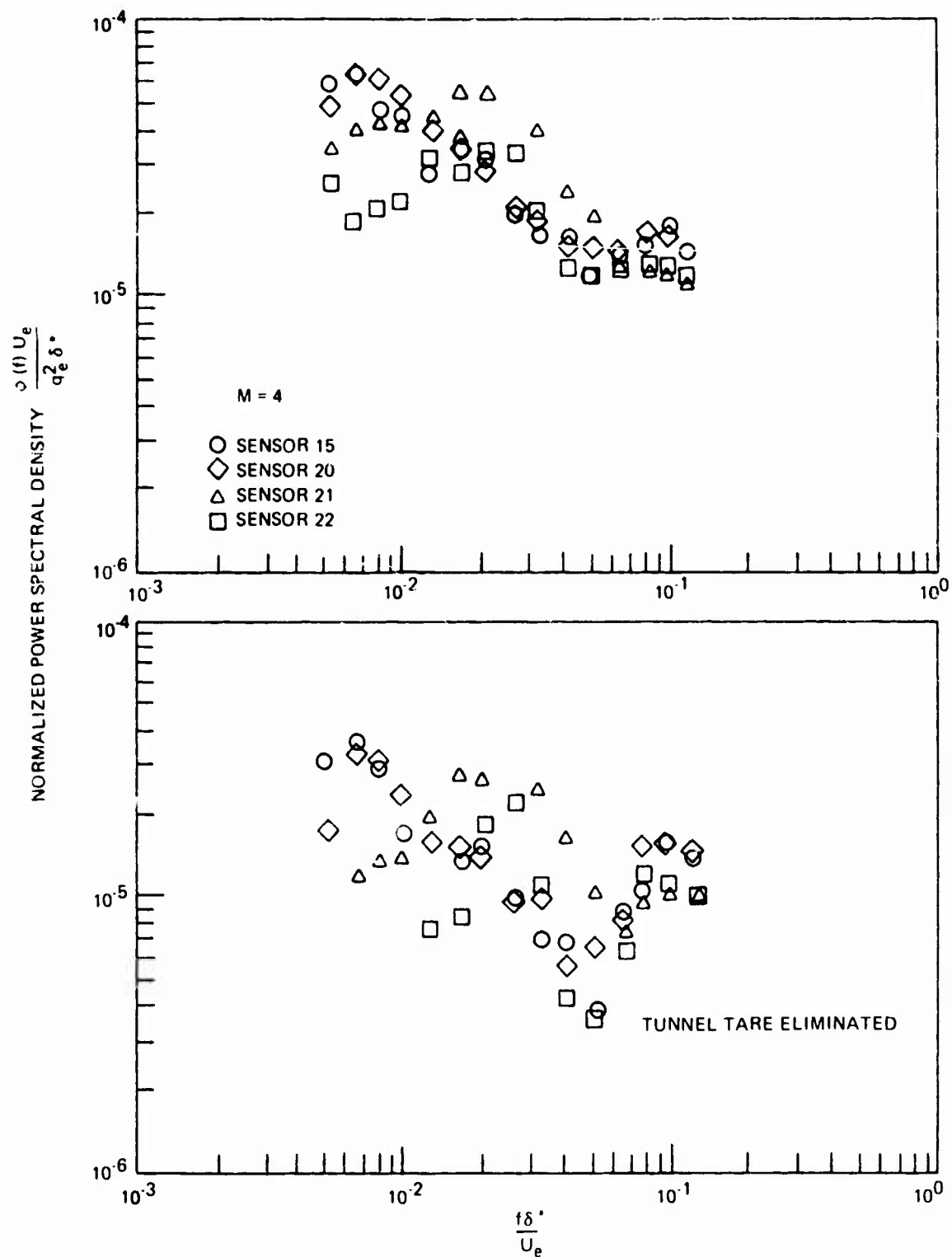
Figure 30. Normalized Power Spectral Density Distribution
for Turbulent Flow ($M_\infty = 4.0$)
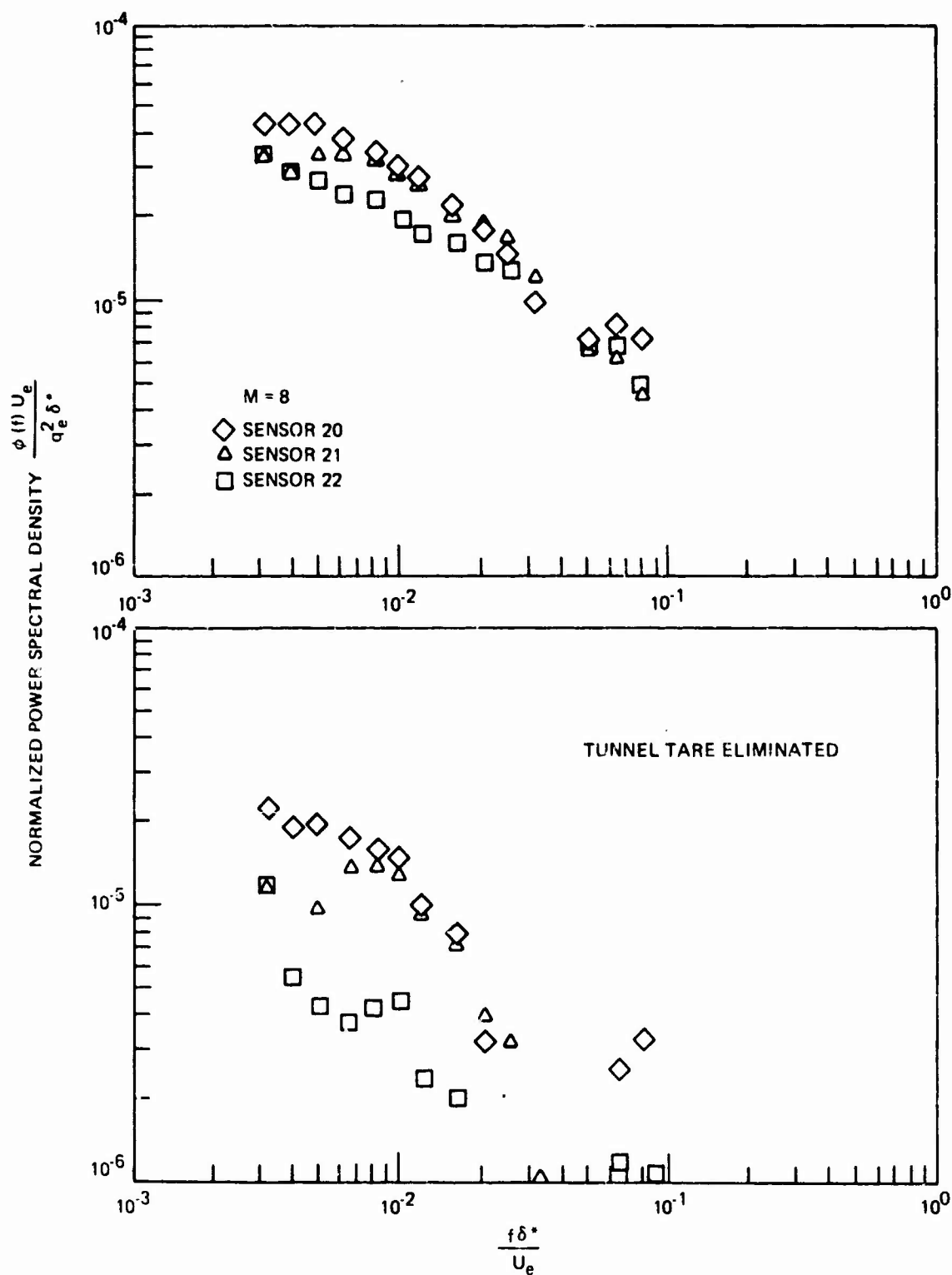
Figure 31. Normalized Power Spectral Density Distribution
for Turbulent Flow ($M_\infty = 8.0$)
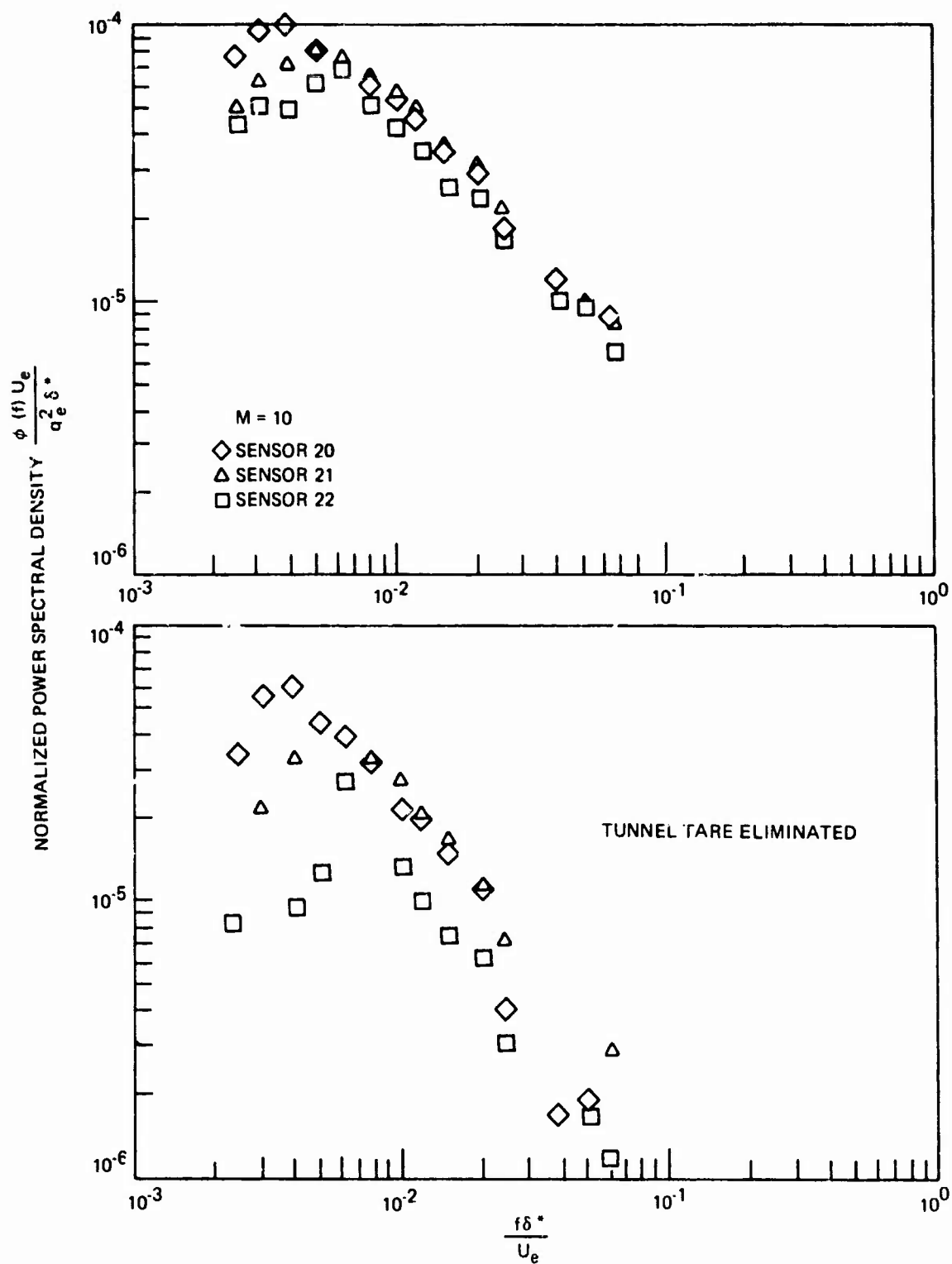
Figure 32. Normalized Power Spectral Density Distribution
for Turbulent Flow ($M_\infty = 10.0$)

54
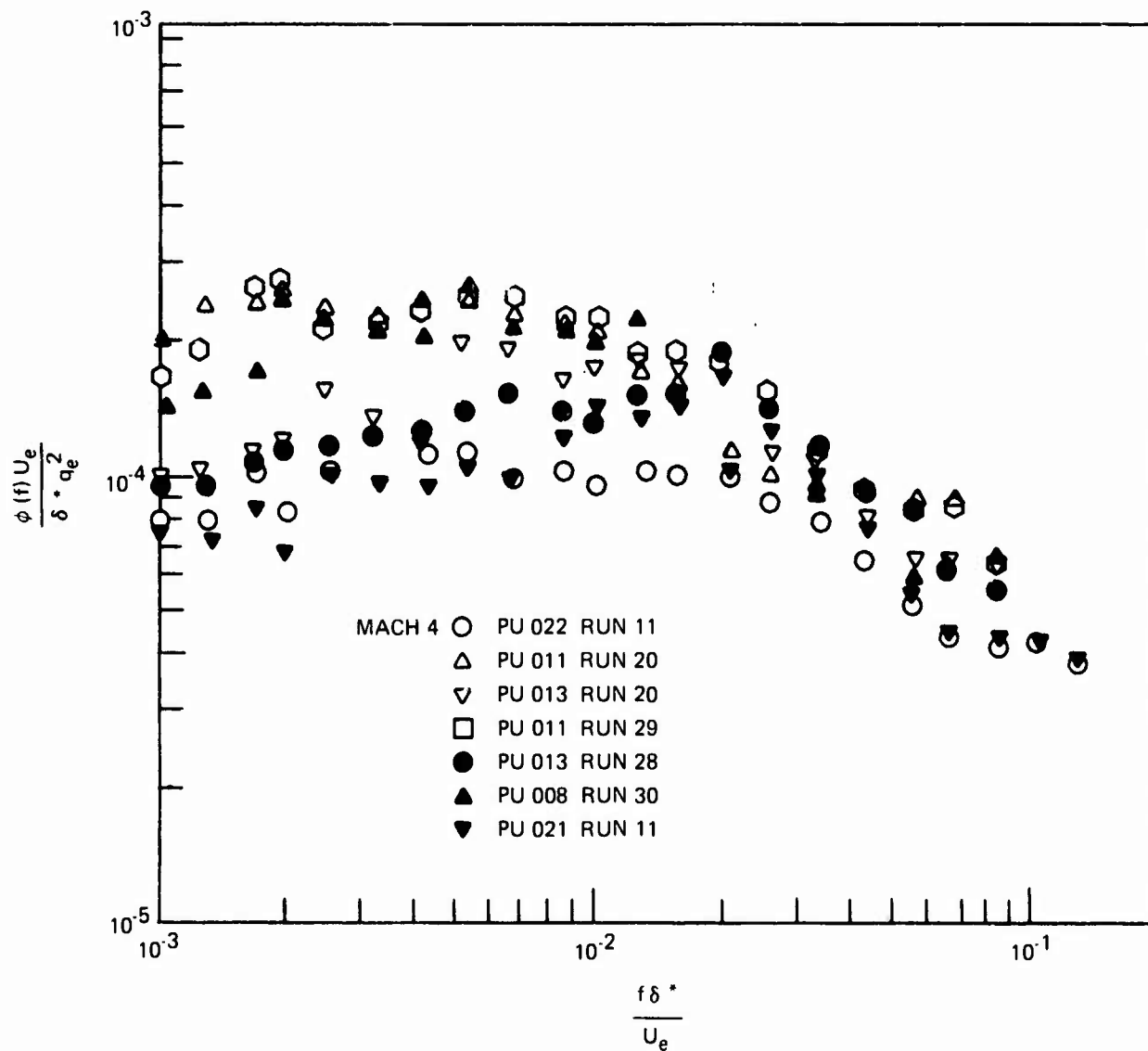
Figure 33. Normalized Power Spectral Density Distribution
for Transitional Flow ($M_\infty = 4.0$)

55
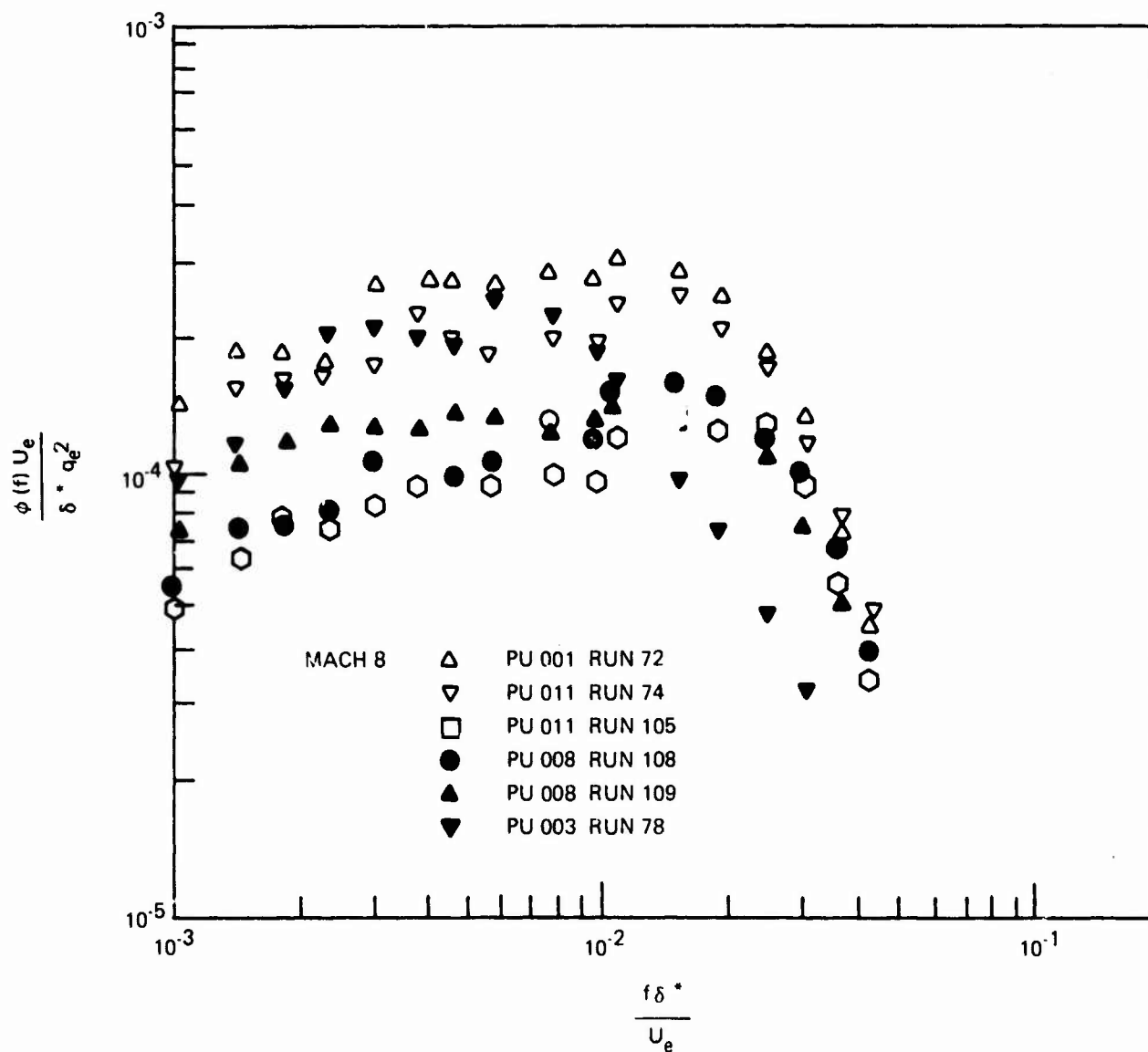
Figure 34. Normalized Power Spectral Density Distribution
for Transitional Flow ($M_\infty = 8.0$)

56
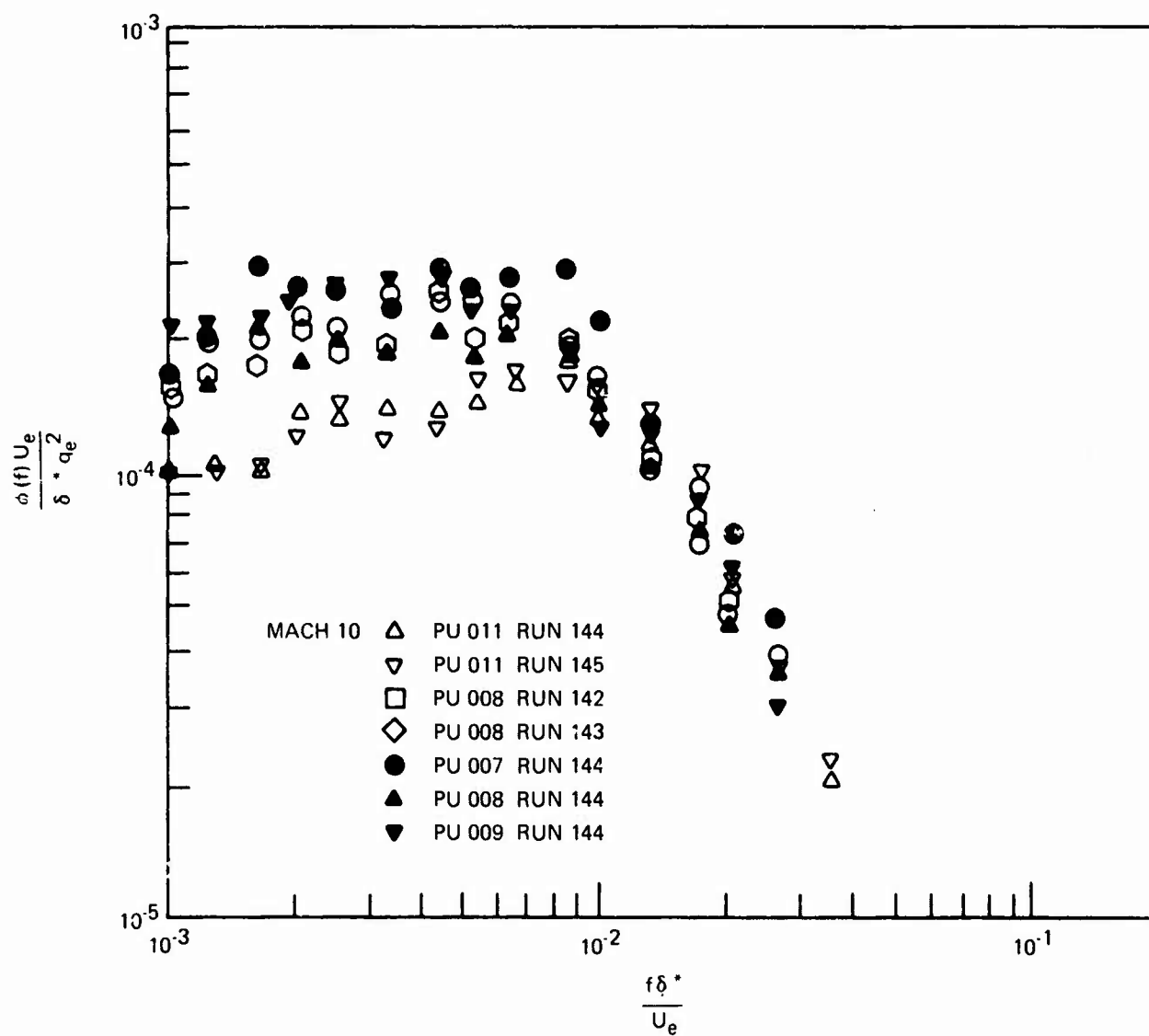
Figure 35. Normalized Power Spectral Density Distribution
for Transitional Flow ($M_\infty = 10.0$)
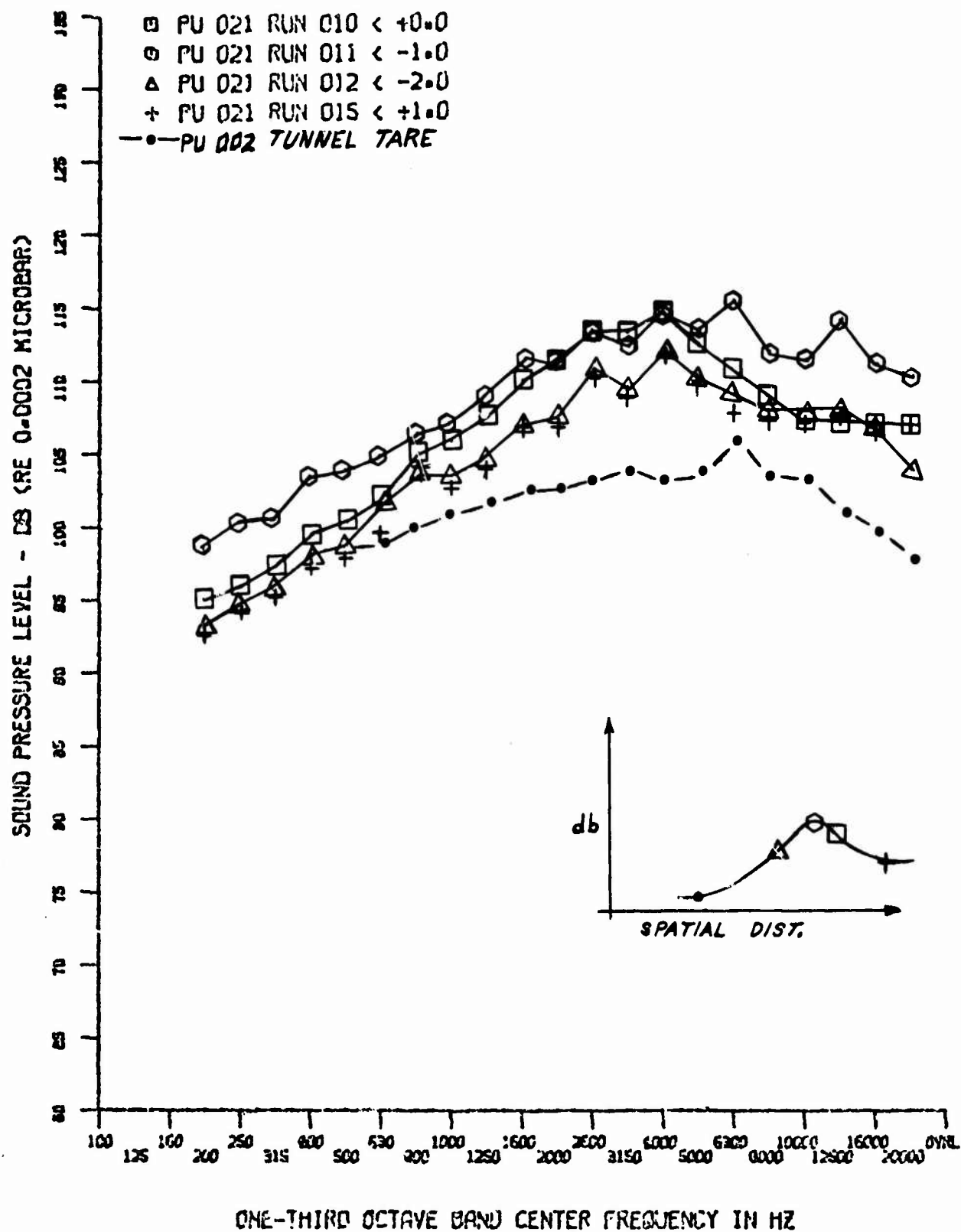
Figure 36. Spectral Distribution for Transitional Flow ($M_\infty = 4.0$)
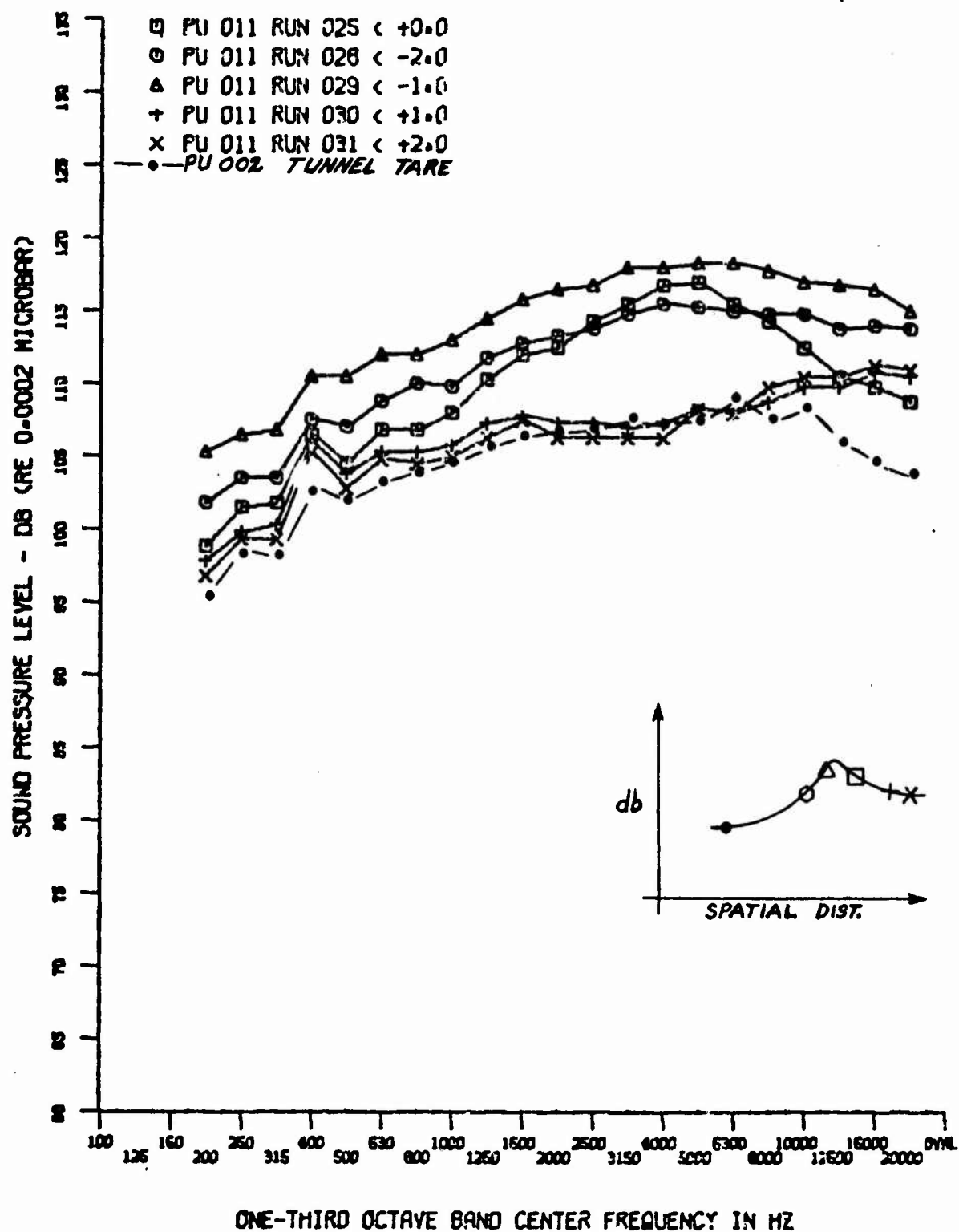
Figure 37. Variation of Spectra in Transition Zone ($M_{\infty} = 4.0$, $R_{e_{\infty}} = 2.8 \times 10^6$)

59
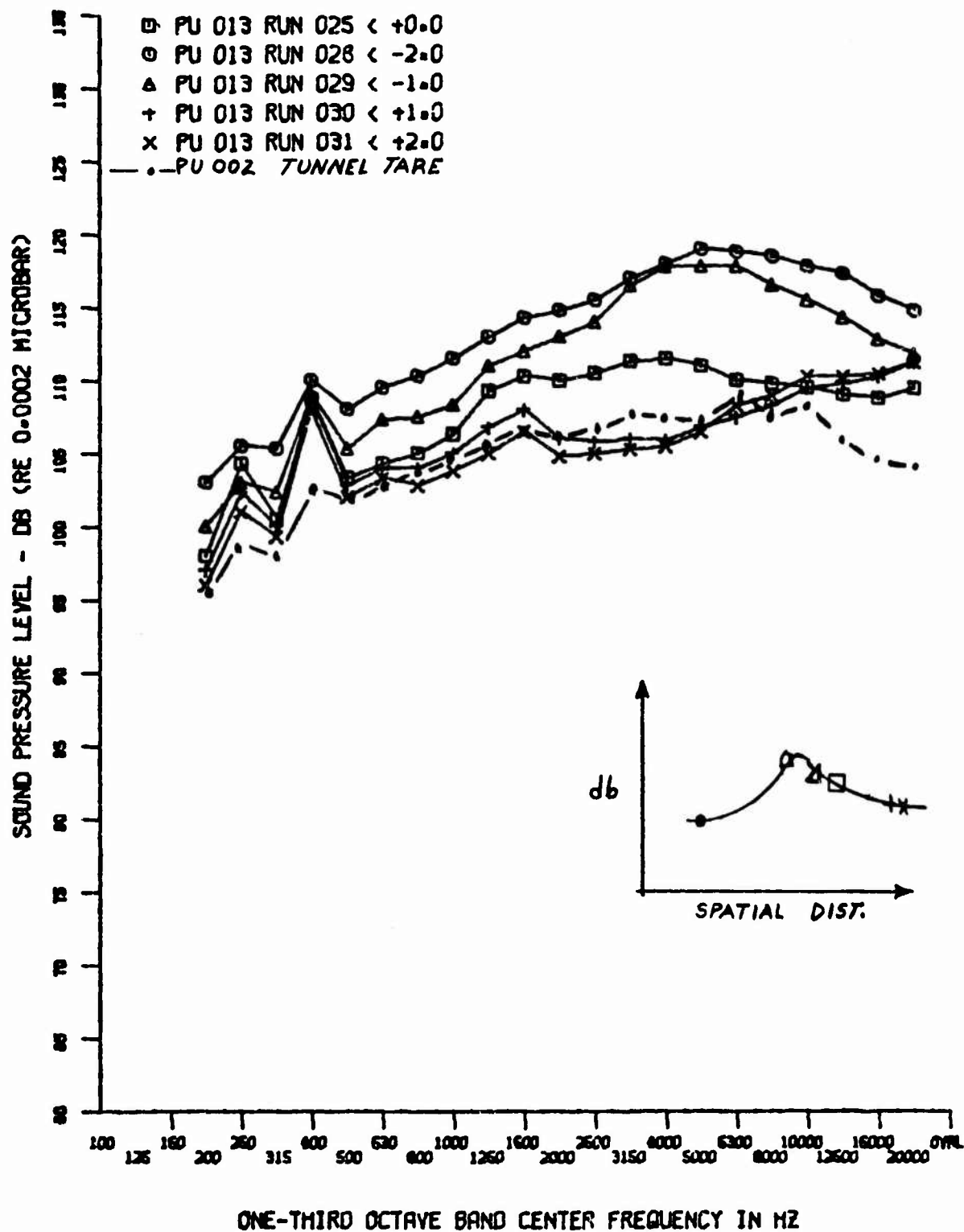
Figure 38. Variation of Transition Spectra in Transition Zone ($M_\infty = 4.0$, $R_{e_\infty} = 2.8 \times 10^6$)
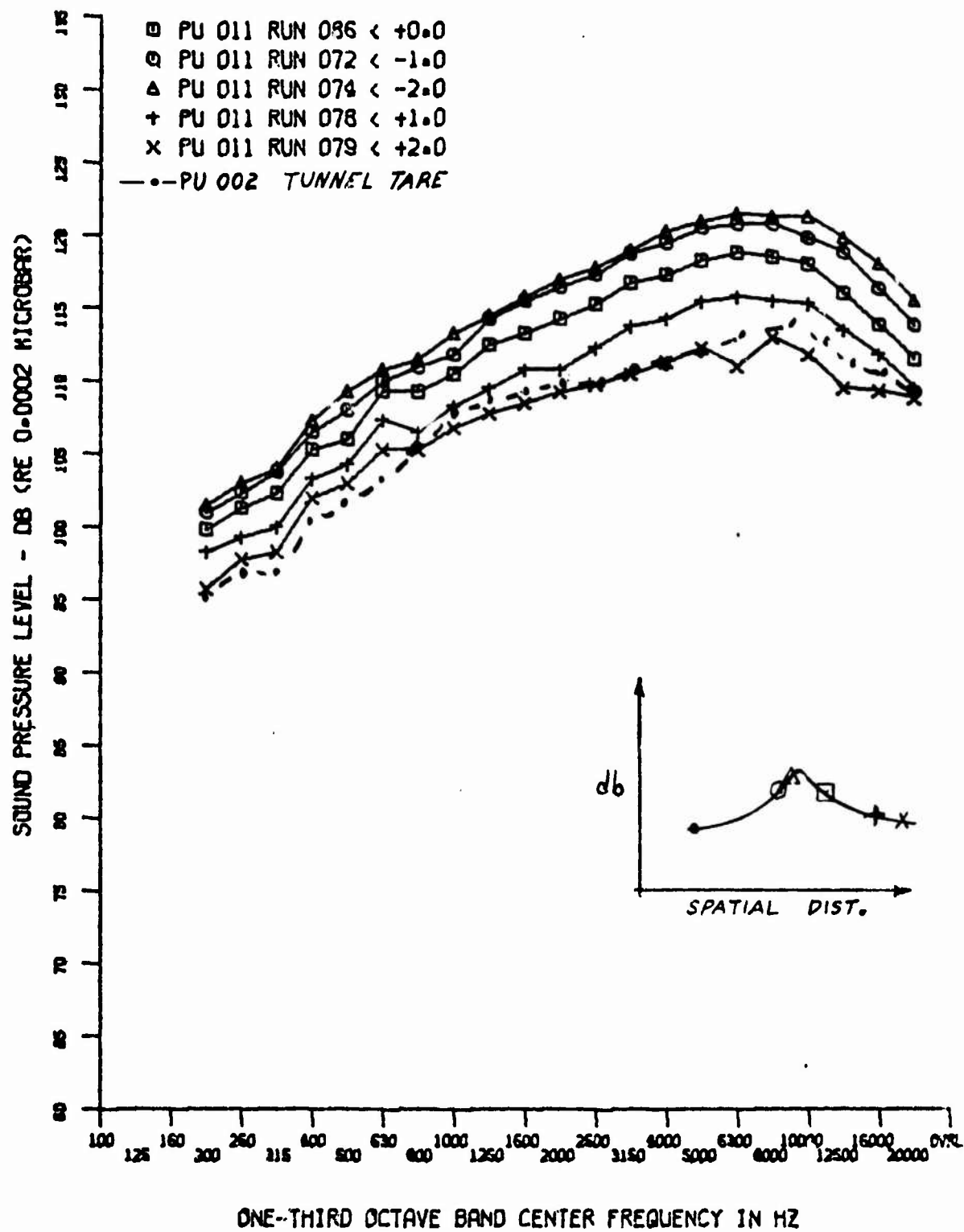
Figure 39. Variation of Spectra in Transition Zone ($M_\infty = 8.0$, $R_{e_\infty} = 2.2 \times 10^6$)

61
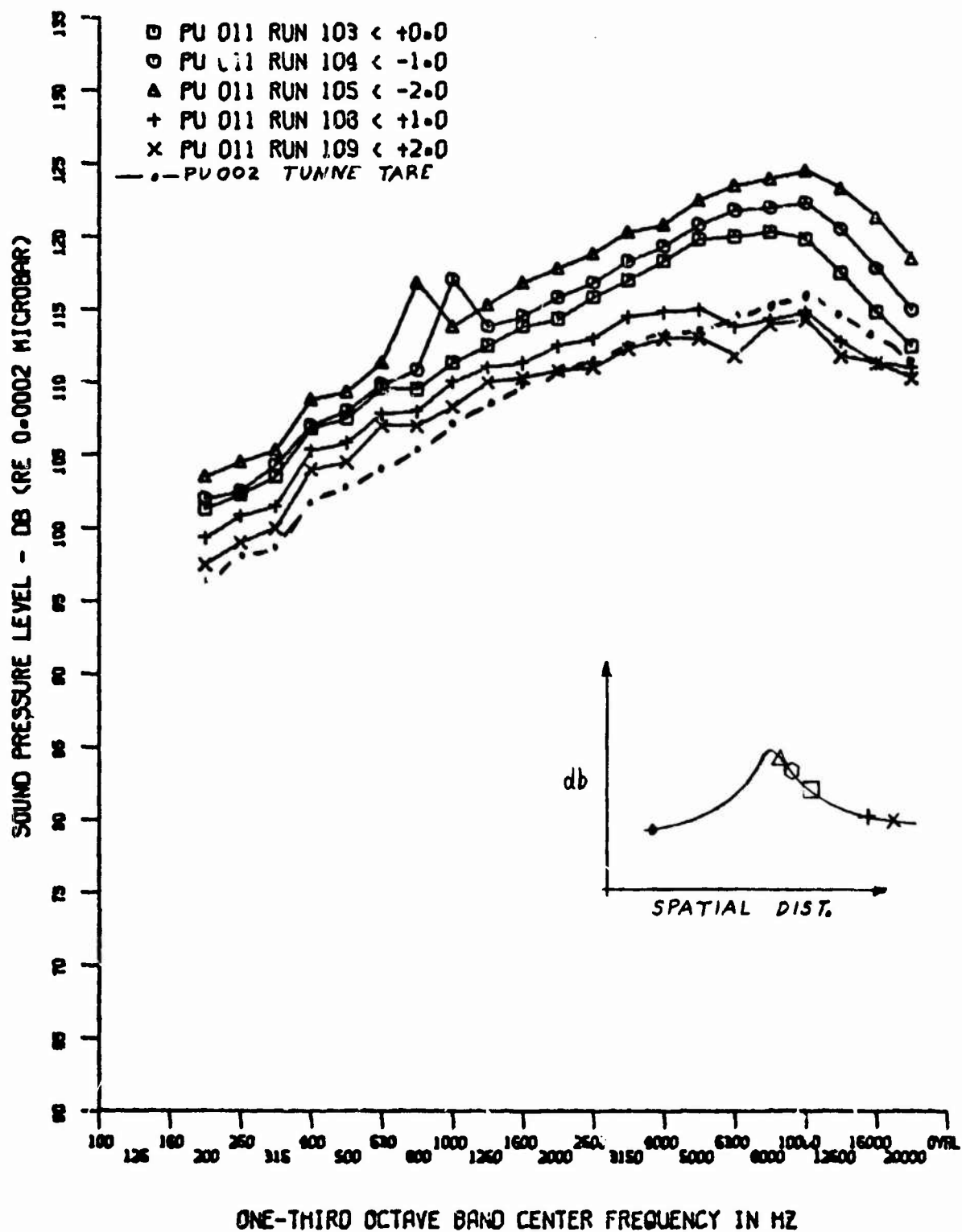
Figure 40. Variation of Transition Spectra in Transition Zone
$(M_\infty = 8.0, \ R_{e_\infty} = 2.8 \times 10^6)$

62

in separated flow (lceward side) and high pressures ($P_{rms} \approx 136$ dB) were measured in turbulent flow (windward side). To show the circumferential variation of pressure spectra, several multiple plots were made using the aft circumferential array of sensors, which at these high angles of attack were down stream from the maximum transition location. Figure 41 shows the nominal circumferential distribution for an angle of attack of approximately zero degrees ($R_{e_\infty} = 2.8 \times 10^6$/ft, $M_\infty = 8$). For the corresponding tunnel condition (with model $\alpha = 7.2°$). Figure 42 gives the various spectra for the aft circumferential array. The severity of the variation in pressure spectra is apparent. Figure 43 compares the pressure spectra for the same sensor but different test runs in turbulent and separated flow. The pressure distributions are similar, however, turbulent flow spectra are approximately 5 to 10 dB higher than that of separated flow.

Typical base pressure spectra are shown in Figures 44 and 45 for several angles of attack (tunnel conditions: $M_\infty = 4$, $R_{e_\infty} = 1.4 \times 10^6$). In general the spectra reduces as the angle of attack is increased. This was evident at the center of the base (Figure 40) and also at sensor 28 located 0.52 r_b from the base center (Figure 45). The contributions of tunnel tare noise to the base spectra cannot be evaluated since the attenuation characteristics of noise across the base expansion wave and trailing shock wave is unknown. Base spectra, however, for the base center ($\alpha = 0$) below 2 kHz when compared to tunnel tare noise (as measured on vehicle nose) is approximately 3 to 5 dB above the noise level. Above 3 kHz the noise level is above base pressure data. Of importance is the affect of Reynolds number on base fluctuating pressure levels. Figure 46 compares the fluctuating pressure levels at Mach 4 for the three Reynolds numbers. Comparing base pressure data at various R_{e_∞}, using data obtained at $R_{e_\infty} = 1.4 \times 10^6$ as a reference reveals an increase of 8 db at $R_{e_\infty} = 2.2 \times 10^6$ and 11 db at $R_{e_\infty} = 2.8 \times 10^6$. Essentially the variation in fluctuating base pressures is directly proportional to Reynolds number. Also shown in Figure 43 is the tunnel tare noise associated with each run. At $R_{e_\infty} = 2.2 \times 10^6$ and 2.8 $\times 10^6$, data is above the tunnel tare noise by 6 to 10 db in the range of frequencies below 4 kHz. Figure 47 shows the pressure spectra for various angles of attack at a R_{e_∞} of 2.2×10^6. The spectra is observed to drop with angle of attack. At high angles (-4°, -7.2°) a discrete frequency (2500 Hz) becomes dominant. This trend is insipid at $\alpha = -2°$ (Figure 47). No apparent reason exists for this frequency. Figure 48 shows the base centerline spectra obtained for Mach 8. Data is significantly distorted at all angles of attack. Similar data was obtained at Mach 10 except for a zero angle of attack where the data was well behaved.

c. Cross Correlation Functions

Cross correlation functions representing space time correlations between two sensors were obtained for turbulent, transitional separated and base flow. Figure 49 represents the space time correlations in turbulent flow for various angles of attack at Mach 4 in the direction of flow. Figure 50 shows the circumferential distribution for the same test condition. A decrease of the peak in the correlation function for increasing sensor separation is apparent. This is attributed to the decay of the turbulent eddies as they travel downstream. Also the curves become broader for increasing sensor spacing, indicating that the high frequency contribution to the correlation function decays more

63

Figure 41. Comparison of Pressure Spectra in Circumferential Direction ($M_\infty = 8.0$, $\alpha = 0°$ $R_{e_\infty} = 2.8 \times 10^6$)
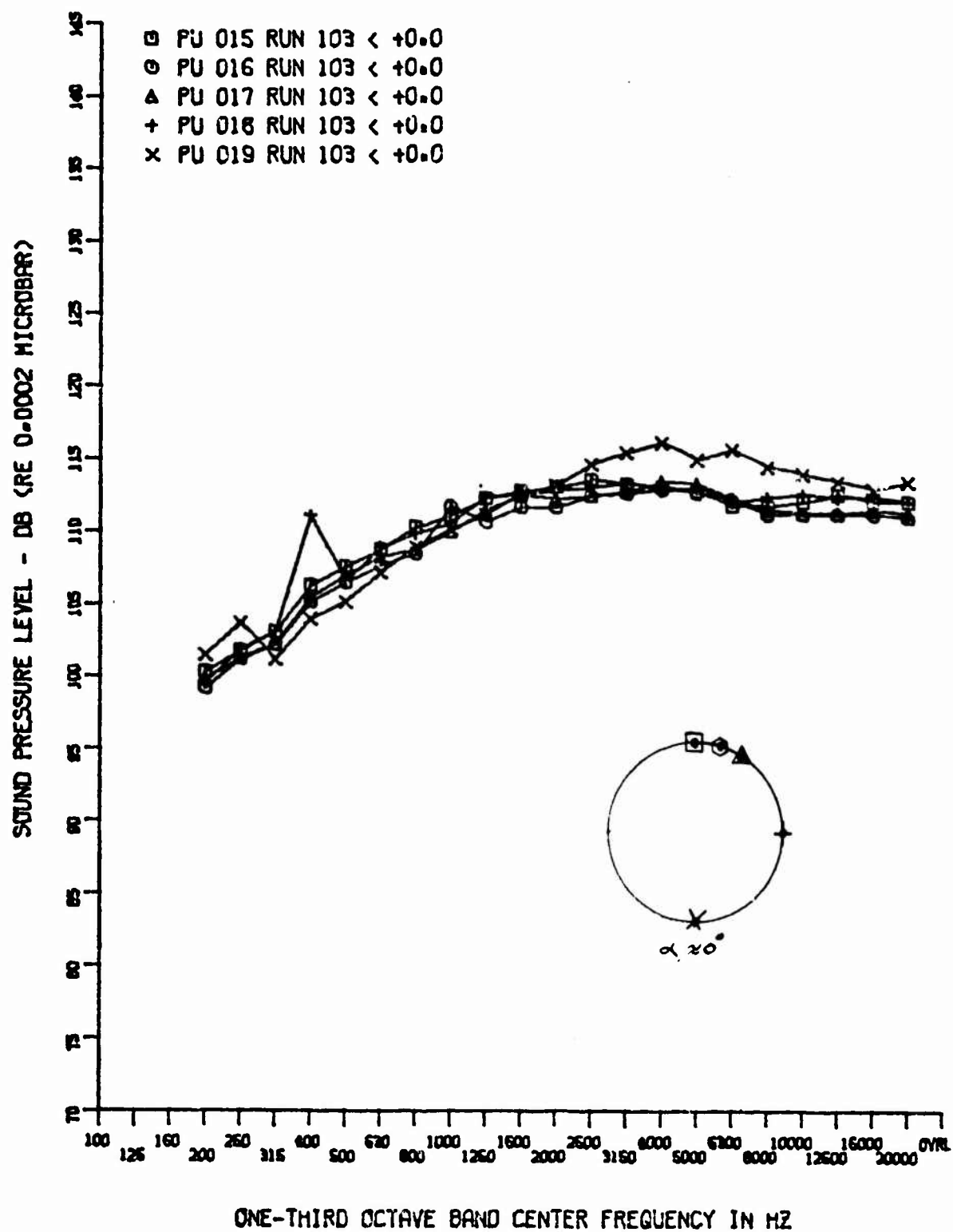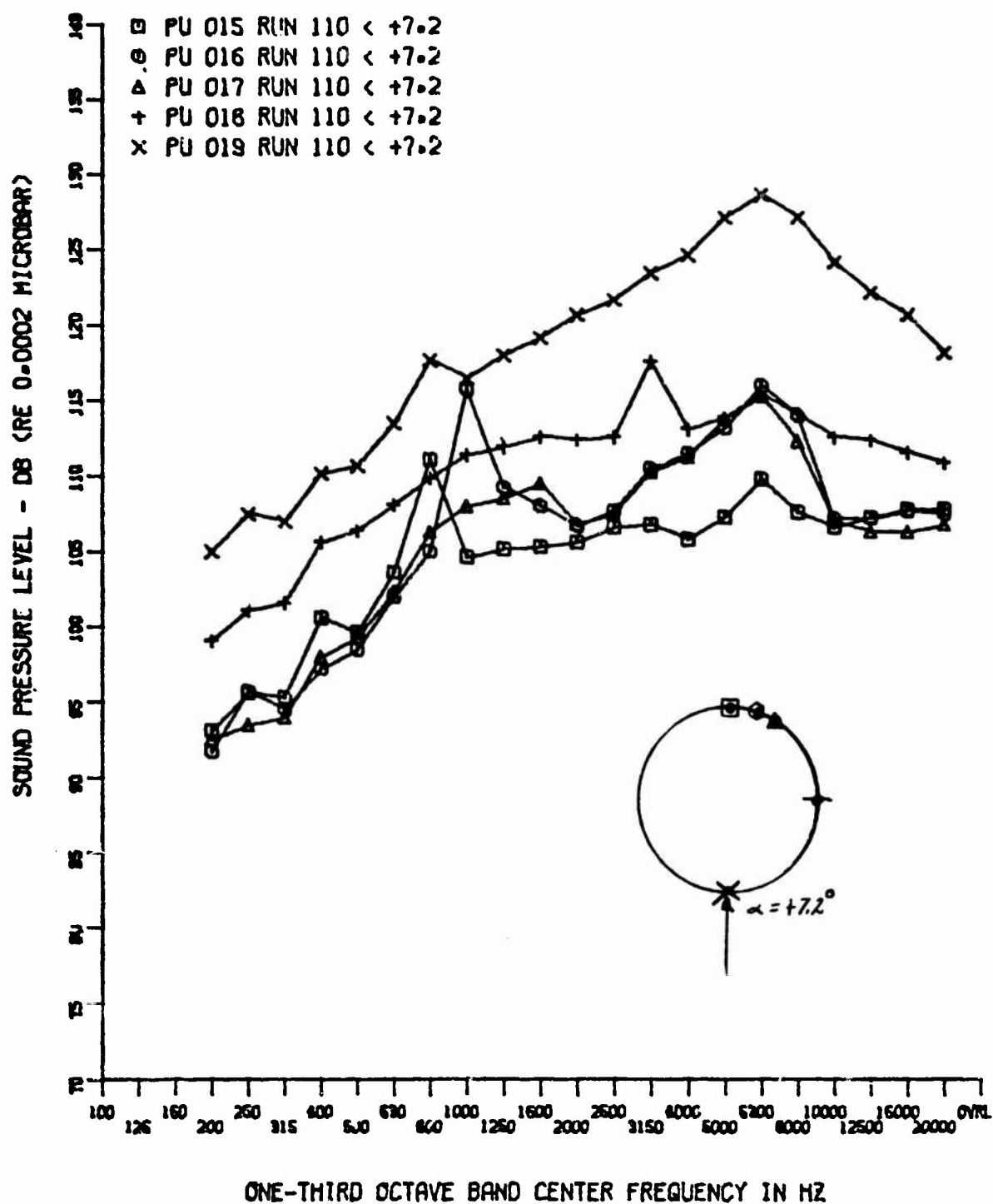
Figure 42. Comparison of Pressure Spectra in Circumferential
Direction (Separated Flow Leeward Sensors),
$(M_\infty = 8.0, \ R_{e_\infty} = 2.8 \times 10^6)$

.65
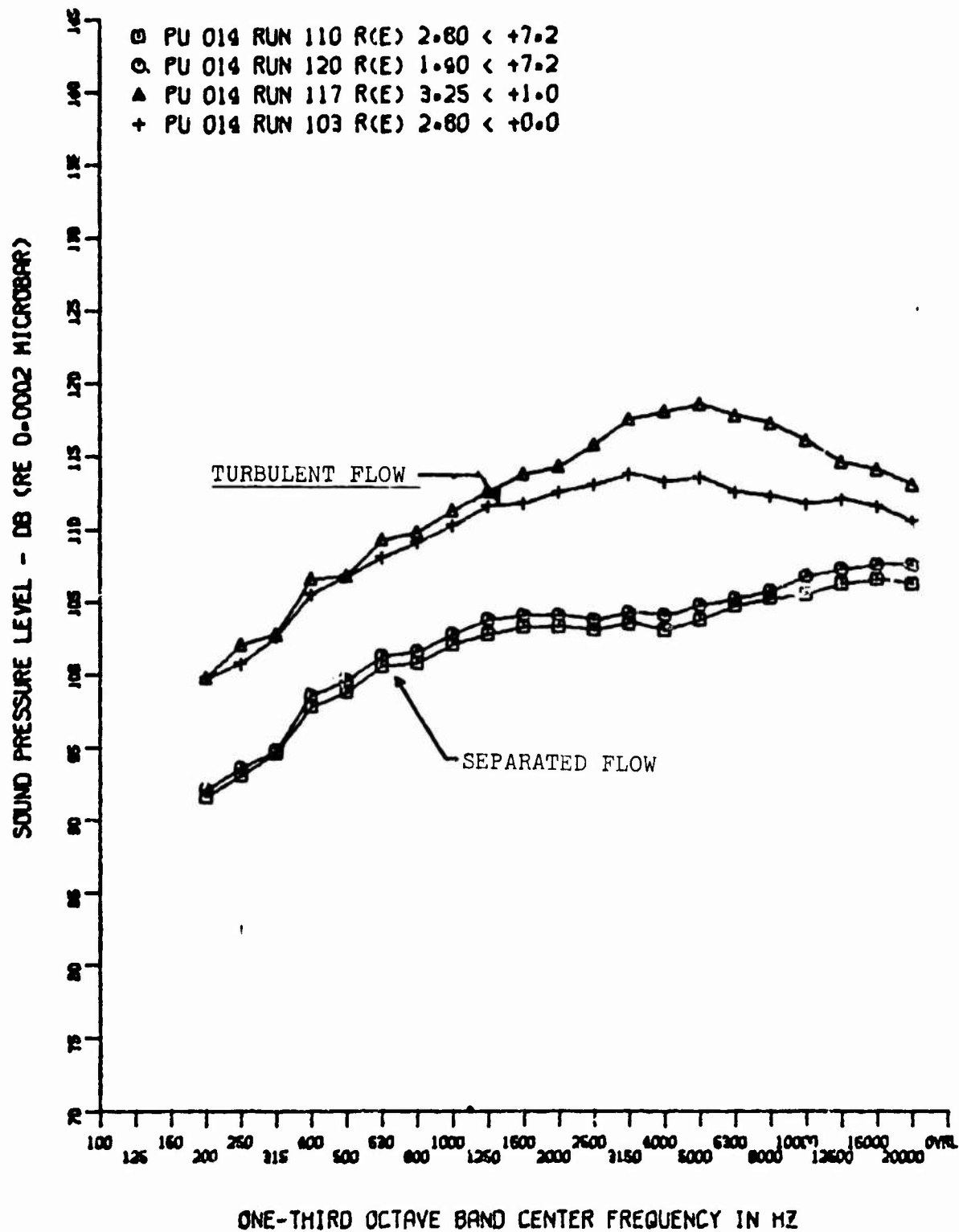
Figure 43. Comparison of Pressure Spectra Separated Flow
Vs. Turbulent Flow ($M_\infty = 8.0$)

66
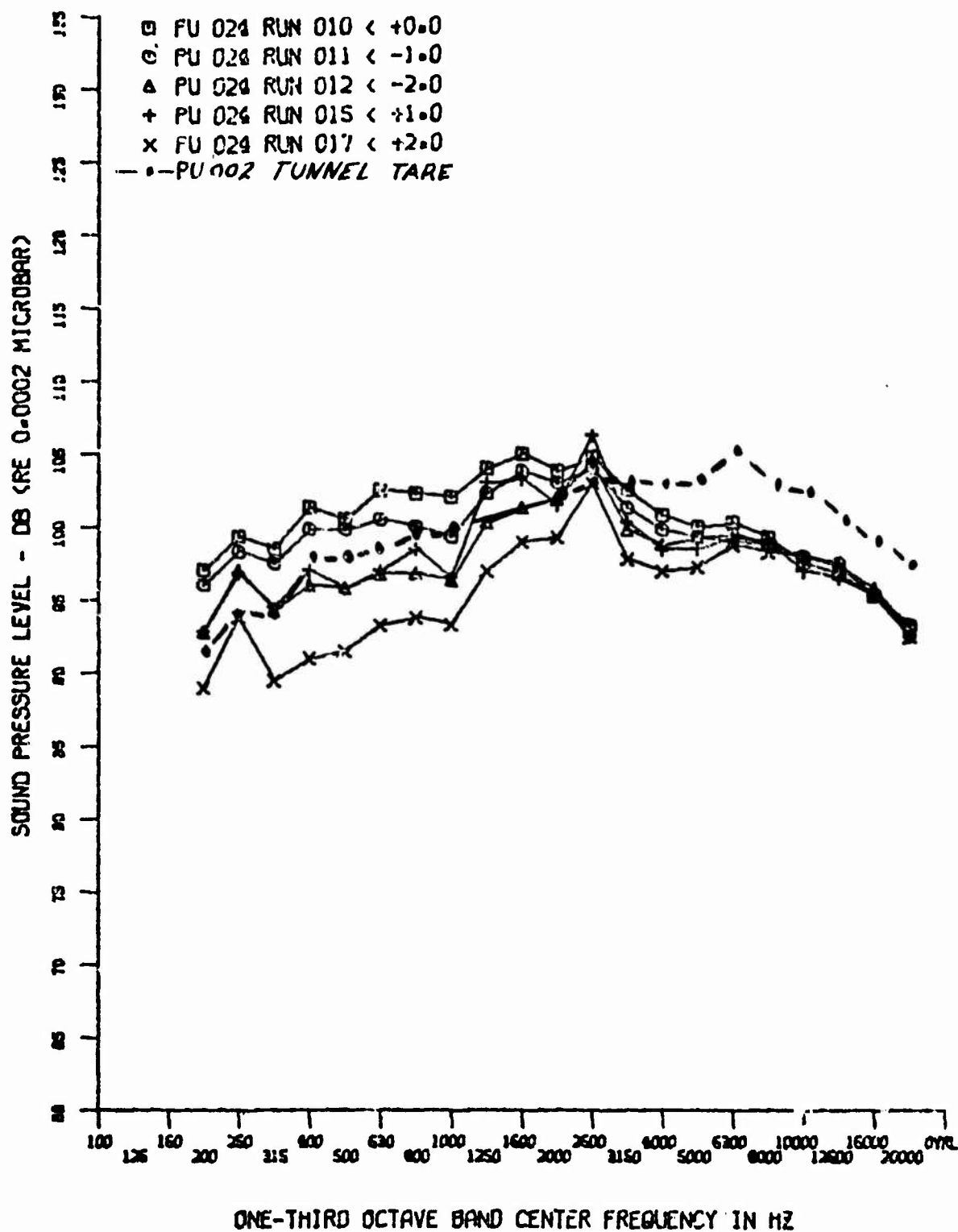
Figure 44. Comparison of Base Flow Pressure Spectra for Various α's (Base Center) ($M_\infty = 4.0$, $R_{e_\infty} = 1.4 \times 10^6$)

67
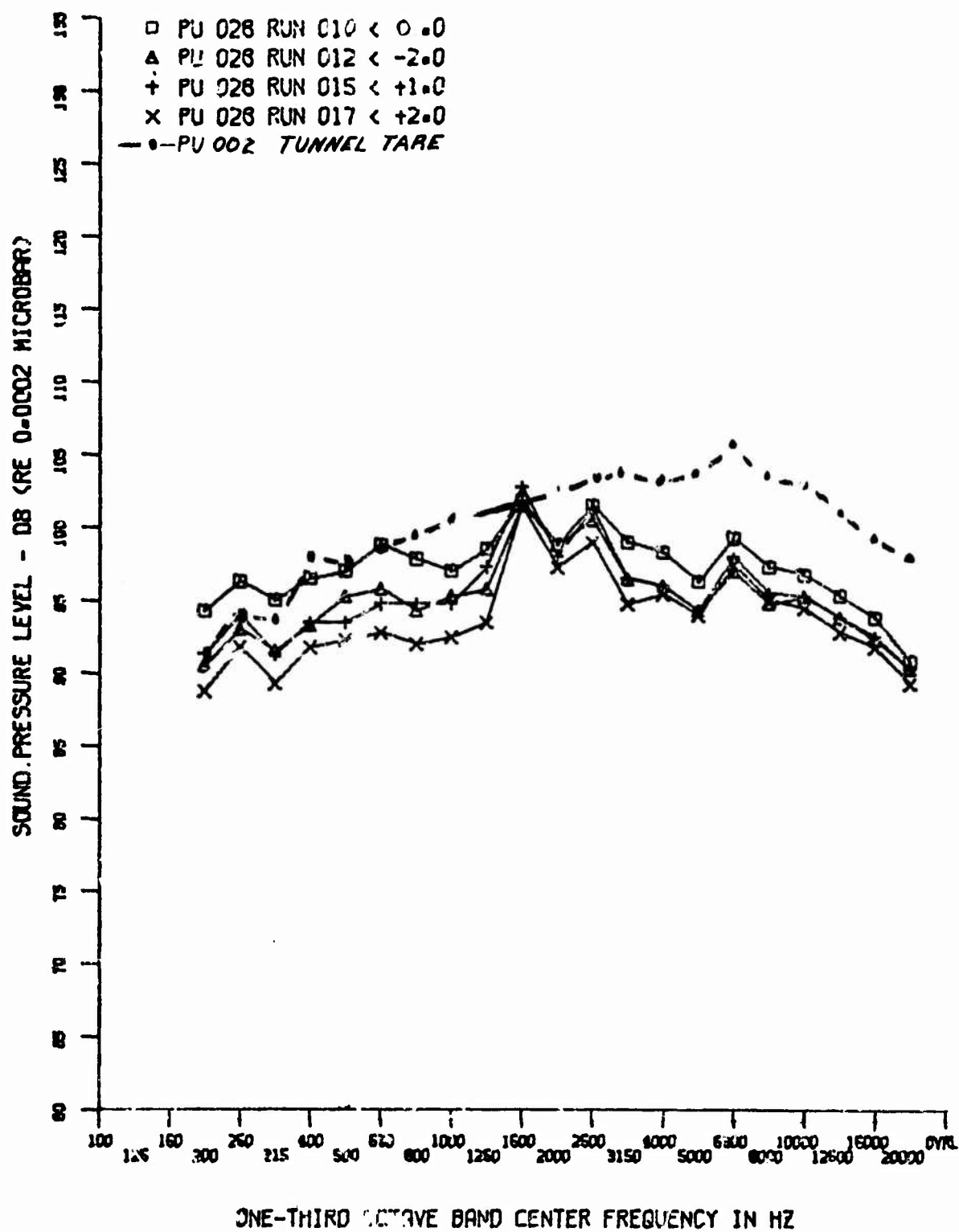
Figure 45. Comparison of Free Flow Pressure Spectra for Various α's ($R_b = 0.52$) $M_\infty = 4.0$, $Re_\infty = 1.4 \times 10^6$

68
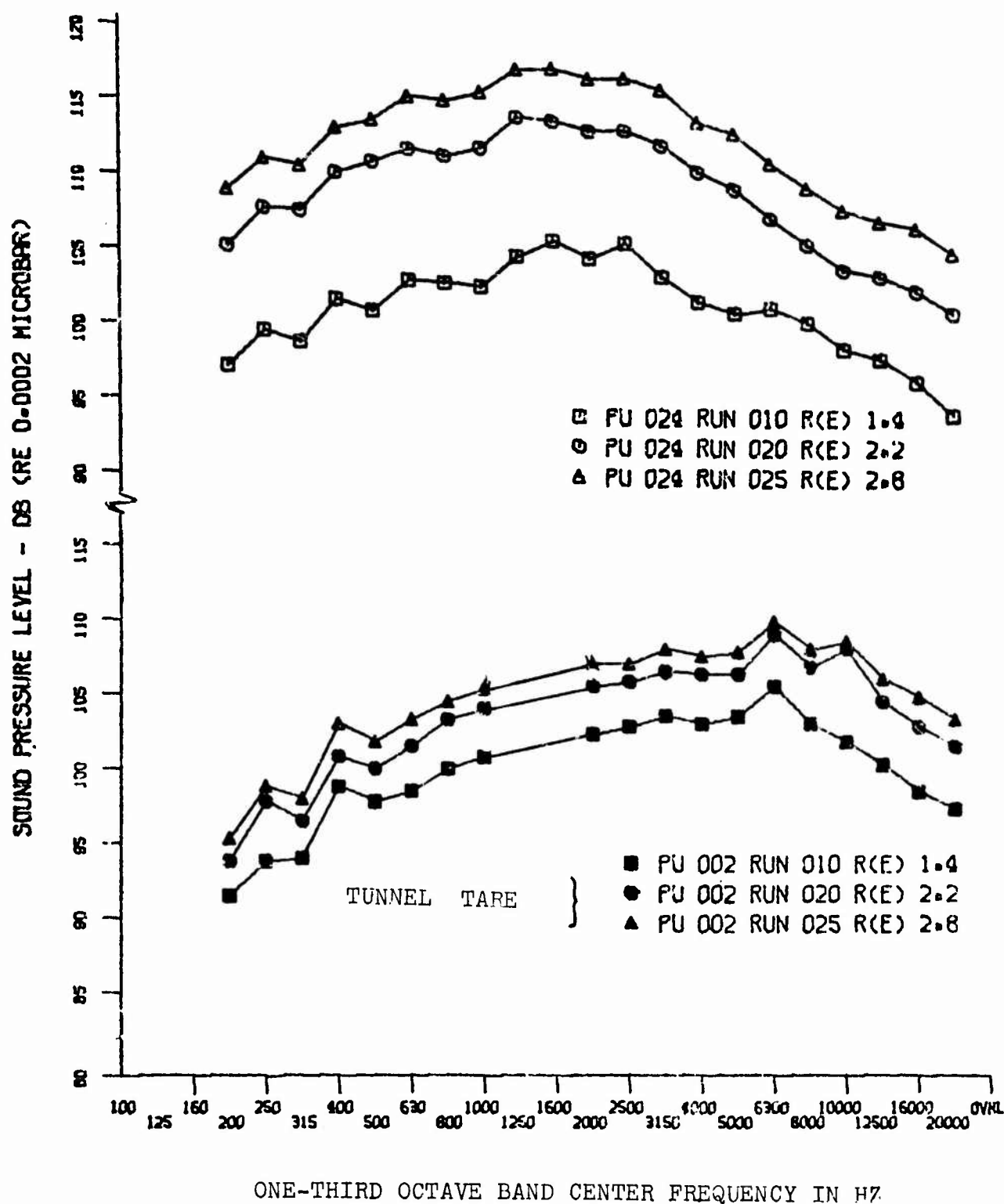
Figure 46. Comparison of Base Flow Pressure Spectra for Various
Reynolds Numbers (Base Center), ($M_\infty = 4.0$)
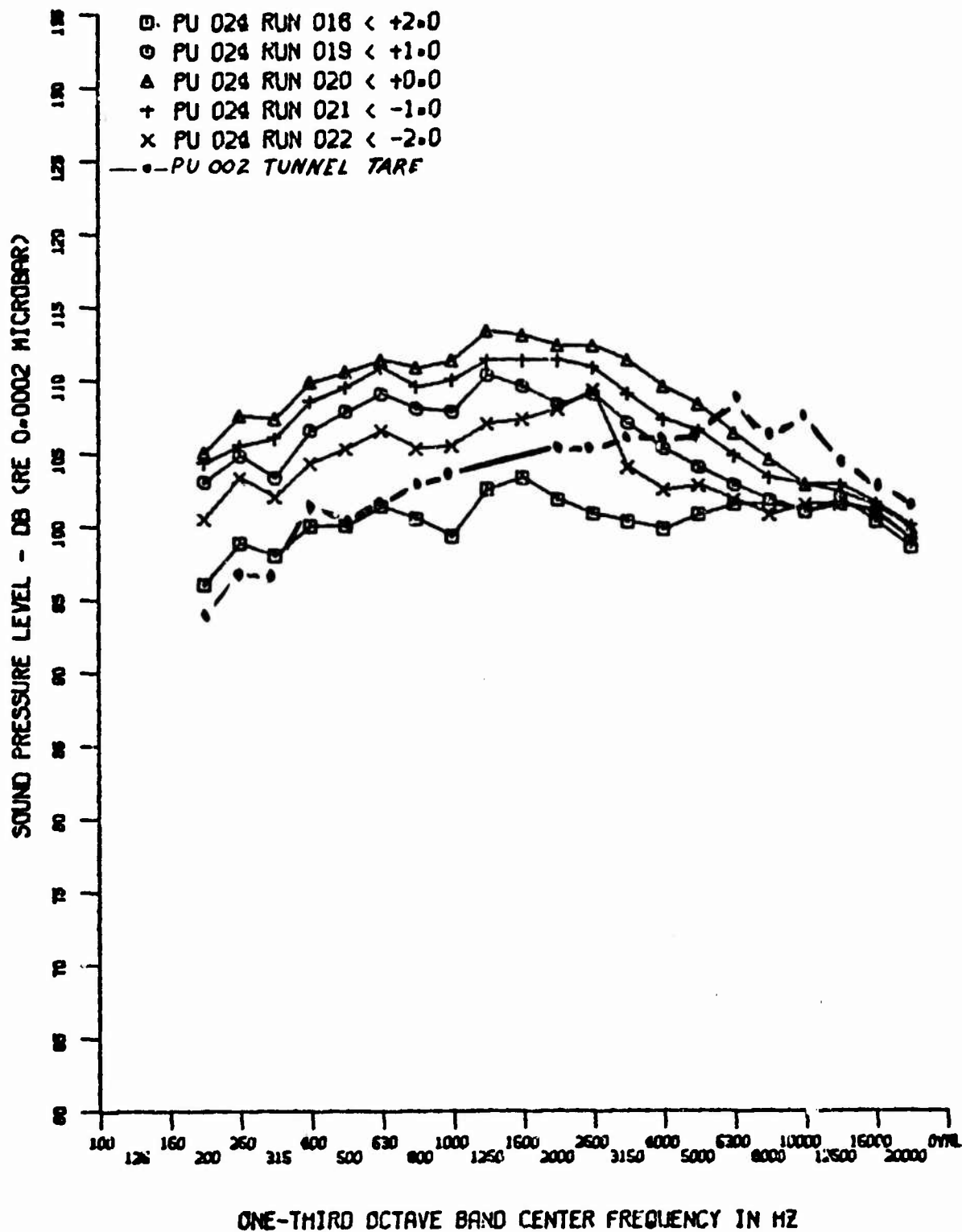
Figure 47. Comparison of Base Flow Pressure Spectra for Various α (Base Center) ($M_\infty = 4.0$, $R_{e_\infty} = 2.2 \times 10^6$)

70
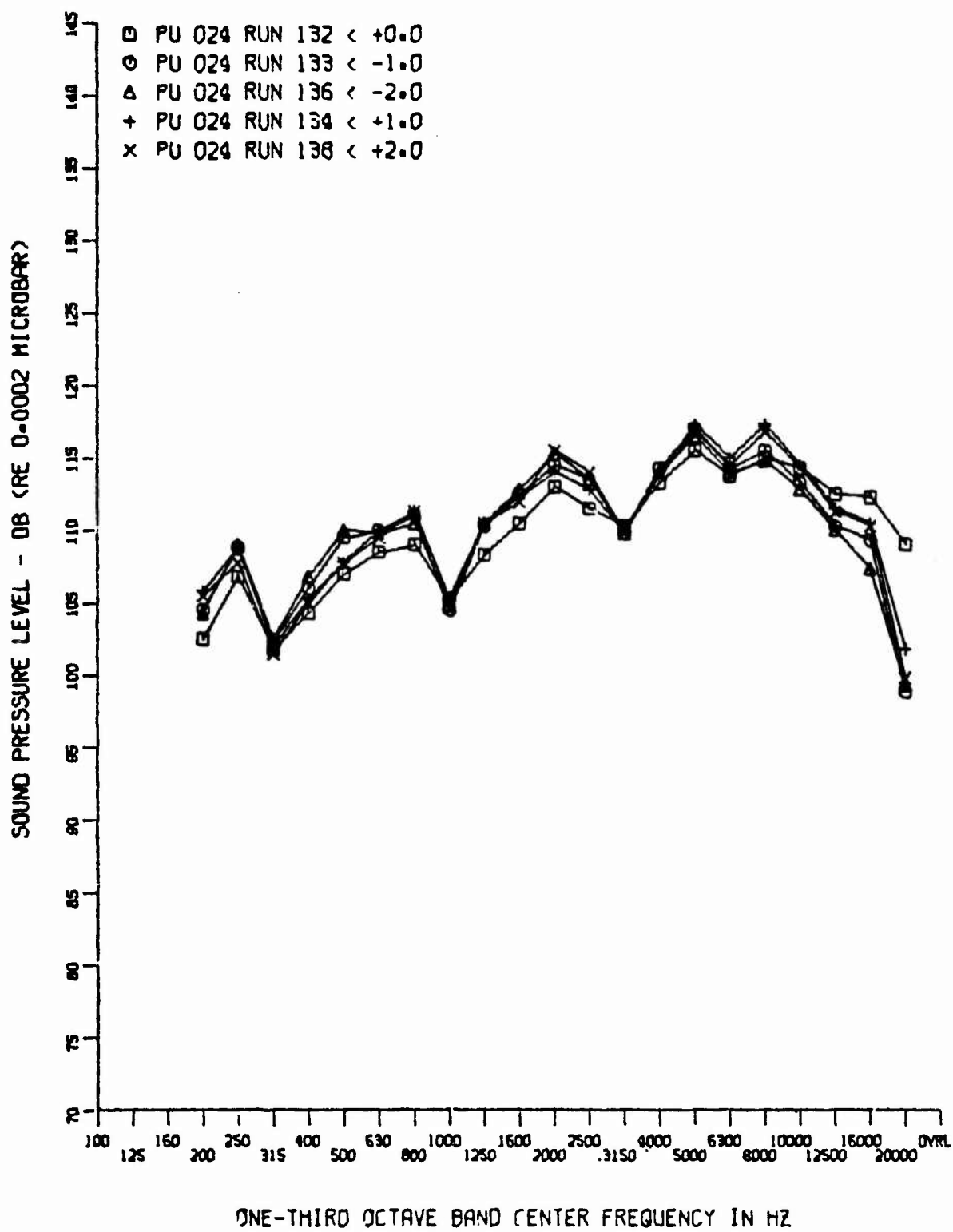
Figure 48. Comparison of Base Flow Pressure Spectra for Various α
(Base Center) ($M_\infty = 10.0$, $R_{e_\infty} = 1.4 \times 10^6$)

71
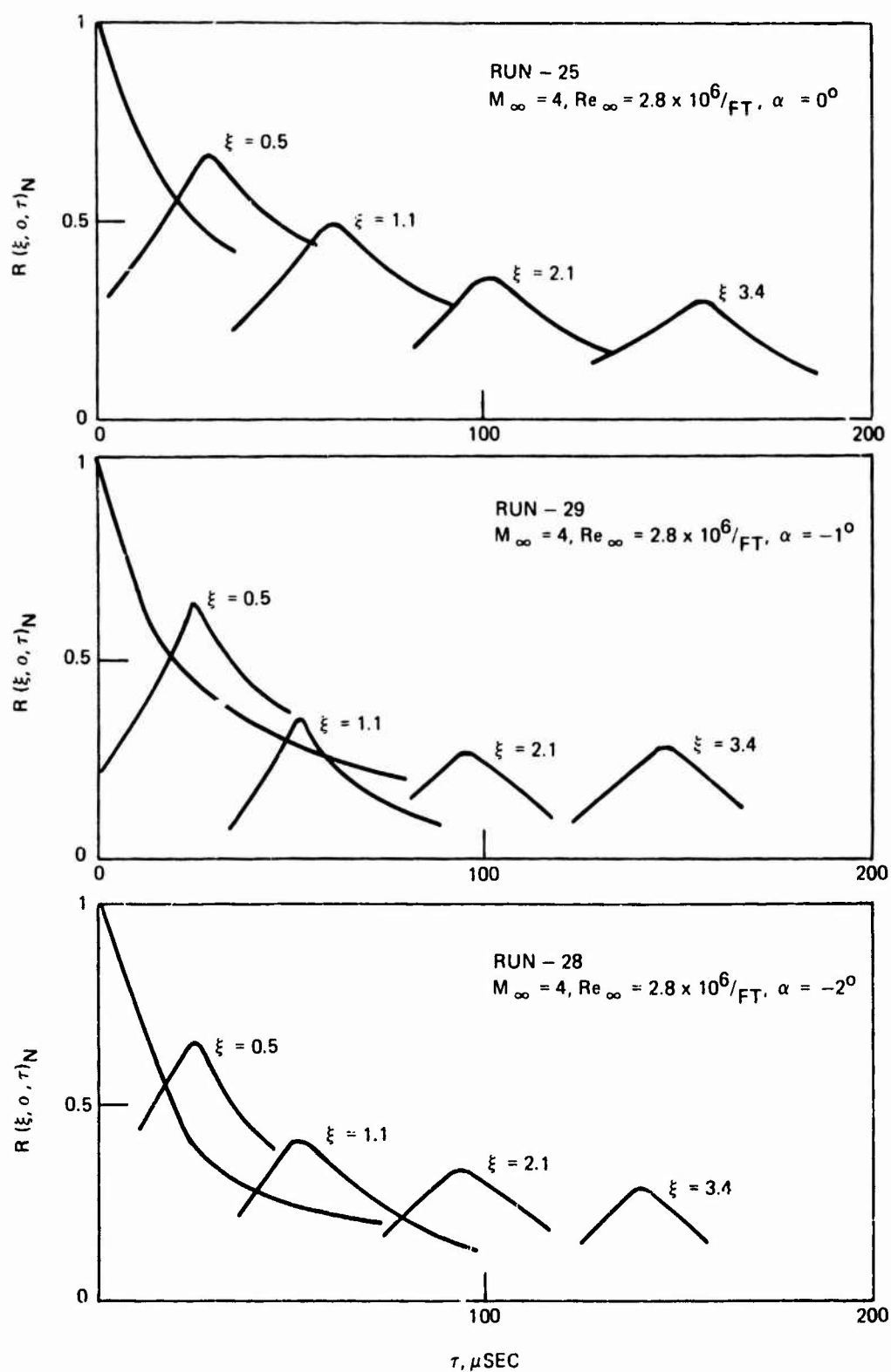
Figure 49. Longitudinal Space-Time Correlations for Turbulent Flow at Various α ($M_\infty = 4.0$, $R_{e_\infty} = 2.8 \times 10^6$)
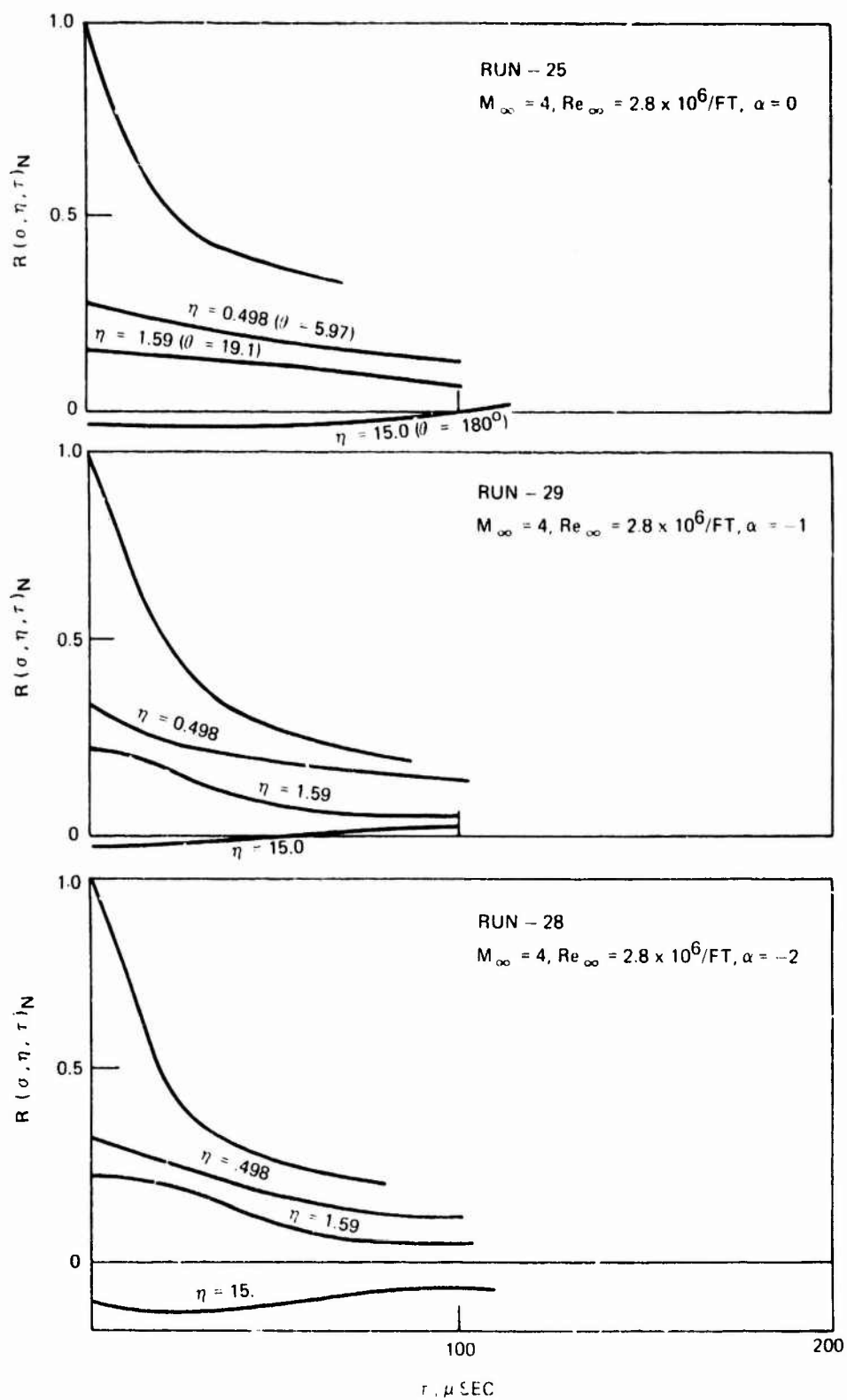
Figure 50. Circumferential Space–Time Correlations for Turbulent Flow at Various α ($M_\infty = 4.0$, $Re_\infty = 2.8 \times 10^6$)

rapidly than the low frequency turbulent eddies. Similar results were obtained by Chyu and Hanly[21]. Figure 51 are typical longitudinal and circumferential spacetime correlations taken at Mach 8 ($Re_\infty = 2.2 \times 10^6$). Tunnel C data, because of the low signal to tunnel noise ratio is not presented. The effects of the noise were to significantly broaden the correlation function such that the autocorrelation curve of the lead sensor would envelop the remaining cross condition functions.

Space time correlation functions for the region of transitional flow are shown in Figure 52. This series of curves indicates no significant variations in correlation functions for various degrees of transition (i.e. onset, peak and decay). Defined in Figure 53 are the corresponding correlation functions in the circumferential direction. Figures 54 compare correlation functions for turbulent and transitional flow. The only significant variation appears in the broad band convection velocity which will be discussed in Section II.2.d. Correlation functions obtained at Mach 8 are given in Figures 55 and 56 (longitudinal, circumferential, respectively). Decay rates indicated by these curves differ from those presented for Mach 4 in that lower decay rates were observed at higher Mach numbers. This trend was also noted at Mach 10 (Figure 57) and may be due to the high tunnel tare noise associated with these test conditions. Figure 58 represent the longitudinal correlation functions at high angles of attack ($\pm 7.2°$, $M_\infty = 8$) from data obtained at the forward array. At this location the forward array is under transitional flow for an angle of attack of $-7.2°$ and under separated flow for $\alpha = +7.2°$. High decay rates are observed under separated flow. Correlation analysis were performed for the four base measurements and no correlation was found to exist.

d. Convection Velocity

Broad band convection velocities were calculated for both transitional flow and turbulent flow. No significant variation was found in the convection velocities with Mach number. Figure 59 defines the broad band convection velocities. Turbulent flow data is similar to that found by other experimenters. Transitional flow follows the same trend and is approximately 60 percent of that for turbulent flow.
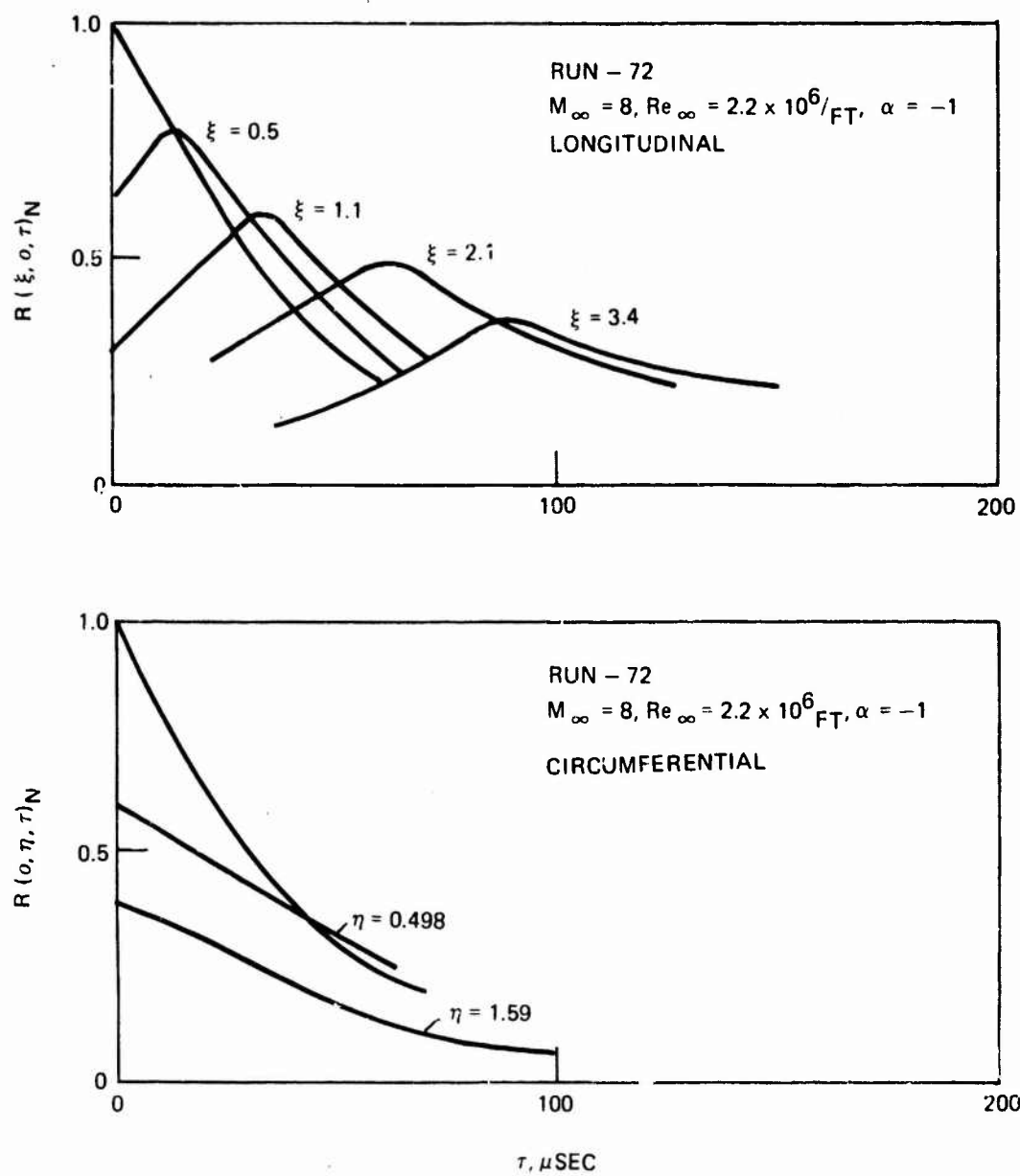
Figure 51. Space-Time Correlations for Turbulent Flow
$(M_\infty = 8.0, \ Re_\infty = 2.2 \times 10^6)$

75
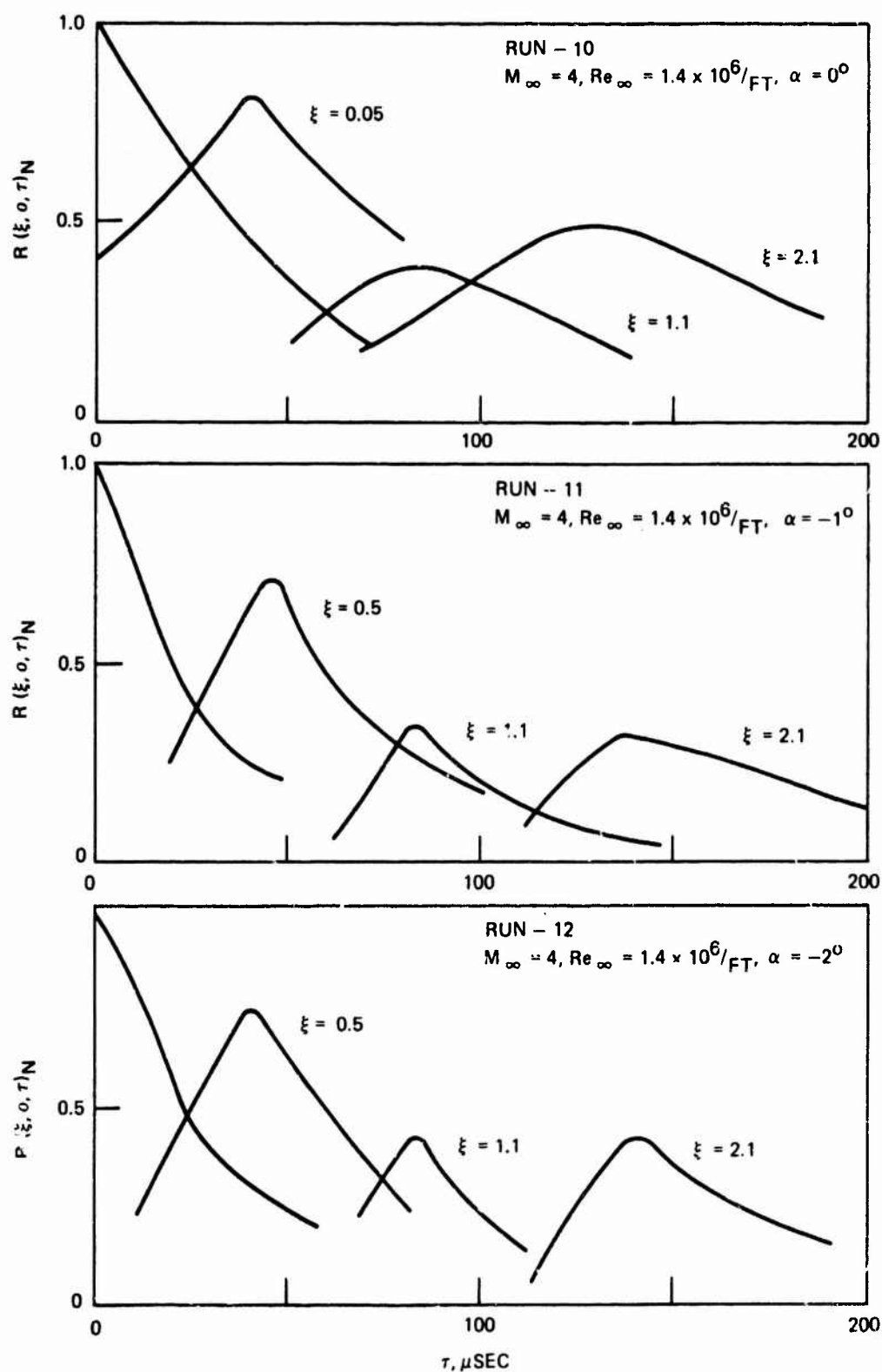
Figure 52. Longitudinal Space-Time Correlations for Transitional
Flow at Various α ($M_\infty = 4.0$, $R_{e_\infty} = 1.4 \times 10^6$)
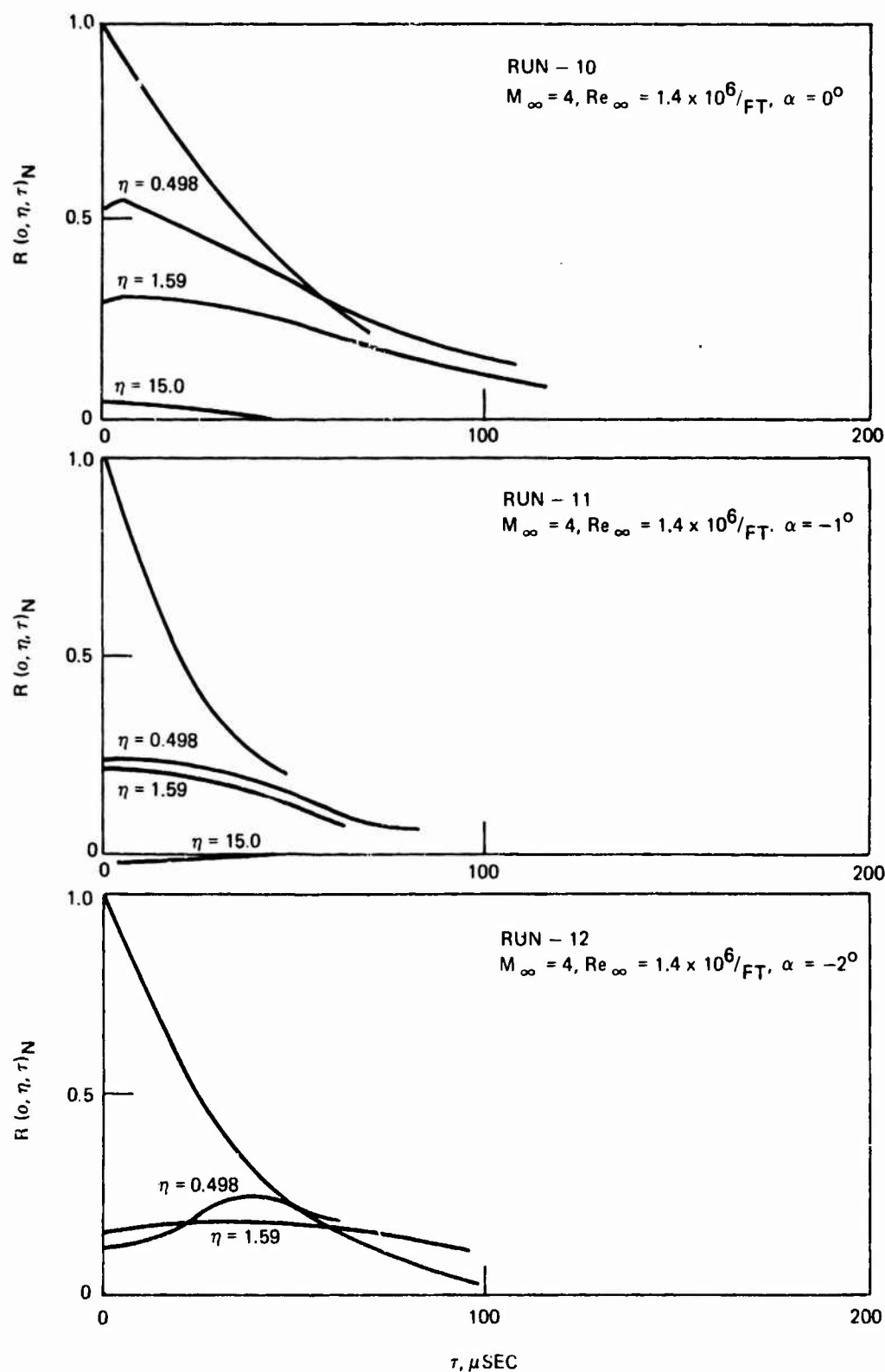
Figure 53. Circumferential Space–Time Correlations for Transitional Flow at Various α ($M_\infty = 4.0$, $R_{e_\infty} = 1.4 \times 10^6$)
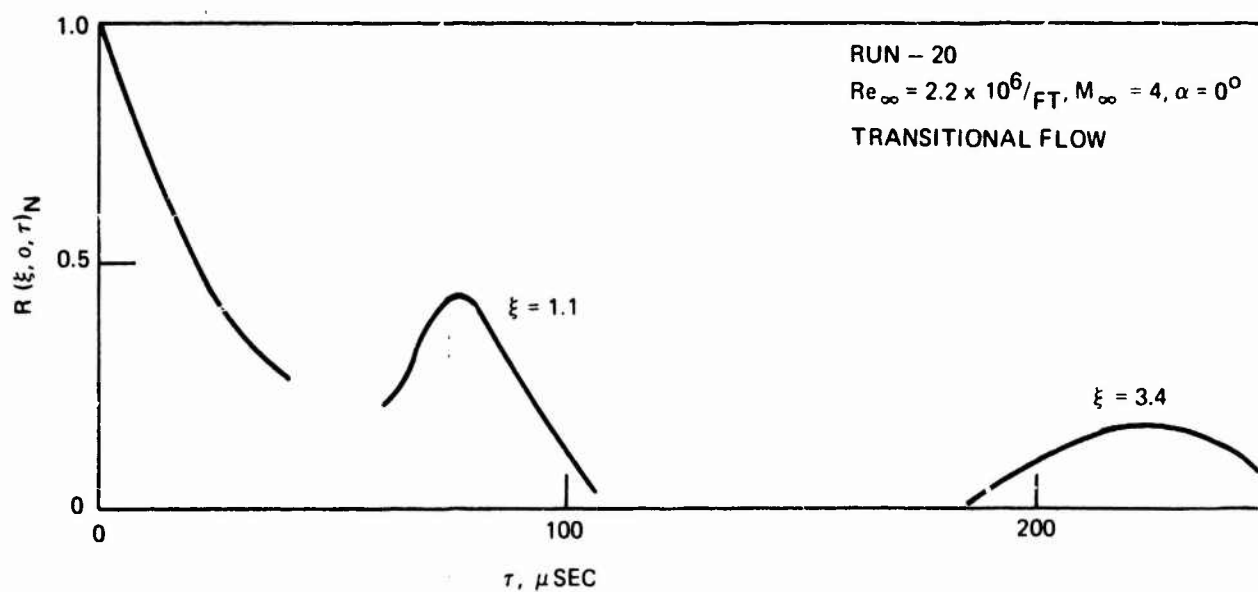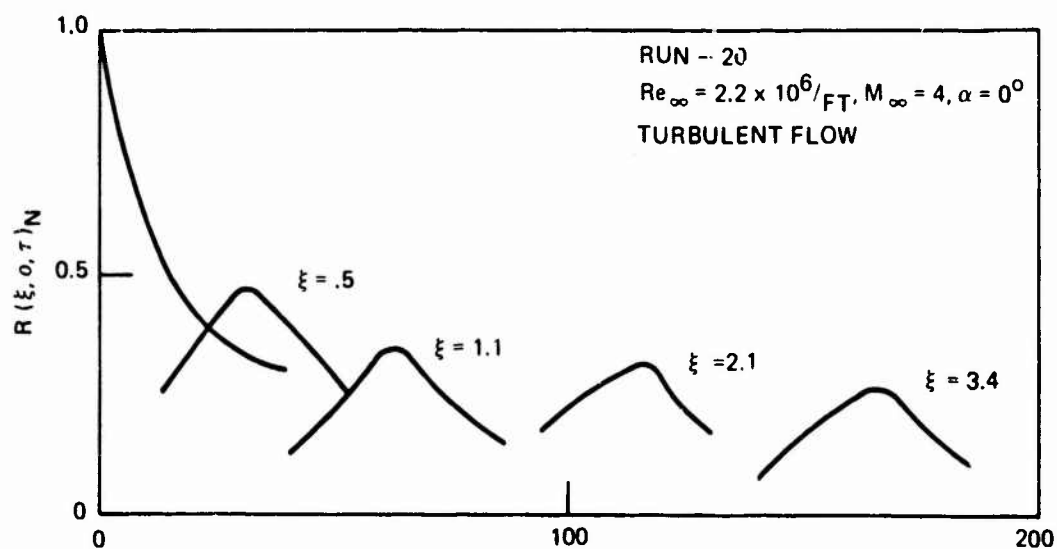
Figure 54. Comparison of Longitudinal Space-Time Correlations for
Transitional and Turbulent Flow ($M_\infty = 4.0$, $R_{e_\infty} = 2.2 \times 10^6$)
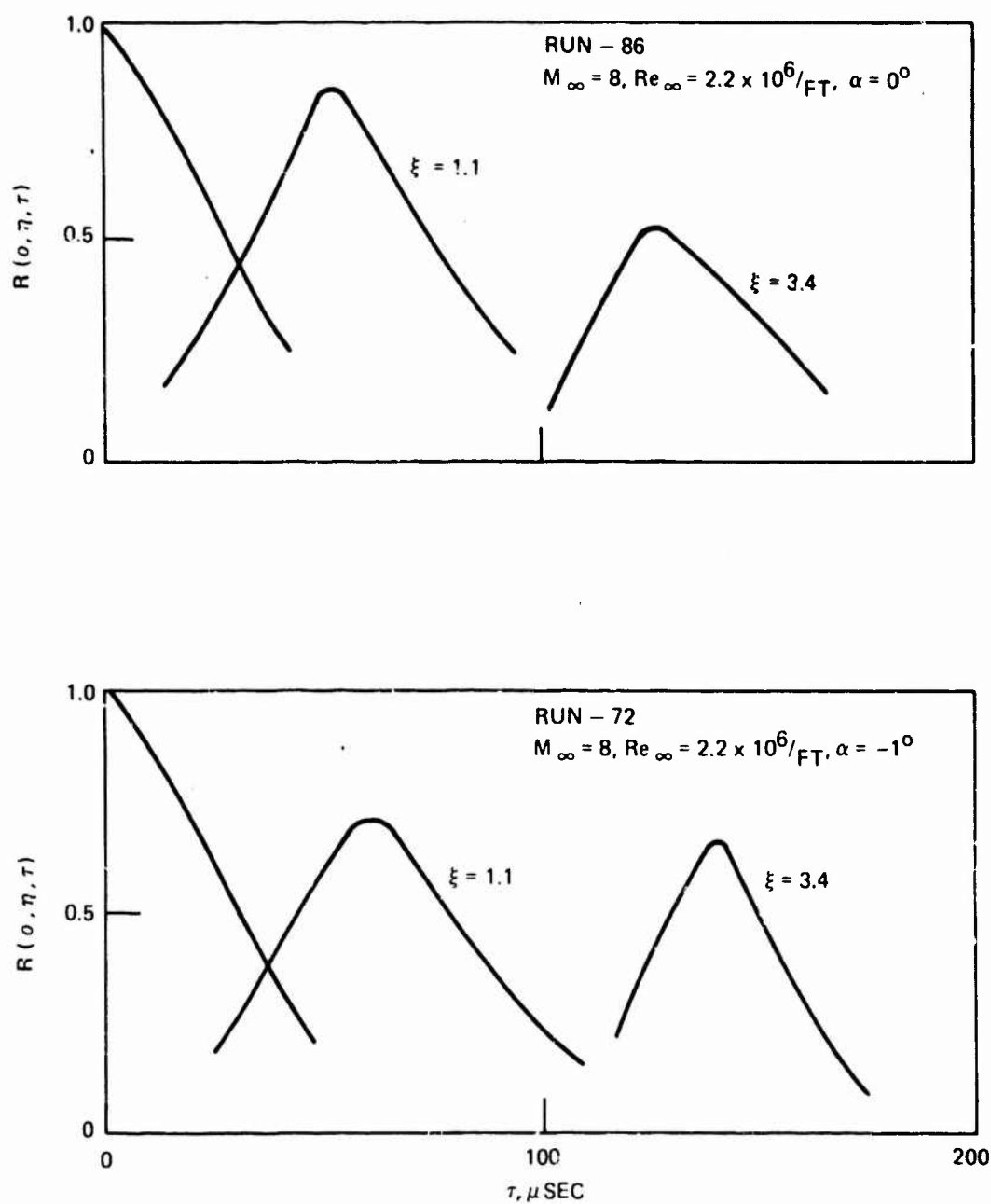
Figure 55. Longitudinal Space-Time Correlations for Transitional
Flow ($M_\infty = 8.0$, $R_{e_\infty} = 2.2 \times 10^6$)
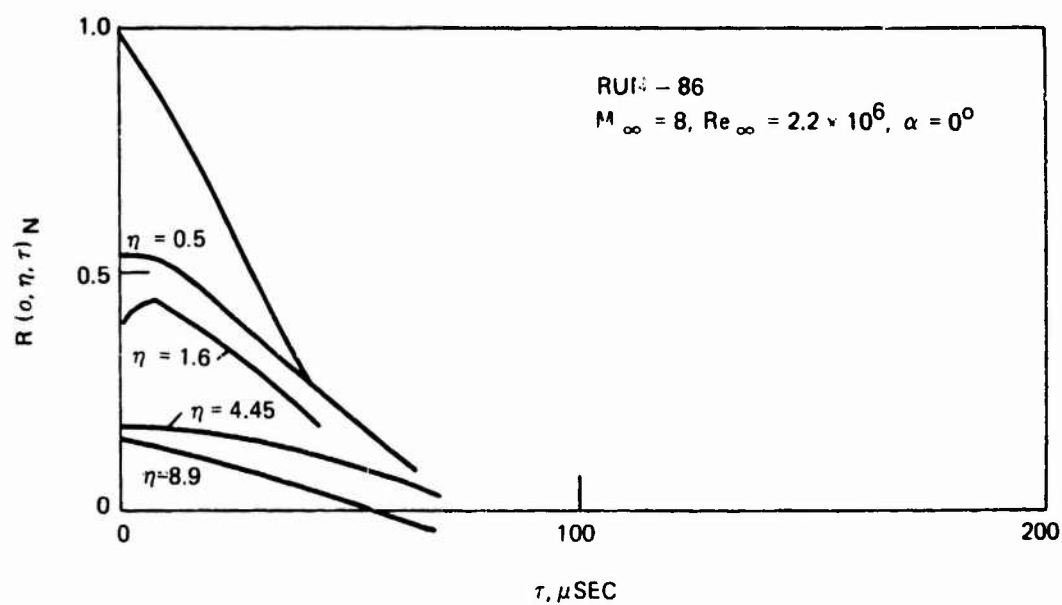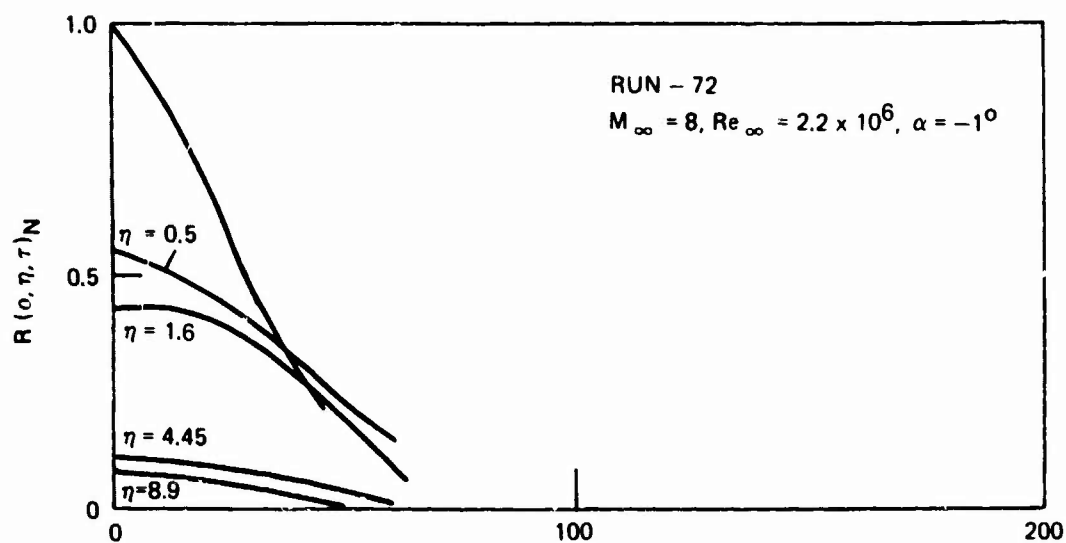
Figure 56. Circumferential Space-Time Correlations for
Transitional Flow ($M_\infty = 8.0$, $R_{e_\infty} = 2.2 \times 10^6$)
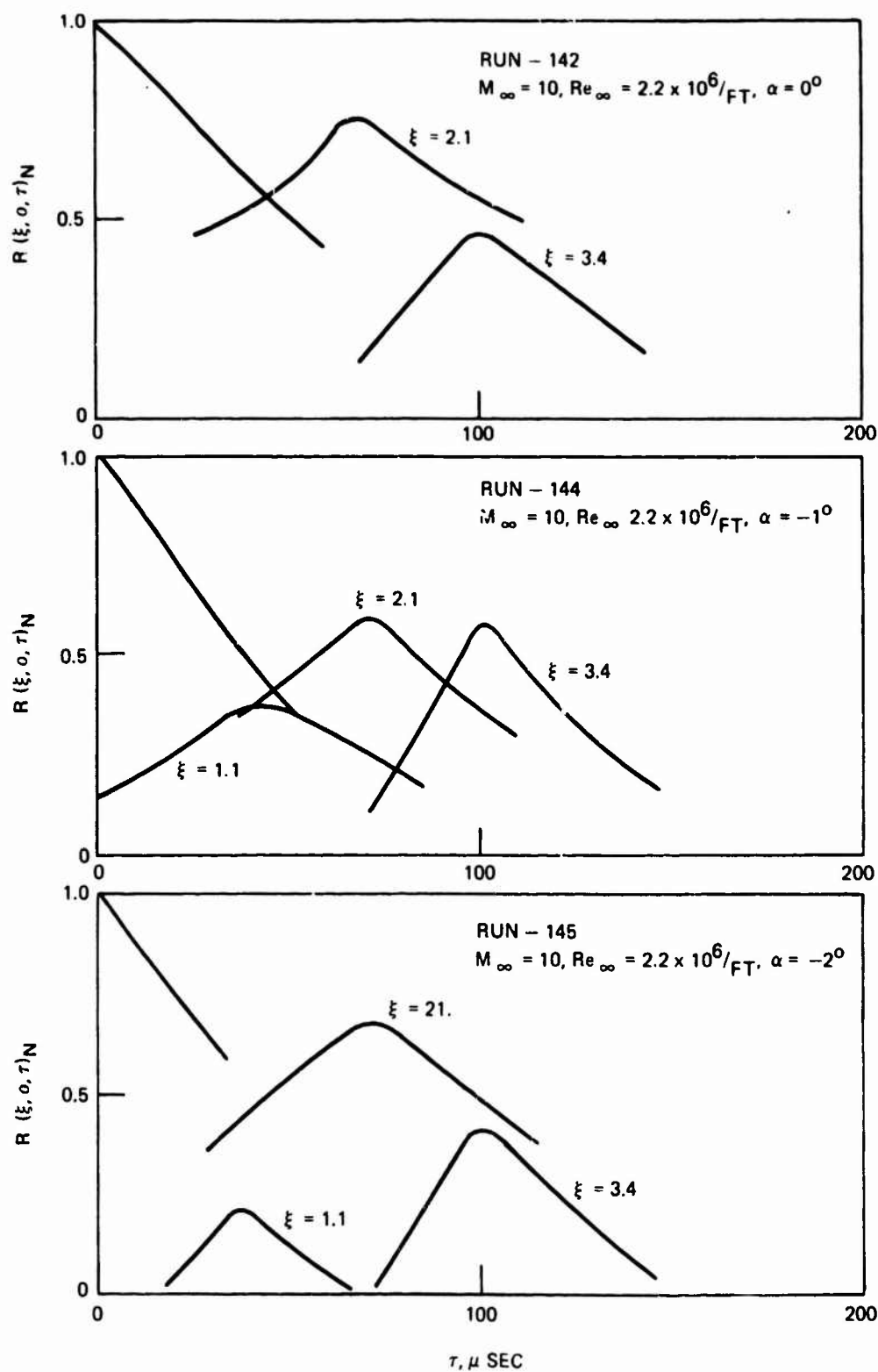
Figure 57. Longitudinal Space–Time Correlations for Transitional
Flow ($M_{\infty} = 10.0$, $R_{e_{\infty}} = 2.2 \times 10^6$)
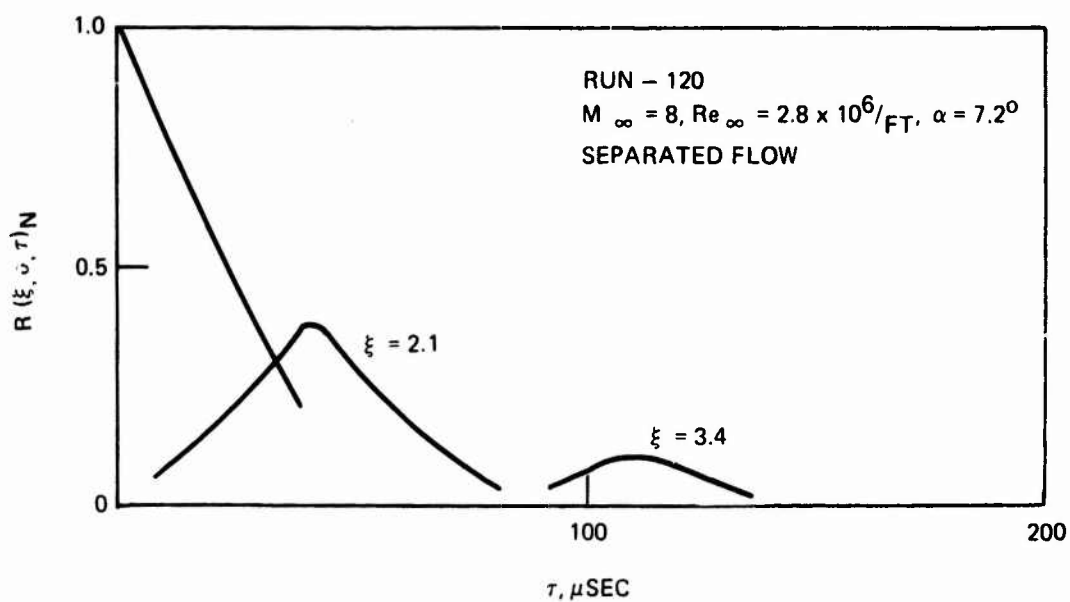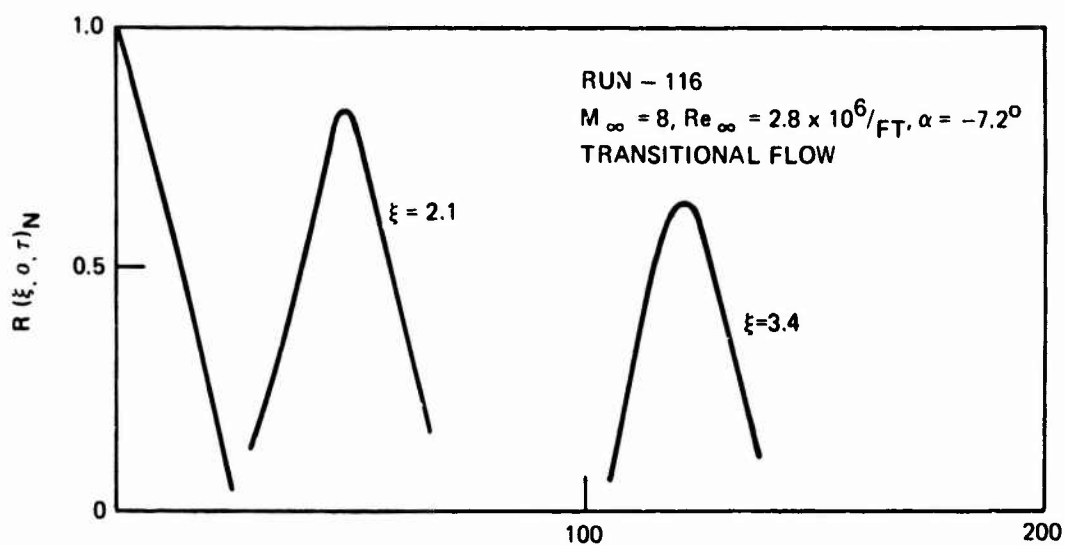
Figure 58. Longitudinal Space–Time Correlations for Separated and Transitional Flow ($M_\infty = 8.0$, $R_{e_\infty} = 3.25 \times 10^6$)

82
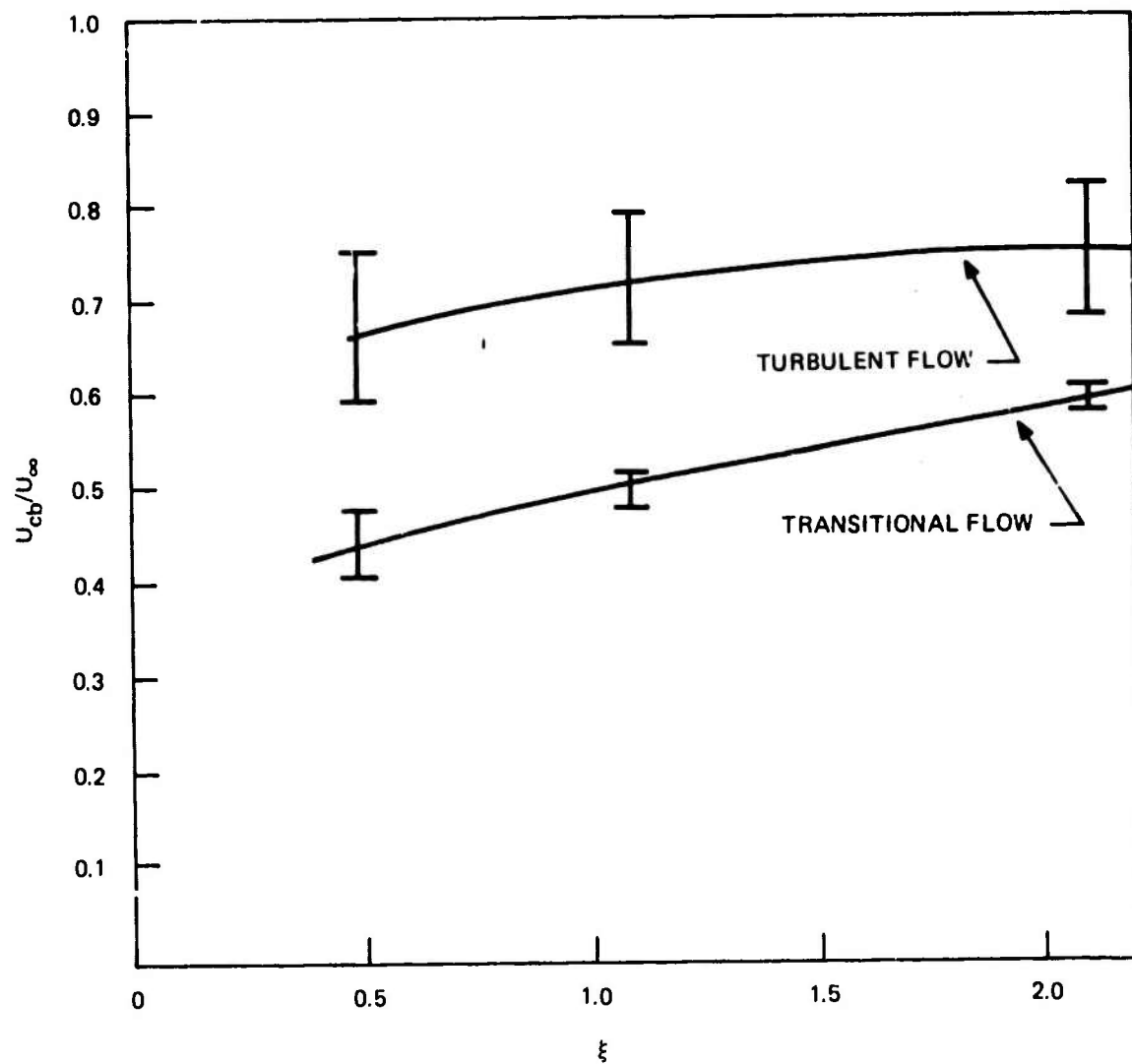
Figure 59. Comparison Between Turbulent and Transitional Broad
Band Convection Velocity

83

SECTION III

SELECTED WIND TUNNEL TEST DATA

1. ACOUSTIC INTENSITY DISTRIBUTIONS

For each test condition two figures are given to define the acoustic intensity distribution P_{rms} (0 Hz to 20 K Hz) along the vehicle. A negative angle of attack (α) places all the zero array sensors on the windward side. Conversely a positive α places the main array (0° array) of sensors on the leeward side. Flagged values ($\diagup$) represent pressure levels at 180° from the main array of sensors. Given angles of attack are nominal test conditions and transition regions (TR) shown on Figures 60 to 85 were deduced from phosphor paint photographs ($M_\infty = 4$ data) and heat transfer data for $M_\infty = 8$ and 10.

2. SPECTRAL DENSITY DISTRIBUTIONS

Spectral density distributions are presented in the form of third octave pressure distributions. For each tunnel condition representative distributions for turbulent, transition region, separated flow region (when applicable) base flow and tunnel tare noise are shown in Figures 86 through 180.
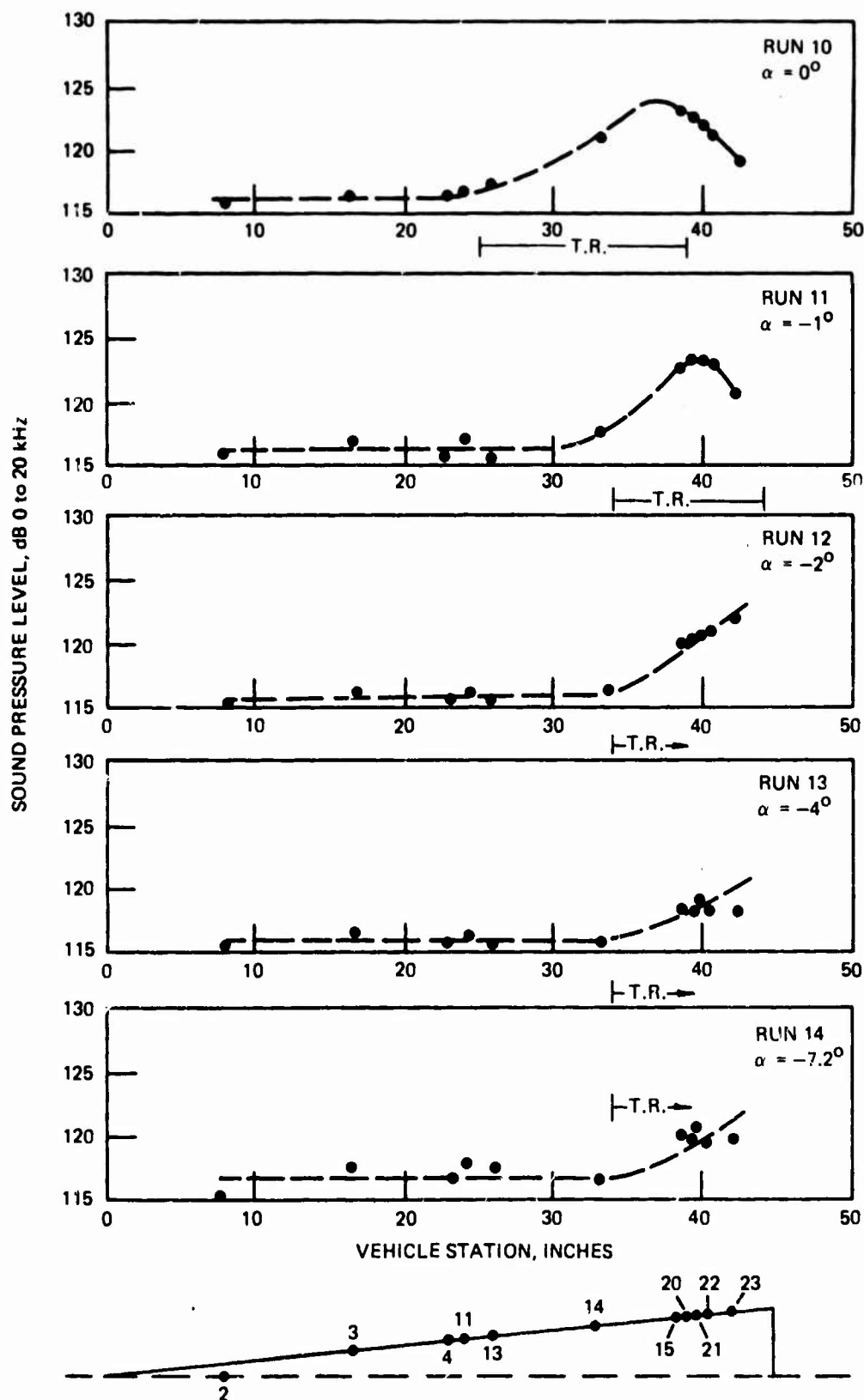
Figure 60. Fluctuating Pressure Distribution Tunnel Condition
$(R_{e_\infty} = 1.4 \times 10^6, \ M_\infty = 4.0, \ R_N = 0.0)$

85
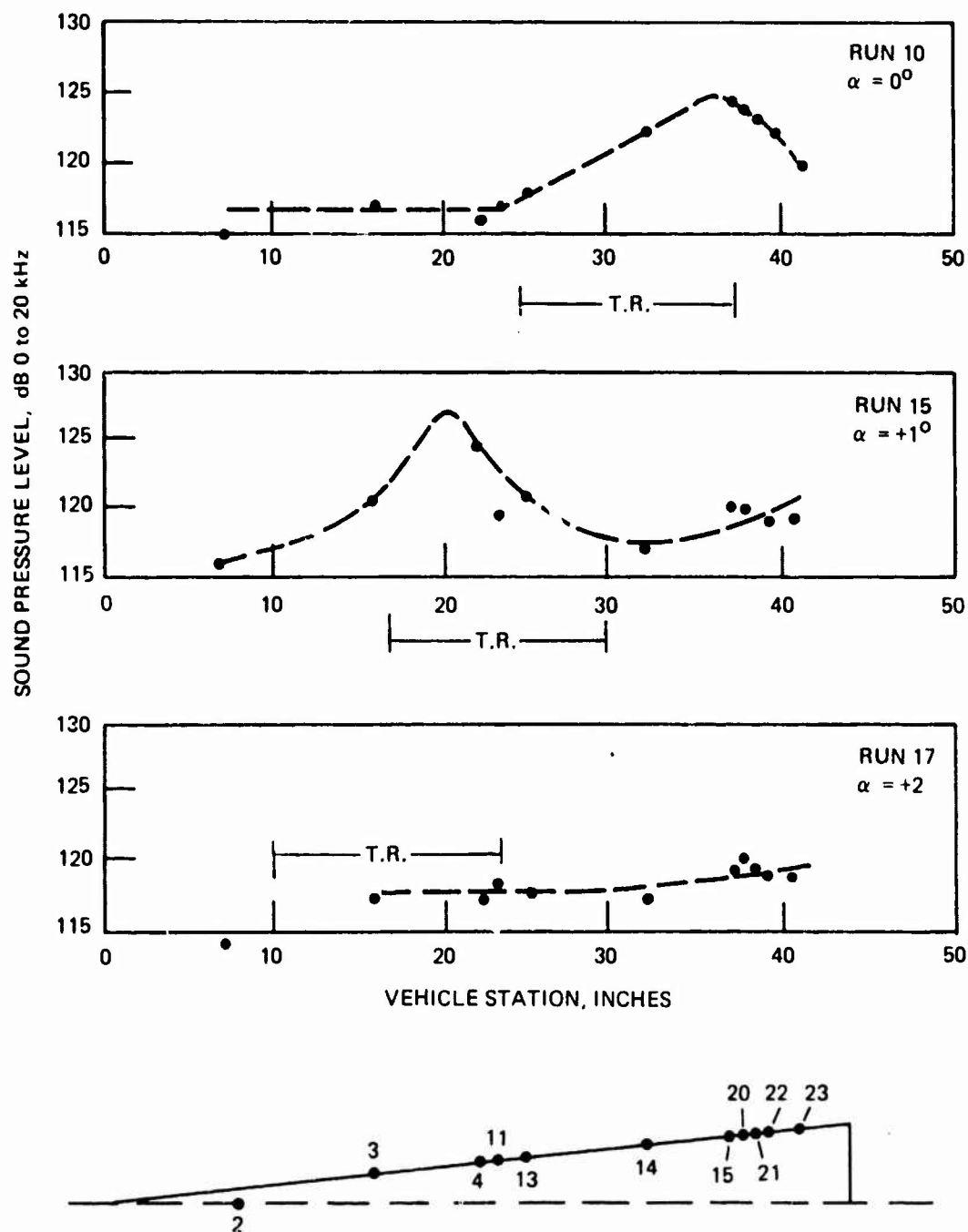
Figure 61. Fluctuating Pressure Distribution Tunnel Condition
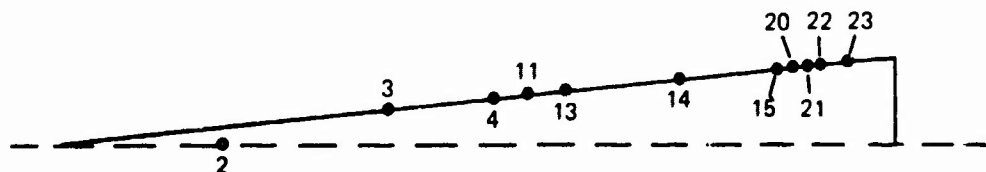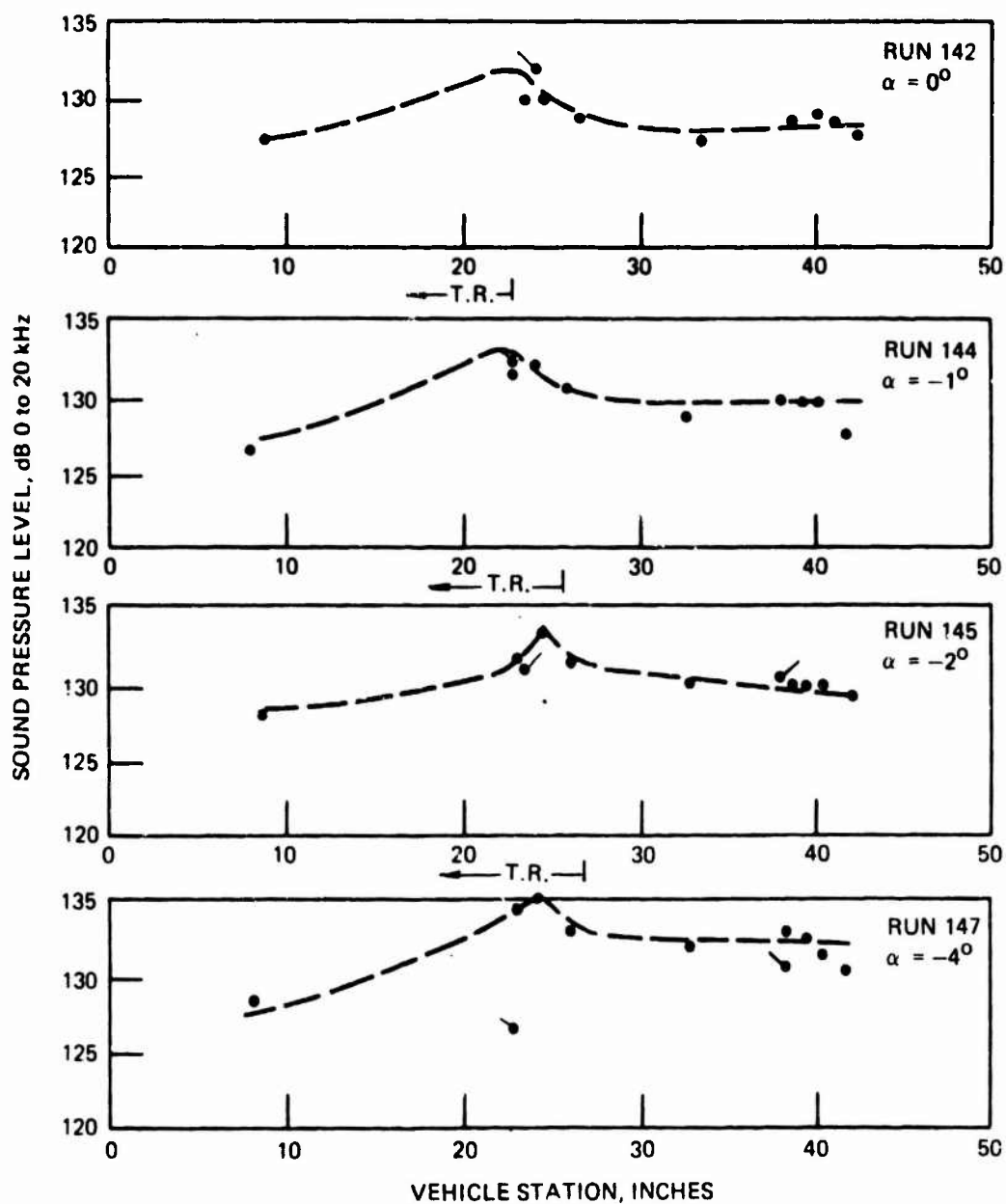$(Re_\infty = 1.4 \times 10^6,\ M_\infty = 4.0,\ R_N = 0.0)$
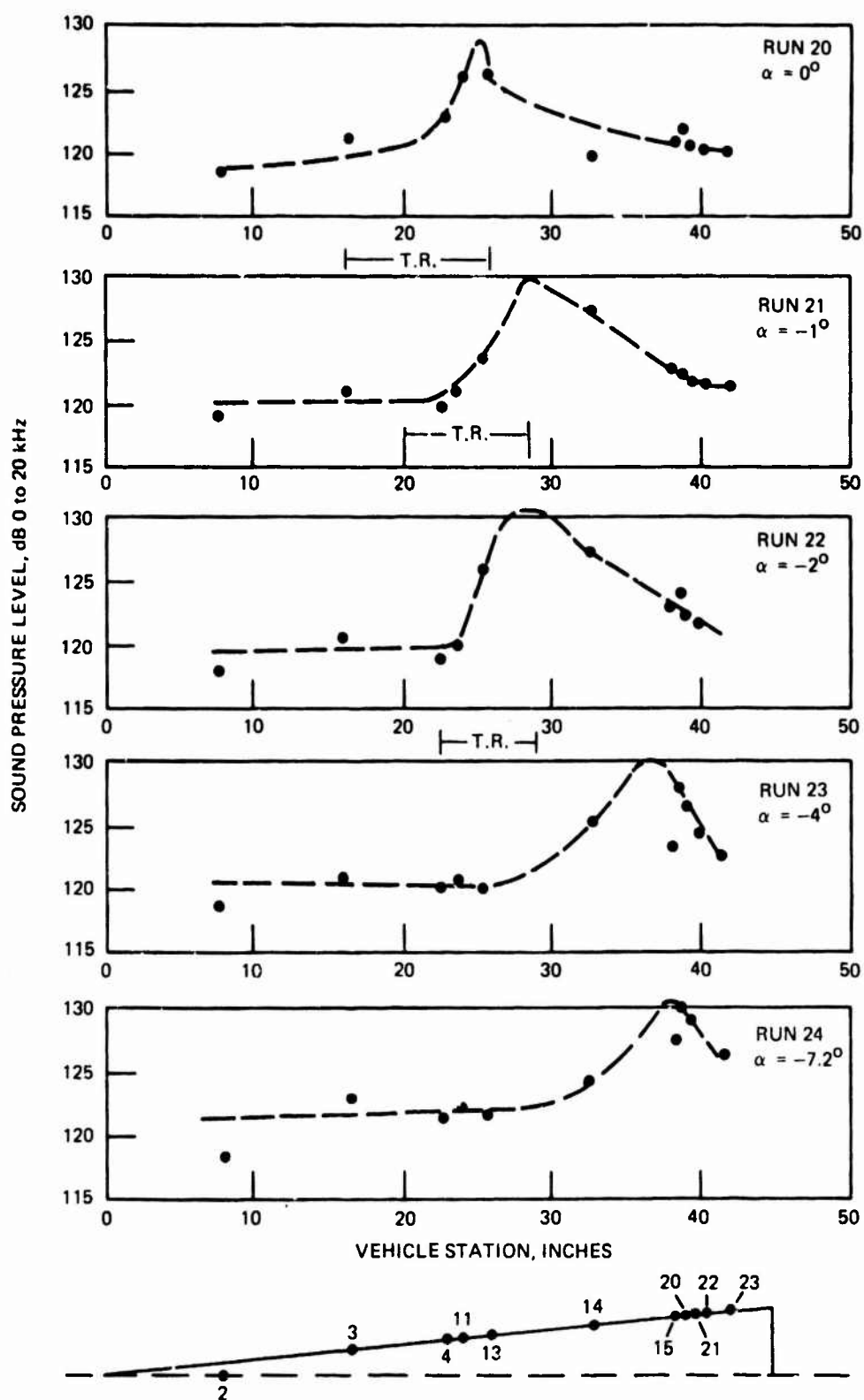
Figure 62. Fluctuating Pressure Distribution Tunnel Condition
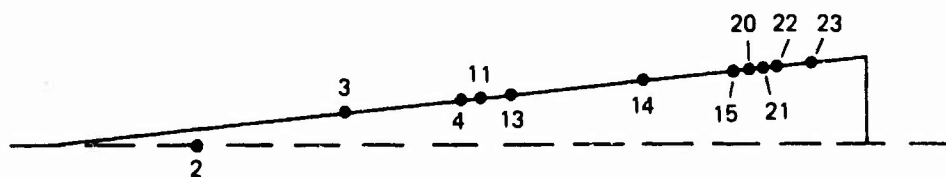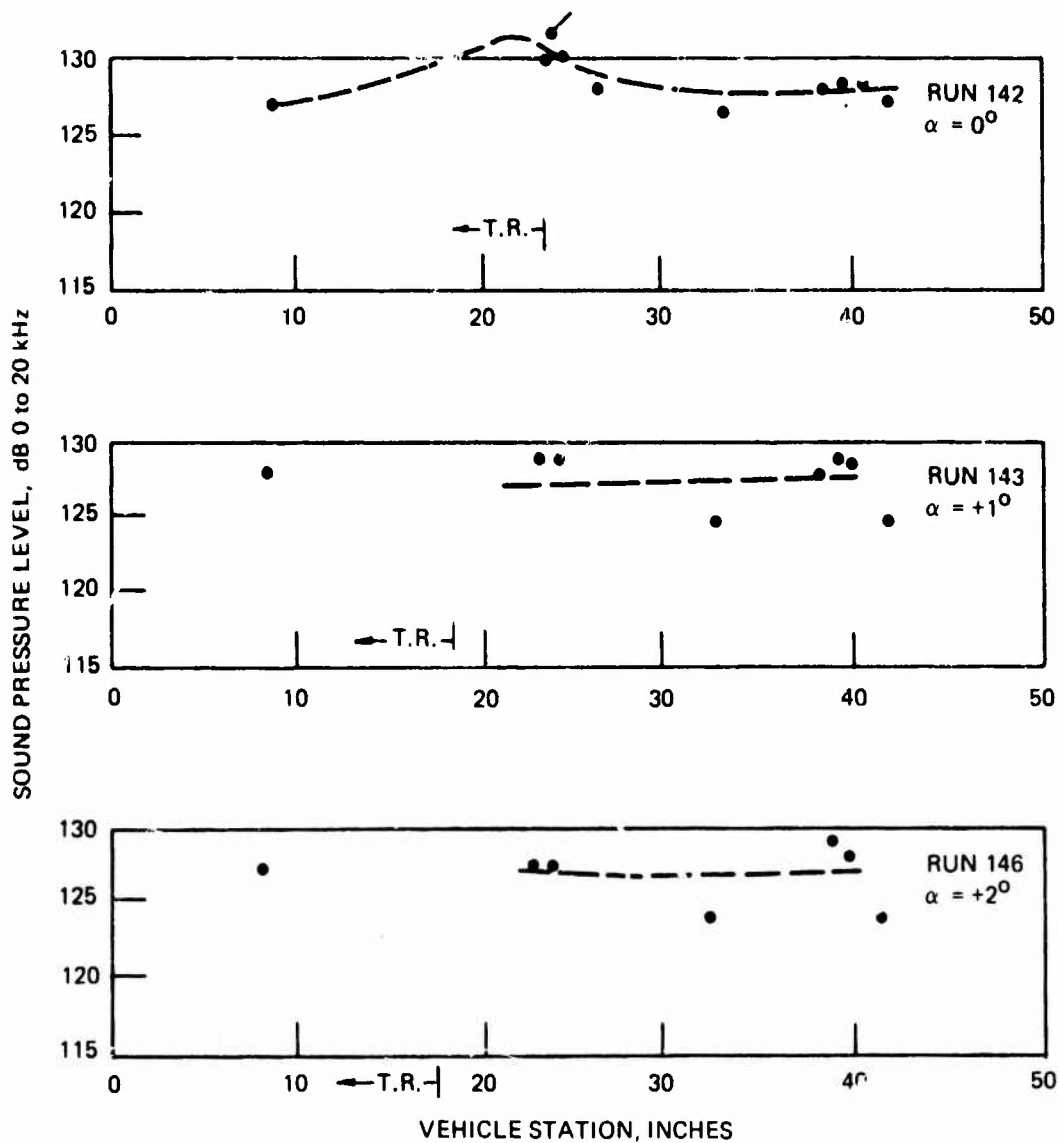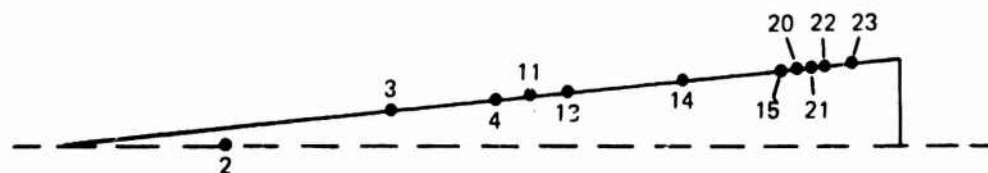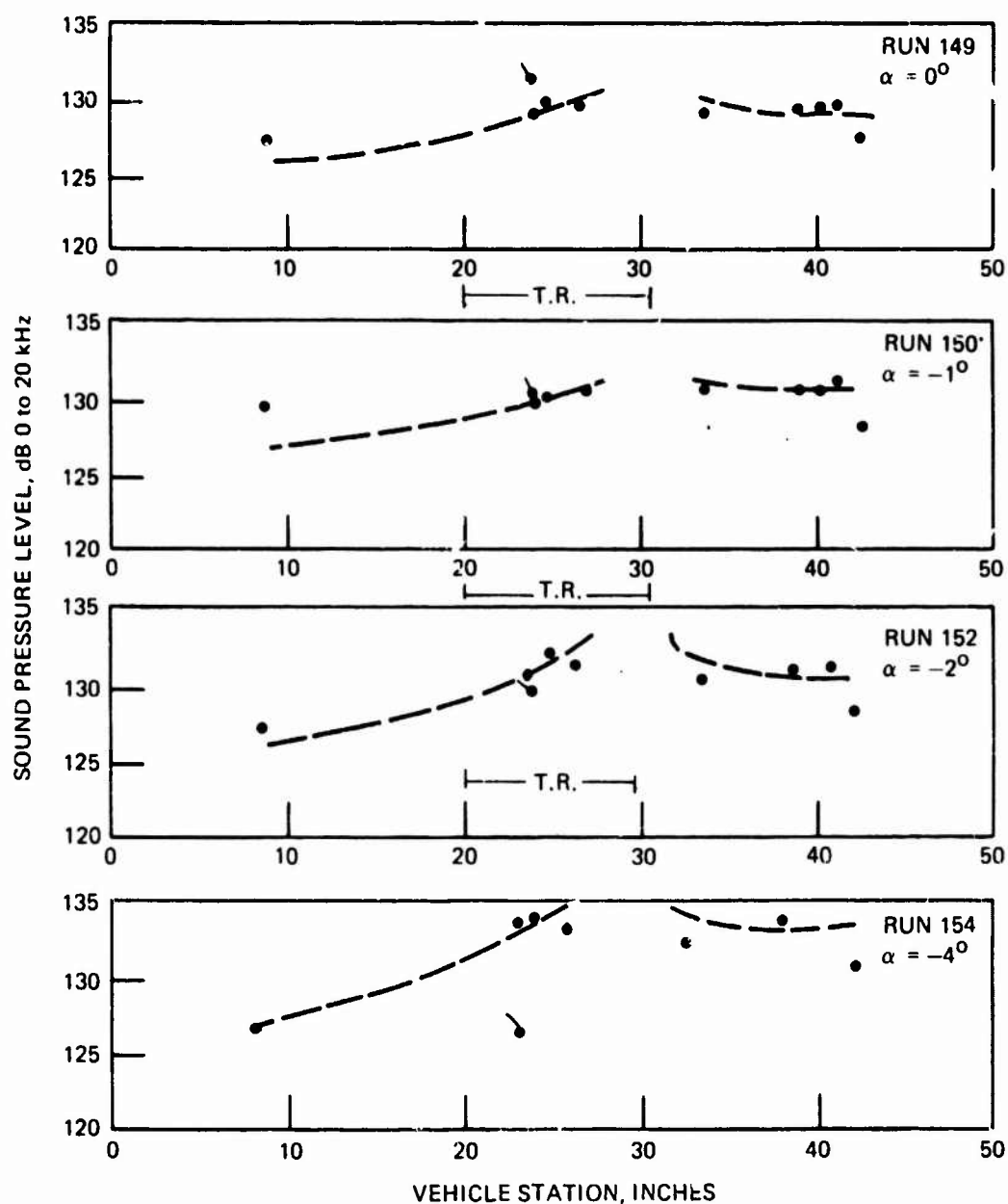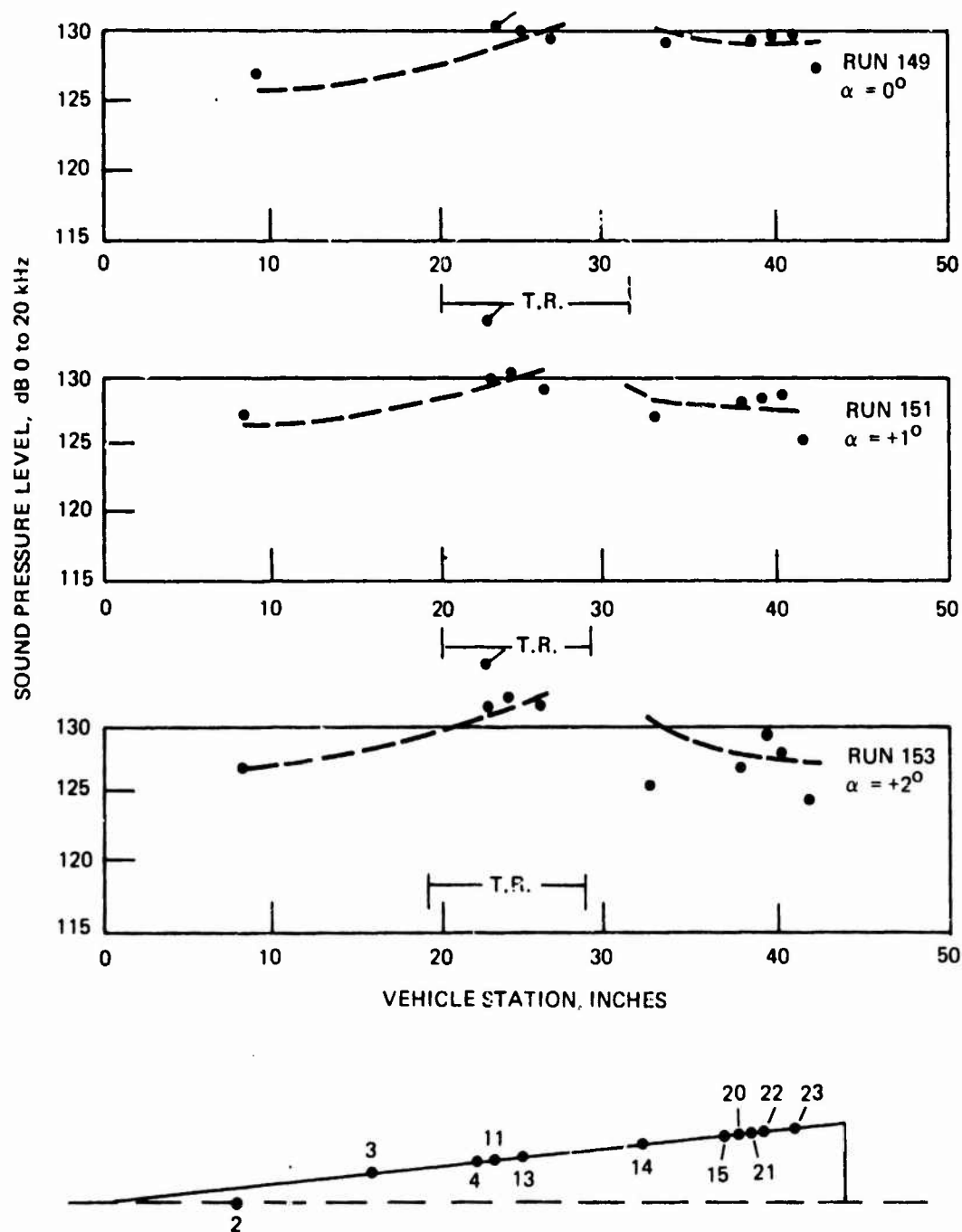$(Re_\infty = 2.2 \times 10^6, \ M_\infty = 4.0, \ R_N = 0.0)$

87
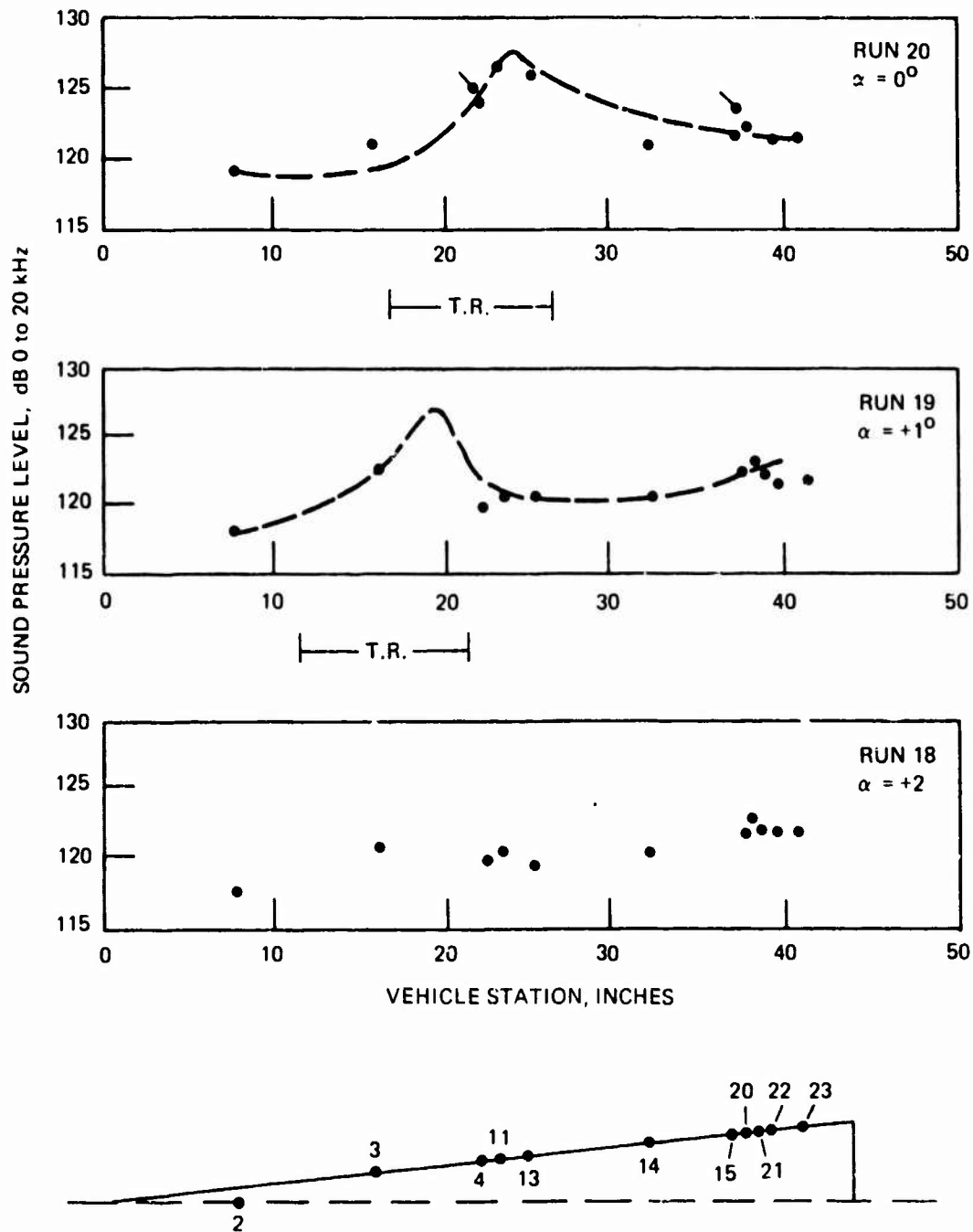
Figure 63. Fluctuating Pressure Distribution Tunnel Condition
$(R_{e_\infty} = 2.2 \times 10^6, \ M_\infty = 4.0, \ R_N = 0.0)$
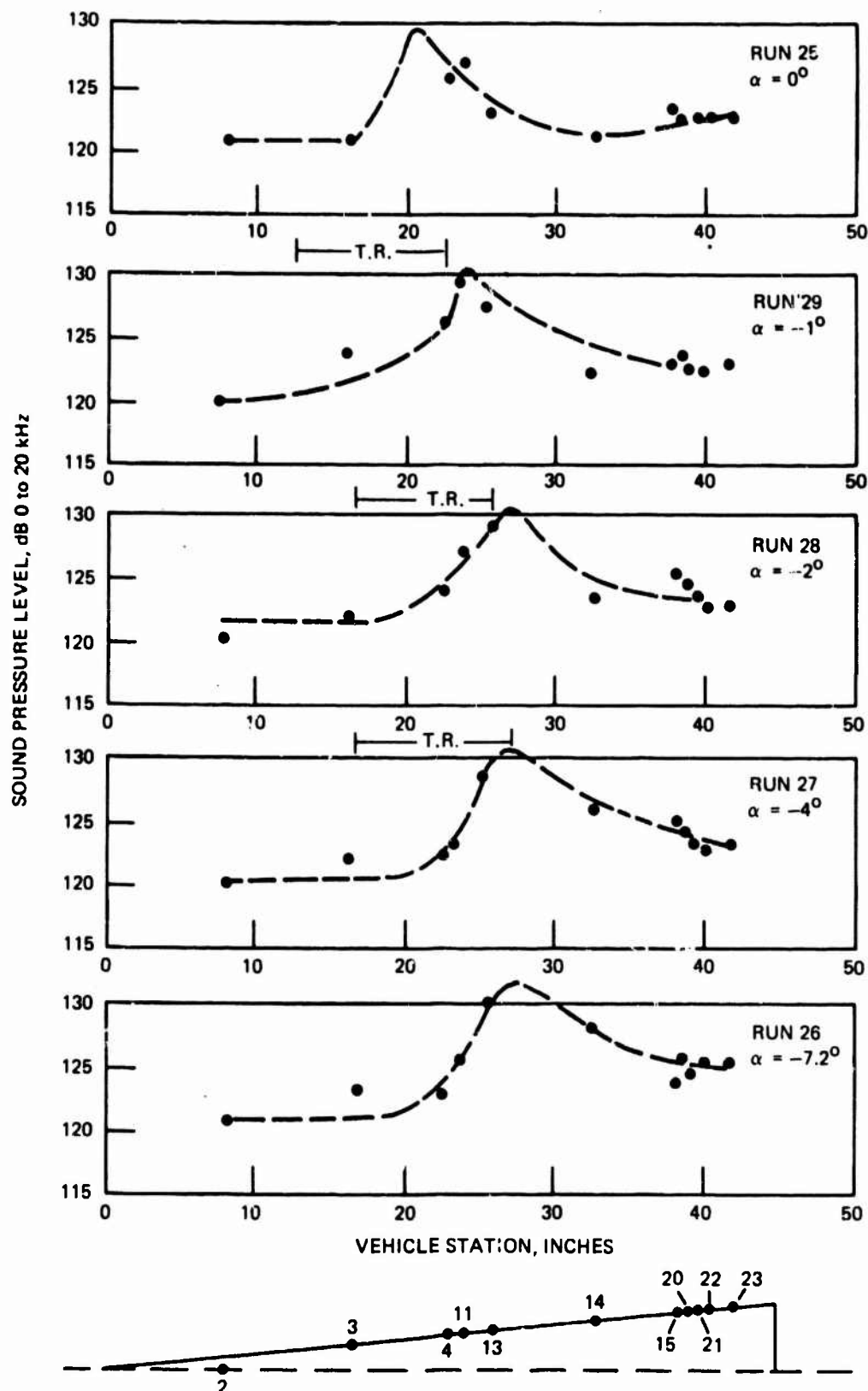
Figure 64. Fluctuating Pressure Distribution Tunnel Condition
$(R_{e_\infty} = 2.8 \times 10^6, \; M_\infty = 4.0, \; R_N = 0.0)$
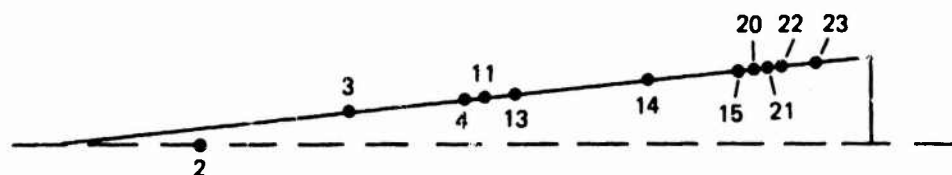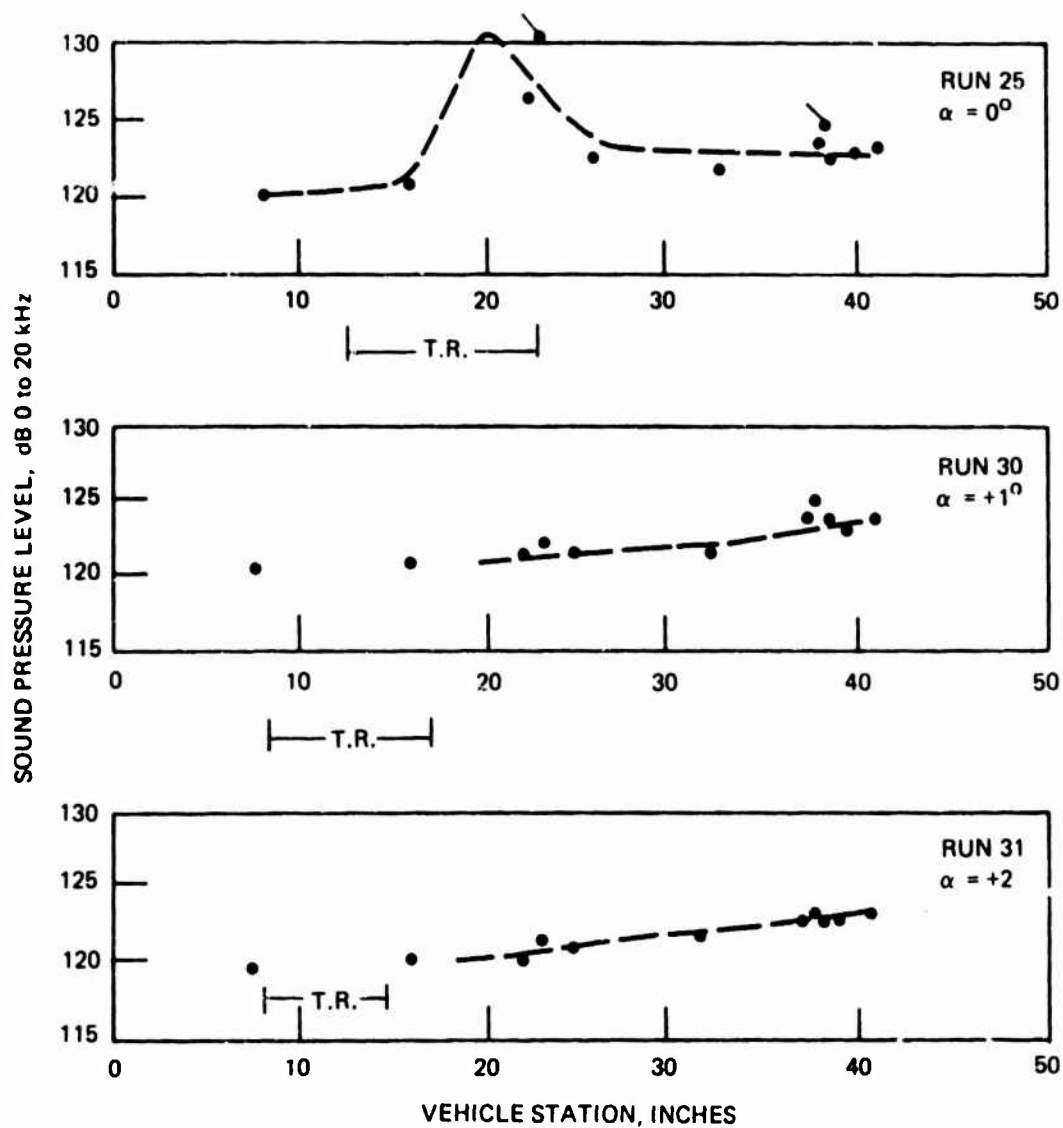
Figure 65. Fluctuating Pressure Distribution Tunnel Condition
($R_{e_\infty} = 2.8 \times 10^6$, $M_\infty = 4.0$, $R_N = 0.0$)

90
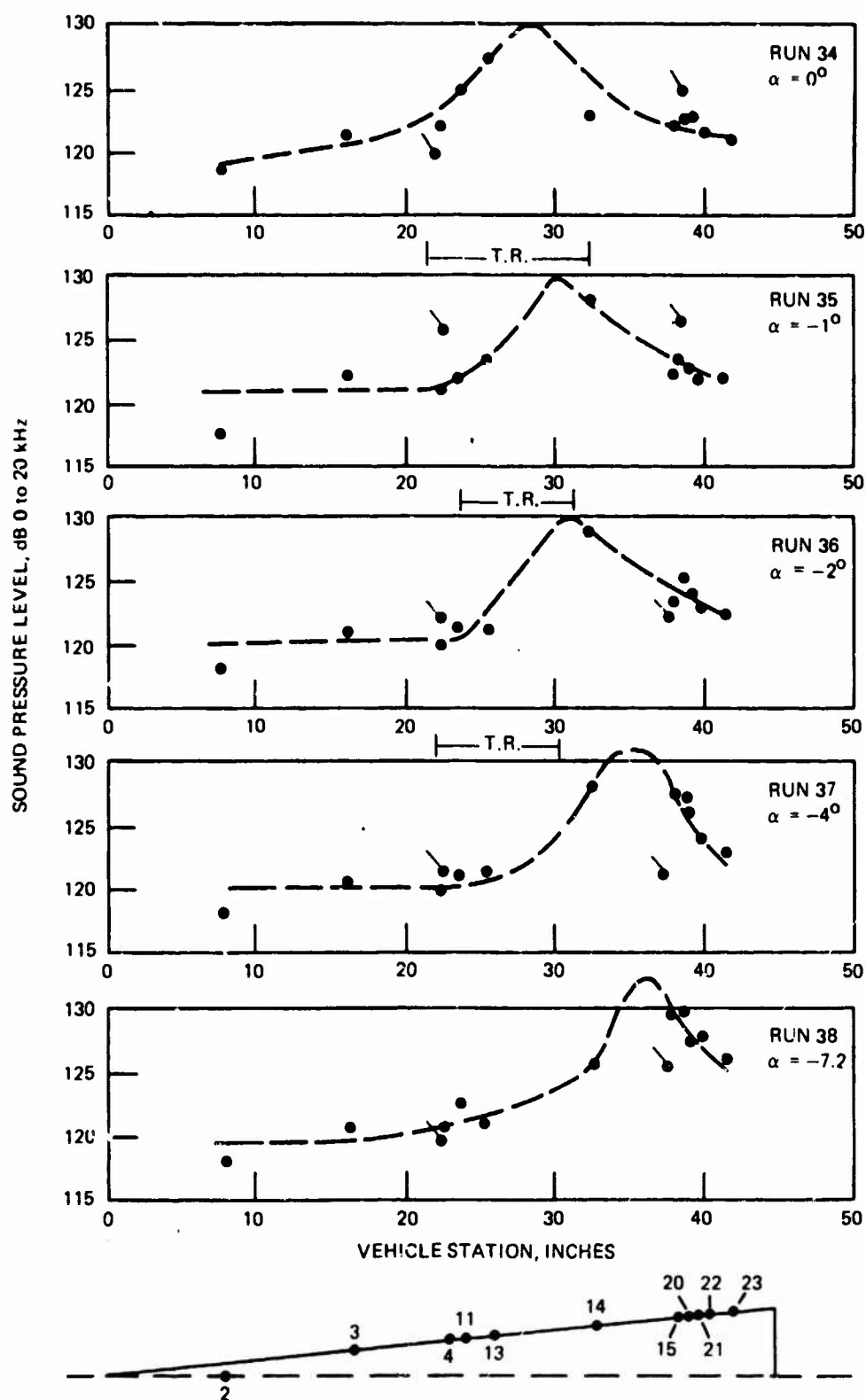
Figure 66. Fluctuating Pressure Distribution Tunnel Condition
$(R_\epsilon^{'\infty} = 2.2 \times 10^6, \ M_\infty = 4.0, \ R_N = 0.055)$

91
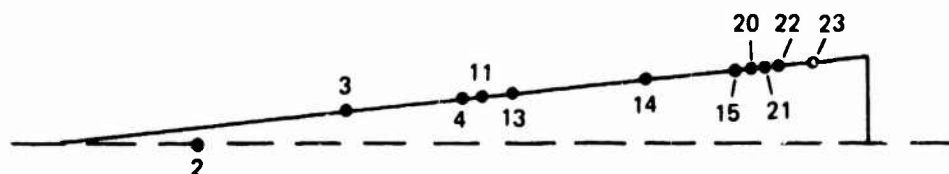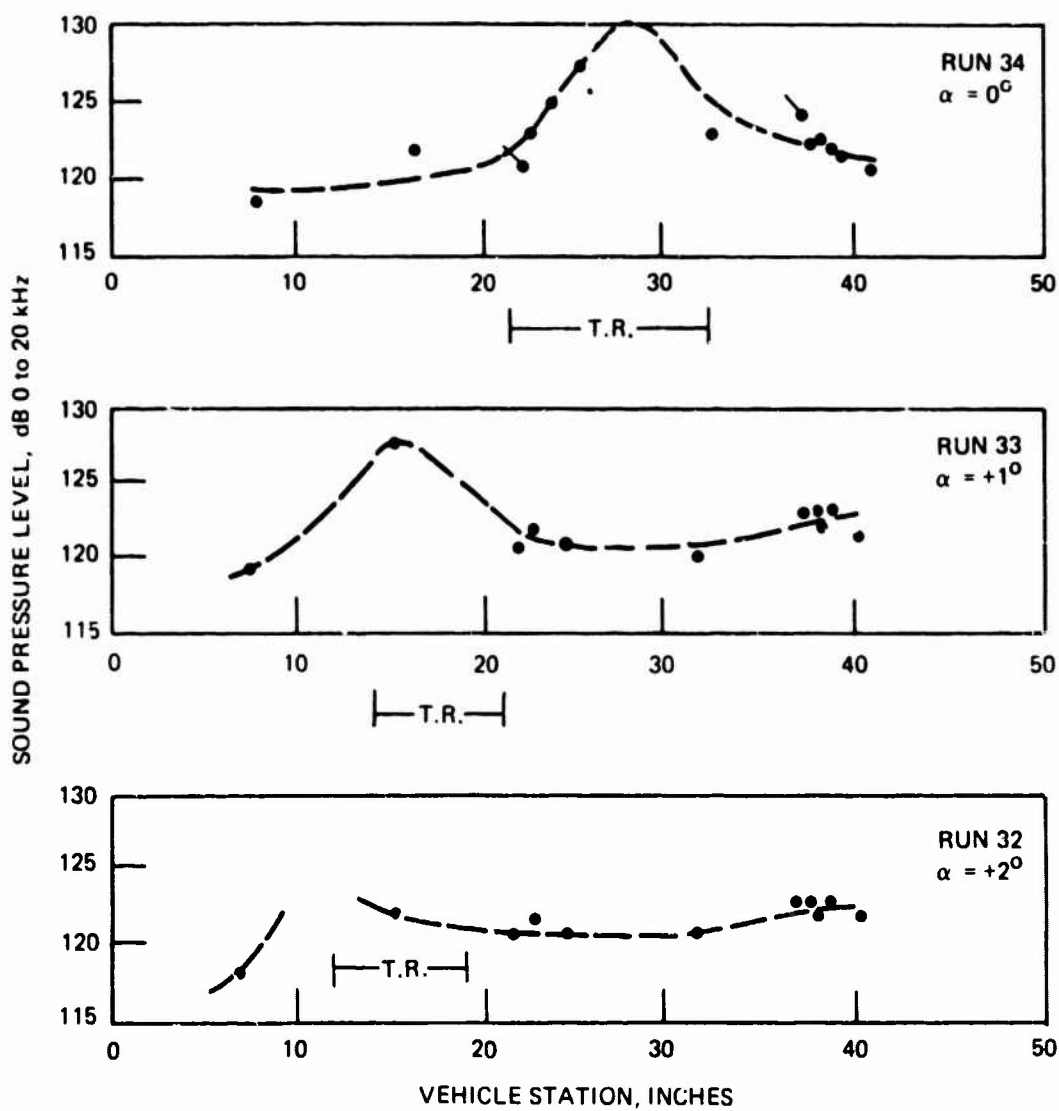
Figure 67. Fluctuating Pressure Distribution Tunnel Condition
$(R_{e_\infty} = 2.2 \times 10^6, \ M_\infty = 4.0, \ R_N = 0.055)$
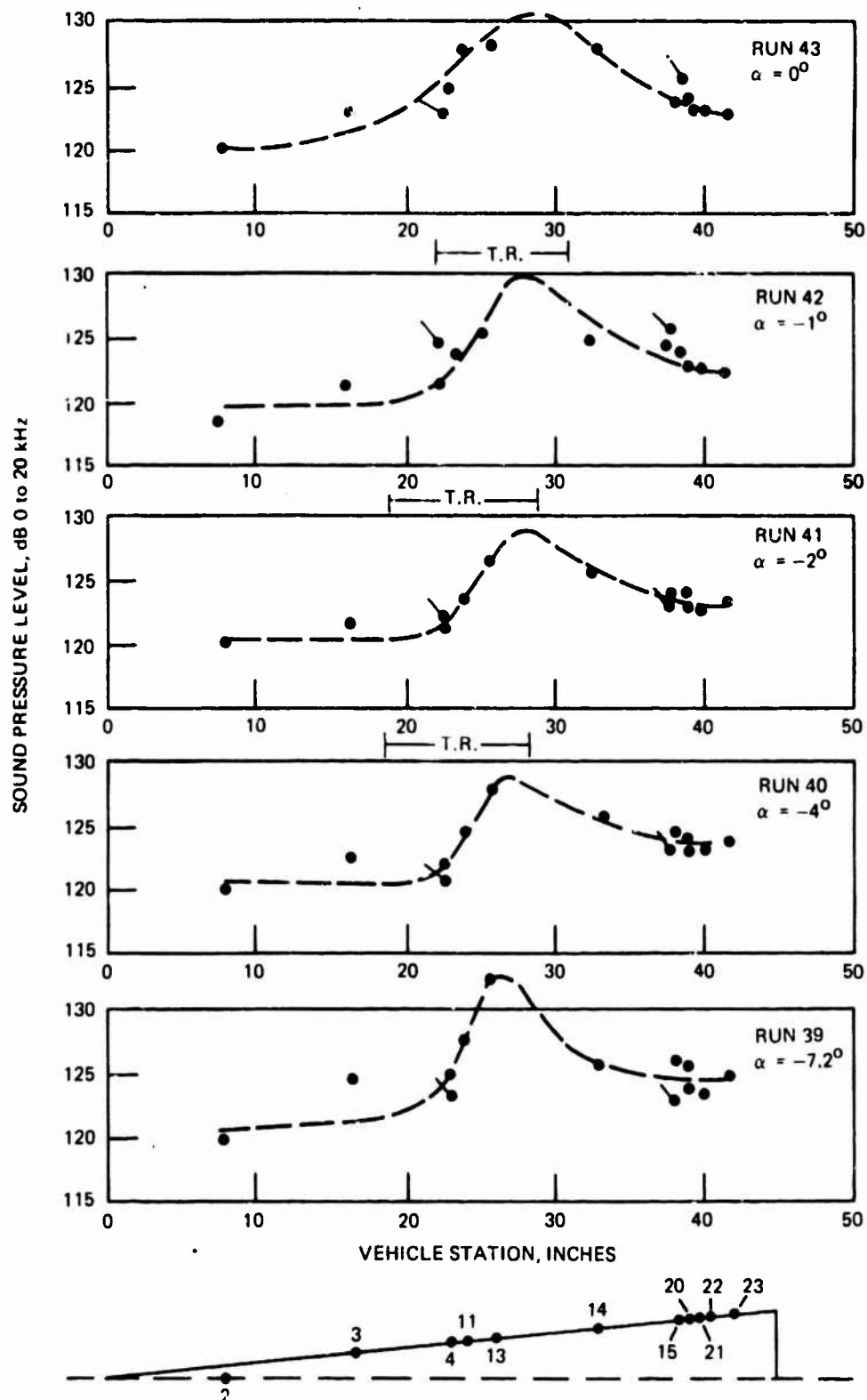
Figure 68. Fluctuating Pressure Distribution Tunnel Condition
$(R_{\theta_\infty} = 3.0 \times 10^6, \ M_\infty = 4.0, \ R_N = 0.11)$

93
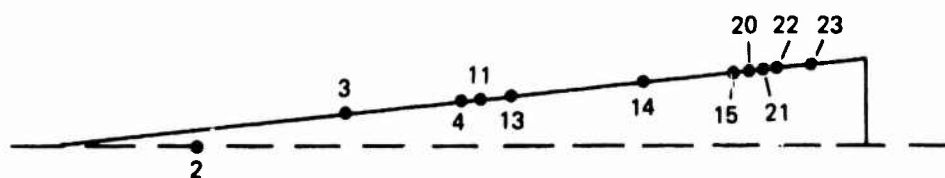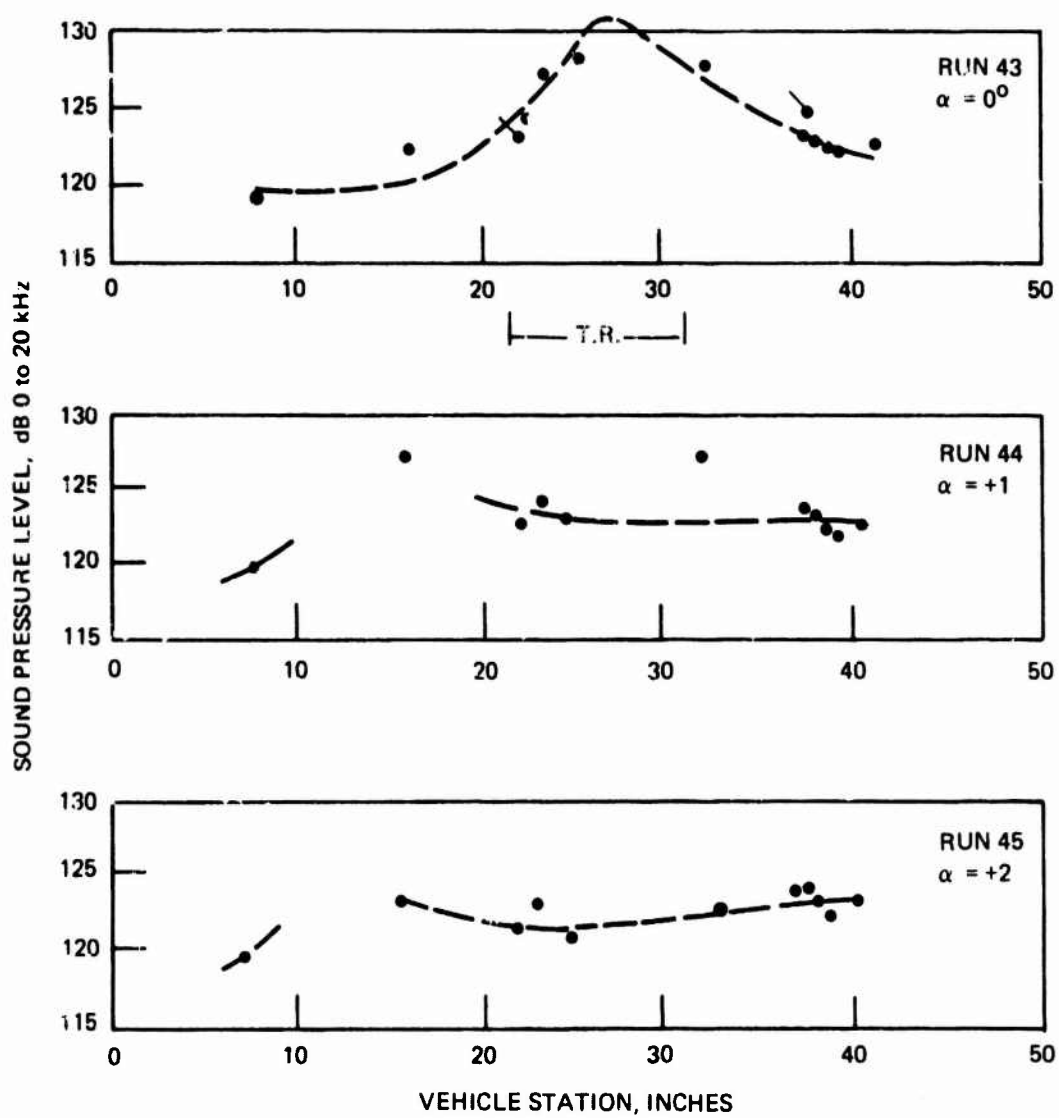
Figure 69. Fluctuating Pressure Distribution Tunnel Condition
$(R_{e_2} = 3.0 \times 10^6, \ M_\infty = 4.0, \ R_N = 0.11)$

94
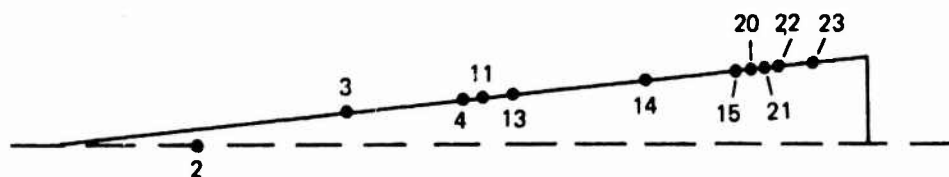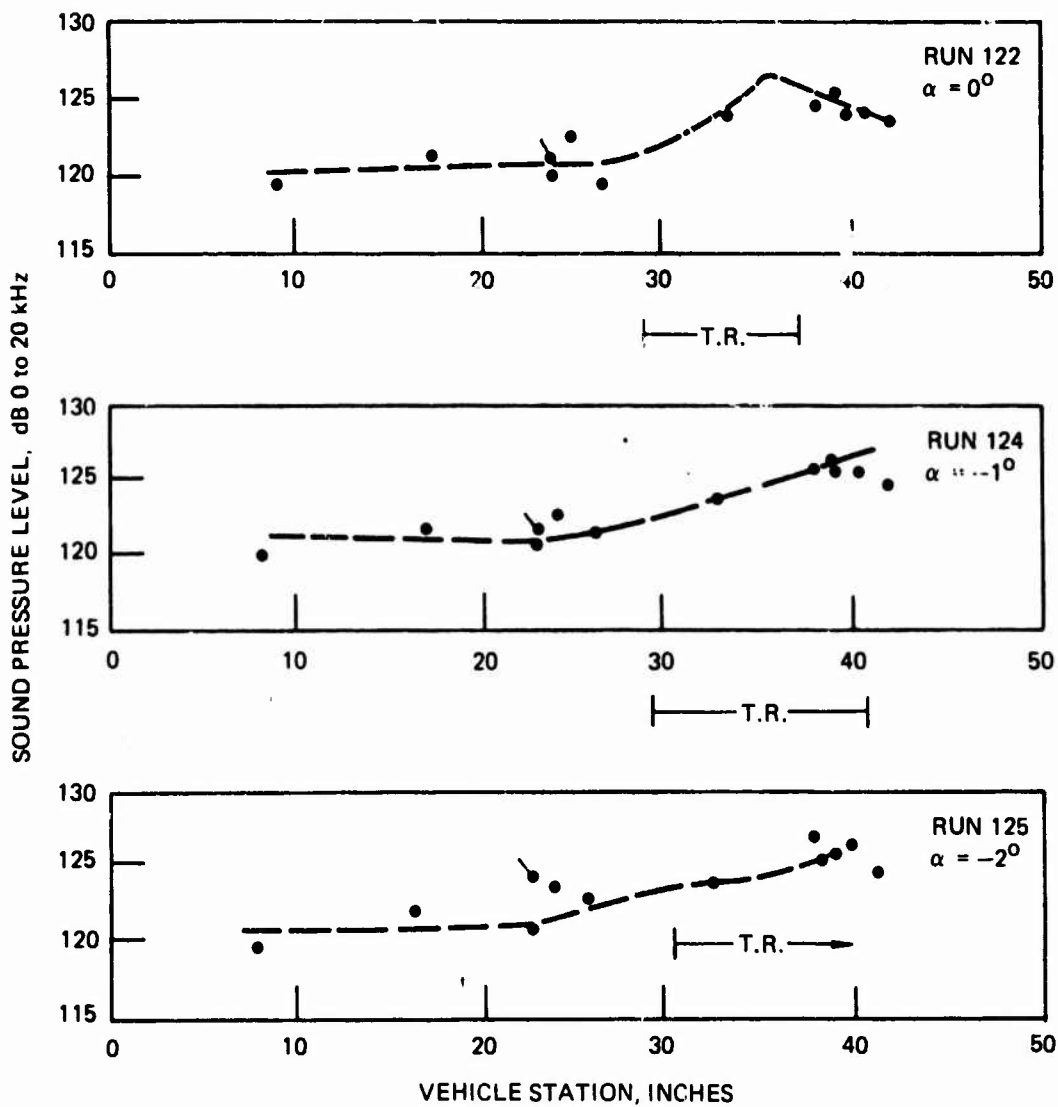
Figure 70. Fluctuating Pressure Distribution Tunnel Condition
($Re_\infty = 1.4 \times 10^6$, $M_\infty = 8.0$, $R_N = 0.0$)
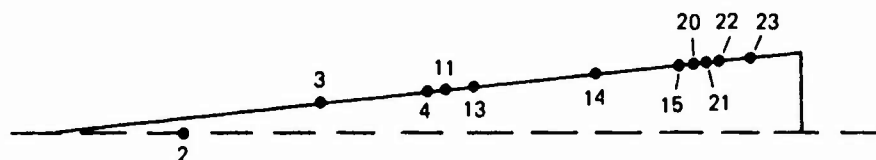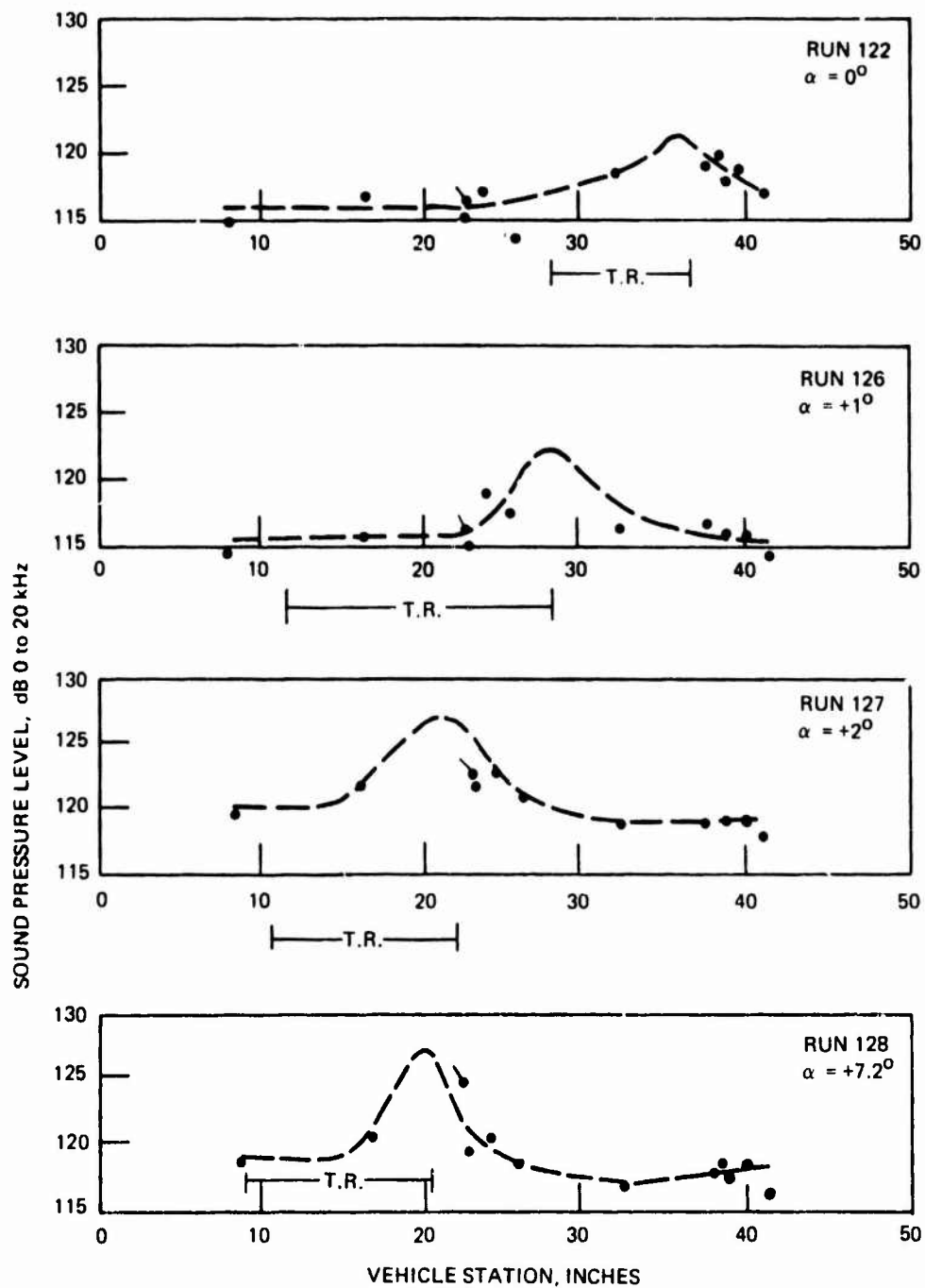
Figure 71. Fluctuating Pressure Distribution Tunnel Condition
$(R_{e_\infty} = 1.4 \times 10^6,\ M_\infty = 8.0,\ R_N = 0.0)$

96
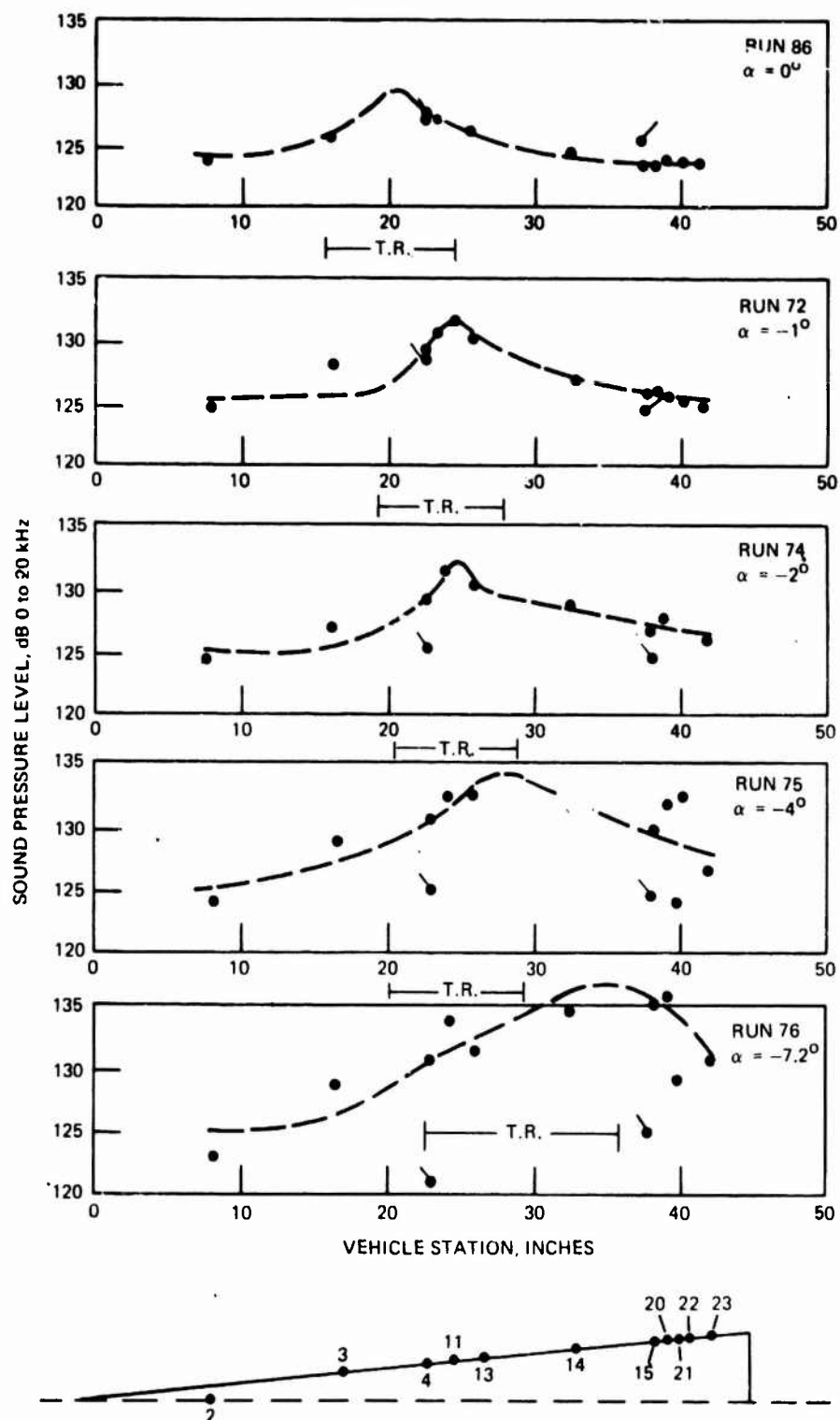
Figure 72. Fluctuating Pressure Distribution Tunnel Condition $(R_{e_\infty} = 2.2 \times 10^6,\ M_\infty = 8.0,\ R_N = 0.0)$
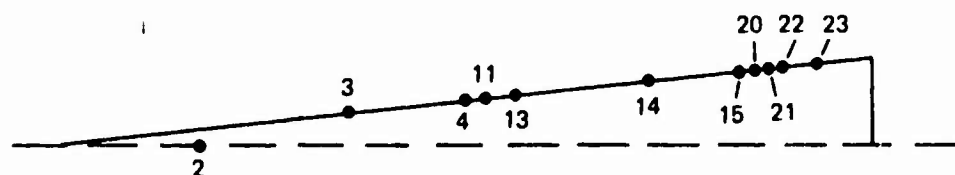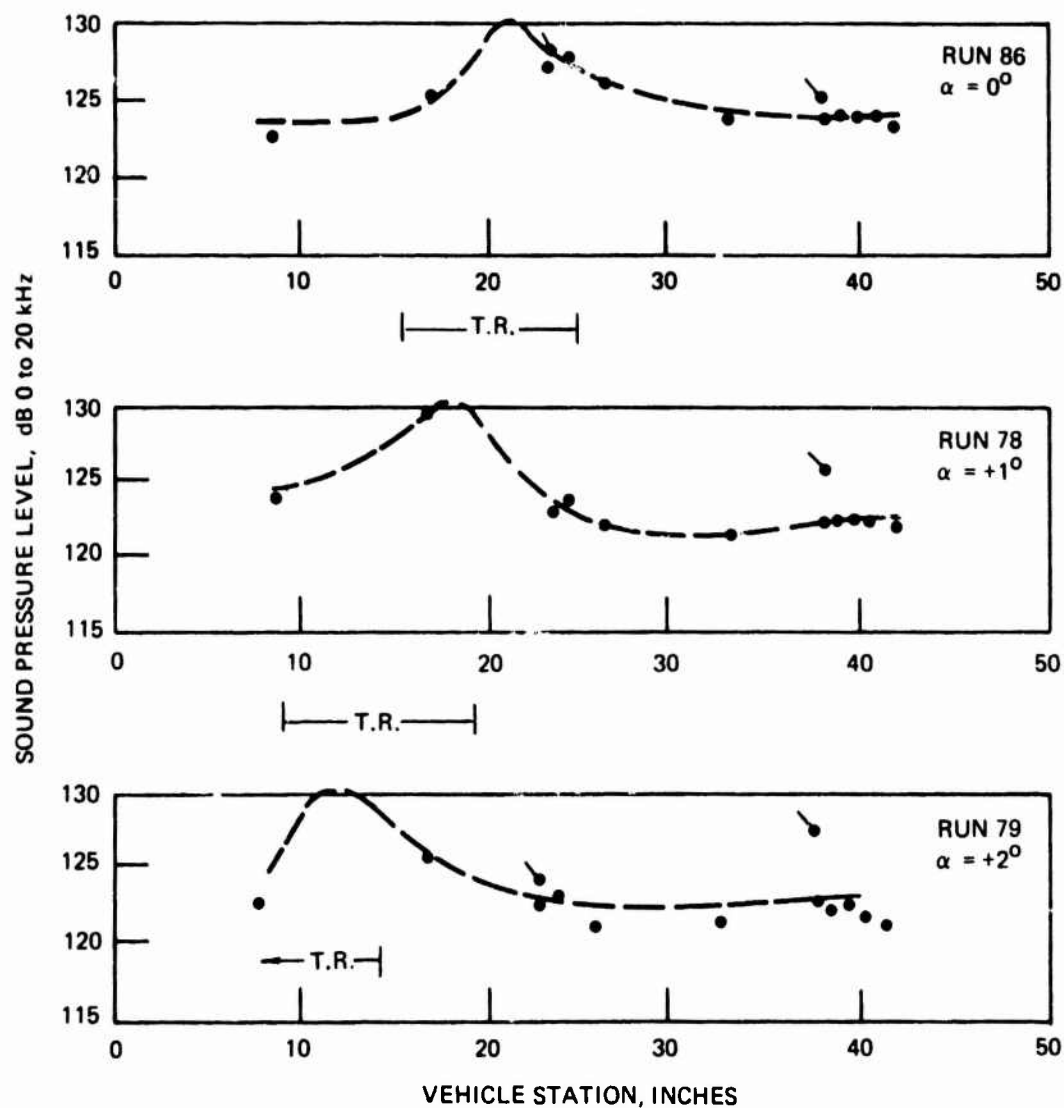
Figure 73. Fluctuating Pressure Distribution Tunnel Condition
(R_{e_∞} = 2.2 x 10^6, M_∞ = 8.0, R_N = 0.0)
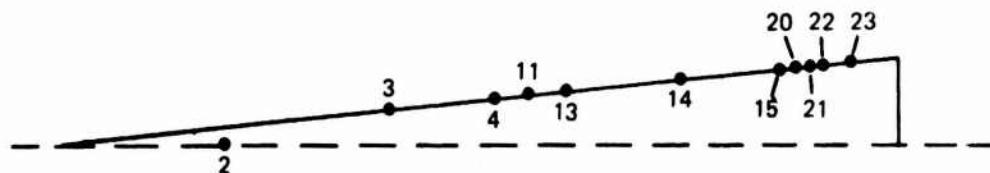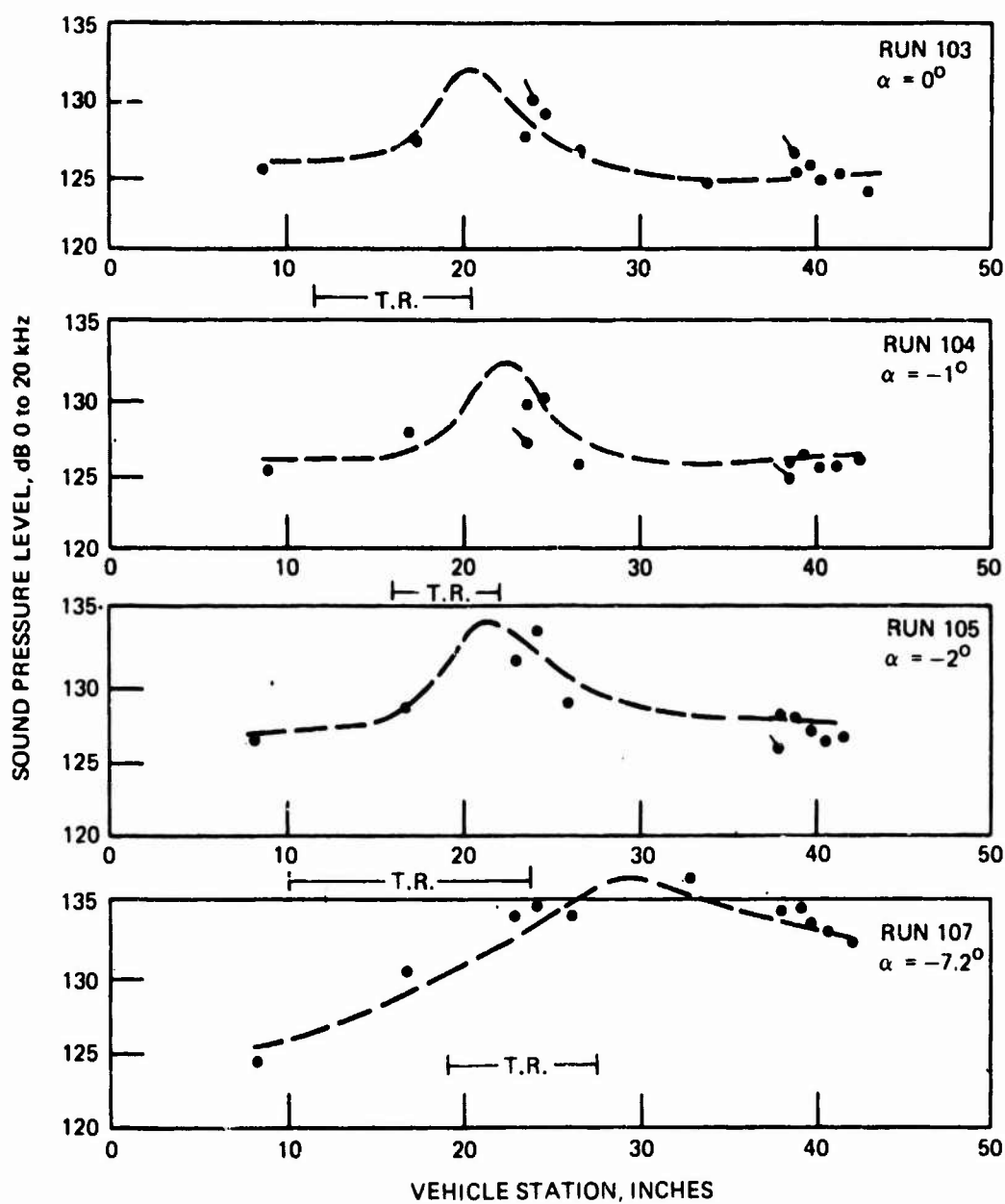
Figure 74. Fluctuating Pressure Distribution Tunnel Condition
($R_{e_\infty} = 2.8 \times 10^6$, $M_\infty = 8.0$, $R_N = 0.0$)

99
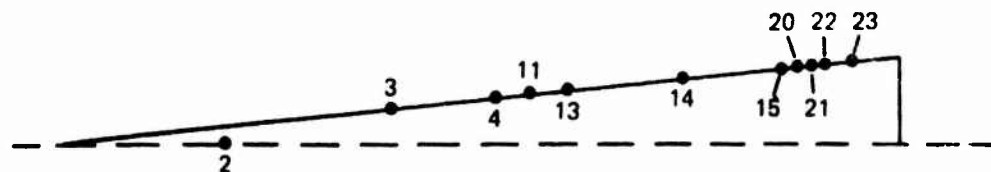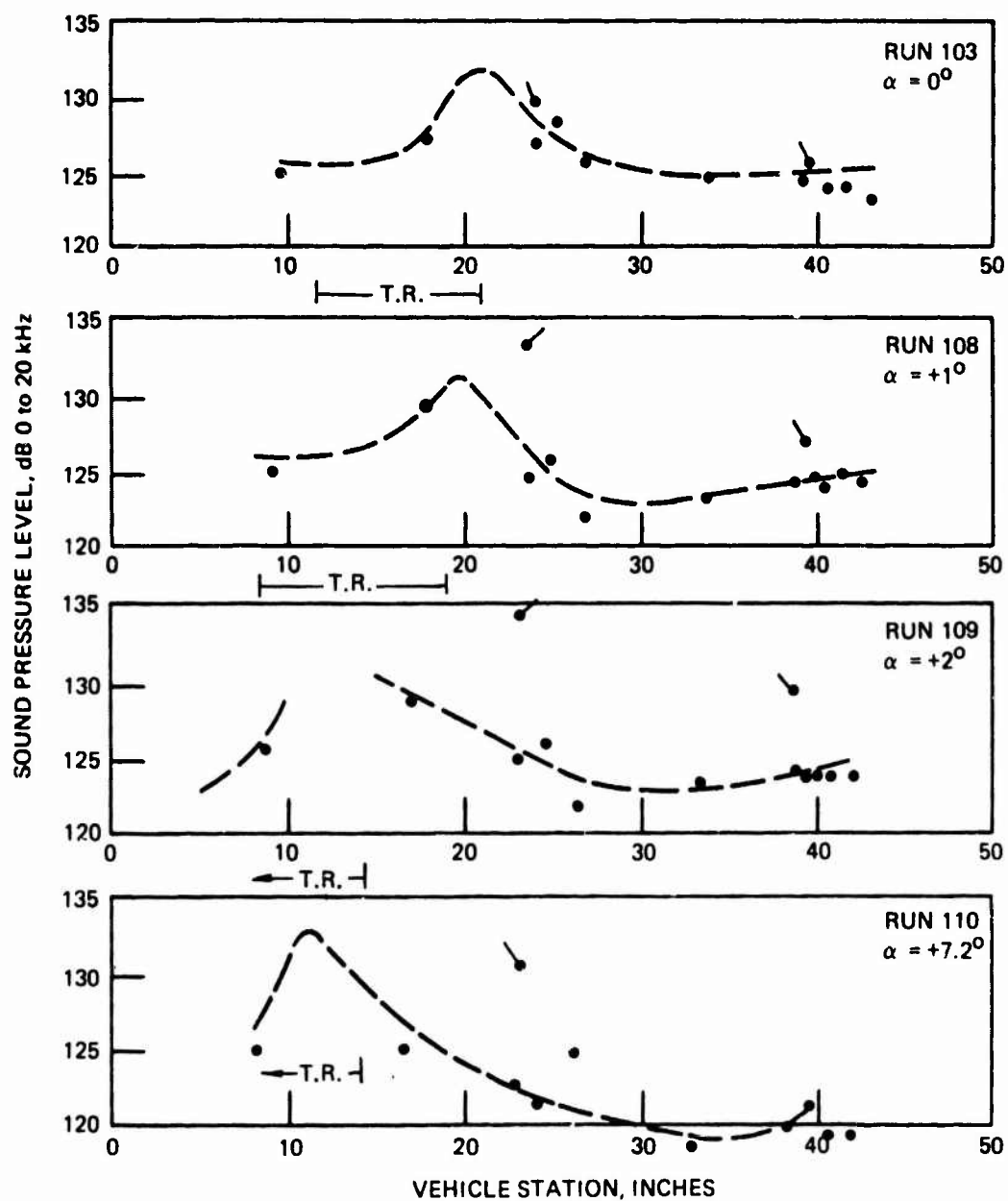
Figure 75. Fluctuating Pressure Distribution Tunnel Condition
$(R_{e_\infty} = 2.8 \times 10^6, \ M_\infty = 8.0, \ R_N = 0.0)$
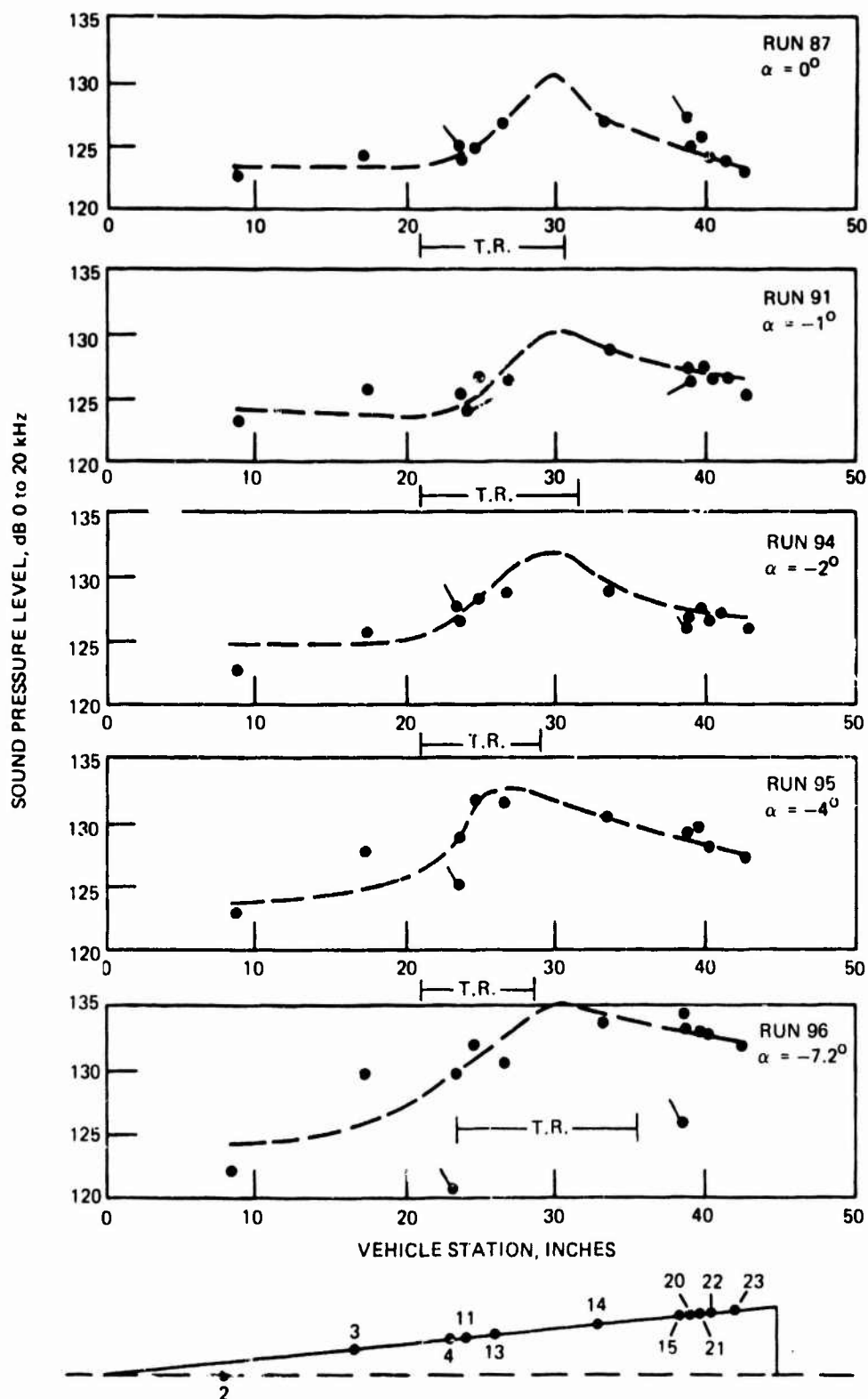
Figure 76. Fluctuating Pressure Distribution Tunnel Condition
$(R_{e_\infty} = 2.2 \times 10^6, \ M_\infty = 8.0, \ R_N = 0.055)$
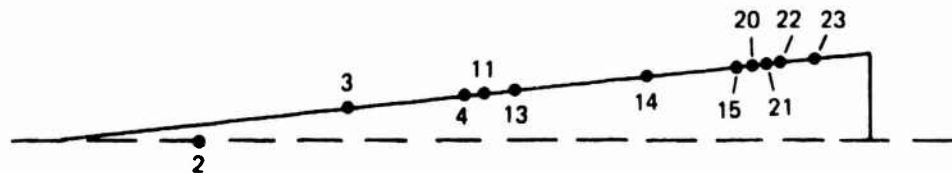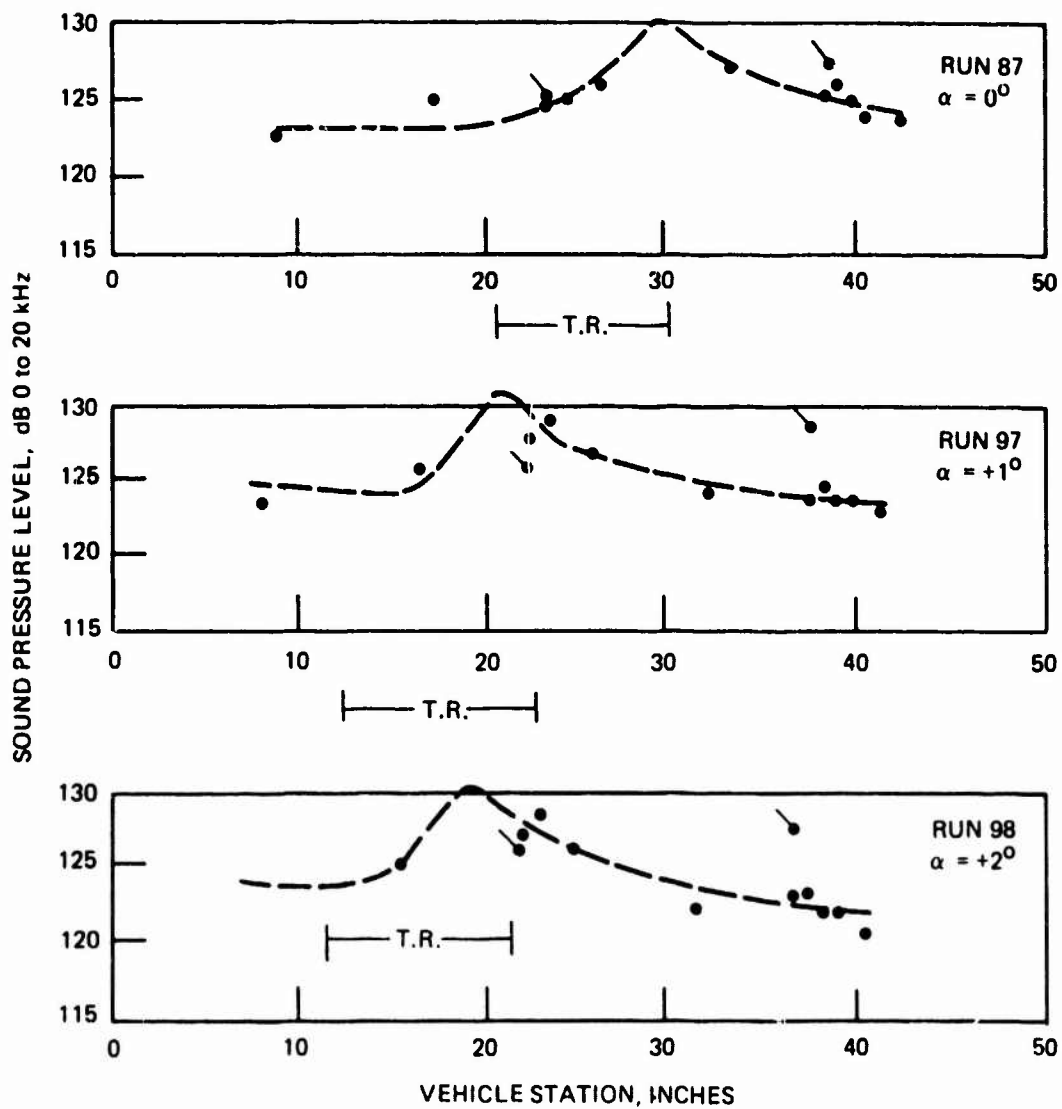
Figure 77. Fluctuating Pressure Distribution Tunnel Condition
($Re_\infty = 2.2 \times 10^6$, $M_\infty = 8.0$, $R_N = 0.055$)

102
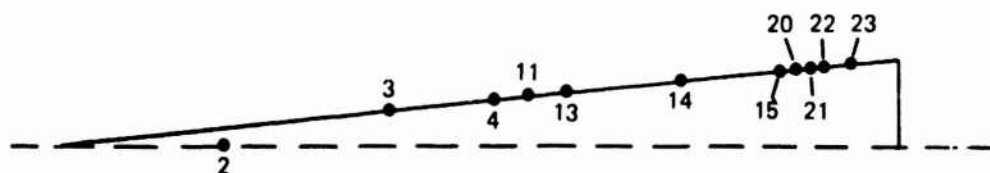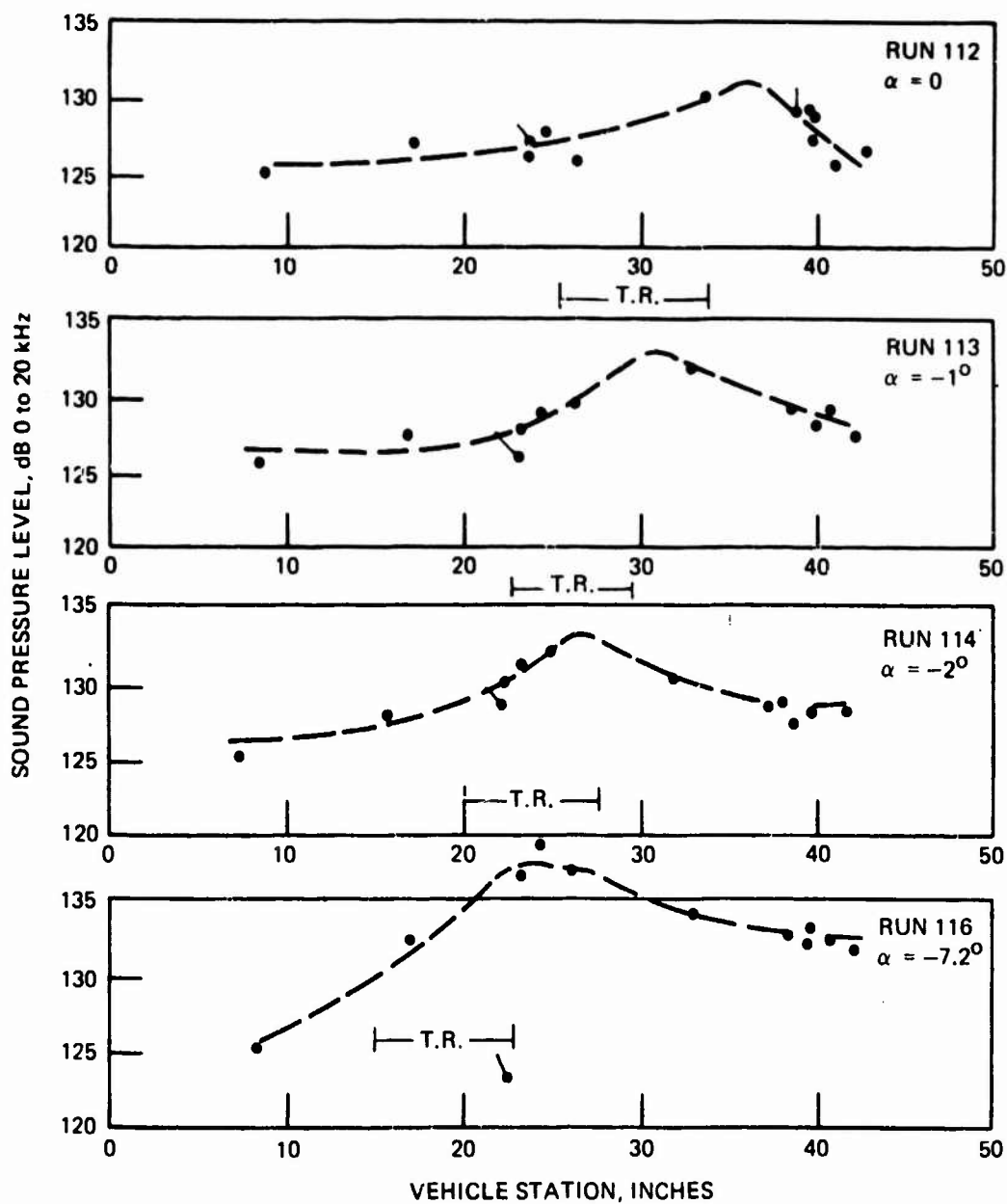
Figure 78. Fluctuating Pressure Distribution Tunnel Condition
$(R_{e_\infty} = 3.25 \times 10^6, M_\infty = 8.0, R_N = 0.11)$
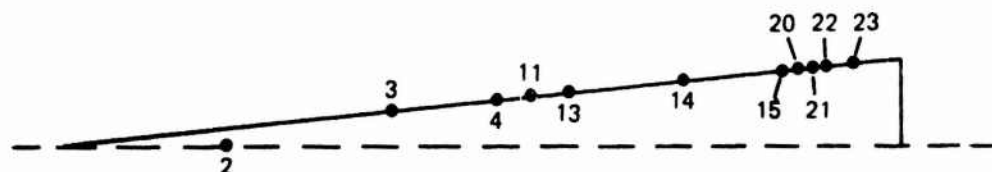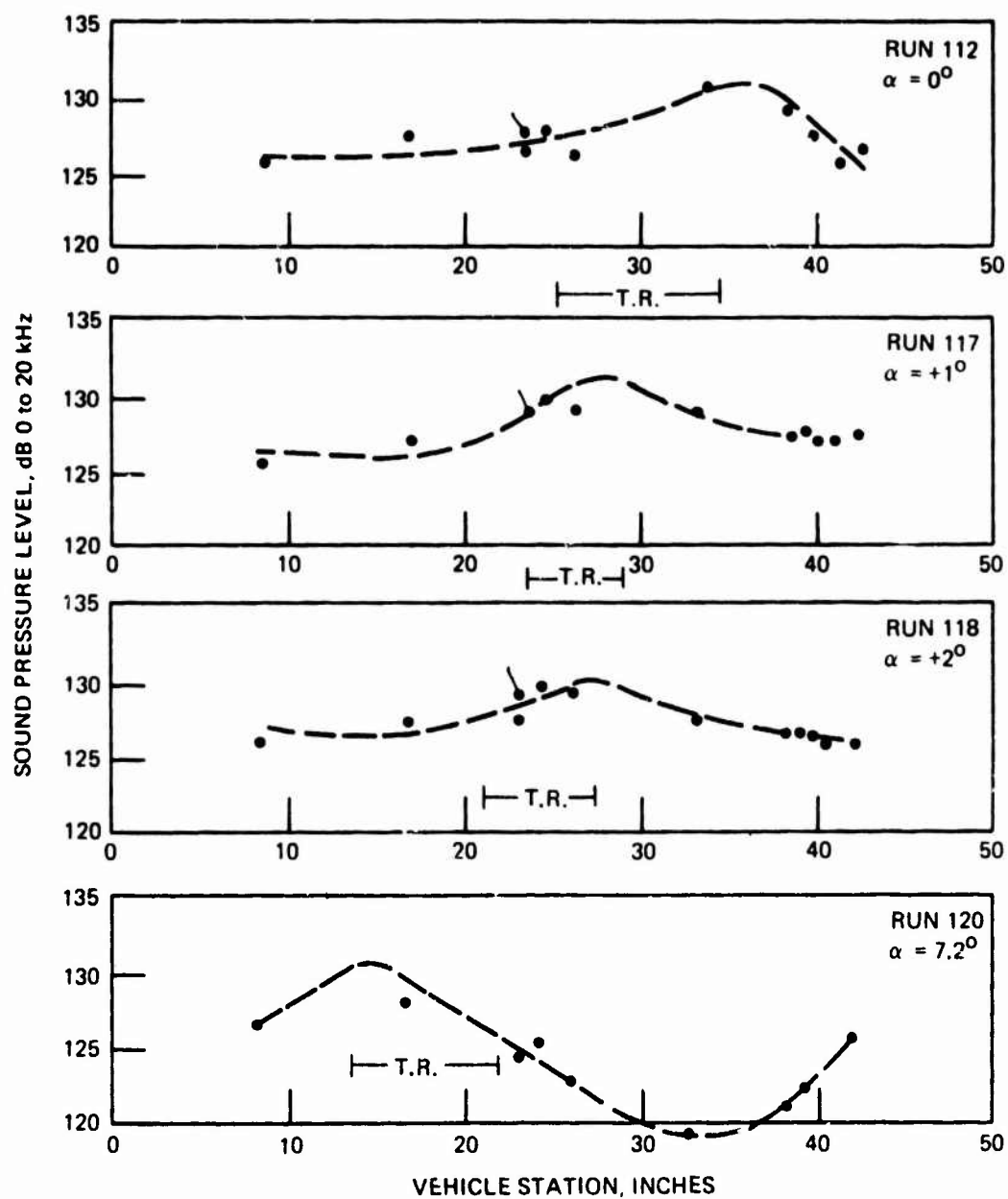
Figure 79. Fluctuating Pressure Distribution Tunnel Condition
$(R_e = 3.25 \times 10^6, \ M_\infty = 8.0, \ R_N = 0.11)$
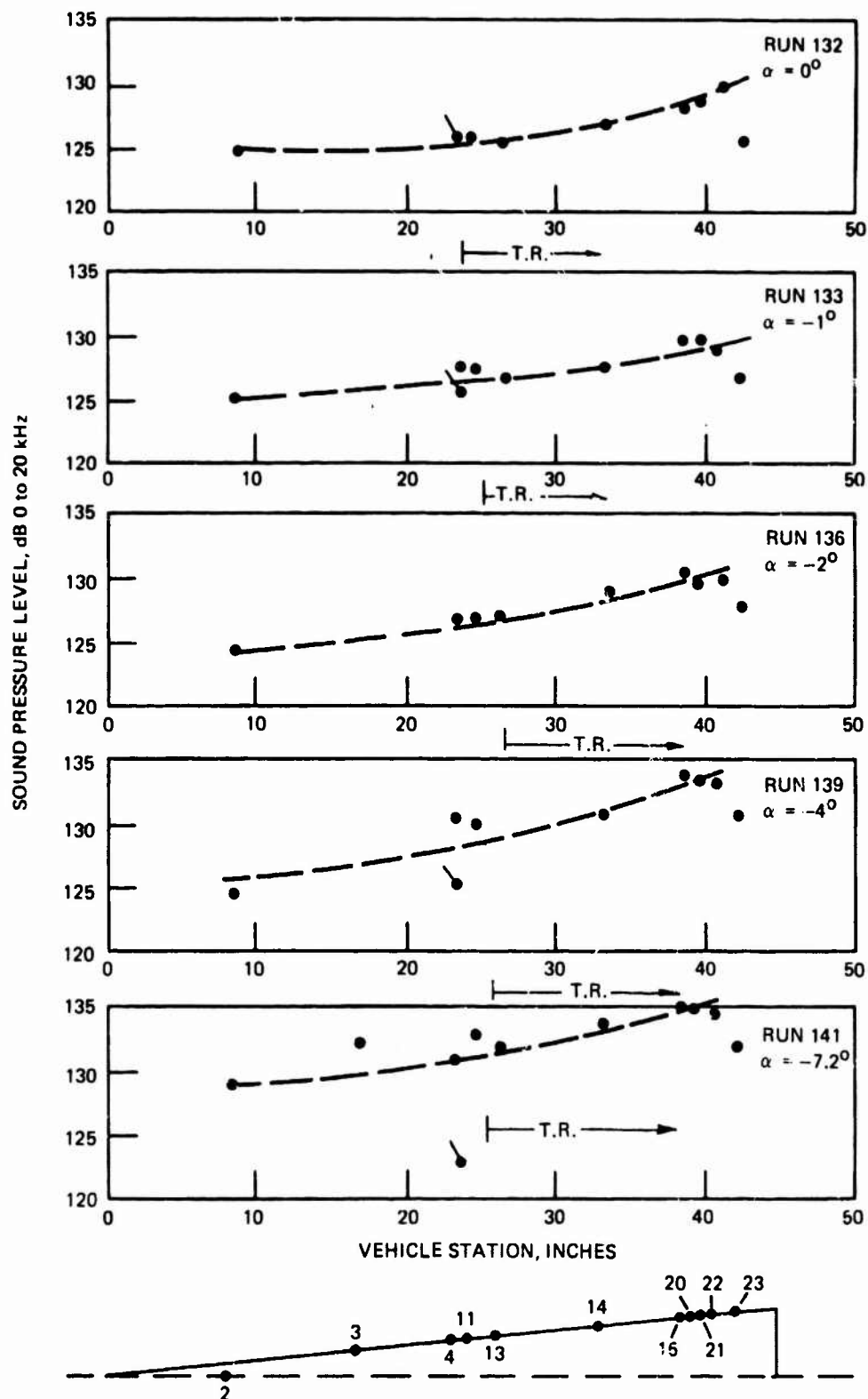
Figure 80. Fluctuating Pressure Distribution Tunnel Condition
$(R_{e_\infty} = 1.4 \times 10^6, \ M_\infty = 10.0, \ R_N = 0.0)$

105
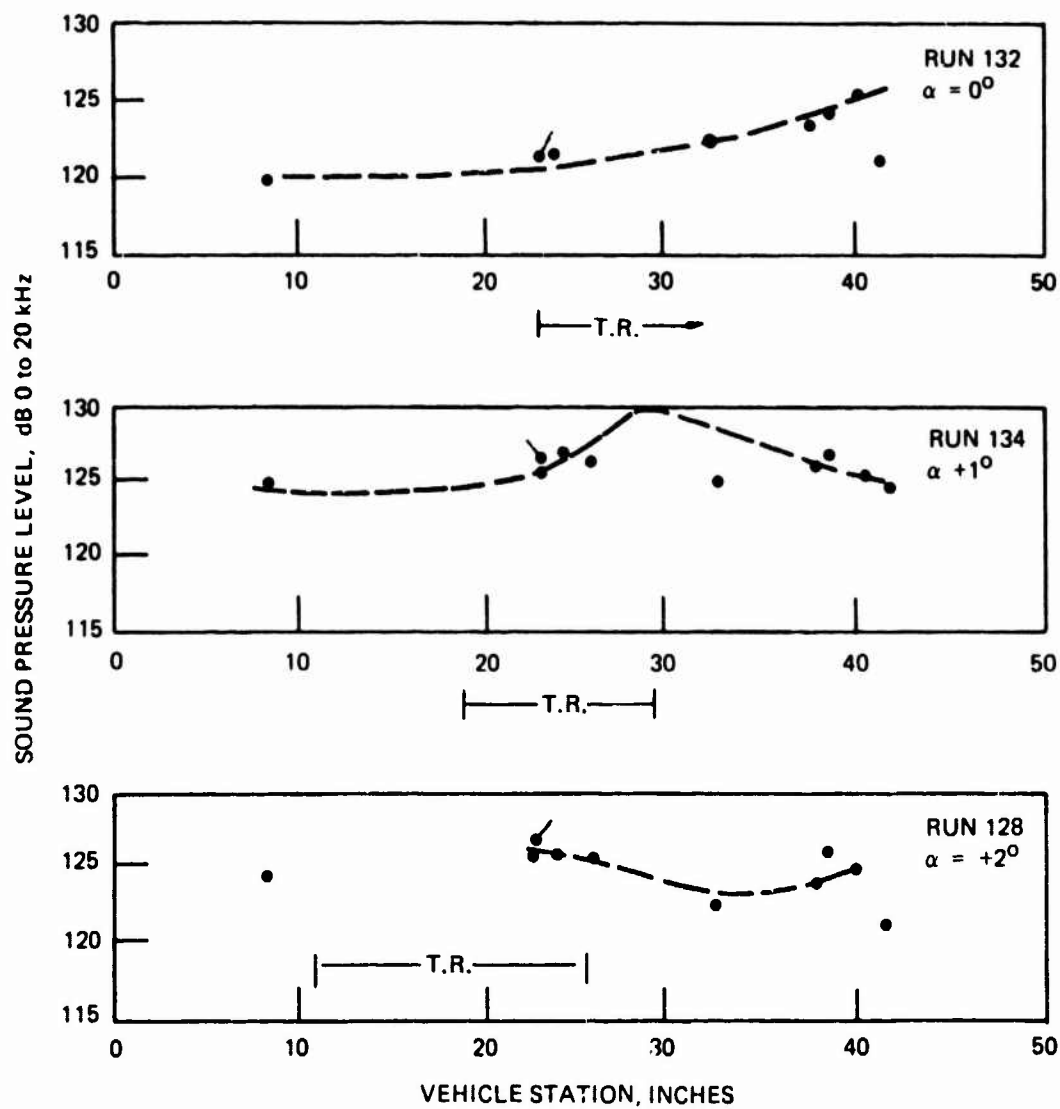
Figure 81. Fluctuating Pressure Distribution Tunnel Condition
$(Re_\infty = 1.4 \times 10^6, \ M_\infty = 10.0, \ R_N = 0.0)$

Figure 82. Fluctuating Pressure Distribution Tunnel Condition
$(Re_\infty = 2.2 \times 10^6, \ M_\infty = 10.0, \ R_N = 0.0)$

107

Figure 83. Fluctuating Pressure Distribution Tunnel Condition
$(R_{e_\infty} = 2.2 \times 106,\ M_\infty = 10.0,\ R_N = 0.0)$

Figure 84. Fluctuating Pressure Distribution Tunnel Condition
$(R_{e_\infty} = 2.2 \times 10^6, \ M_\infty = 10.0, \ R_N = 0.055)$

109

Figure 85. Fluctuating Pressure Distribution Tunnel Condition
$(R_{e_\infty} = 2.2 \times 10^6, \ M_\infty = 10.0, \ R_N = 0.055)$
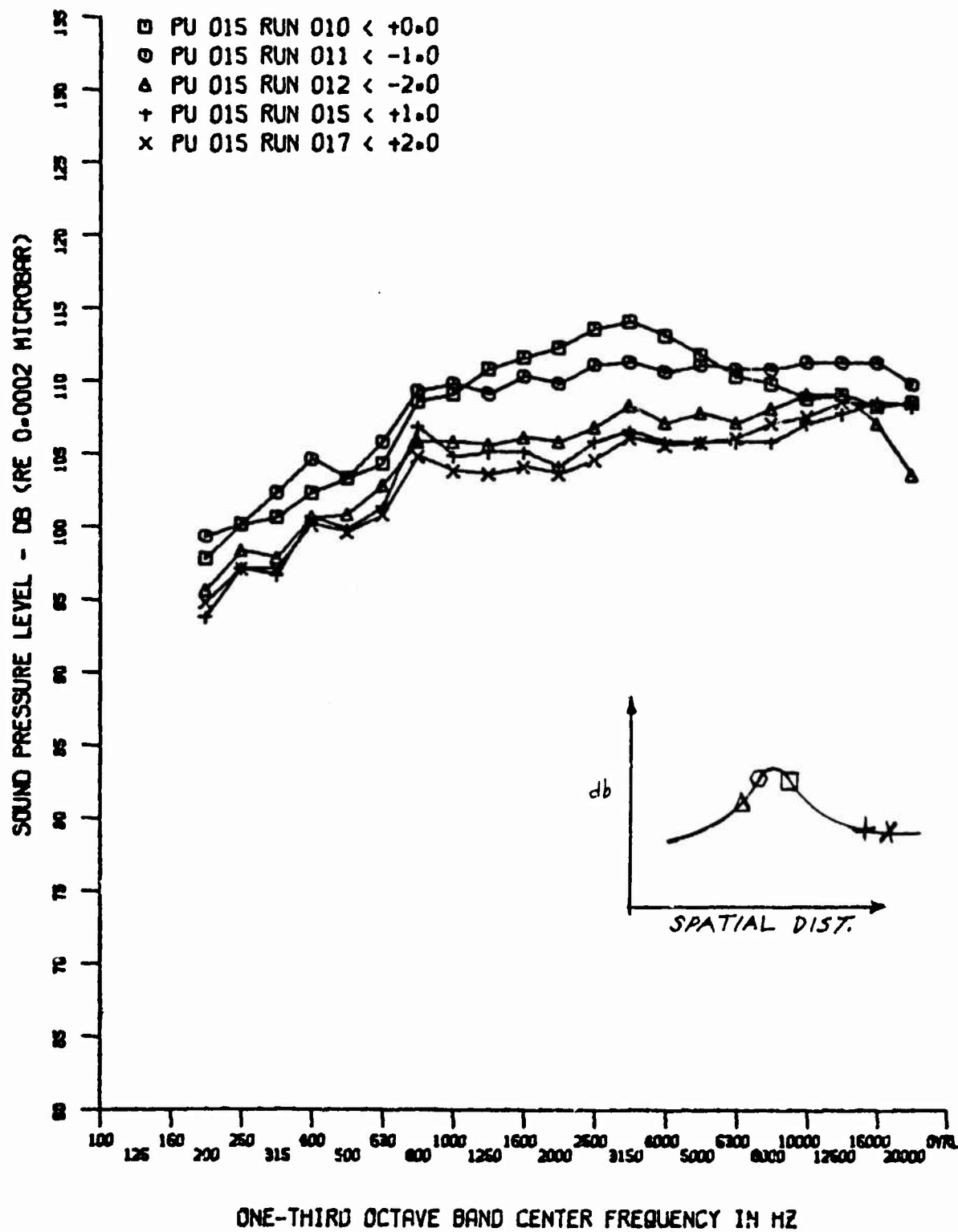
Figure 86. Comparison of Spectra in Transition Zone
$(M_\infty = 4, \ R_{\theta_\infty} = 1.4 \times 10^6, \ R_N = 0)$

111
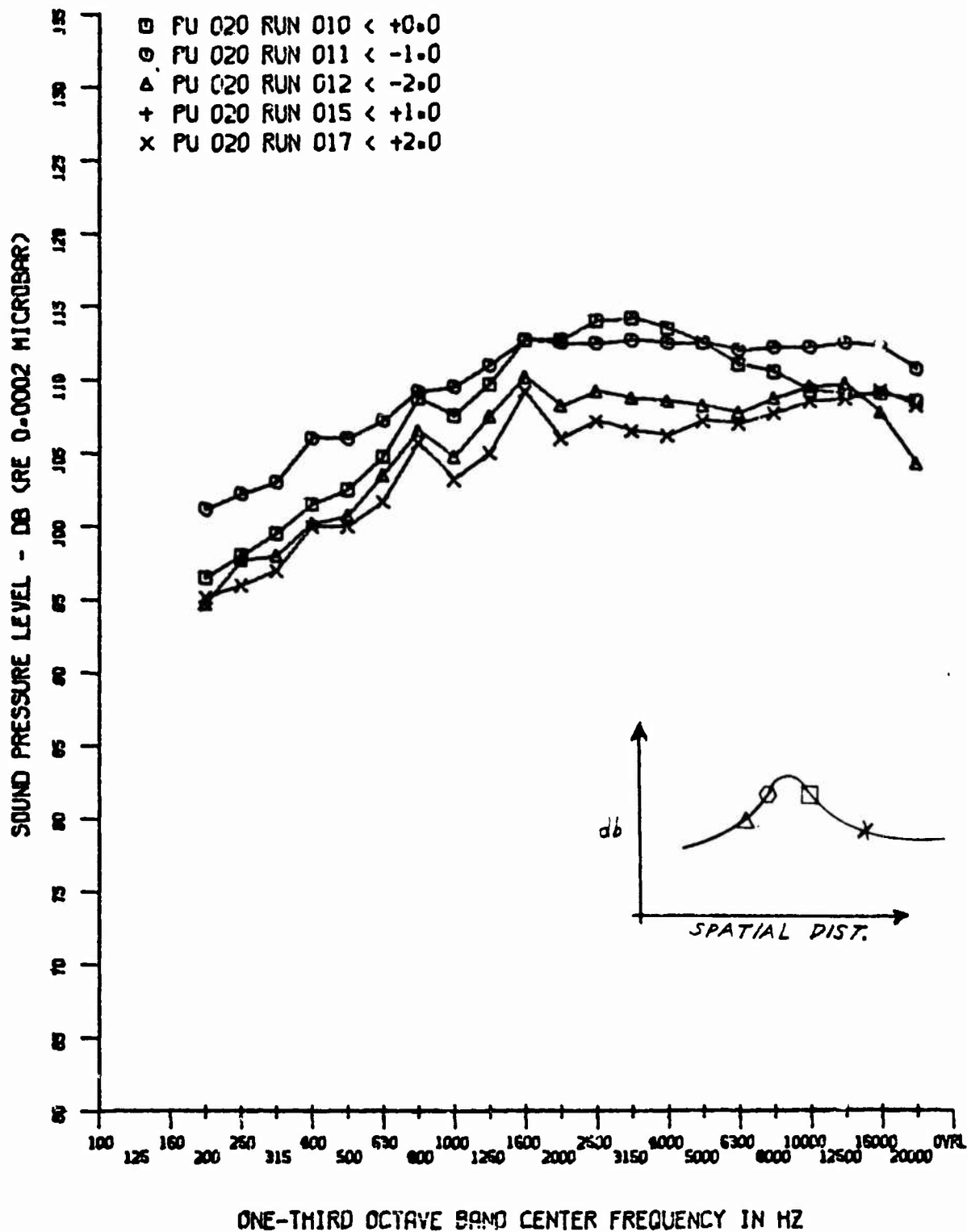
Figure 87. Comparison of Spectra in Transition Zone
$(M_\infty = 4, \ R_{e_\infty} = 1.4 \times 10^6, \ R_N = 0)$

112
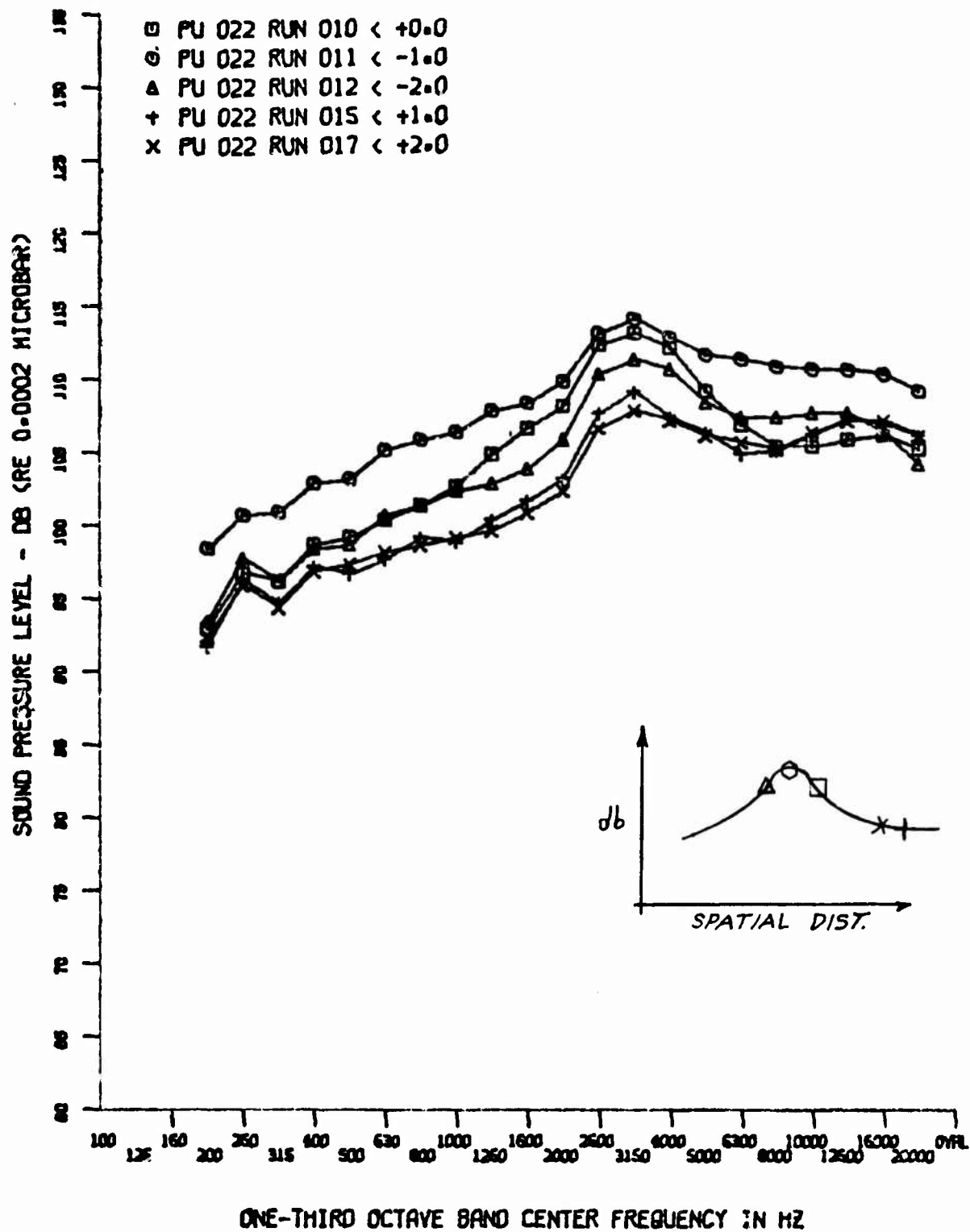
Figure 88. Comparison of Spectra in Transition Zone ($M_\infty = 4$, $Re_\infty = 1.4 \times 10^6$, $R_N = 0$)

113
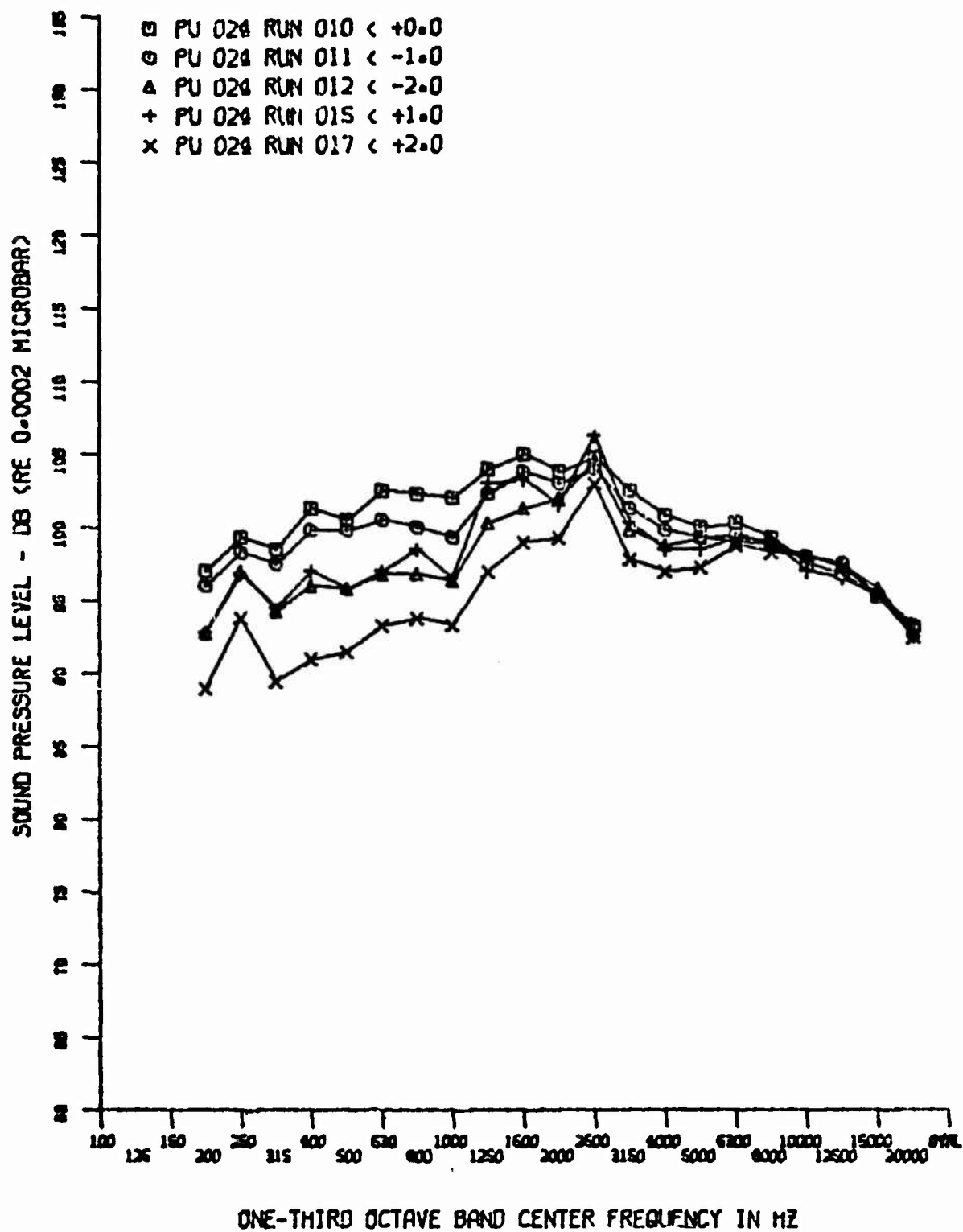
Figure 89. Base Spectra at Various α ($M_\infty = 4$, $Re_\infty = 1.4 \times 10^6$, $R_N = 0$)

114
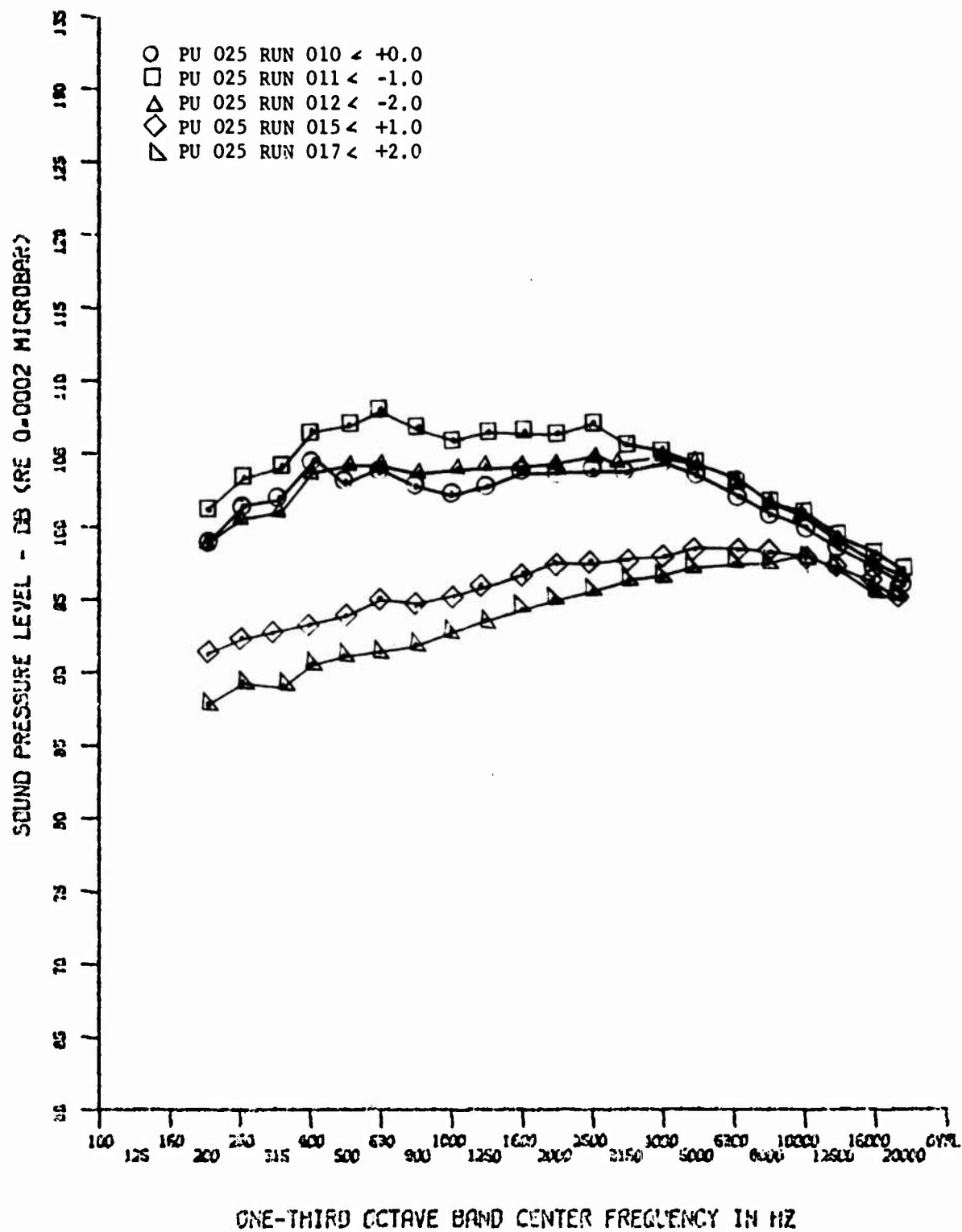
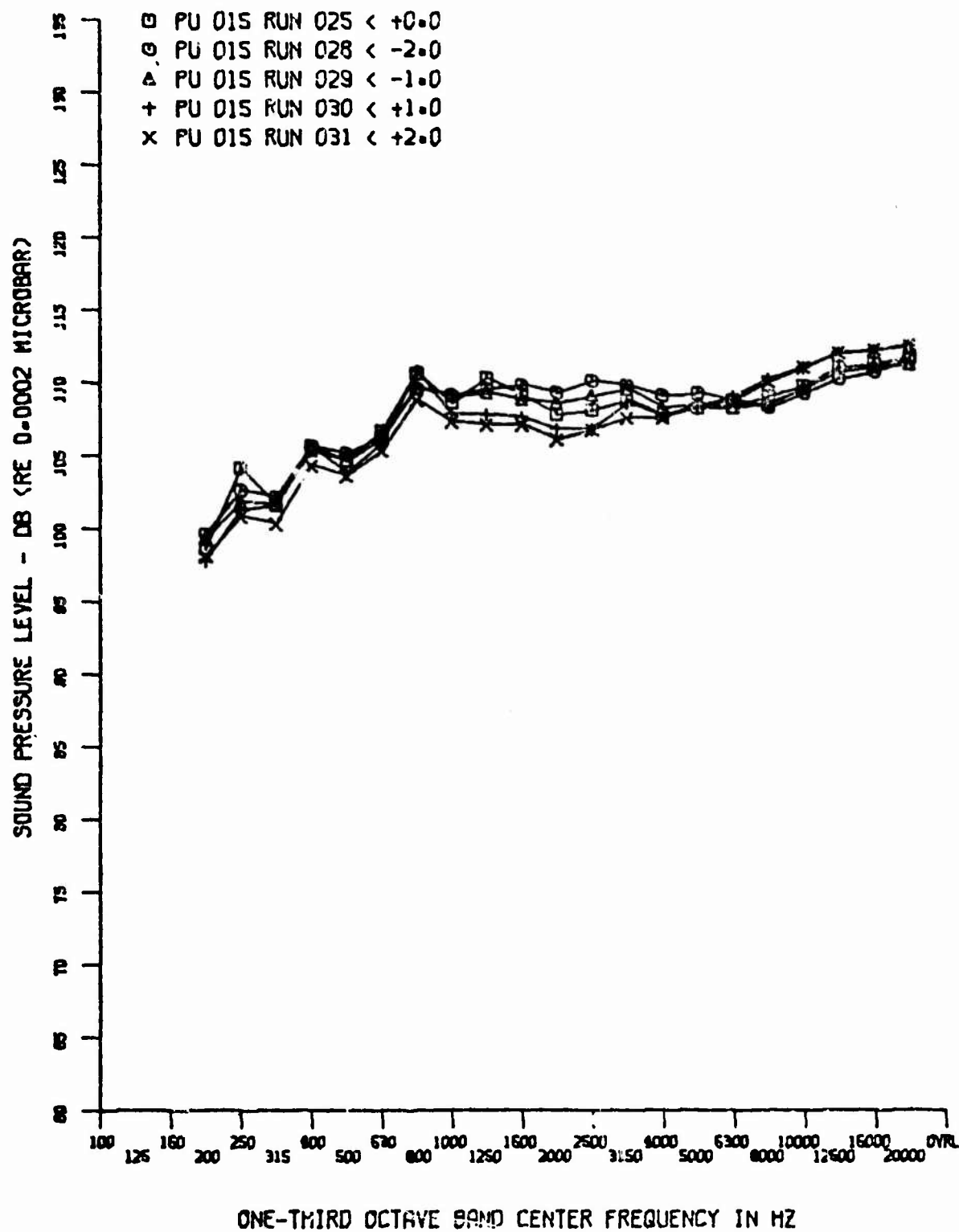Figure 90. Base Spectra at Various α ($M_\infty = 4$, $Re_\infty = 1.4 \times 10^6$, $R_N = 0$)

115
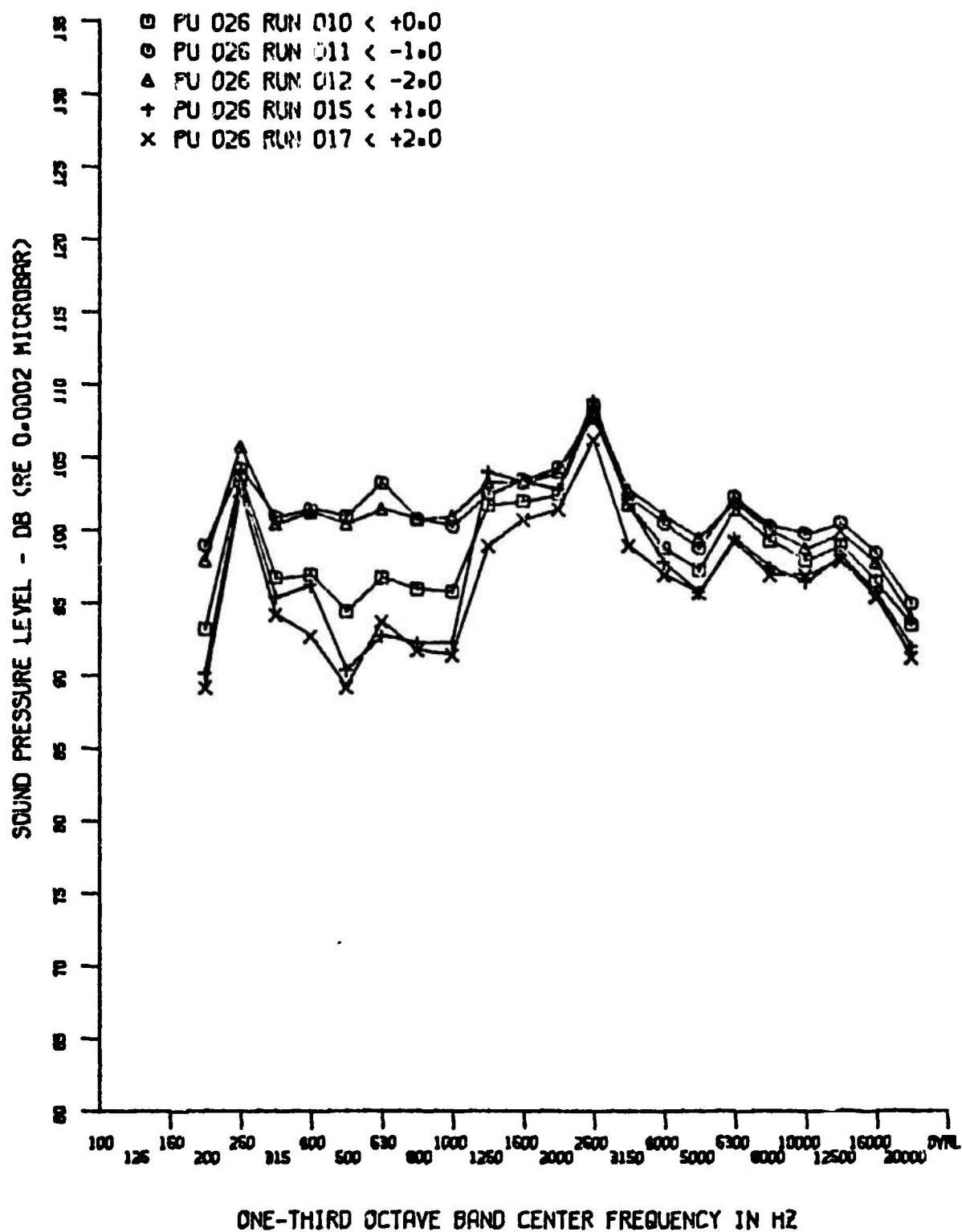
Figure 91. Base Spectra at Various α ($M_\infty = 4$, $Re_\infty = 1.4 \times 10^6$, $R_N = 0$)

116
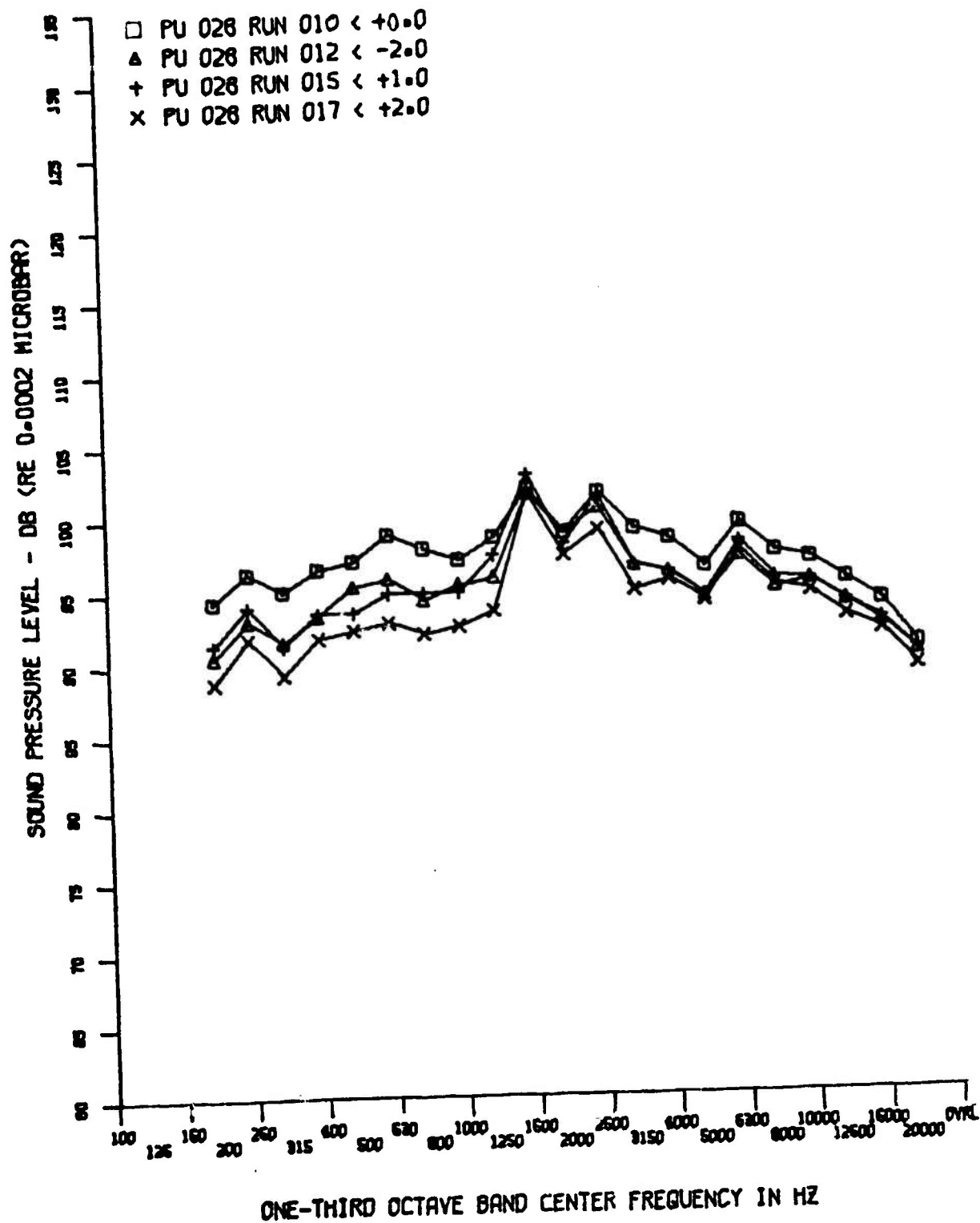
Figure 92. Base Spectra at Various α ($M_\infty = 4$, $Re_\infty = 1.4 \times 10^6$, $R_N = 0$)

117
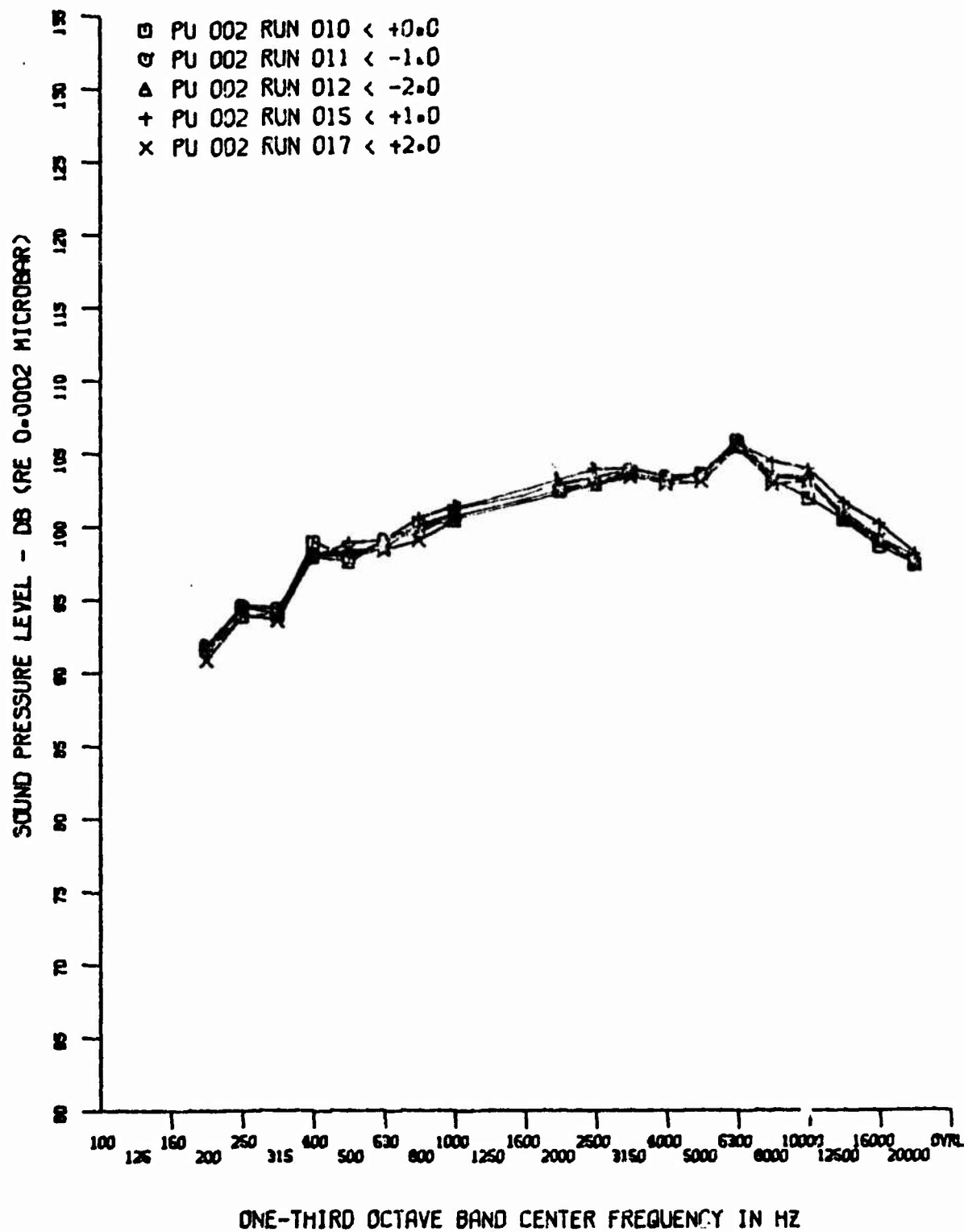
Figure 93. Tunnel Tare Noise ($M_\infty = 4$, $Re_\infty = 1.4 \times 10^6$, $R_N = 0$)
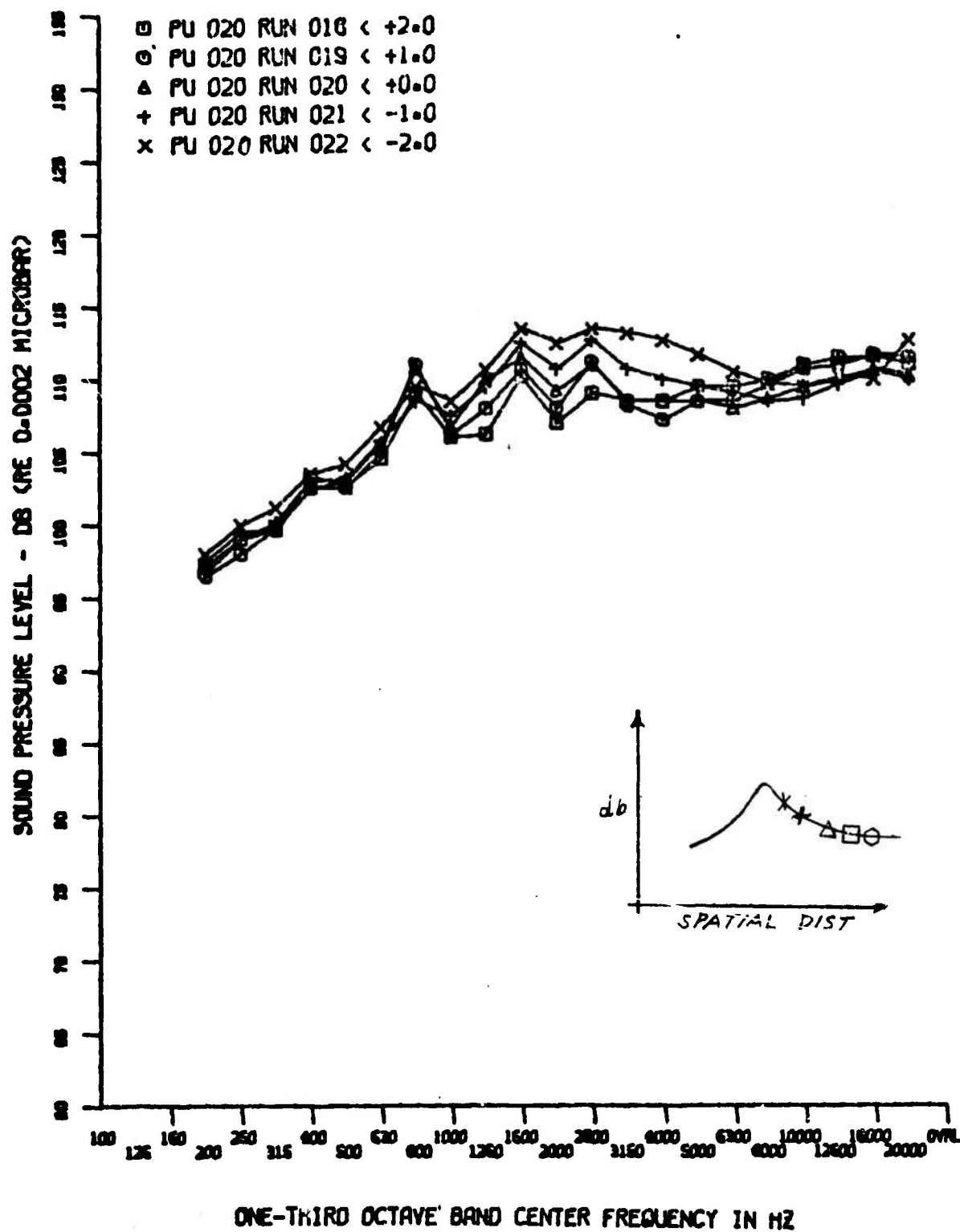
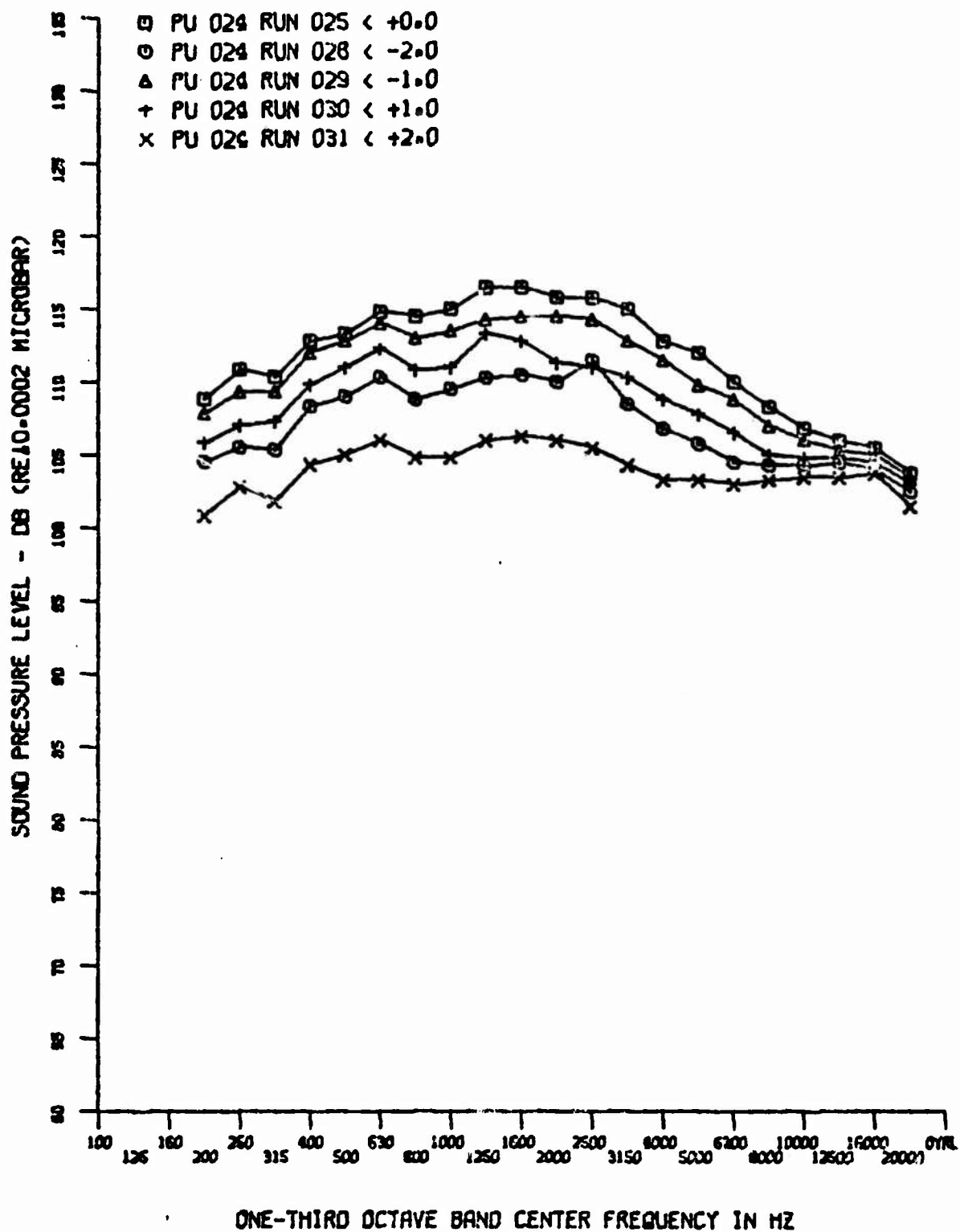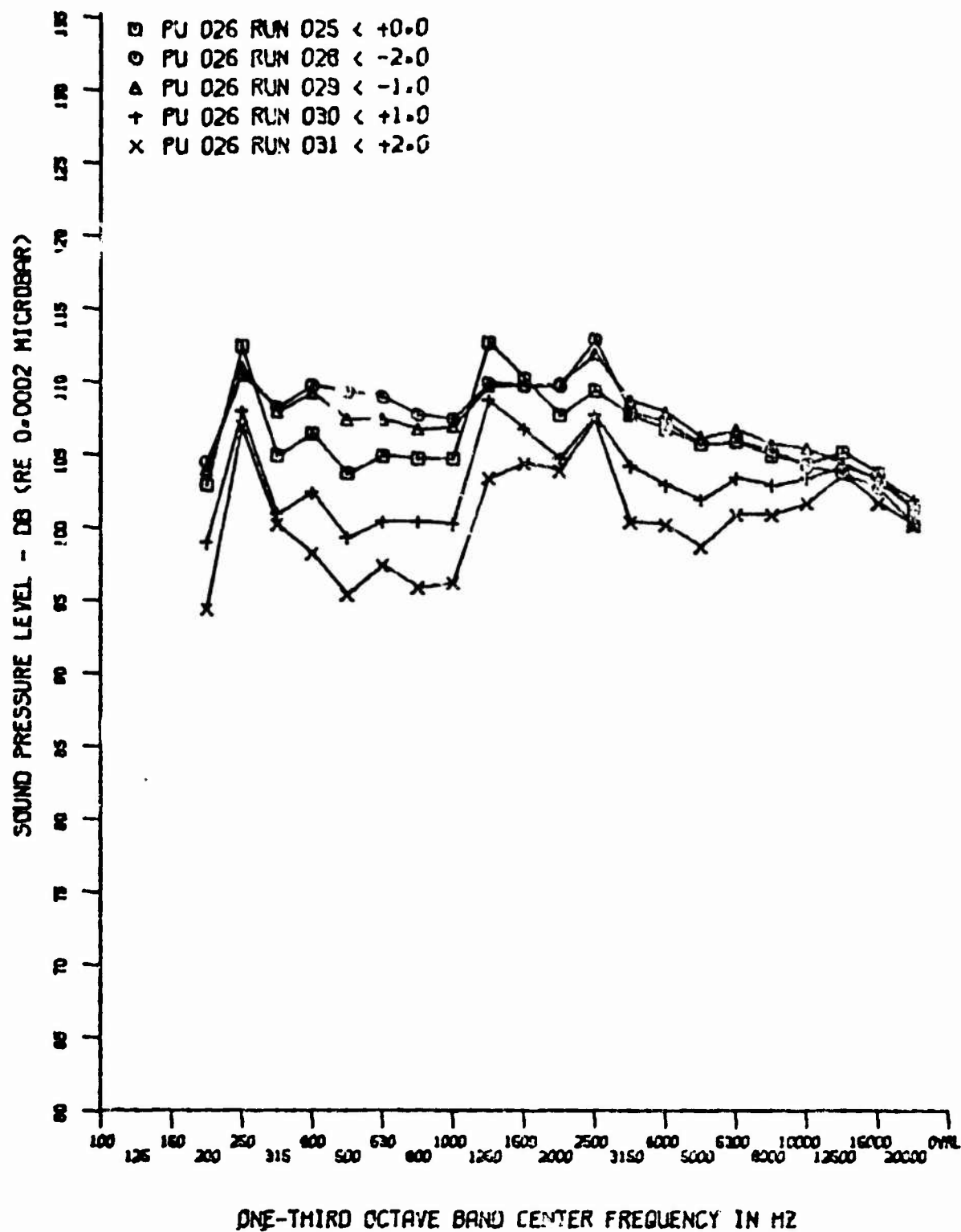Figure 94. Comparison of Spectra in Transition Zone ($M_\infty = 4$, $Re_\infty = 2.2 \times 10^6$, $R_N = 0$)

119
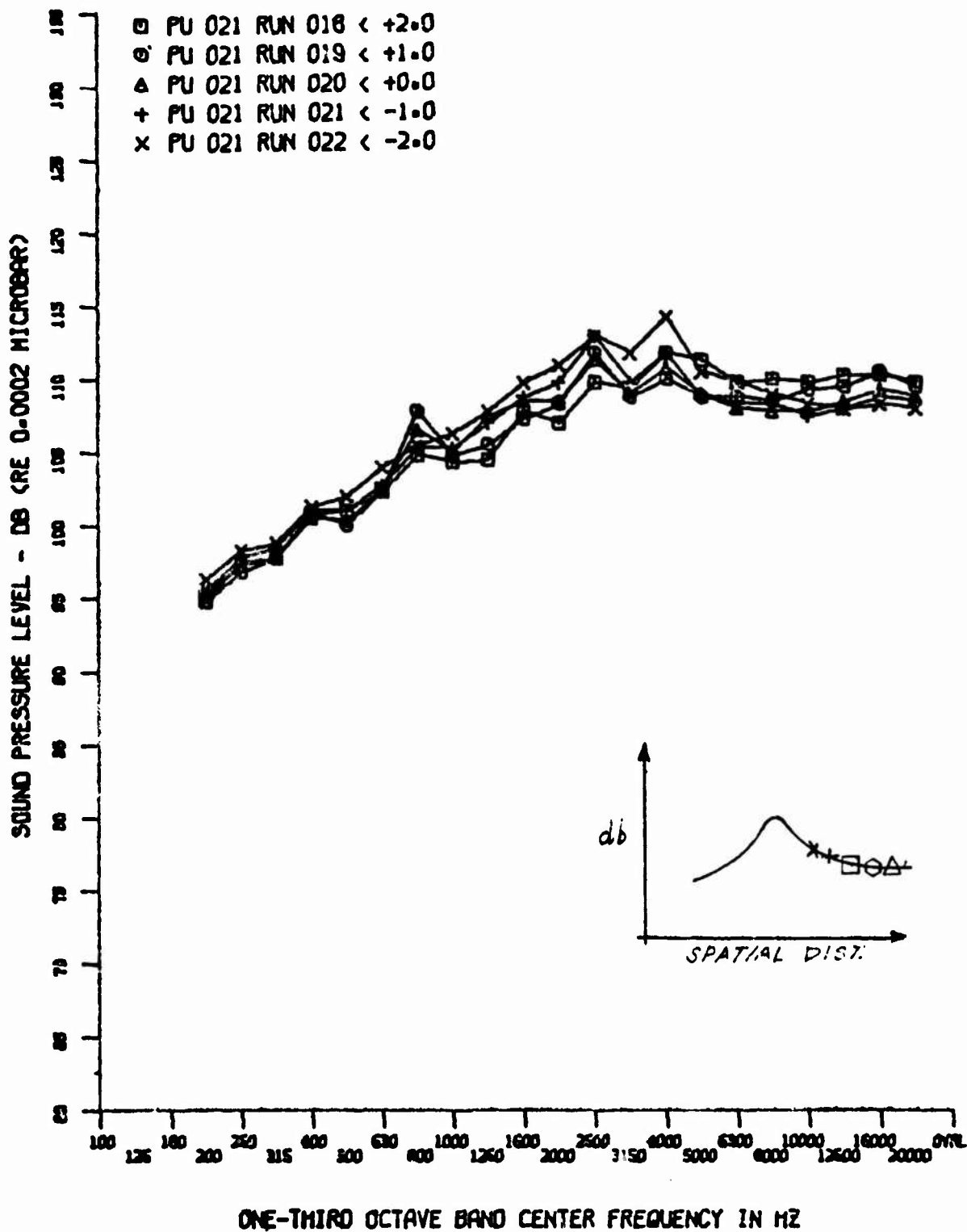
Figure 95. Transition Region and Turbulent Flow Spectra ($M_\infty = 4$, $Re_\infty = 2.2 \times 10^6$, $R_N = 0$)
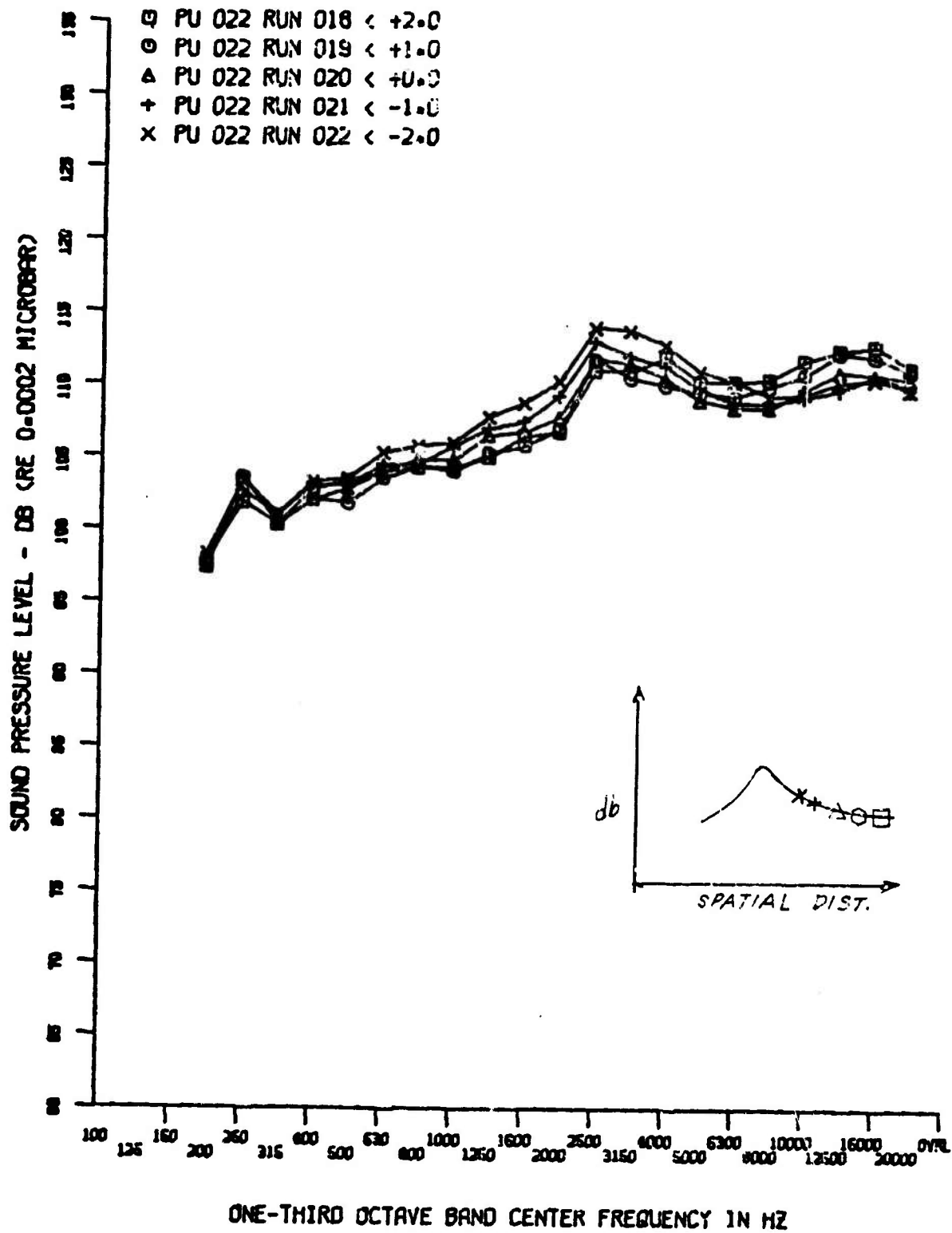
Figure 96. Transition Region and Turbulent Flow Spectra ($M_\infty = 4$, $Re_\infty = 2.2 \times 10^6$, $R_N = 0$)

121
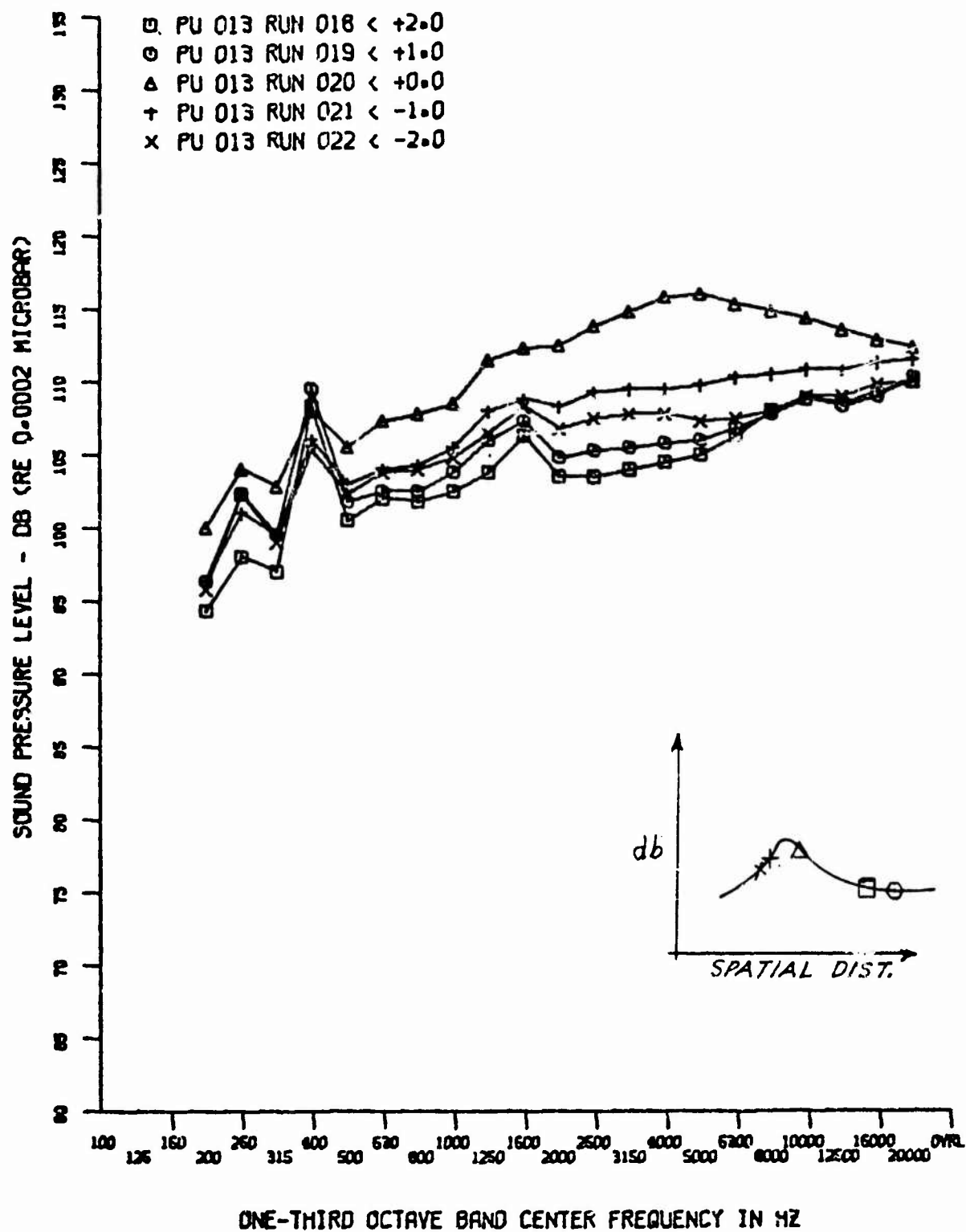
Figure 97. Transition Region and Turbulent Flow Spectra ($M_{\infty} = 4$, $Re_{\infty} = 2.2 \times 10^6$, $R_N = 0$)

122
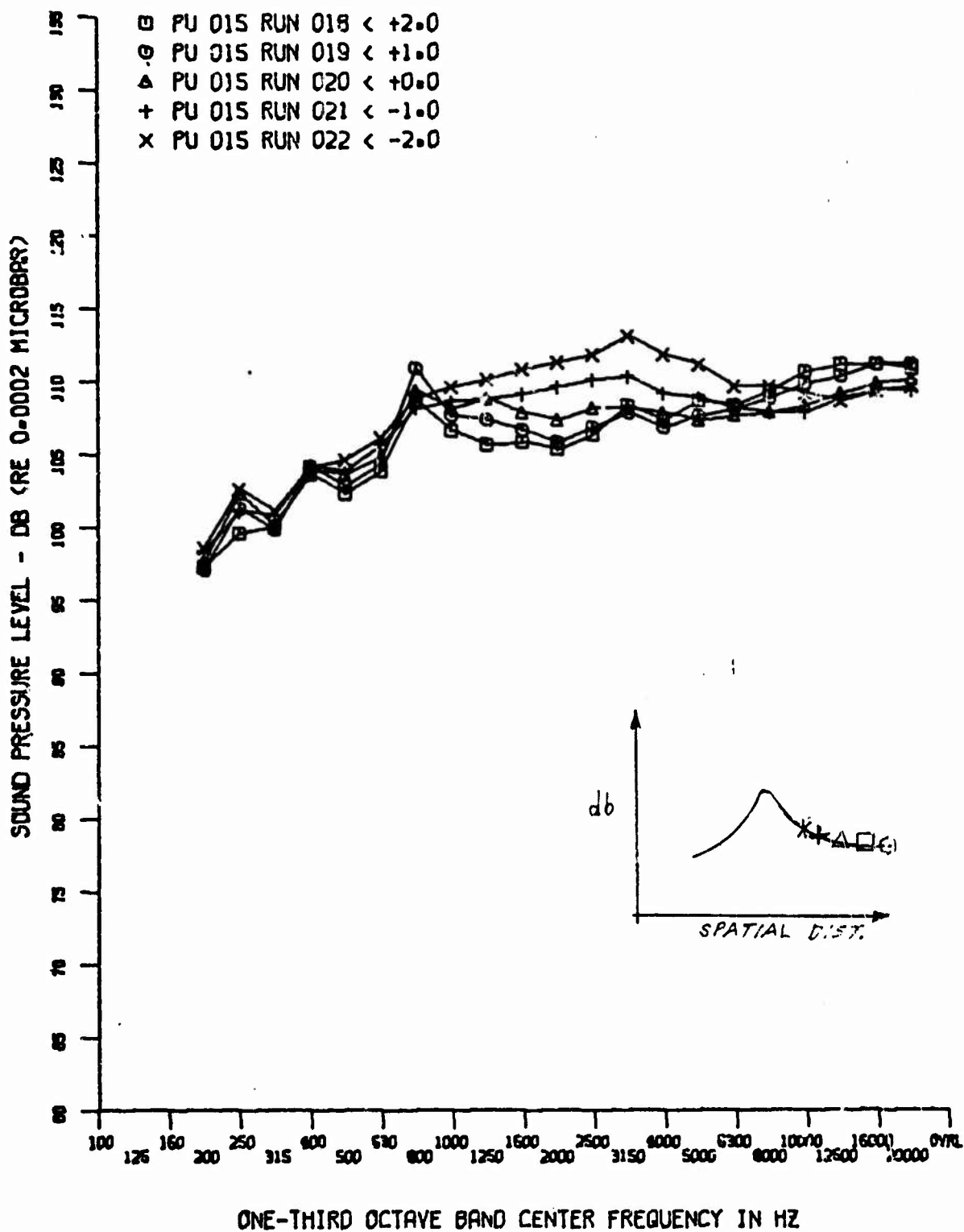
Figure 98. Transition Region and Turbulent Flow Spectra (M = 4, $Re_\infty = 2.2 \times 10^6$, $R_N = 0$)

123
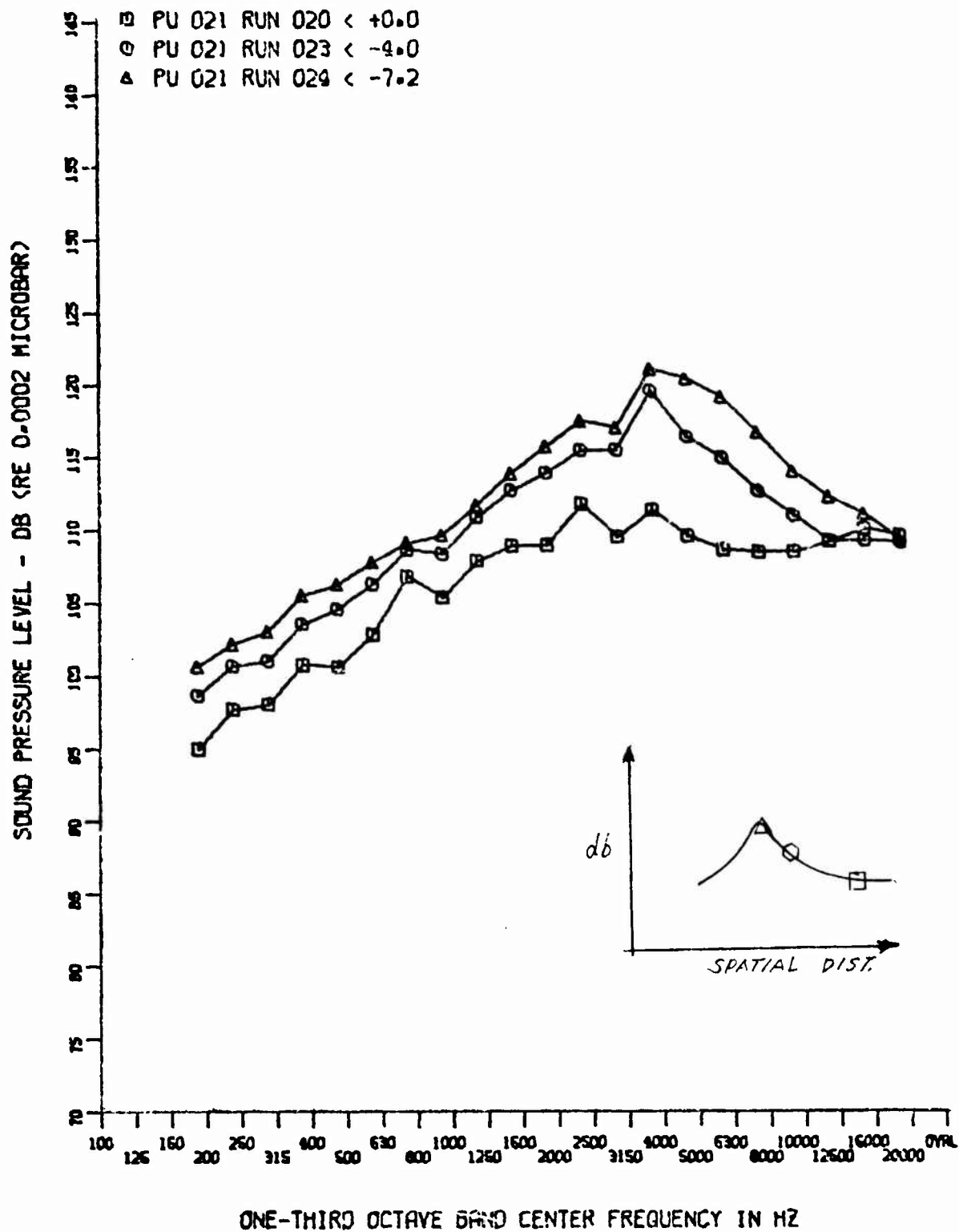
Figure 99. Transition Region and Turbulent Flow Spectra ($M_\infty = 4$, $Re_\infty = 2.2 \times 10^6$, $R_N = 0$)
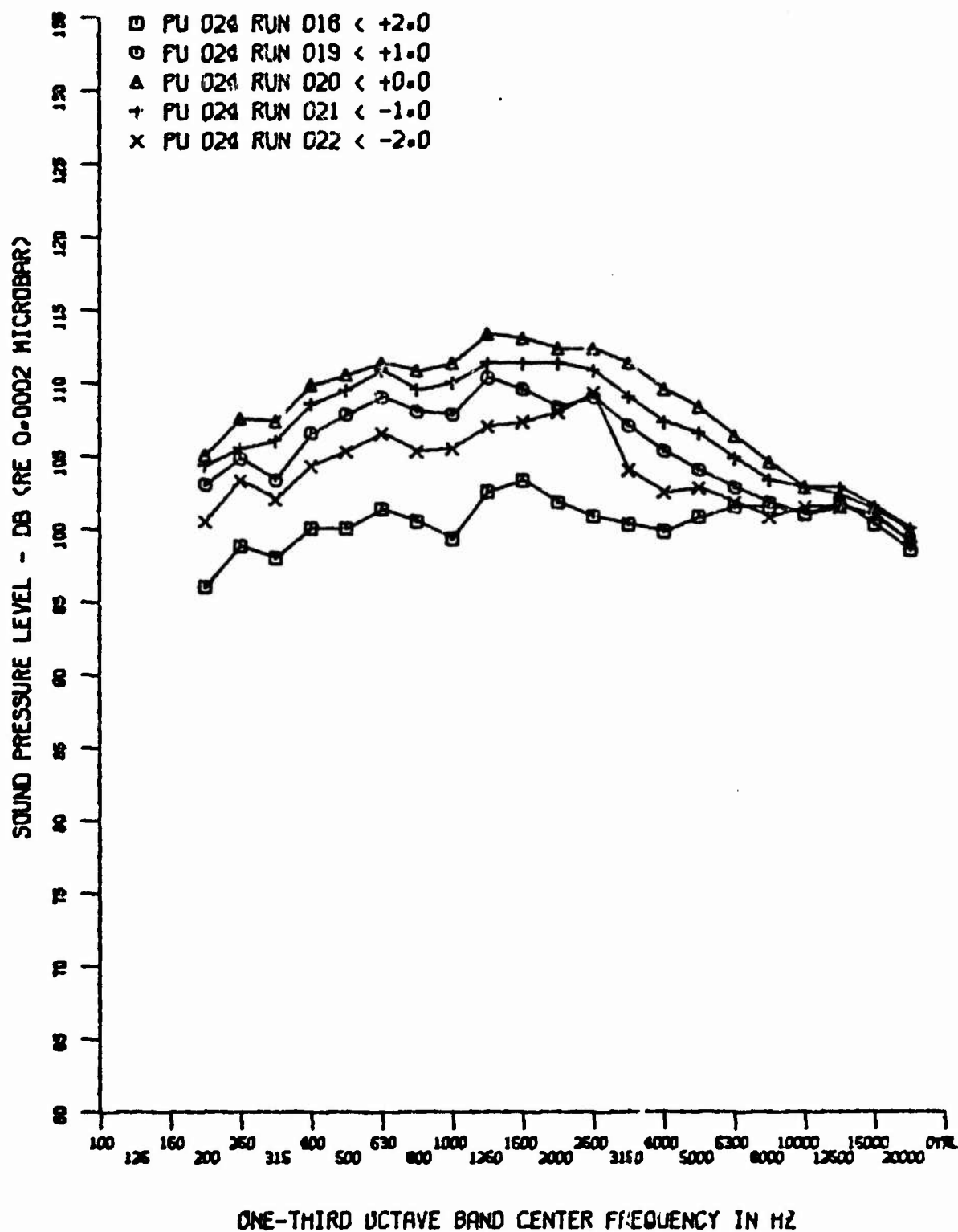
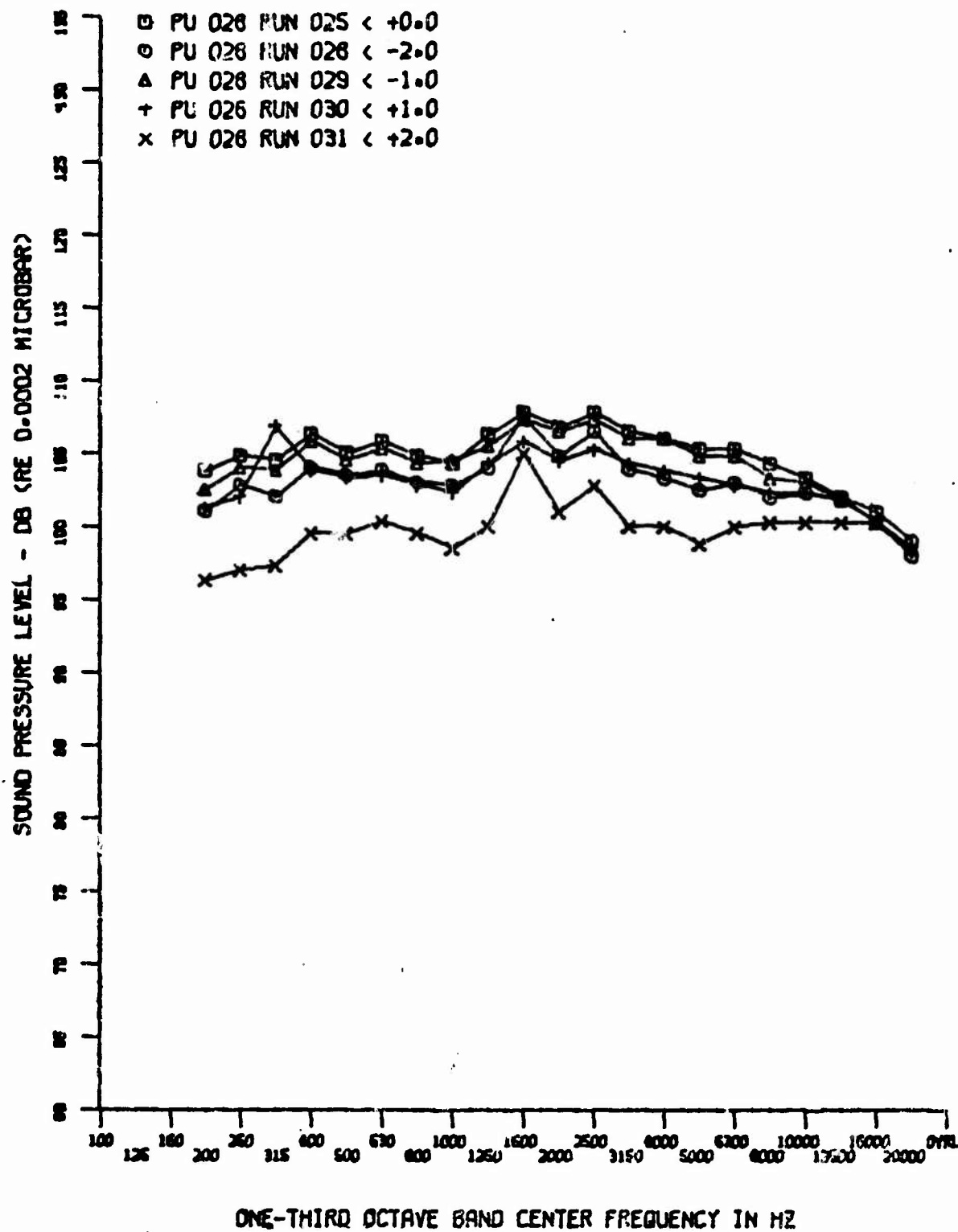Figure 100. Base Spectra at Various α ($M_\infty = 4$, $Re_\infty = 2.2 \times 10^6$, $R_N = 0$)
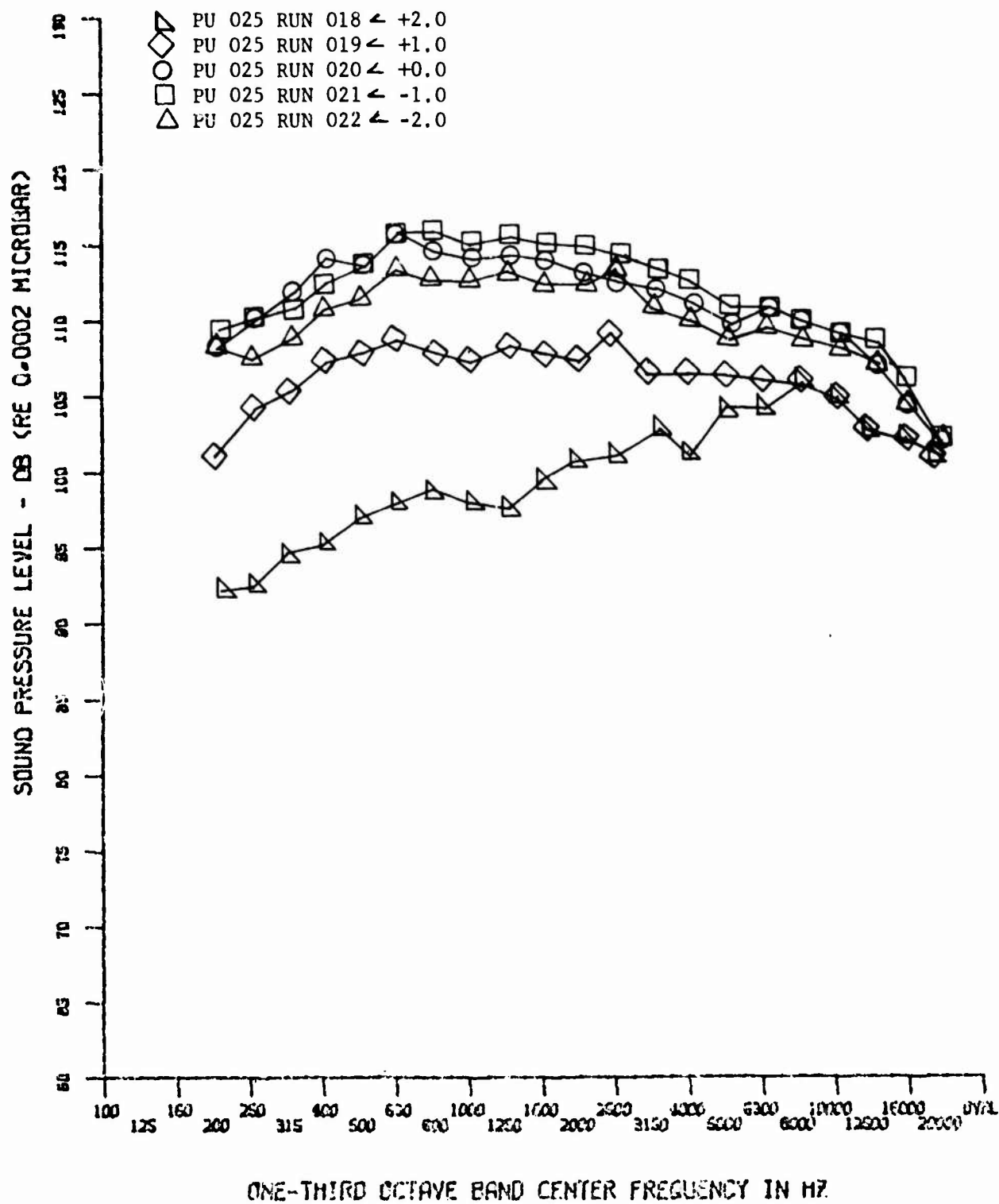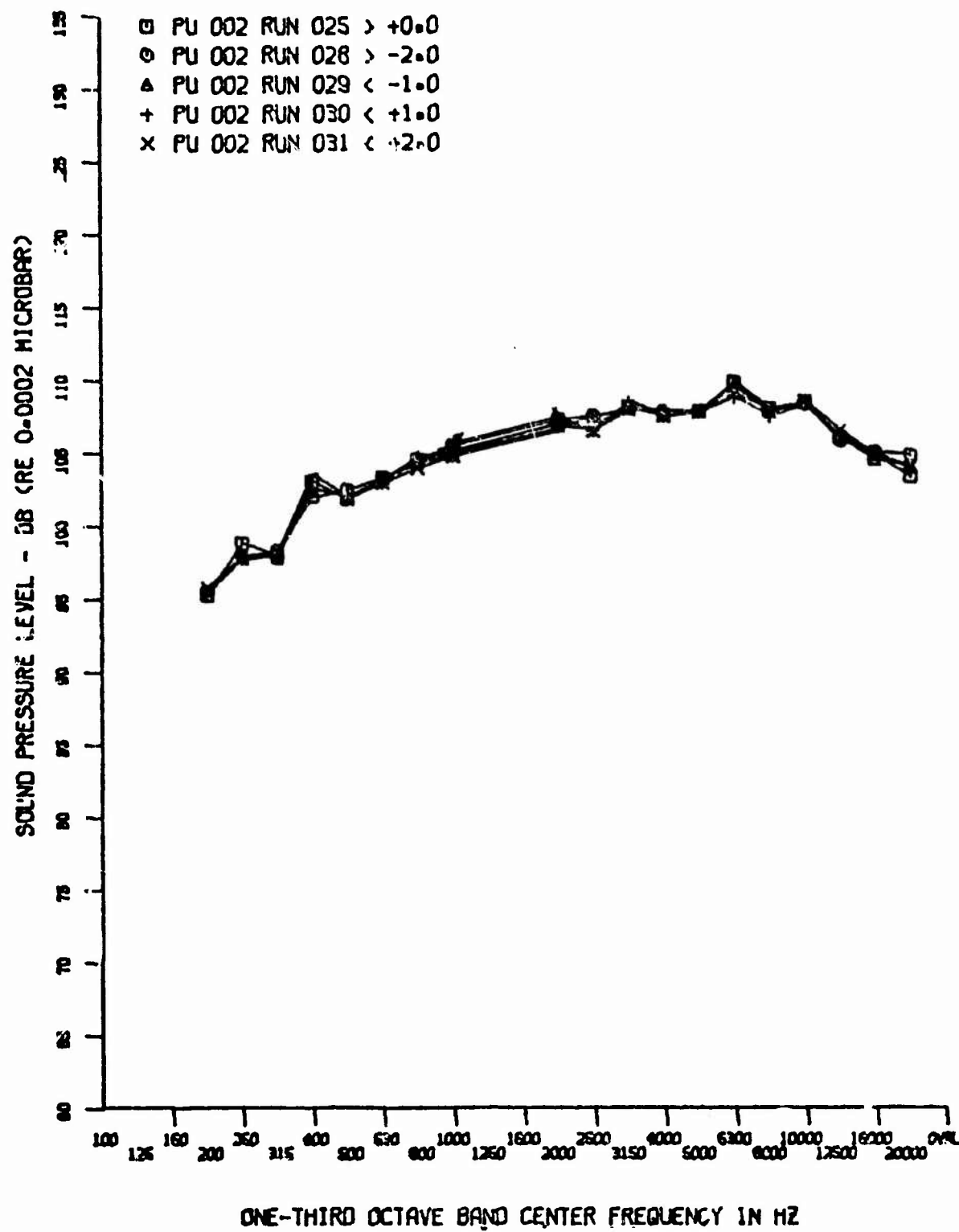
Figure 101. Base Spectra at Various α ($M_\infty = 4$, $Re_\infty = 2.2 \times 10^6$, $R_N = 0$)

126
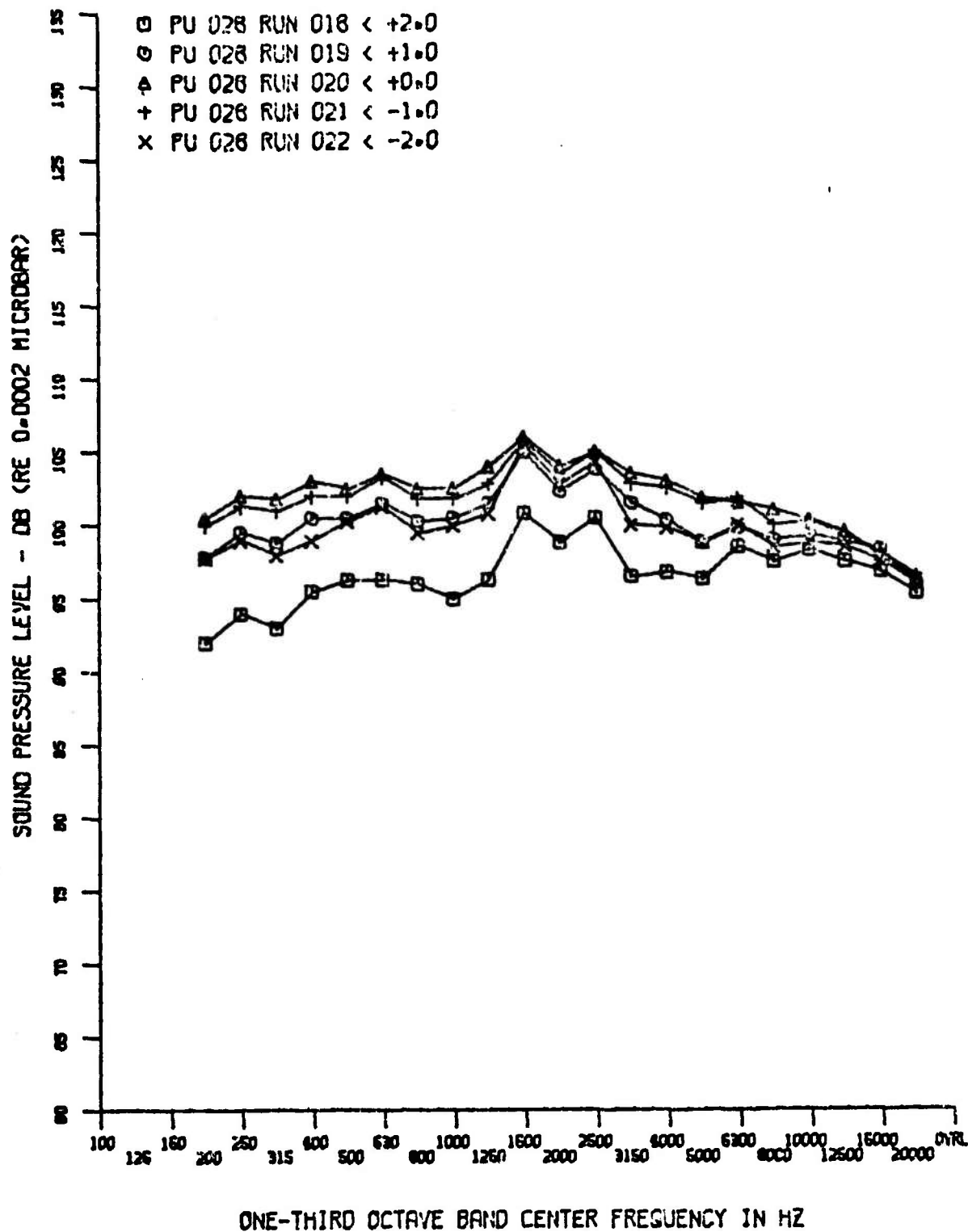
Figure 102. Base Spectra at Various α ($M_\infty = 4$, $Re_\infty = 2.2 \times 10^6$, $R_N = 0$)

127
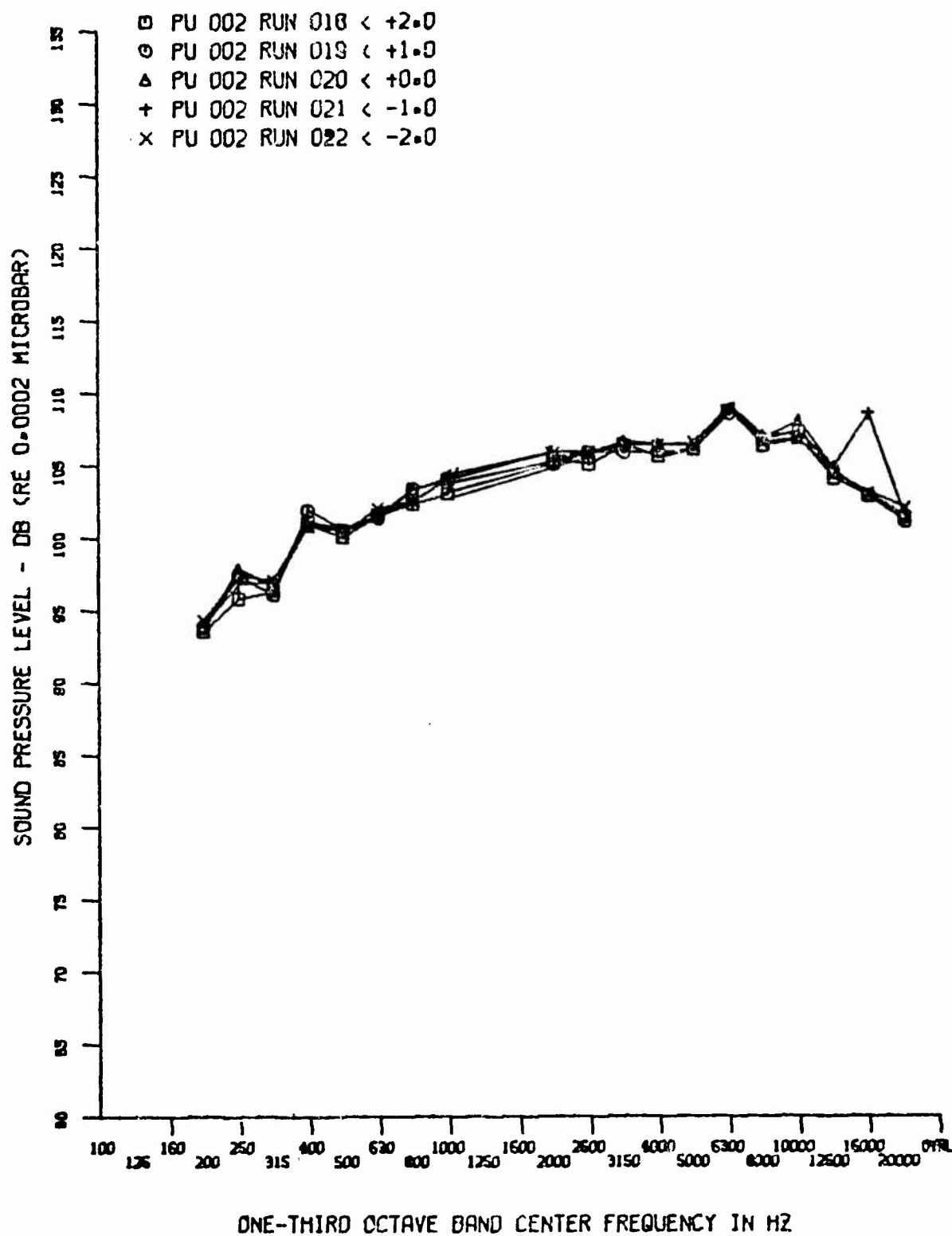
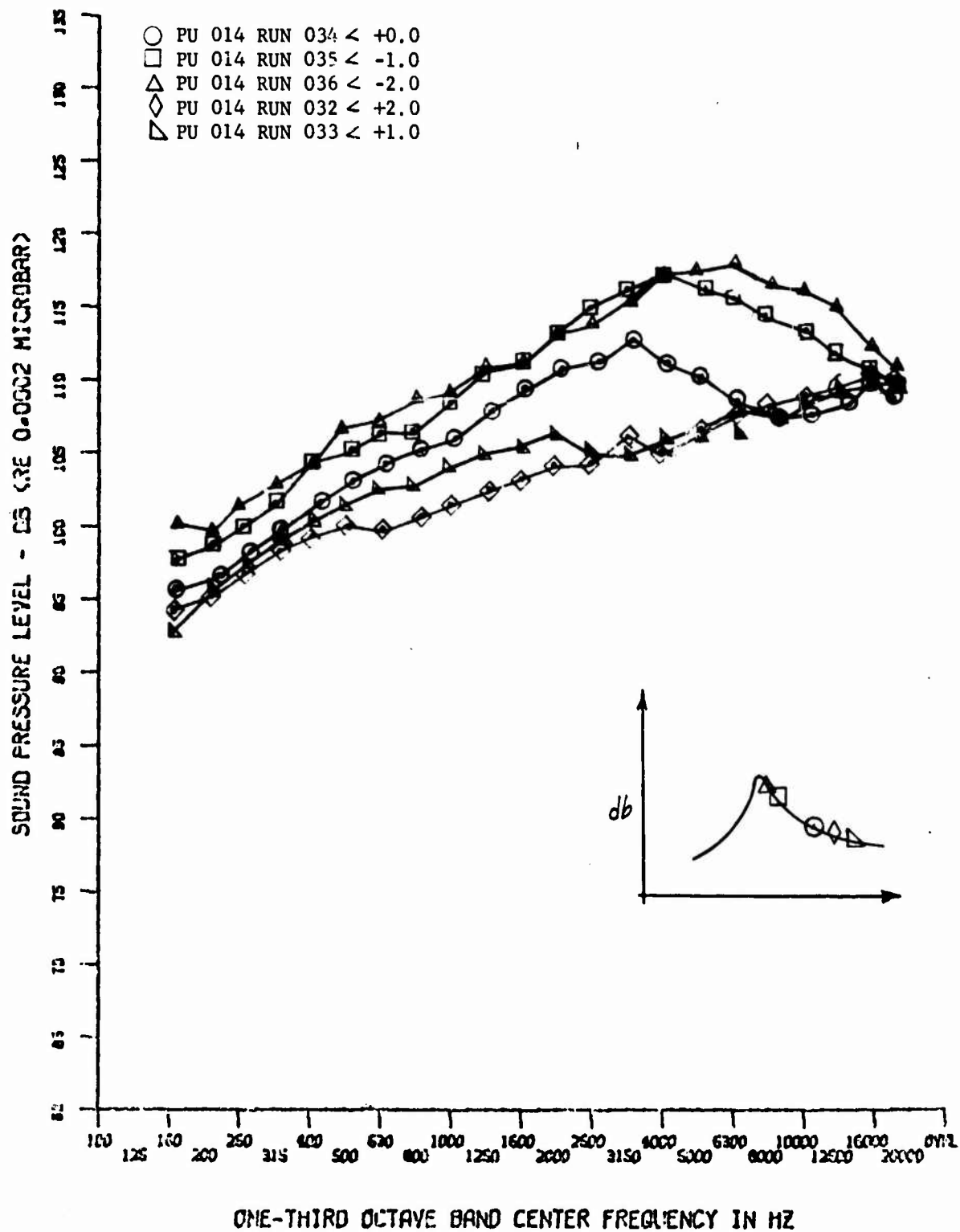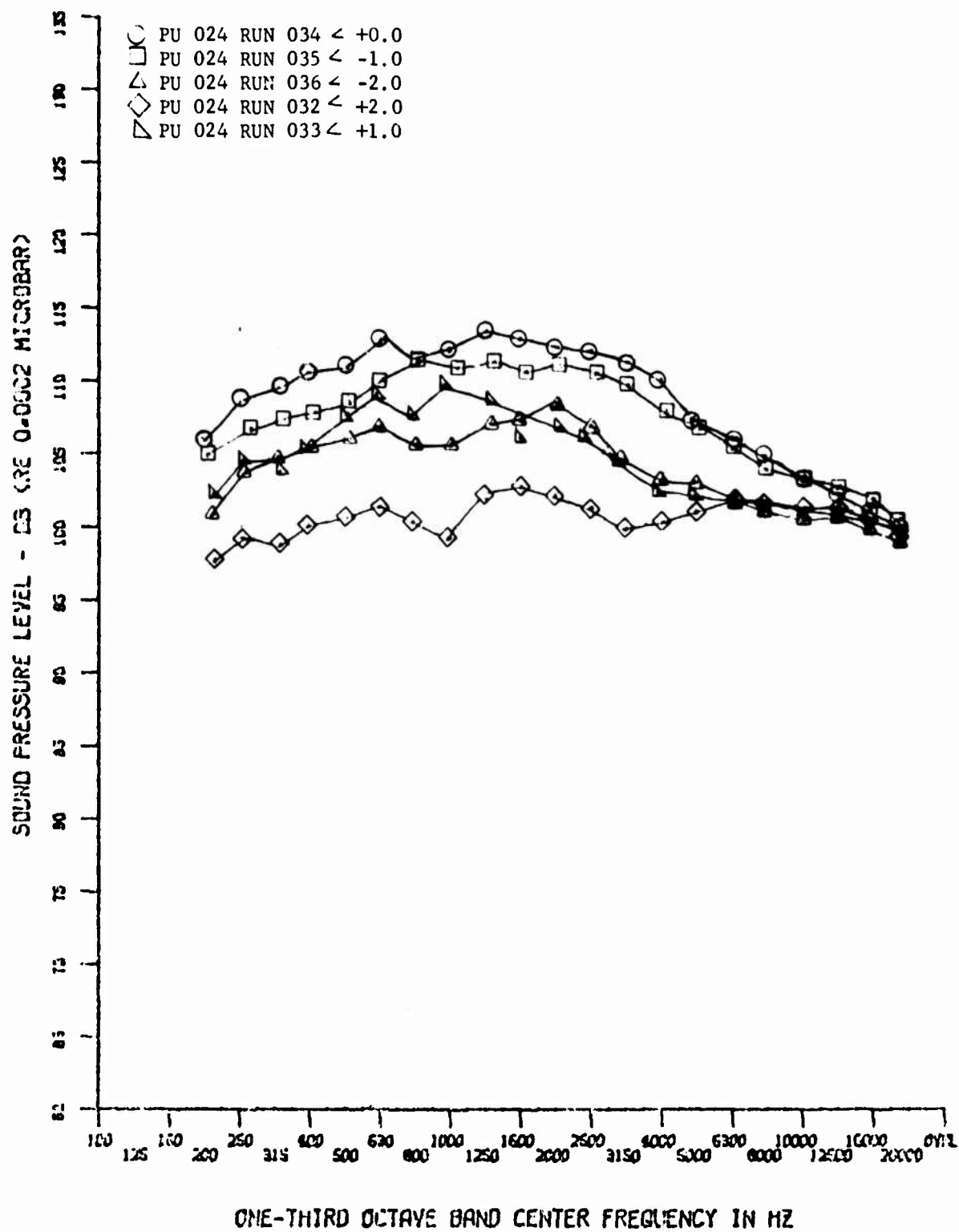Figure 103. Tunnel Tare Noise ($M_\infty = 4$, $Re_\infty = 2.2 \times 10^6$, $R_N = 0$)
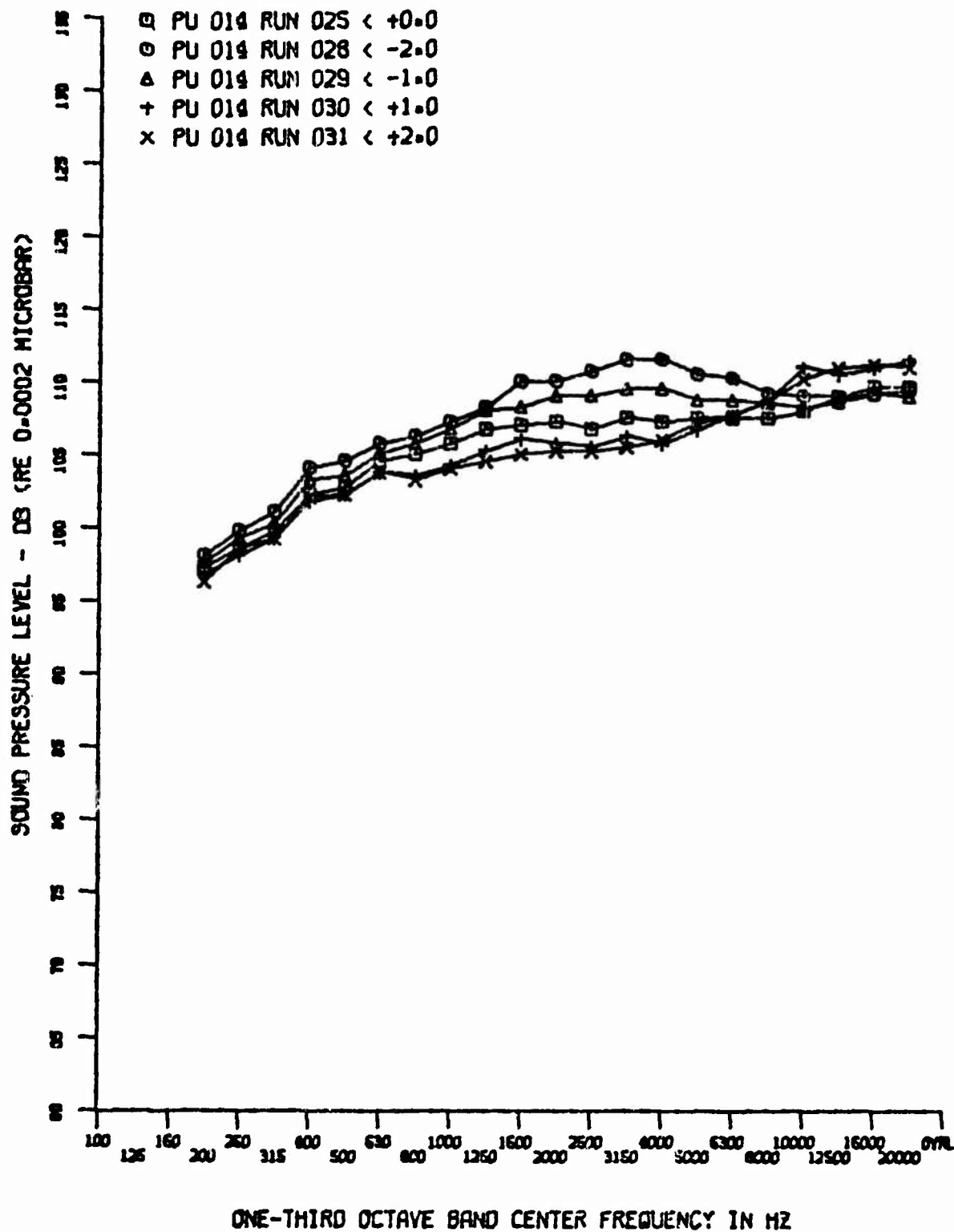
Figure 104. Turbulent Flow Spectra at Various α ($M_\infty = 4$, $Re_\infty = 2.8 \times 10^6$, $R_N = 0$)

129

Figure 105. Turbulent Flow Spectra at Various α ($M_\infty = 4$, $Re_\infty = 2.8 \times 10^6$, $R_N = 0$)

130
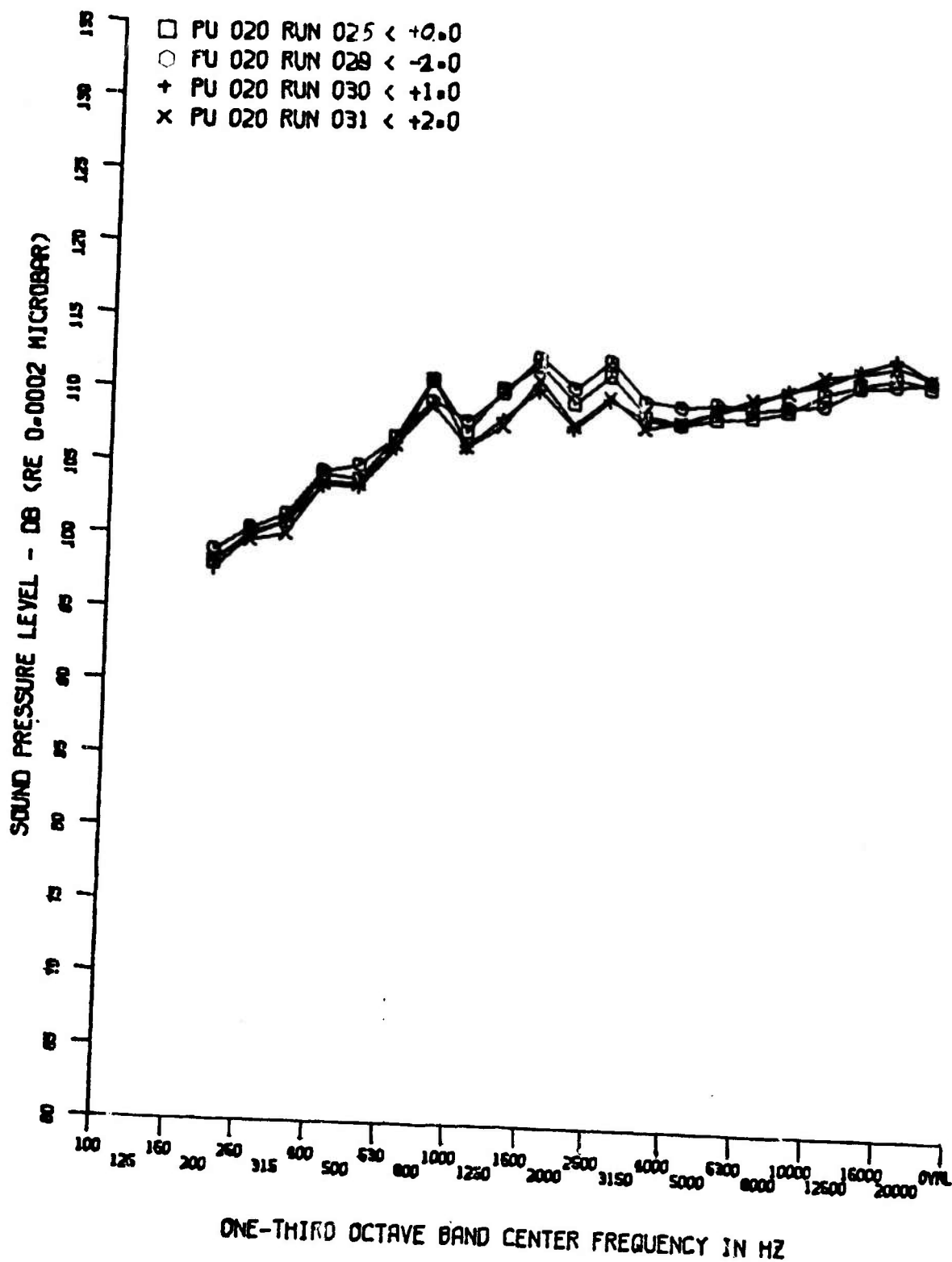
Figure 106. Turbulent Flow Spectra at Various α ($M_\infty = 4$, $Re_\infty = 2.8 \times 10^6$, $R_N = 0$)

131
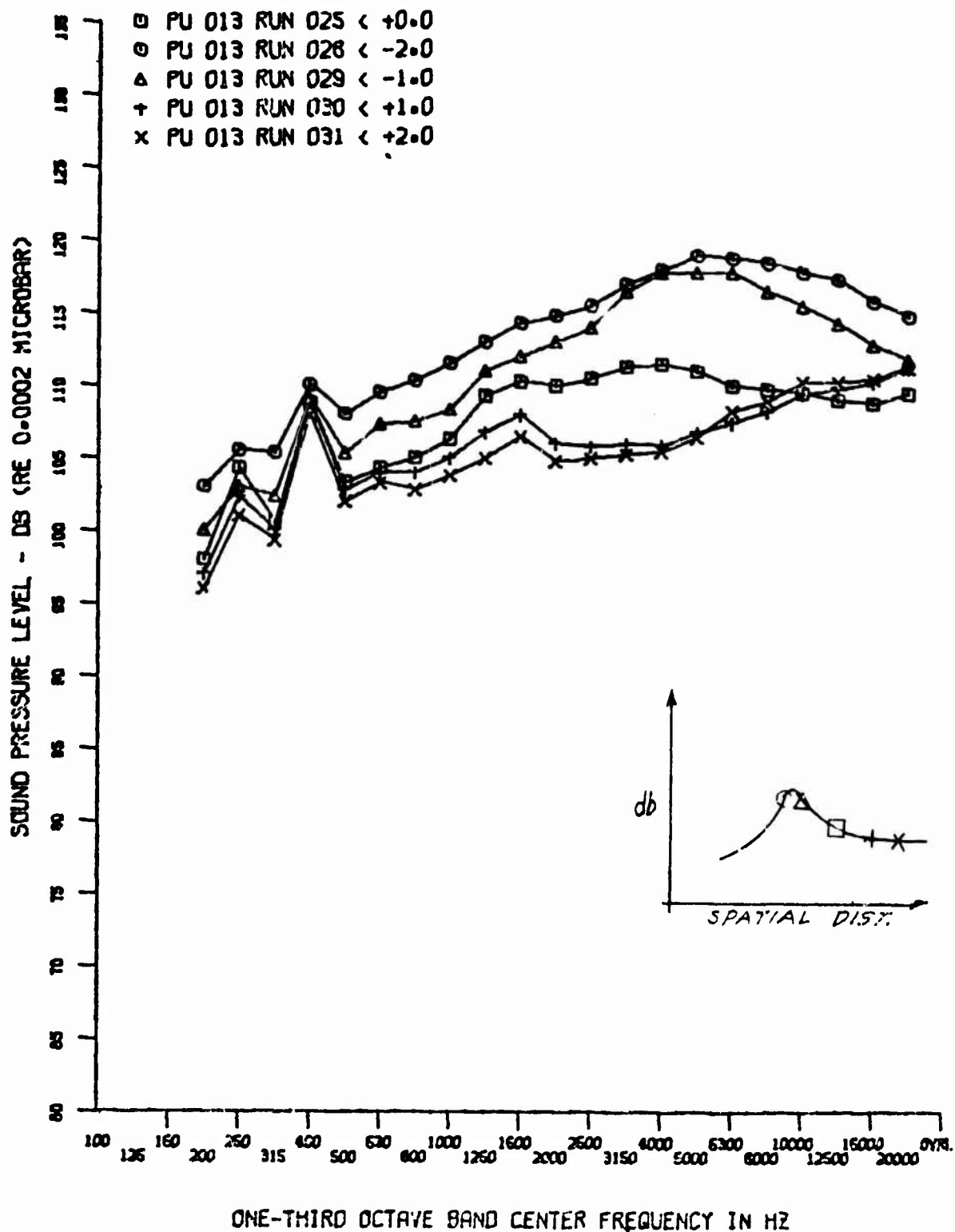
Figure 107. Comparison of Spectra in Transition Zone ($M_\infty = 4$, $Re_\infty = 2.8 \times 10^6$, $R_N = 0$)

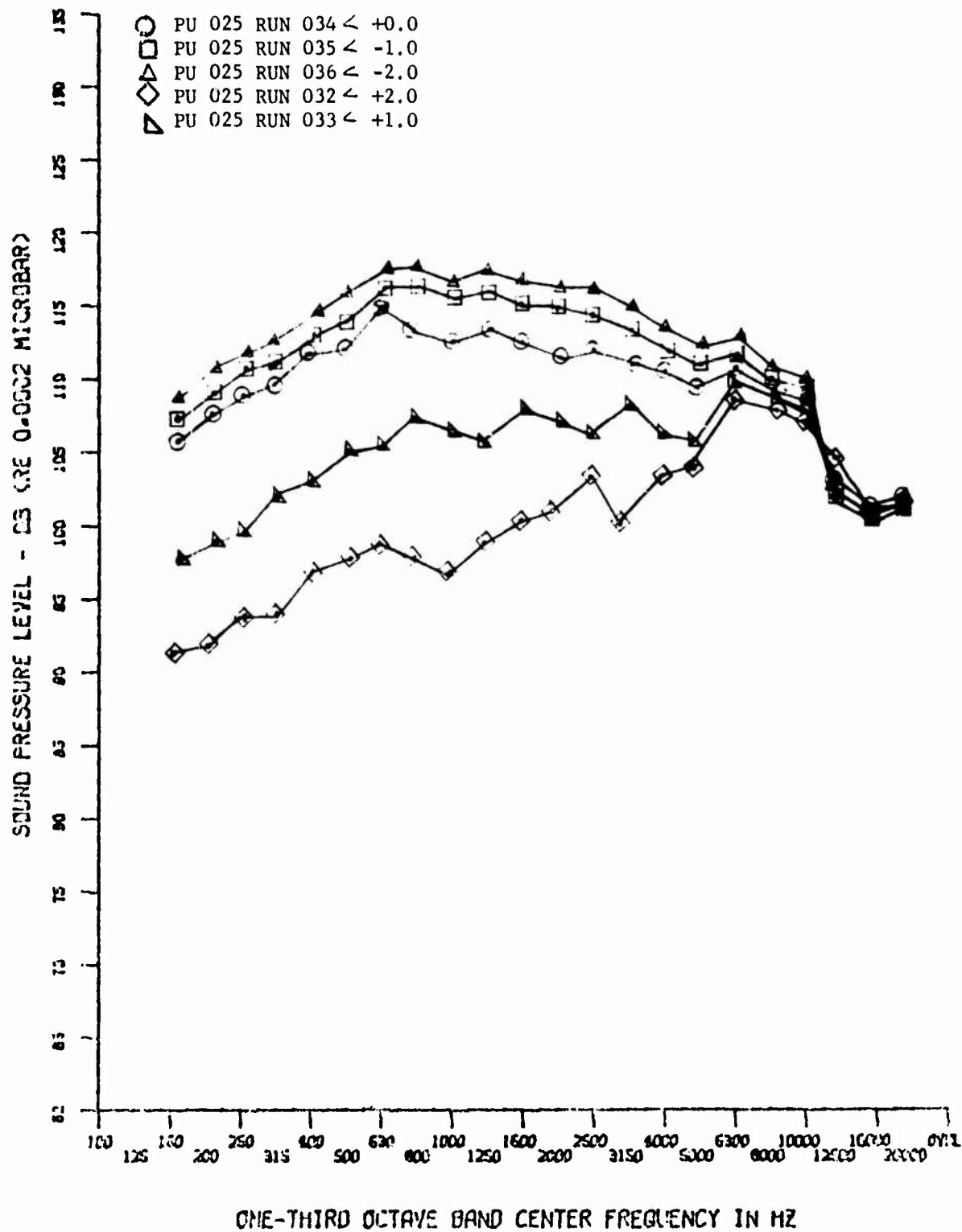Figure 108. Base Spectra at Various α ($M_\infty = 4$, $Re_\infty = 2.8 \times 10^6$, $R_N = 0$)

133

Figure 109. Base Spectra at Various α ($M_\infty = 4$, $Re_\infty = 2.8 \times 10^6$, $R_N = 0$)

Figure 110. Base Spectra at Various α ($M_\infty = 4$, $Re_\infty = 2.8 \times 10^6$, $R_N = 0$)

135

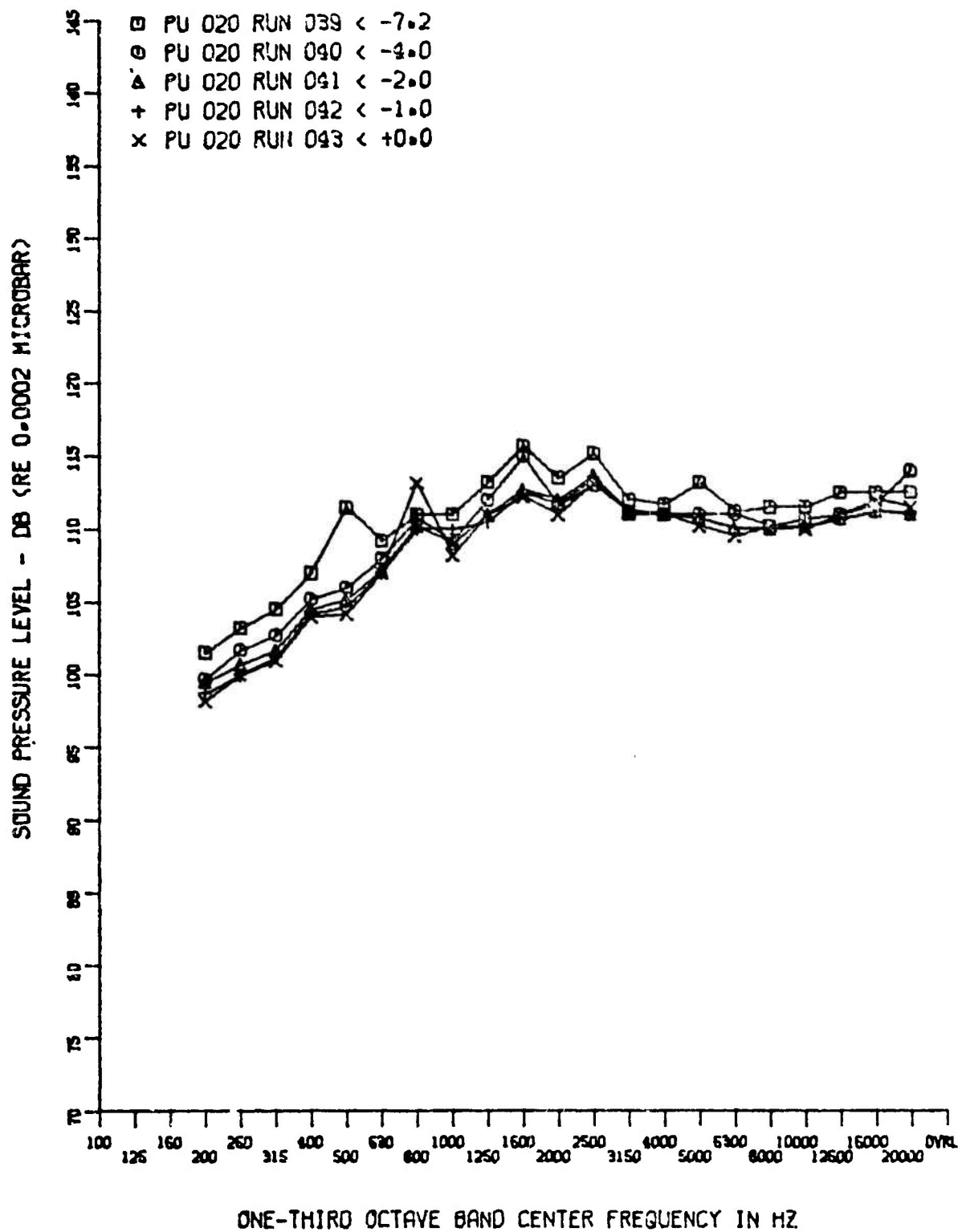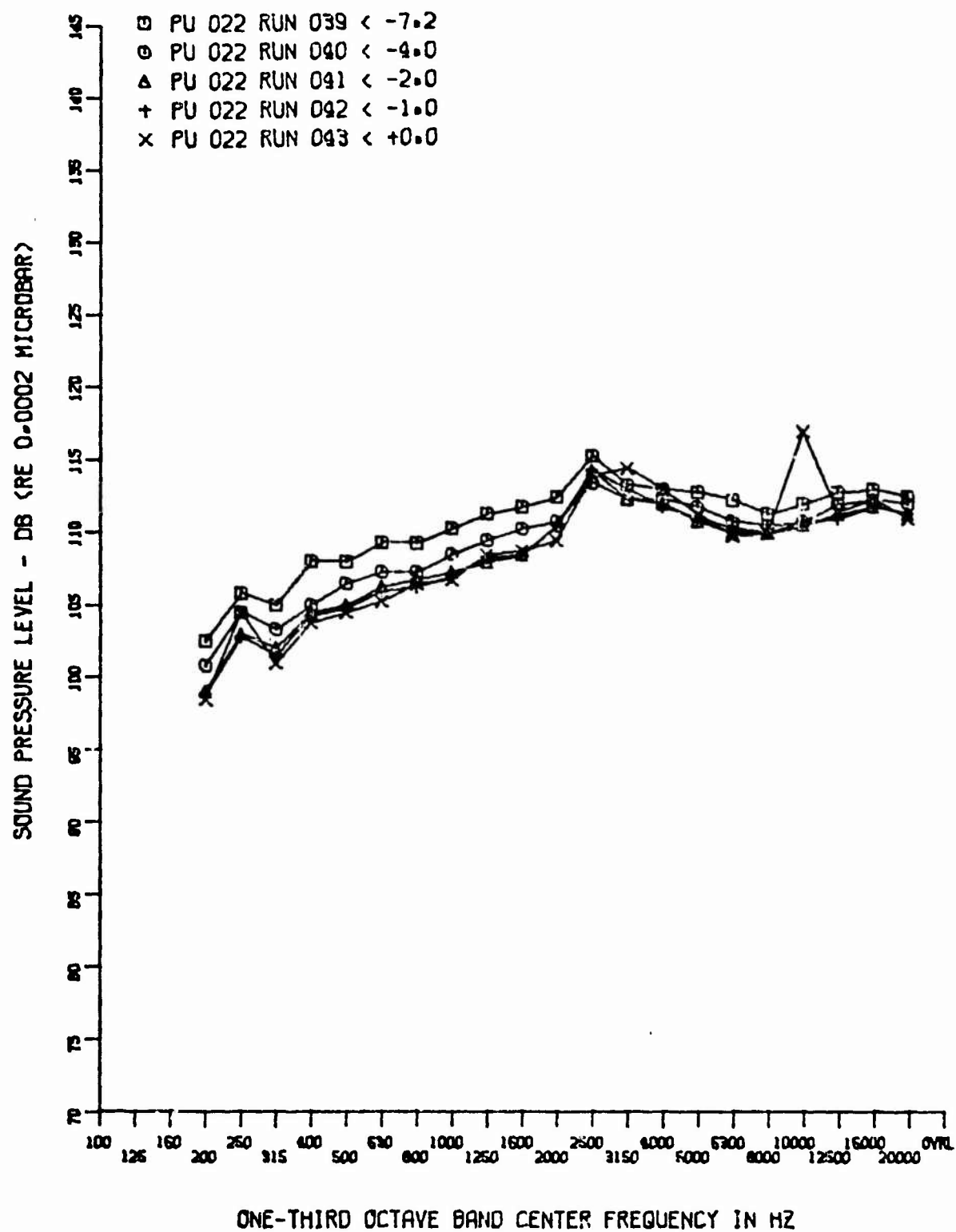Figure 111. Tunnel Tare Noise ($M_\infty = 4$, $R_\infty = 2.8 \times 10^6$, $R_N = 0$)

136

Figure 112. Comparison of Spectra in Transition Zone ($M_\infty = 4$, $Re_\infty = 2.2 \times 10^6$, $R_N = 0.055$)
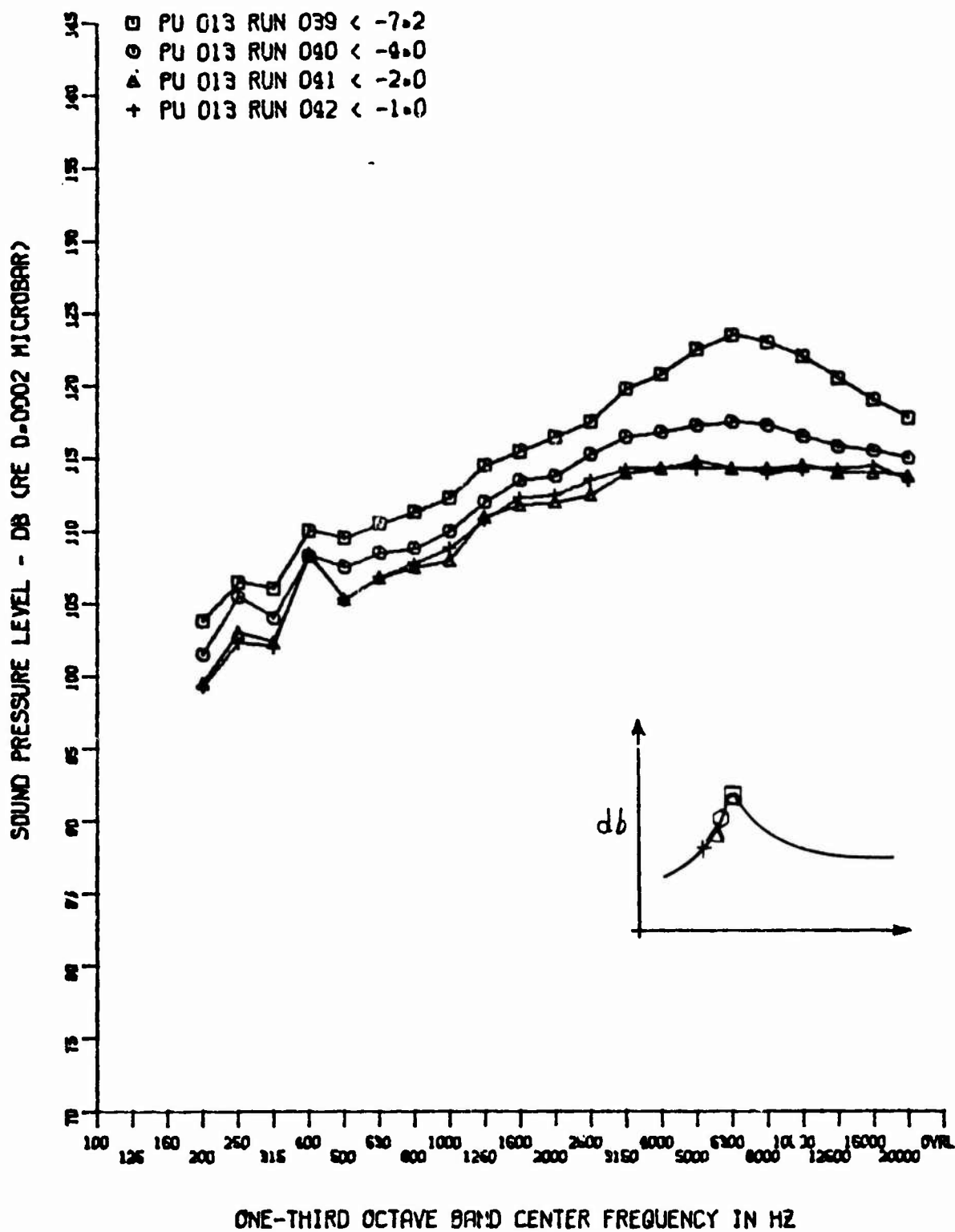
137
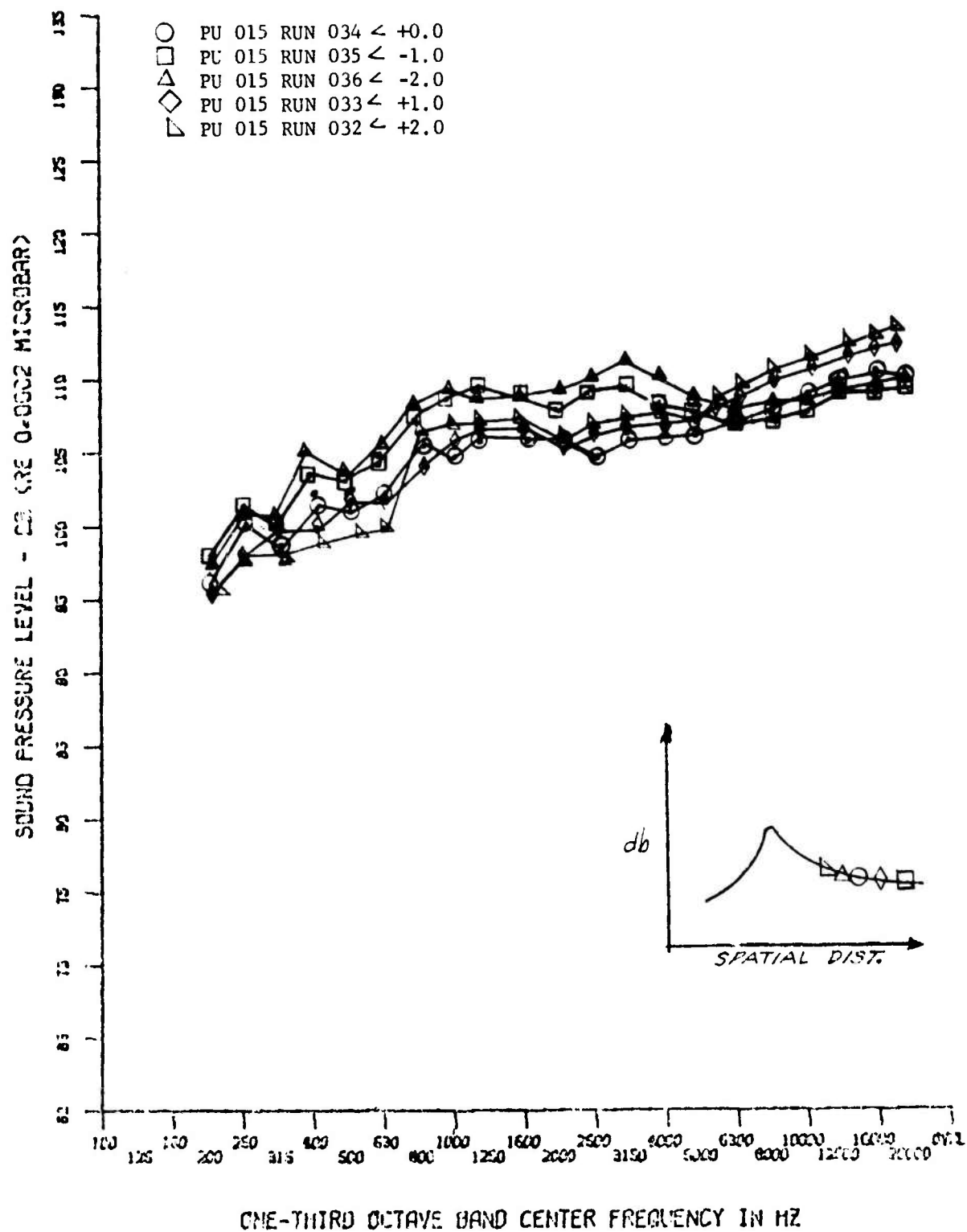
Figure 113. Comparison of Spectra in Transition Zone ($M_\infty = 4$, $Re_\infty = 2.2 \times 10^6$, $R_N = 0.055$)

138

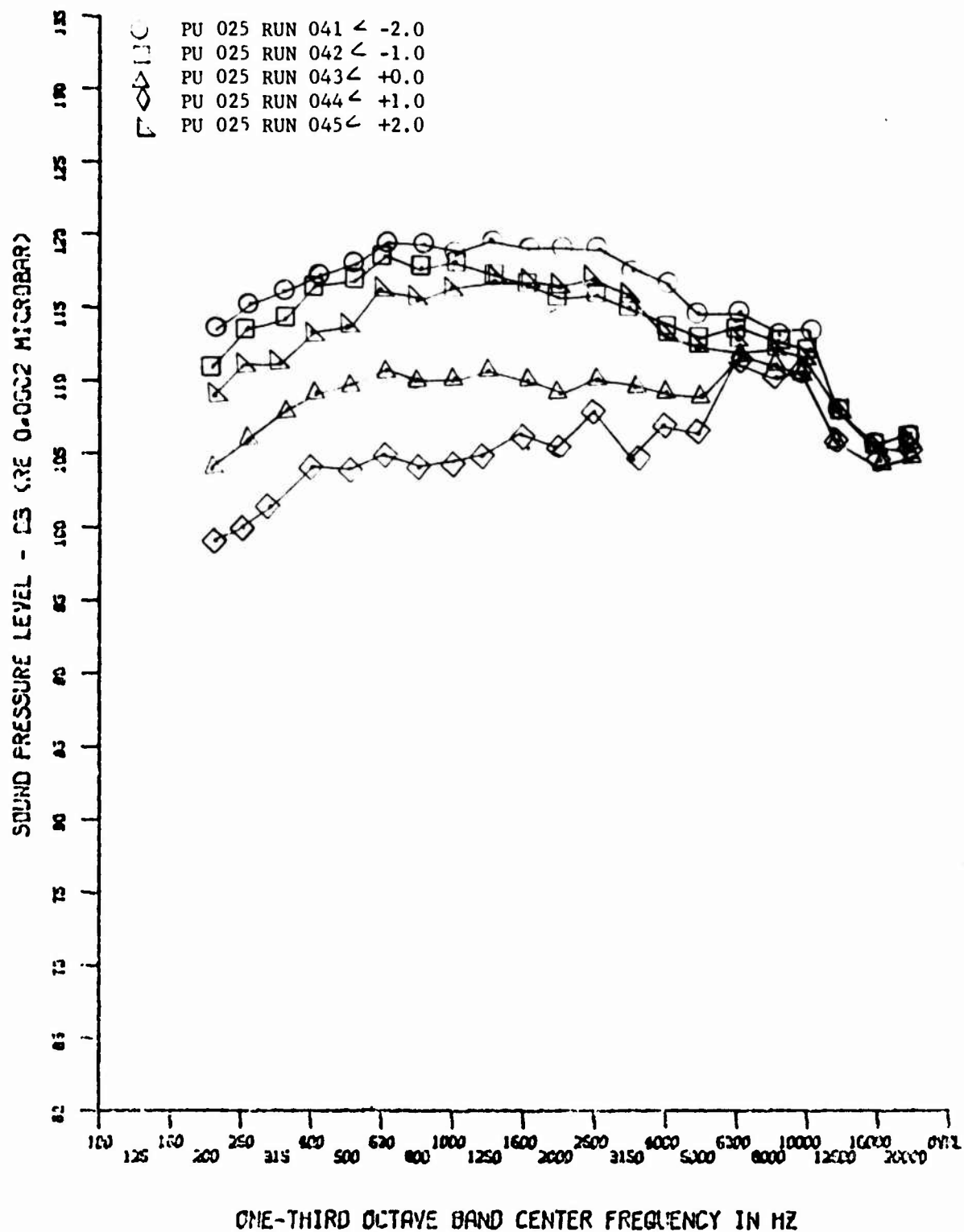Figure 114. Base Spectra at Various ($M_\infty = 4$, $Re_\infty = 2.2 \times 10^6$, $R_N = 0.055$)

Figure 115. Base Spectra at Various ($M_\infty = 4$, $Re_\infty = 2.2 \times 10^6$, $R_N = 0.055$)

140
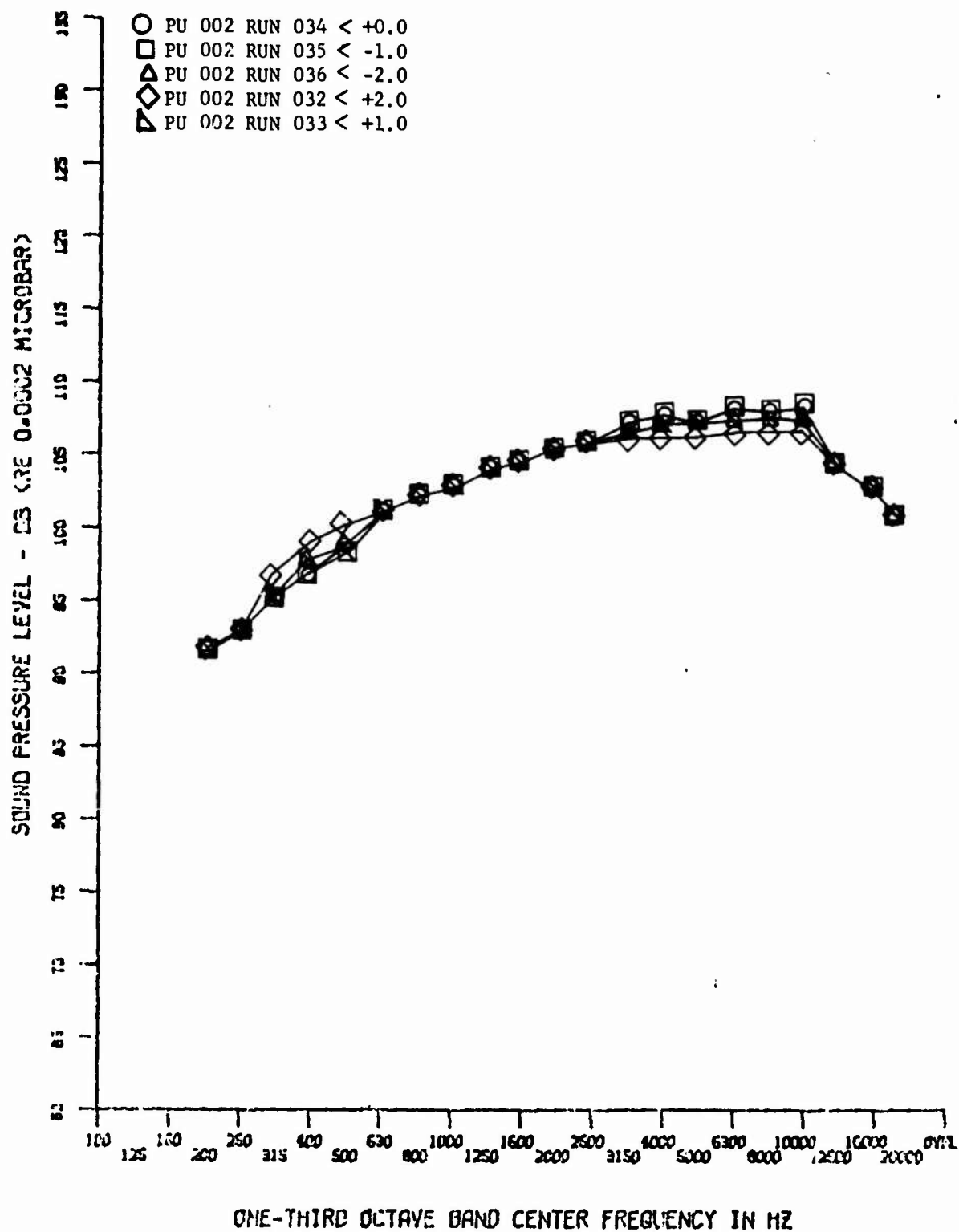
Figure 116. Tunnel Tare Noise ($M_\infty = 4$, $Re_\infty = 2.2 \times 10^6$, $R_N = 0.055$)

141

Figure 117.   Turbulent Flow Spectra ($M_\infty = 4$, $Re_\infty = 3.0 \times 10^6$, $R_N = 0.11$)

142
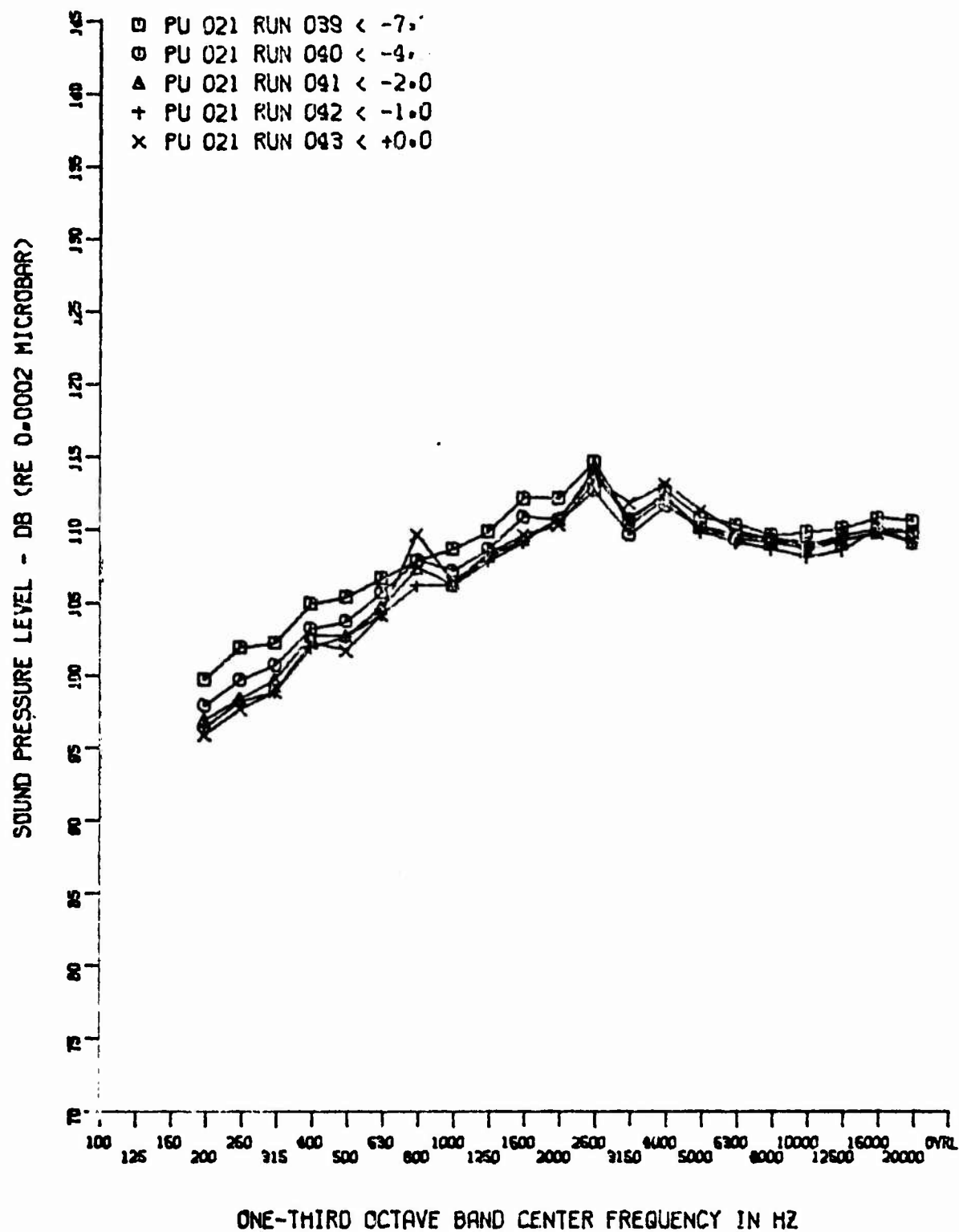
Figure 118. Turbulent Flow Spectra ($M_\infty = 4$, $Re_\infty = 3.0 \times 10^6$, $R_N = 0.11$)

143

Figure 119. Turbulent Flow Spectra ($M_\infty = 4$, $Re_\infty = 3.0 \times 10^6$, $R_N = 0.11$)

Figure 120. Comparison of Spectra in Transition Zone ($M_\infty = 4$, $Re_\infty = 3.0^6 \times 10$, $R_N = 0.11$)

145
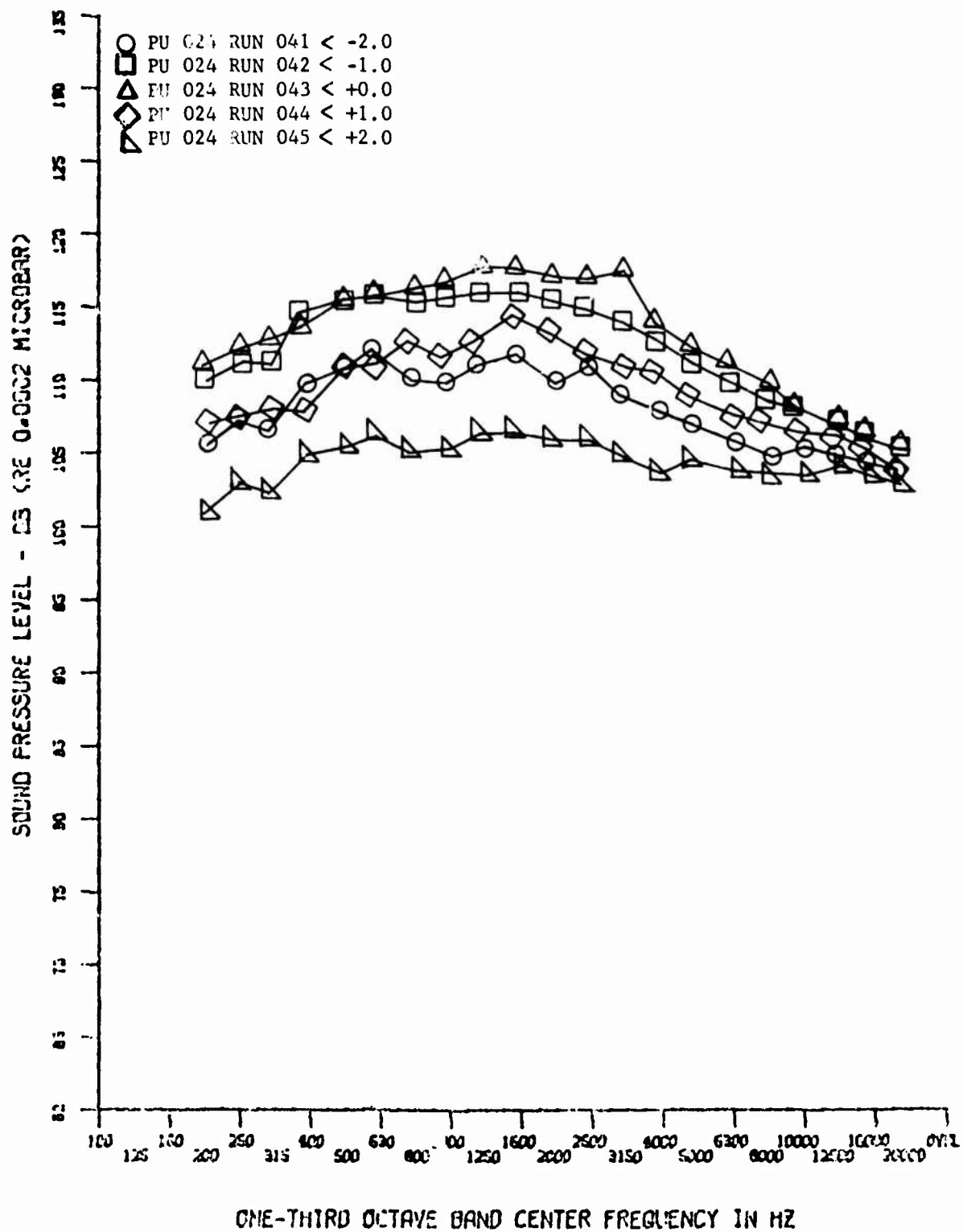
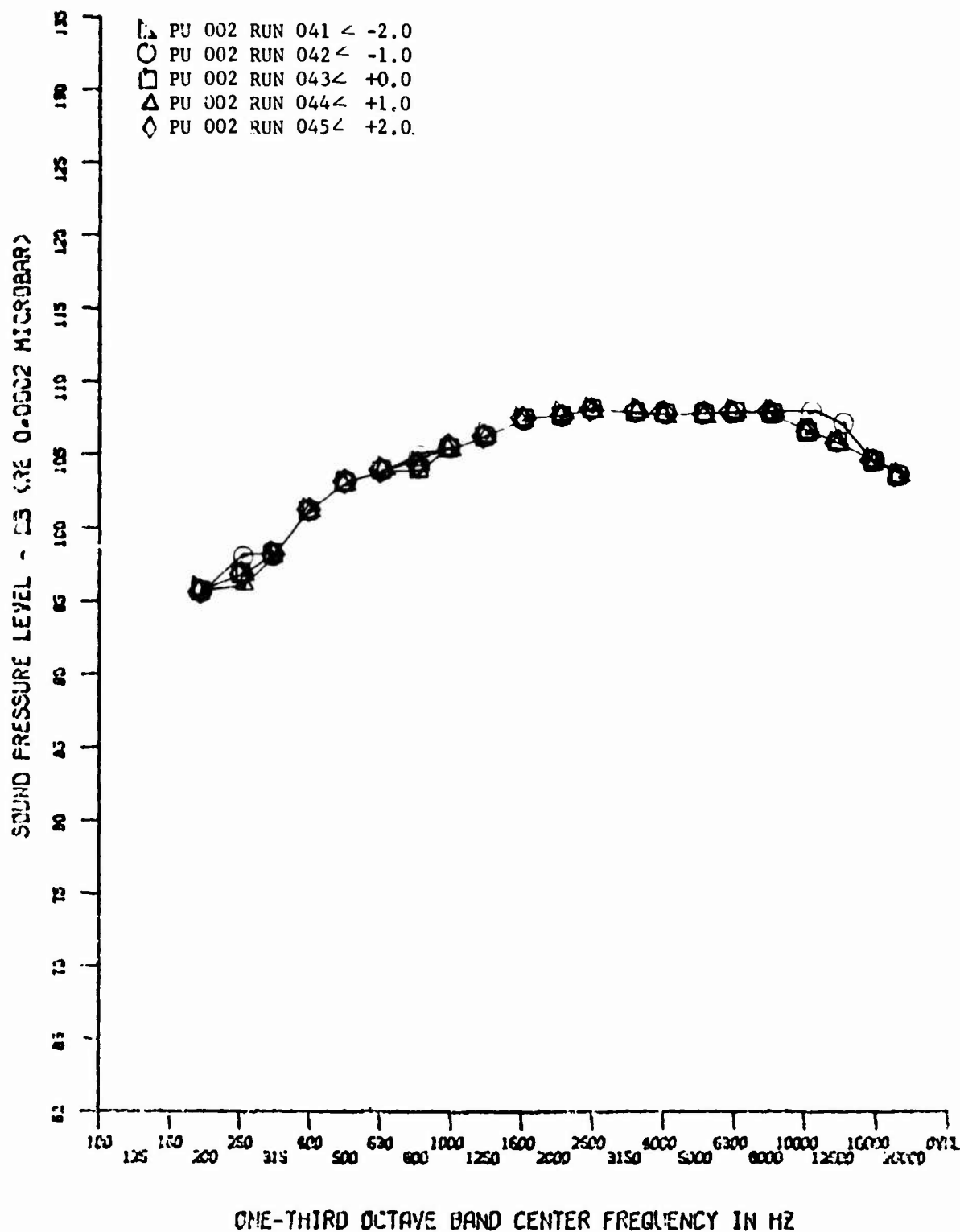Figure 121. Base Spectra at Various ($M_\infty = 4$, $Re_\infty = 3.0 \times 10^6$, $R_N = 0.11$)

146

Figure 122. Base Spectra at Various ($M_\infty = 4$, $Re_\infty = 3.0 \times 10^6$, $R_N = 0.11$)

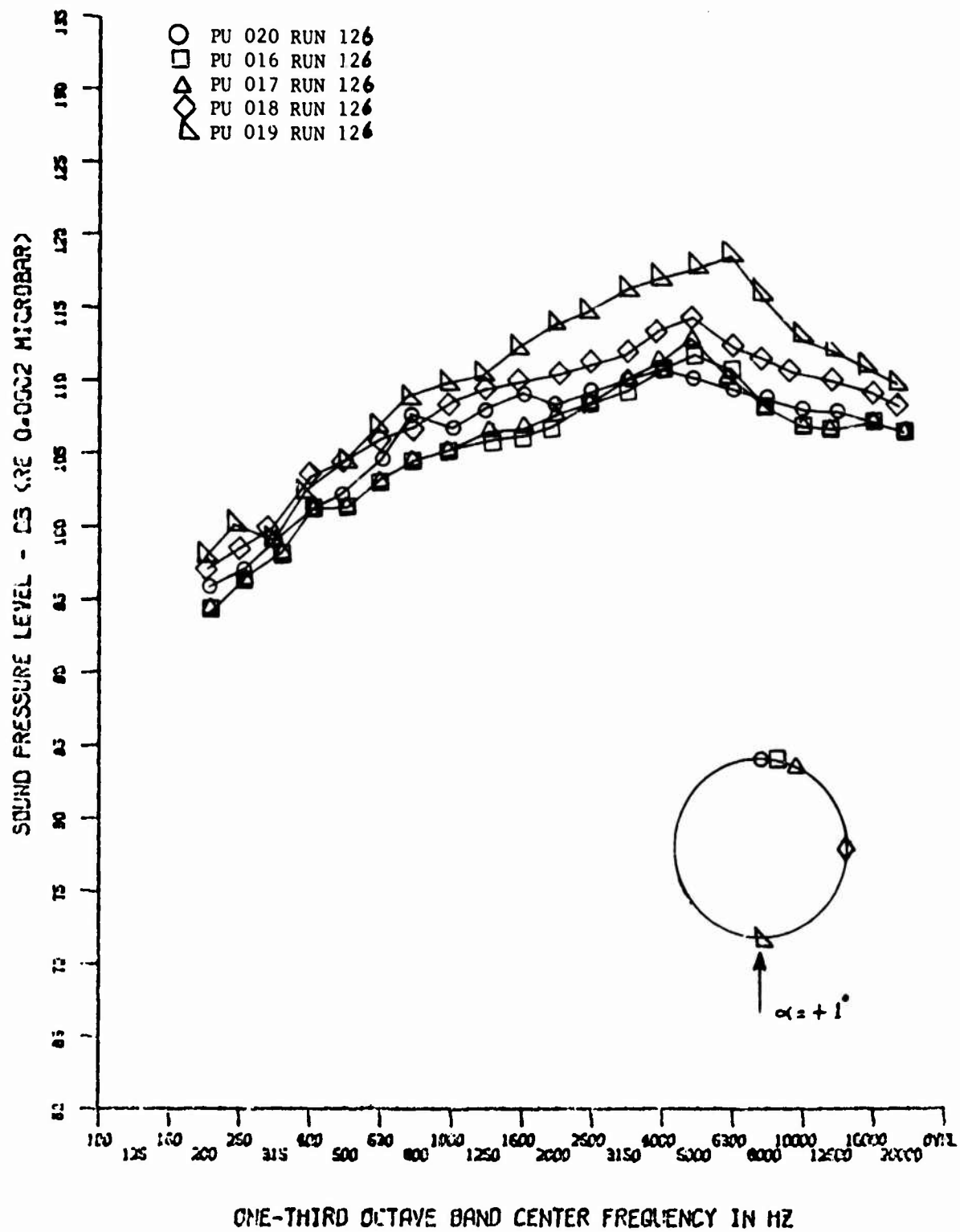Figure 123. Tunnel Tare Noise ($M_\infty = 4$, $Re_\infty = 3.0 \times 10^6$, $R_N = 0$)

148

Figure 124. Turbulent Flow Spectra Circumferential Variation ($M_\infty = 8$, $Re_\infty = 1.4 \times 10^6$, $R_N = 0$)
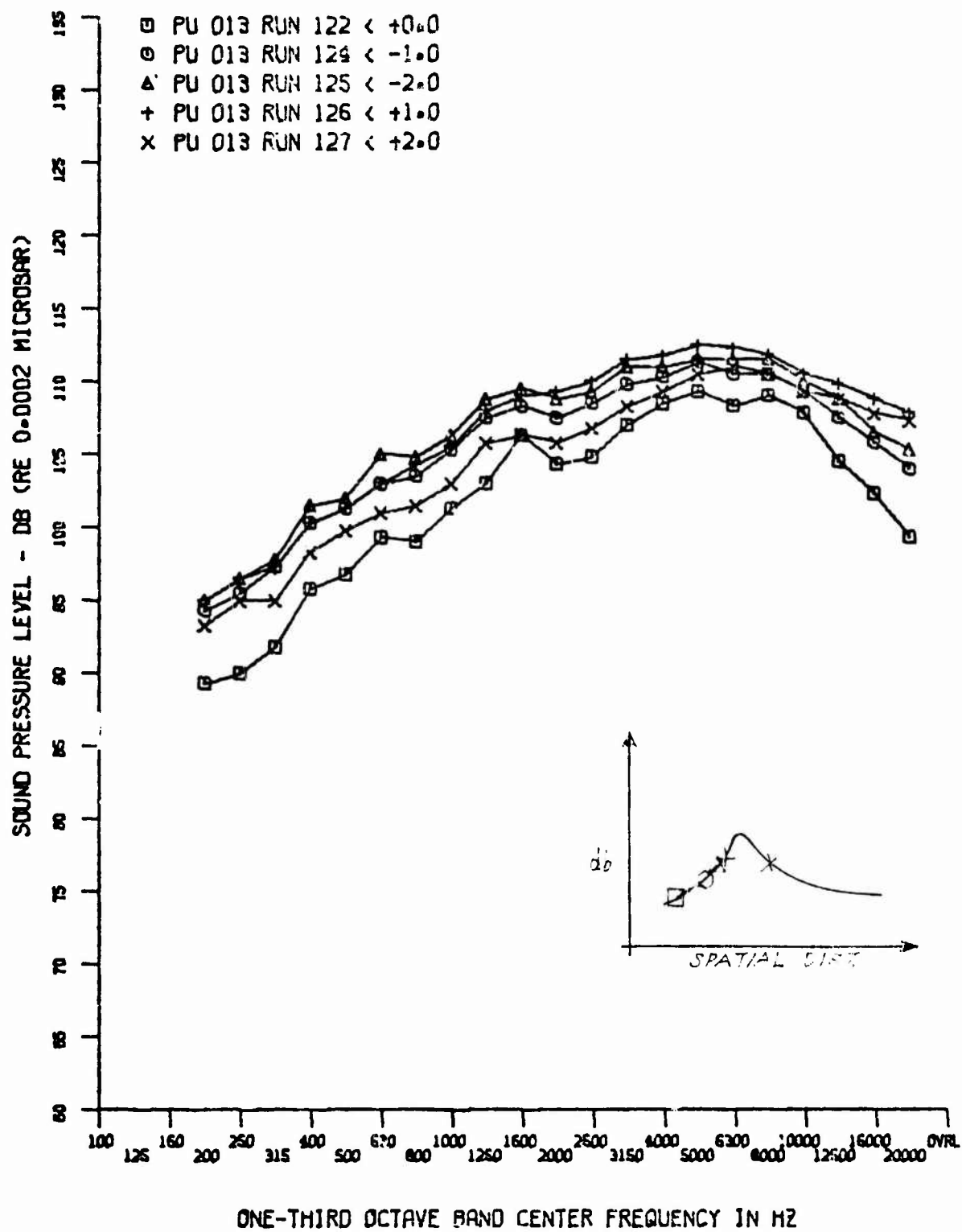
149

Figure 125. Comparison of Spectra in Transition Zone ($M_\infty = 8$, $Re_\infty = 1.4 \times 10^6$, $R_N = 0$)

Figure 126. Comparison of Spectra in Transition Zone ($M_\infty = 8$, $Re_\infty = 1.4 \times 10^6$, $R_N = 0$)
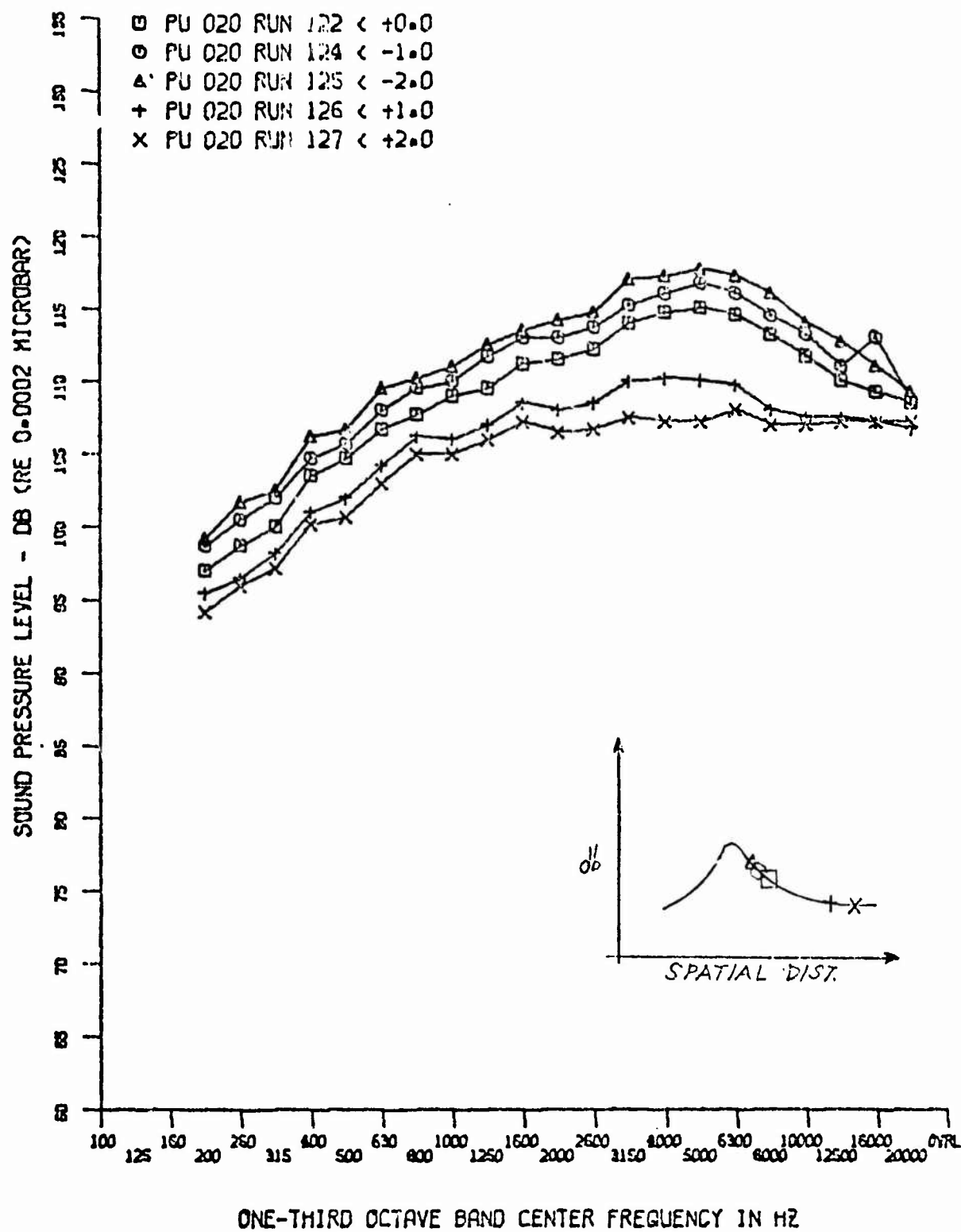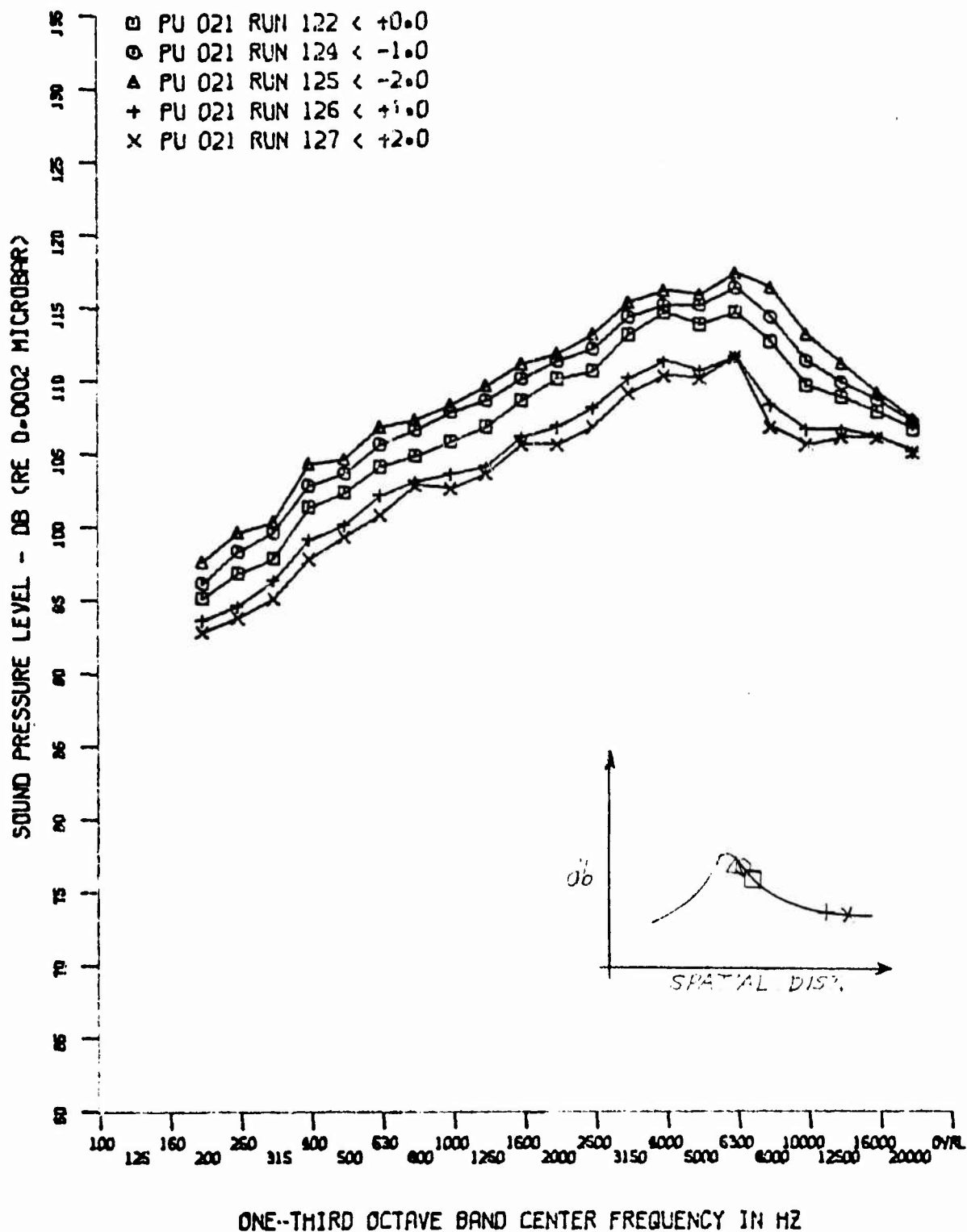
151

Figure 127. Comparison of Spectra in Transition Zone ($M_\infty = 8$, $Re_\infty = 1.4 \times 10^6$, $R_N = 0$)

Figure 128. Comparison of Spectra in Transition Zone ($M_\infty = 8$, $Re_\infty = 1.4 \times 10^6$, $R_N = 0$)
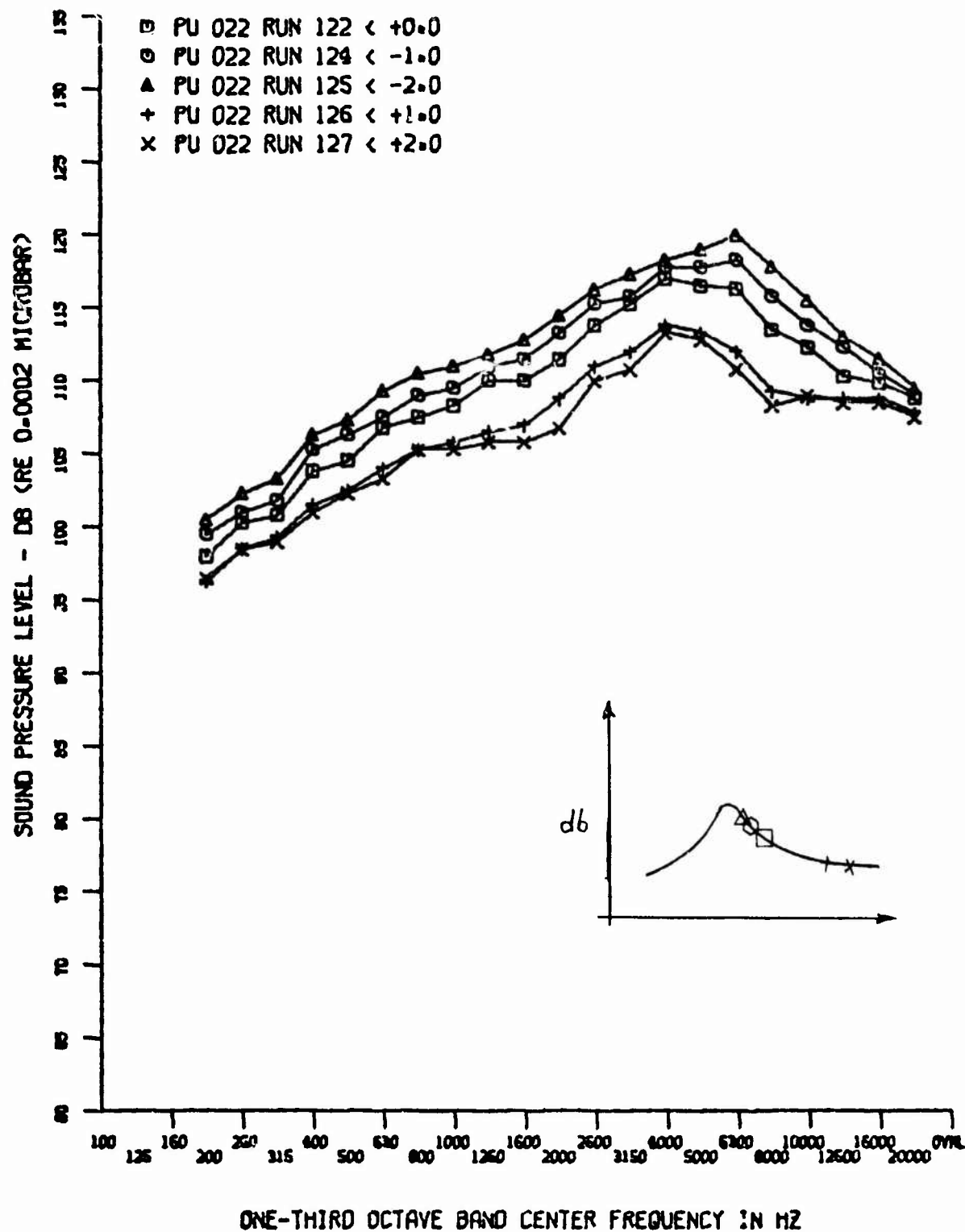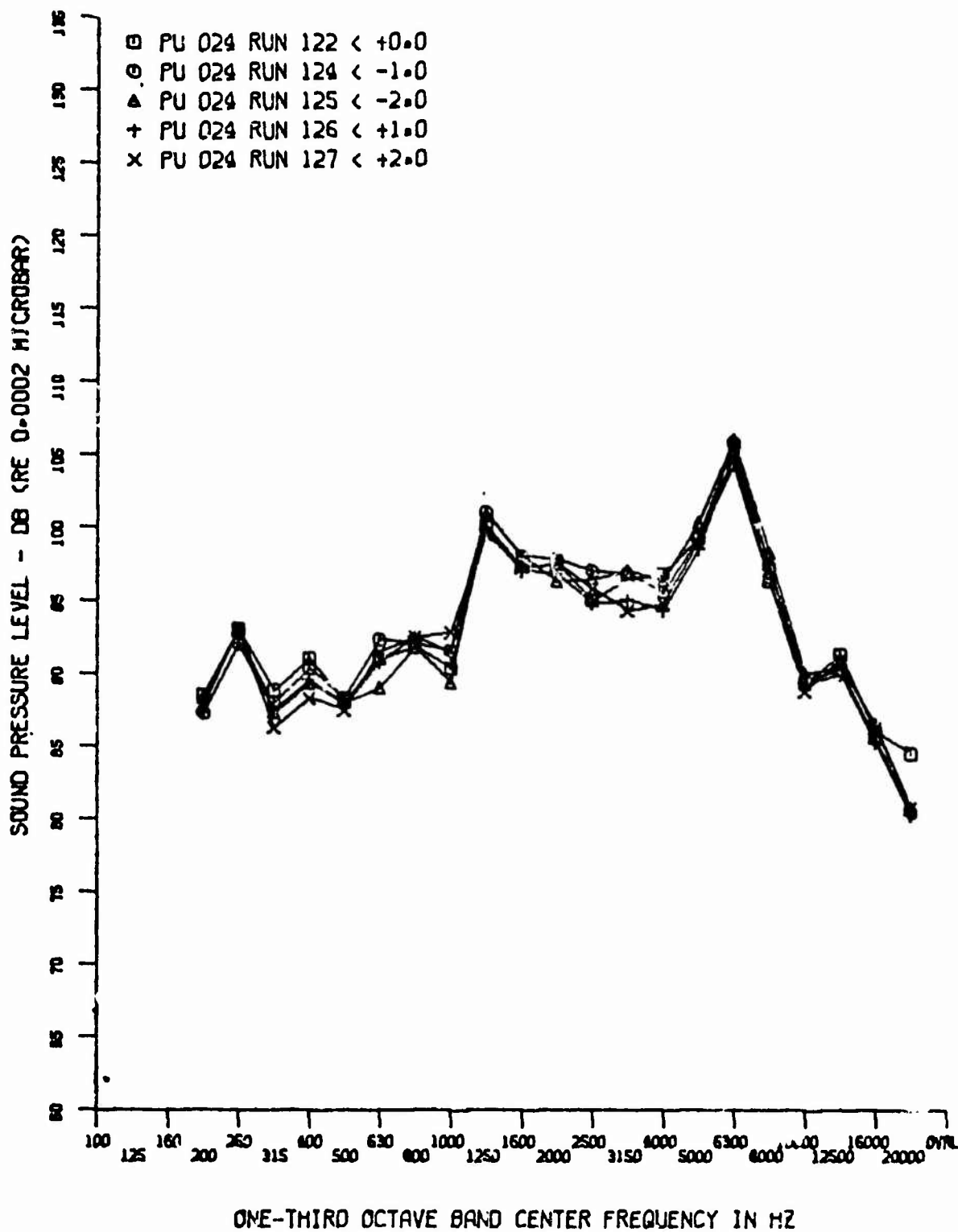
153

Figure 129. Base Spectra at Various ($M_\infty = 8$, $Re_\infty = 1.4 \times 10^6$, $R_N = 0$)

154

Figure 130. Base Spectra at Various ($M_\infty = 8$, $Re_\infty = 1.4 \times 10^6$, $R_N = 0$)

Figure 131. Base Spectra at Various ($M_\infty = 8$, $Re_\infty = 1.4 \times 10^6$, $R_N = 0$)
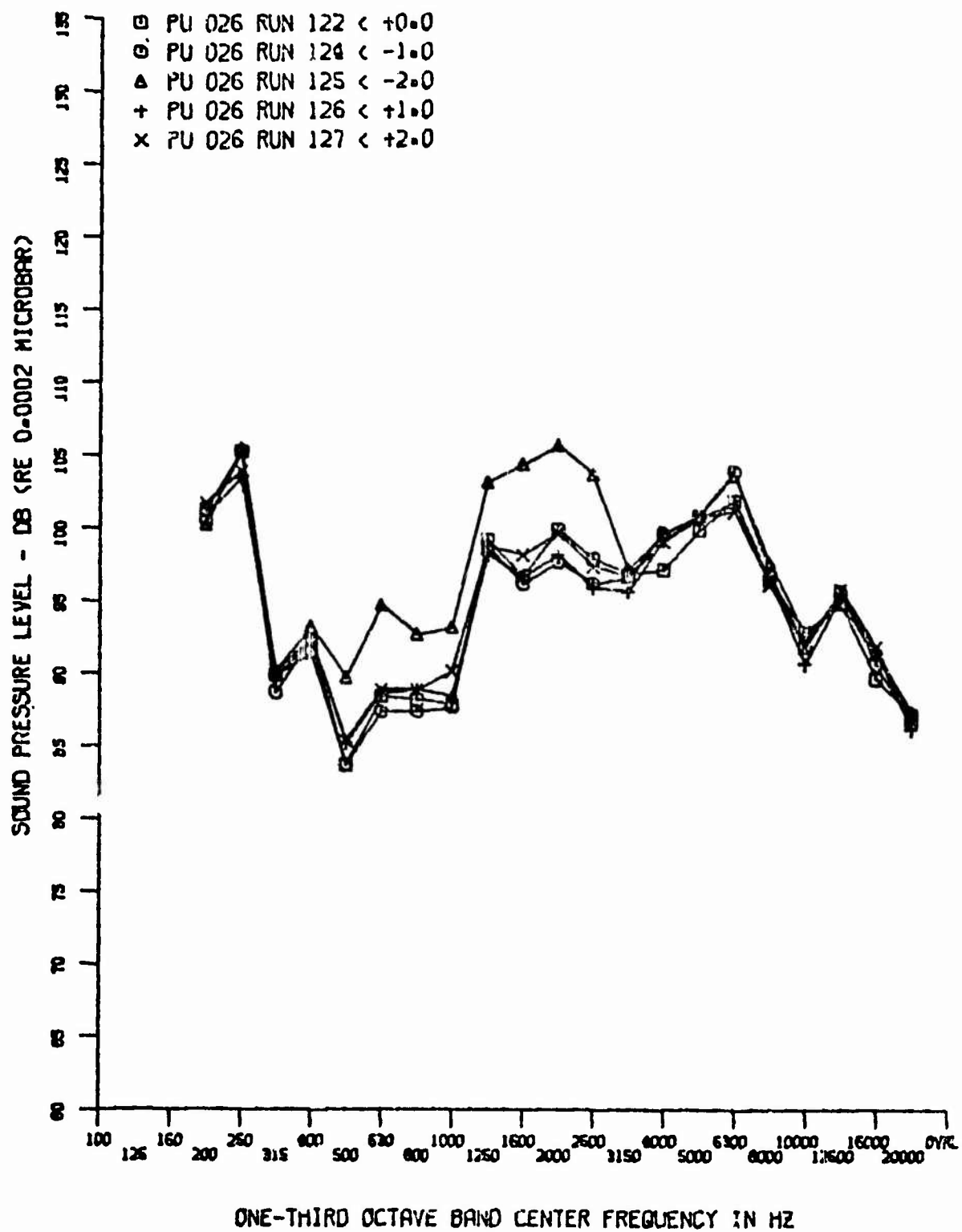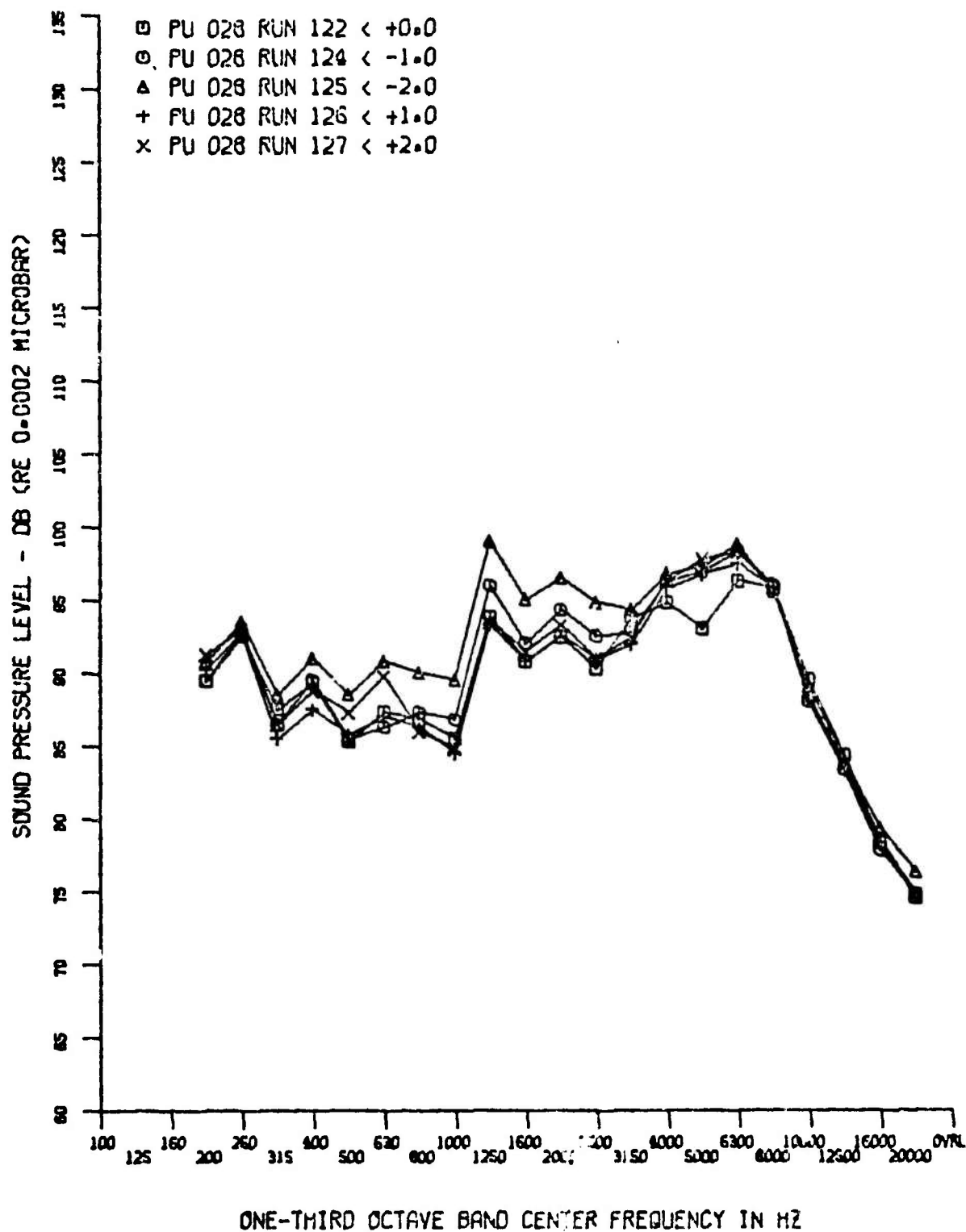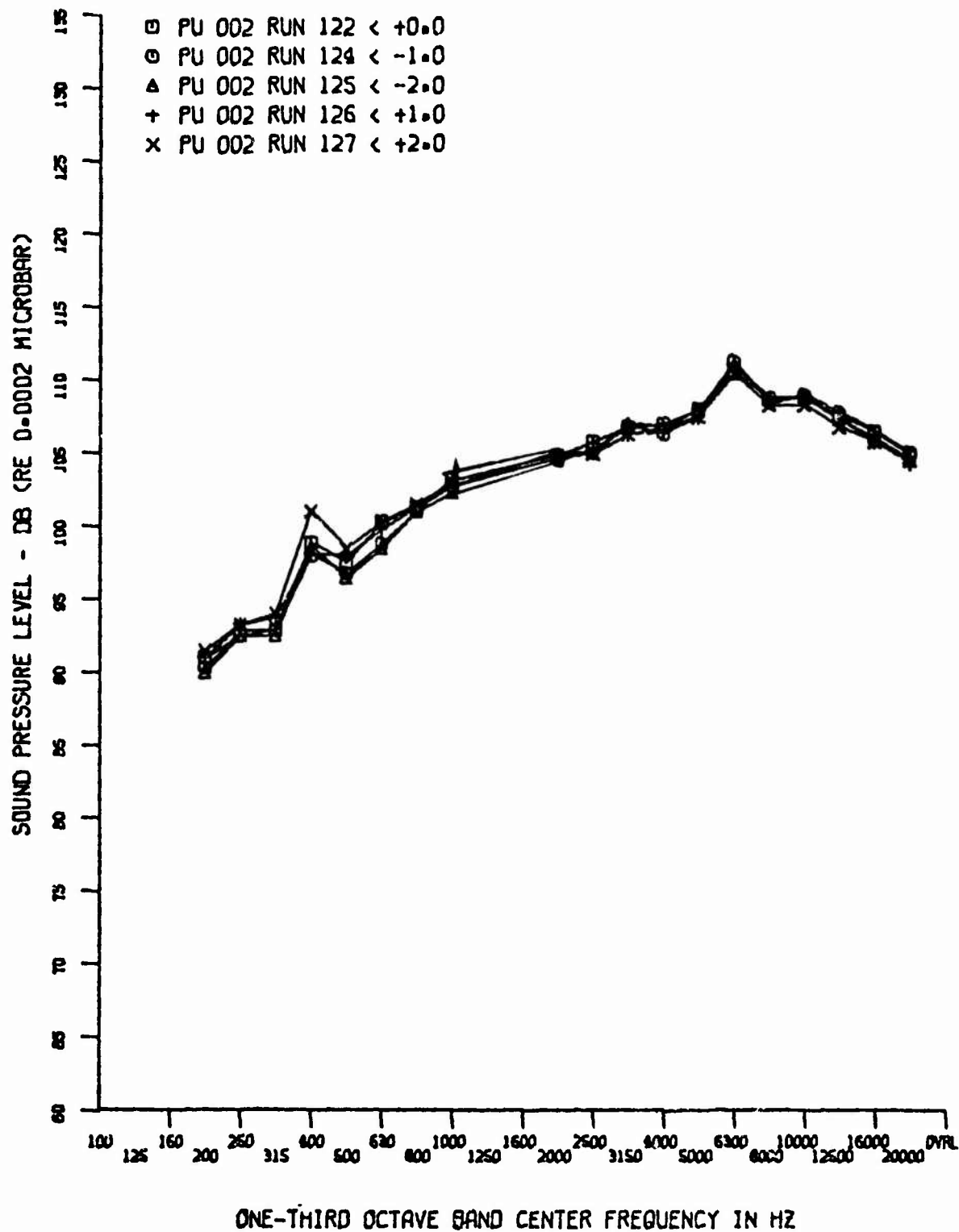
Figure 132. Tunnel Tare Noise ($M_\infty = 8$, $Re_\infty = 1.4 \times 10^6$, $R_N = 0$)

157
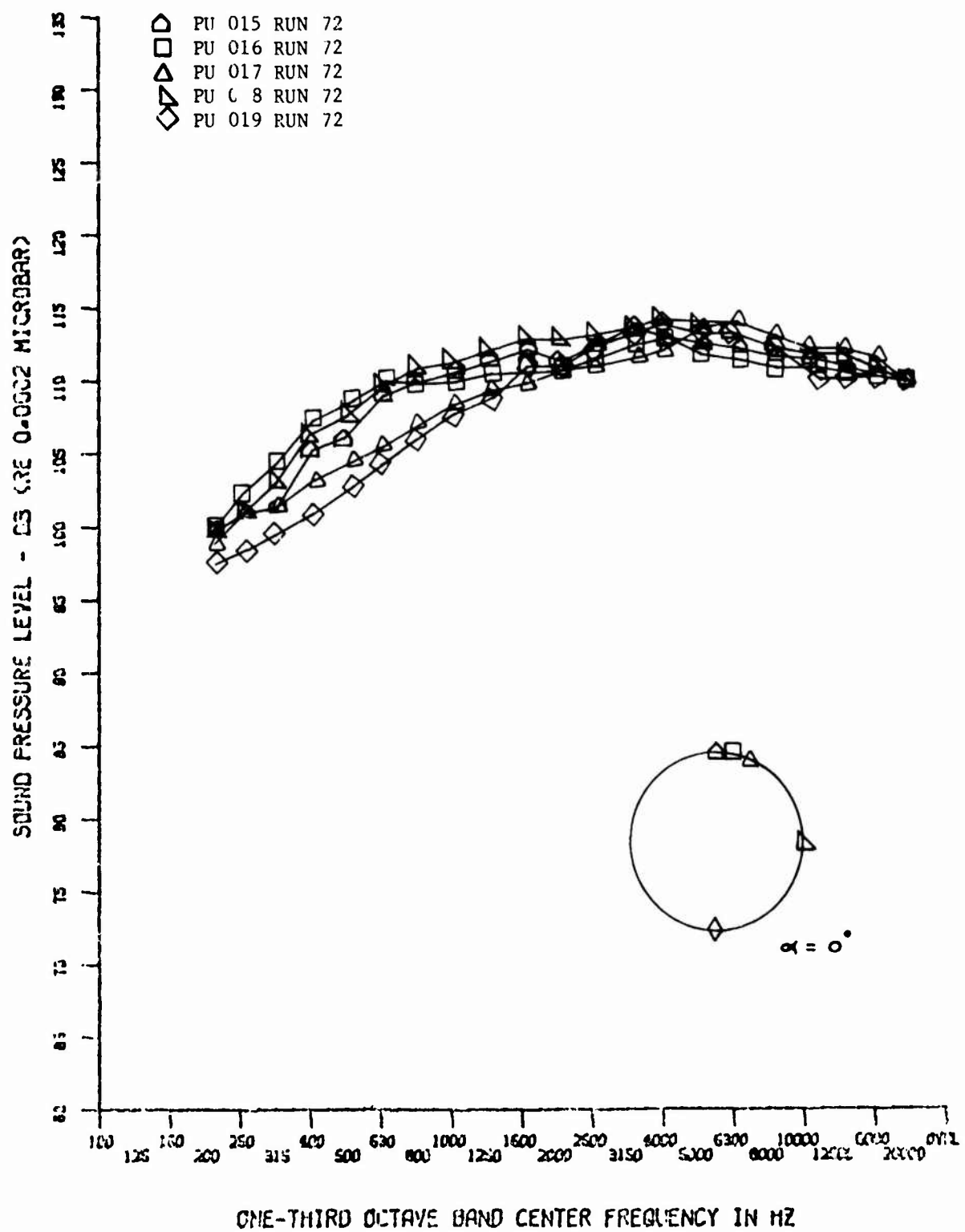
Figure 133. Turbulent Flow Spectra Circumferential Variation ($M_\infty = 8$, $Re_\infty = 2.2 \times 10^6$, $R_N = 0$)
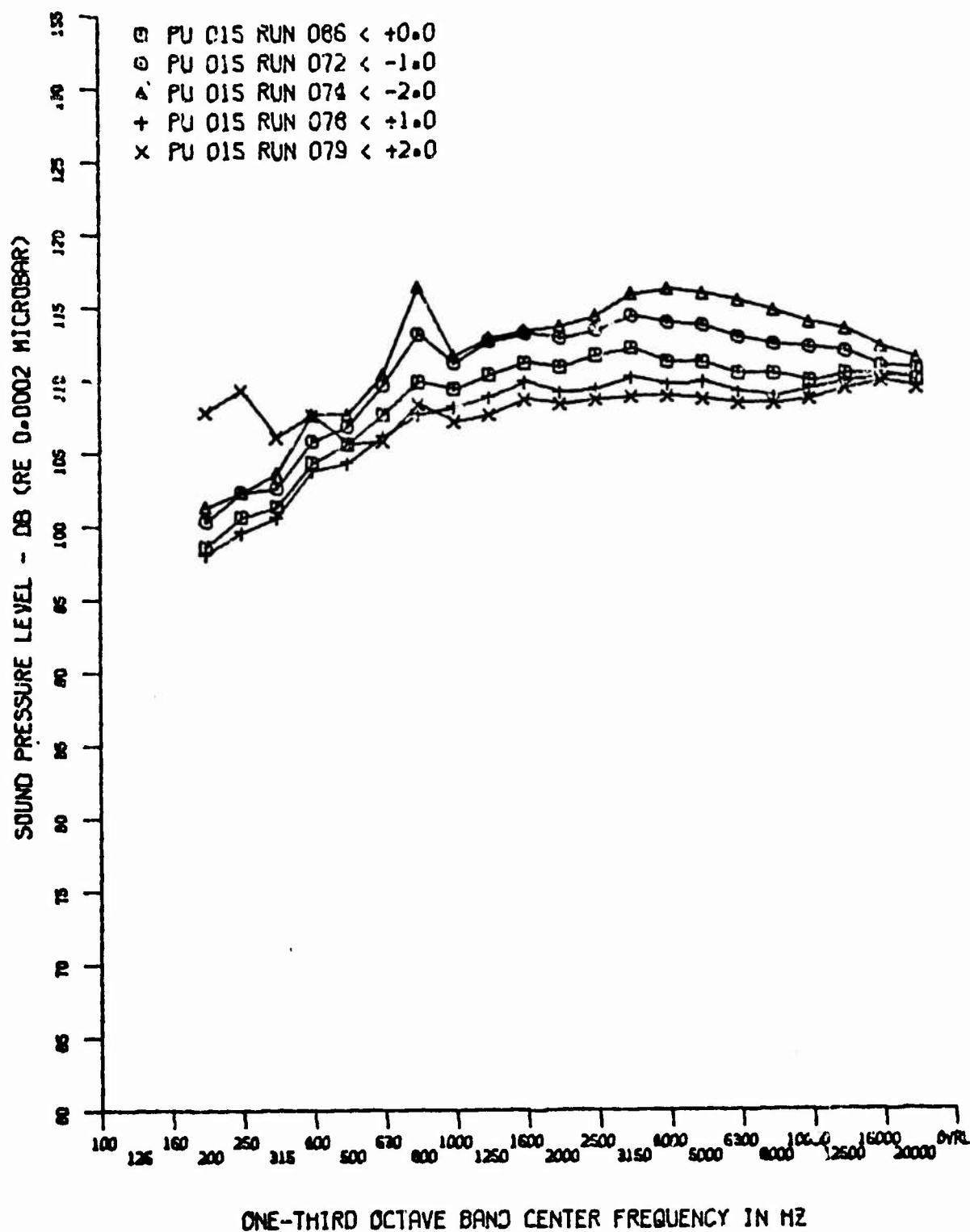
158

Figure 134. Turbulent Flow Spectra ($M_\infty = 8$, $Re_\infty = 2.2 \times 10^6$, $R_N = 0$)
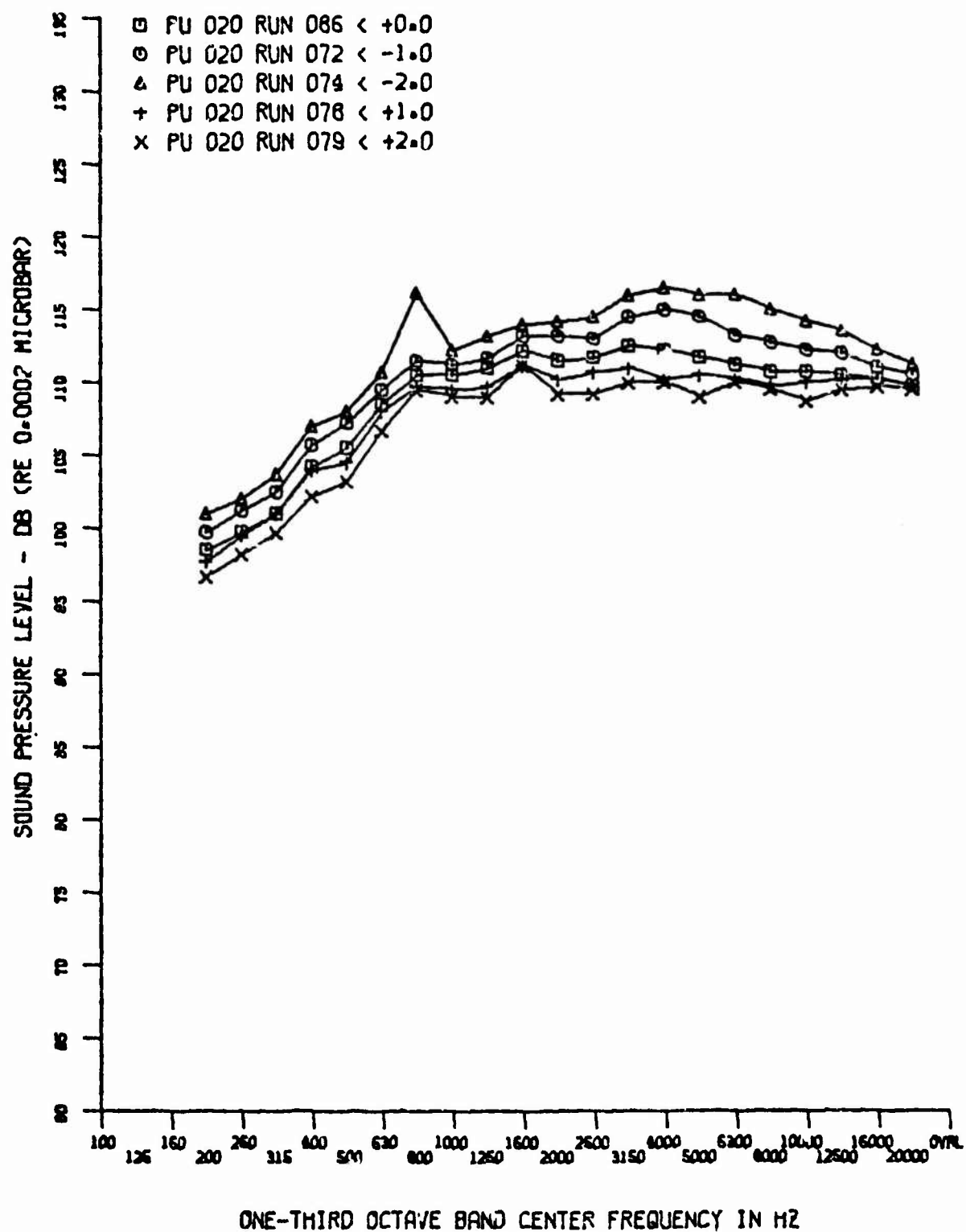
Figure 135. Turbulent Flow Spectra ($M_\infty = 8$, $Re_\infty = 2.2 \times 10^6$, $R_N = 0$)

160

Figure 136. Comparison of Spectra in Transition Zone ($M_\infty = 8$, $Re_\infty = 2.2 \times 10^6$, $R_N = 0$)

Figure 137. Comparison of Spectra in Transition Zone ($M_\infty = 8$, $Re_\infty = 2.2 \times 10^6$, $R_N = 0$)

162
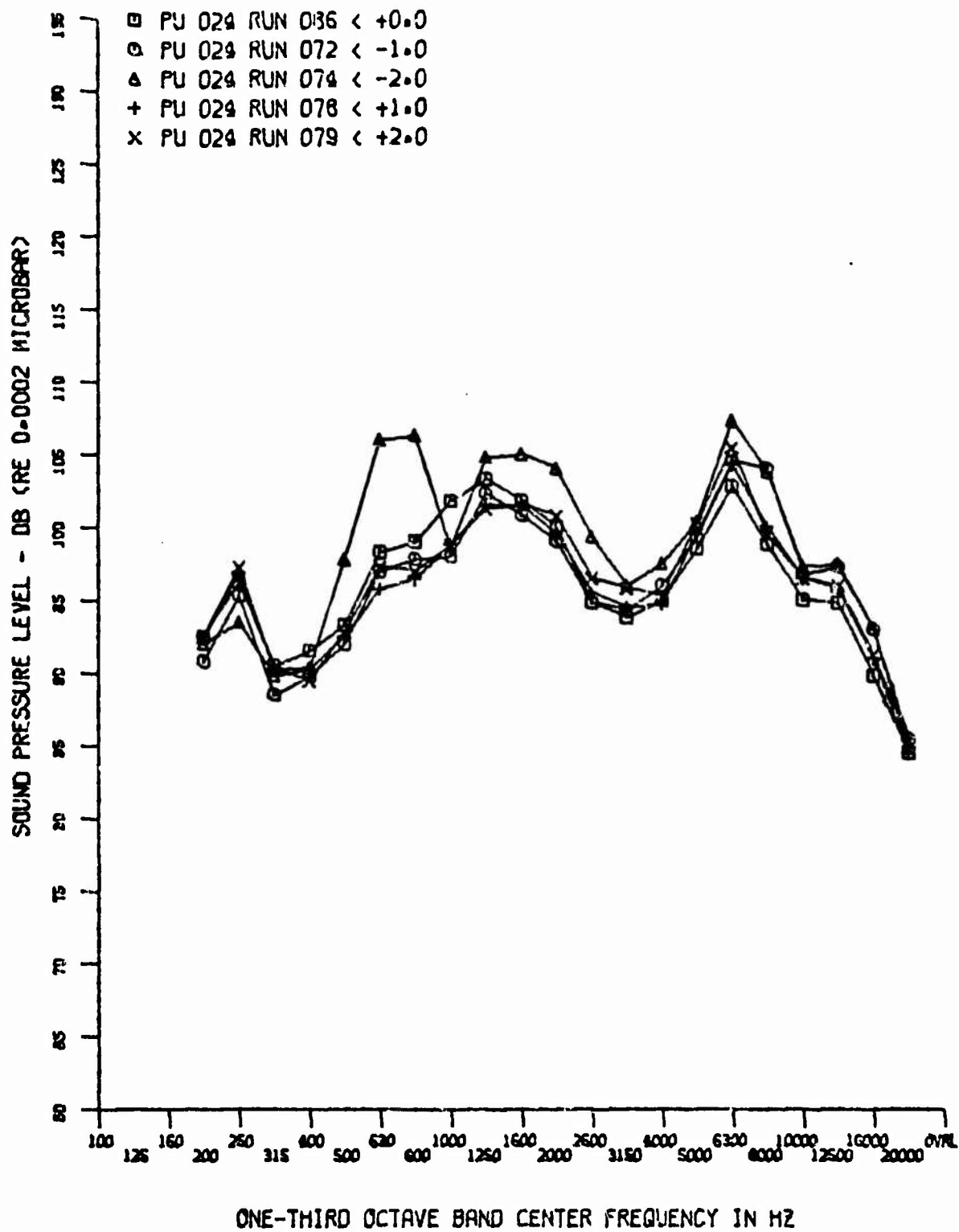
Figure 138.   Base Spectra at Various ($M_\infty = 8$, $Re_\infty = 2.2 \times 10^6$, $R_N = 0$)

163

Figure 139. Base Spectra at Various ($M_\infty = 8$, $Re_\infty = 2.2 \times 10^6$, $R_N = 0$)
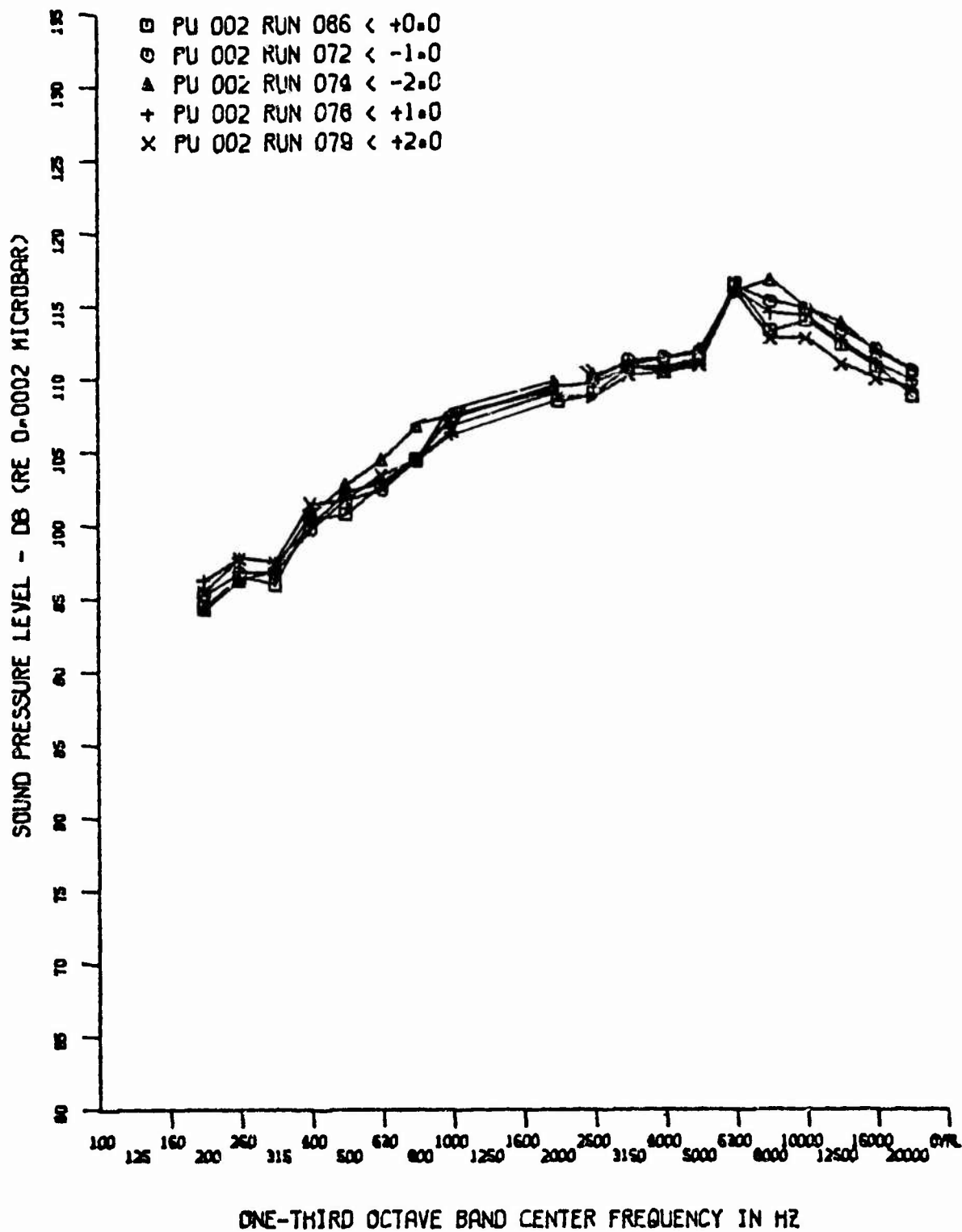
Figure 140. Tunnel Tare Noise ($M_\infty = 8$, $Re_\infty = 2.2 \times 10^6$, $R_N = 0$)
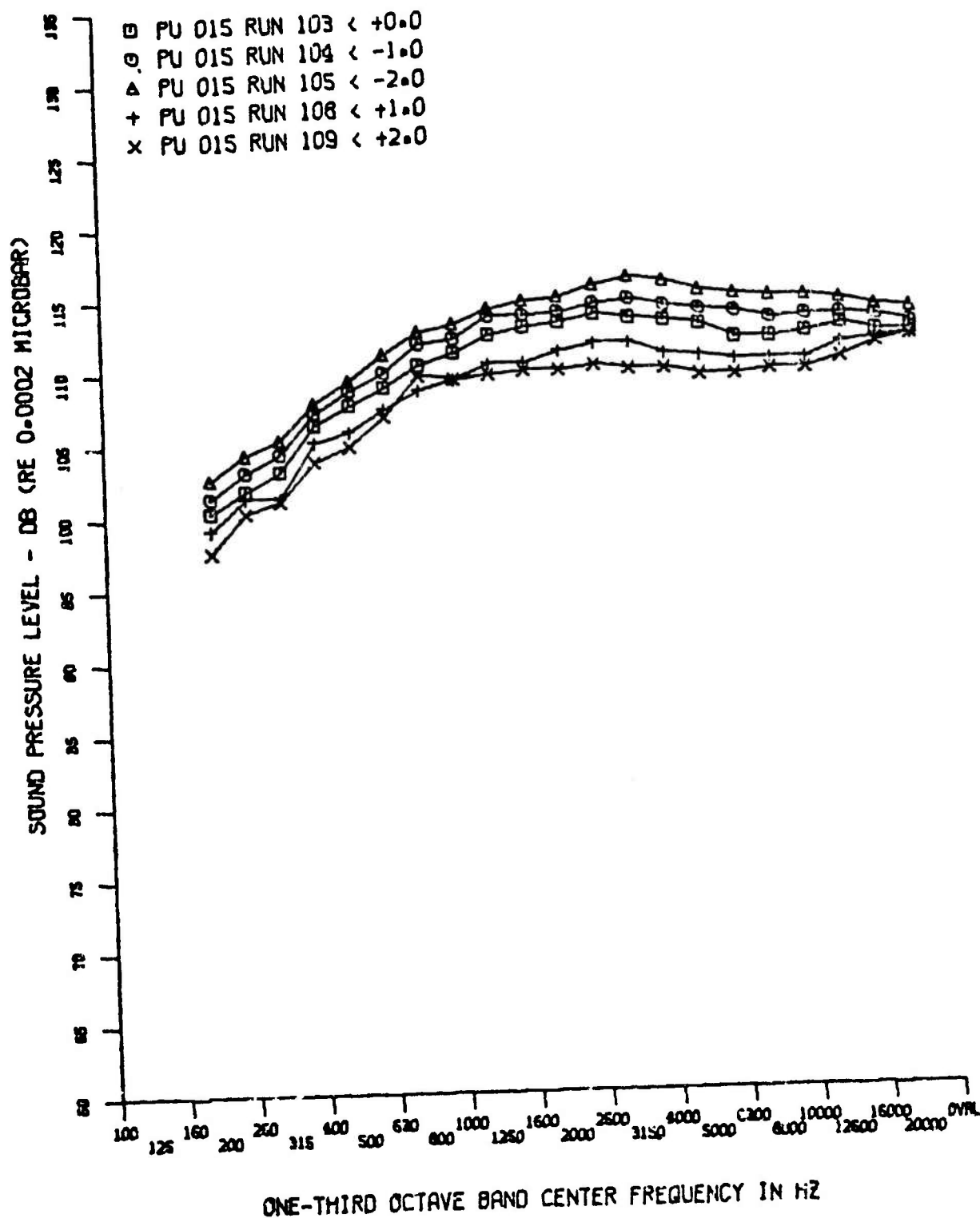
Figure 141. Turbulent Flow Spectra ($M_\infty = 8$, $Re_\infty = 2.8 \times 10^6$, $R_N = 0$)
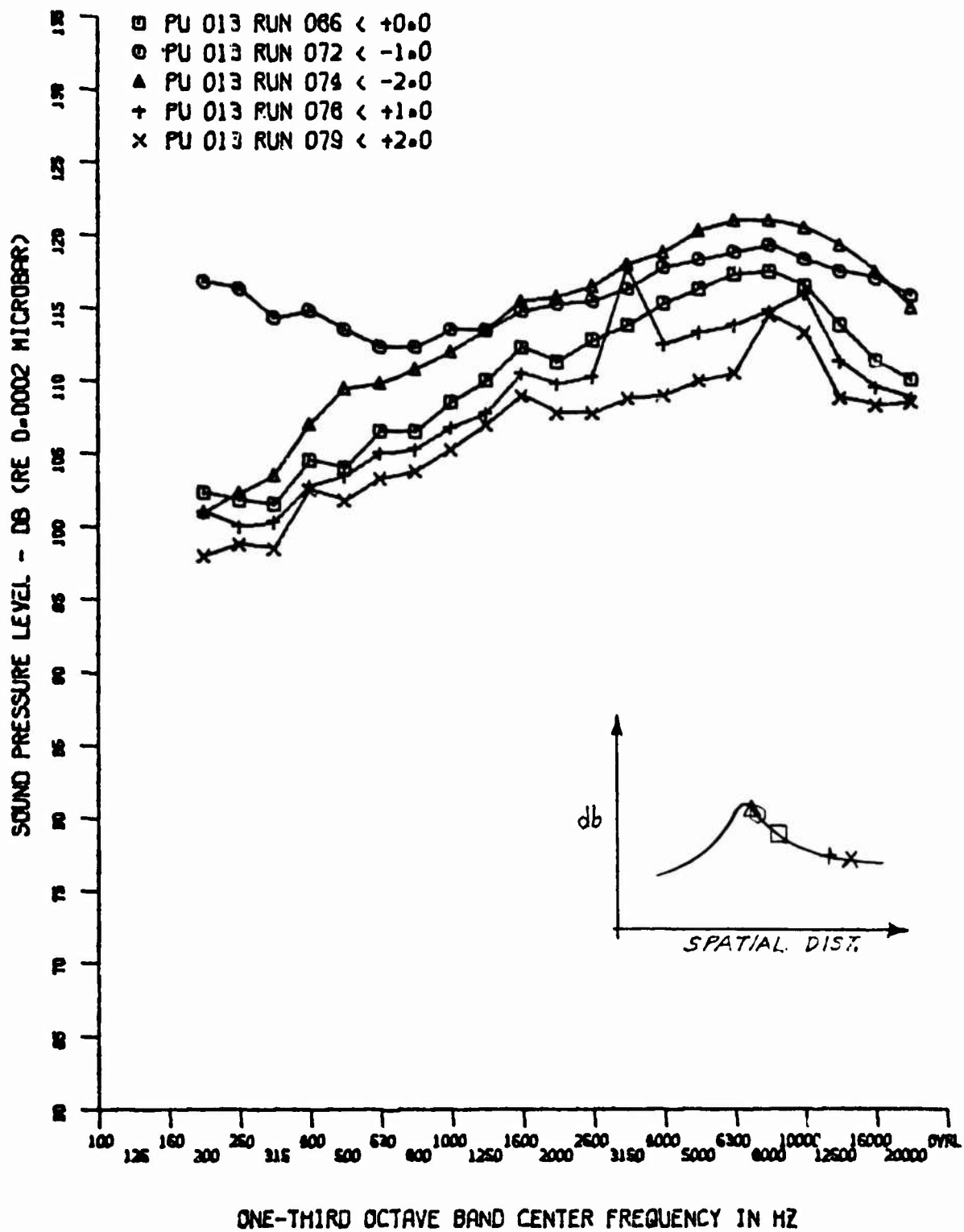
166
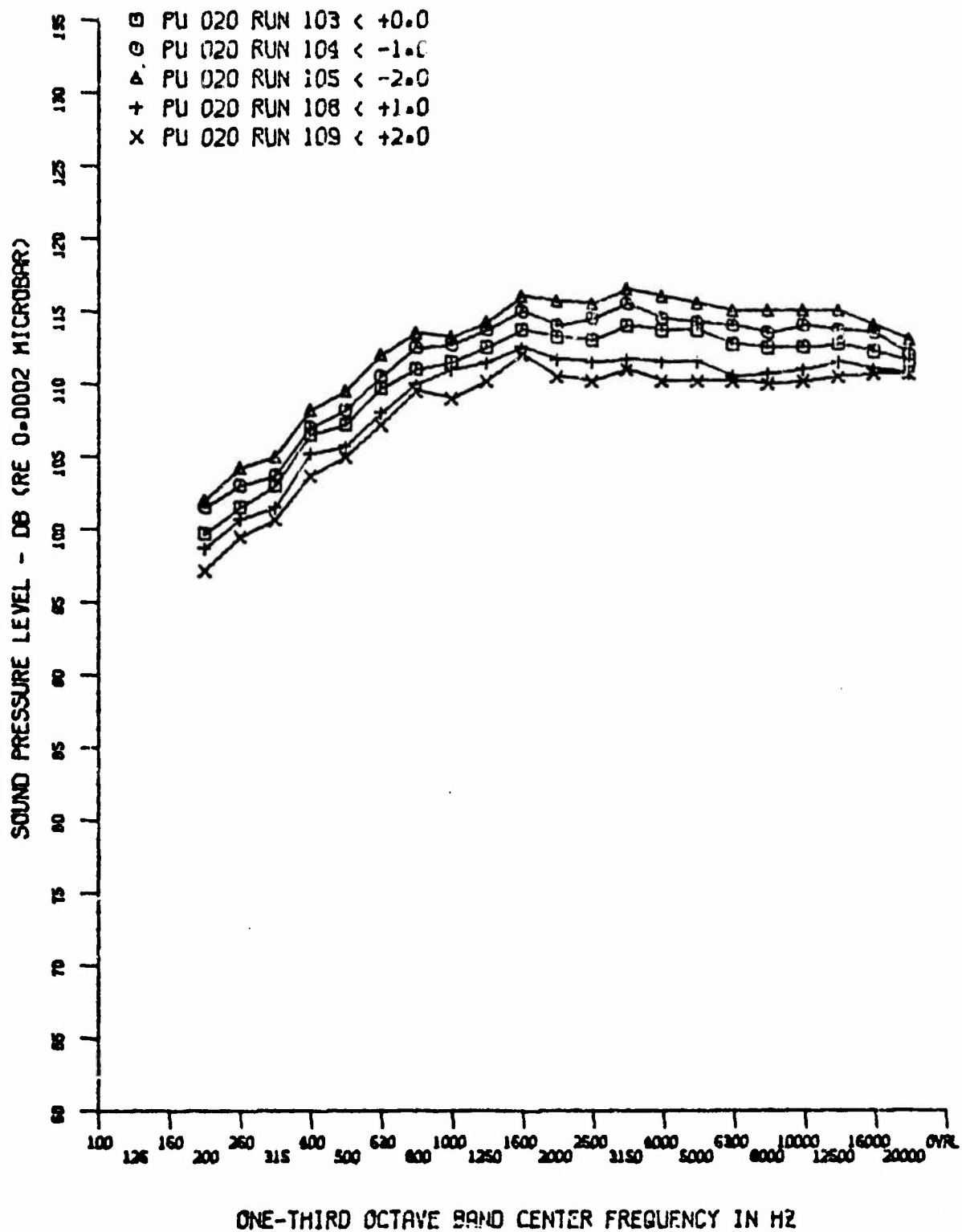
Figure 142. Turbulent Flow Spectra ($M_\infty = 8$, $Re_\infty = 2.8 \times 10^6$, $R_N = 0$)

167
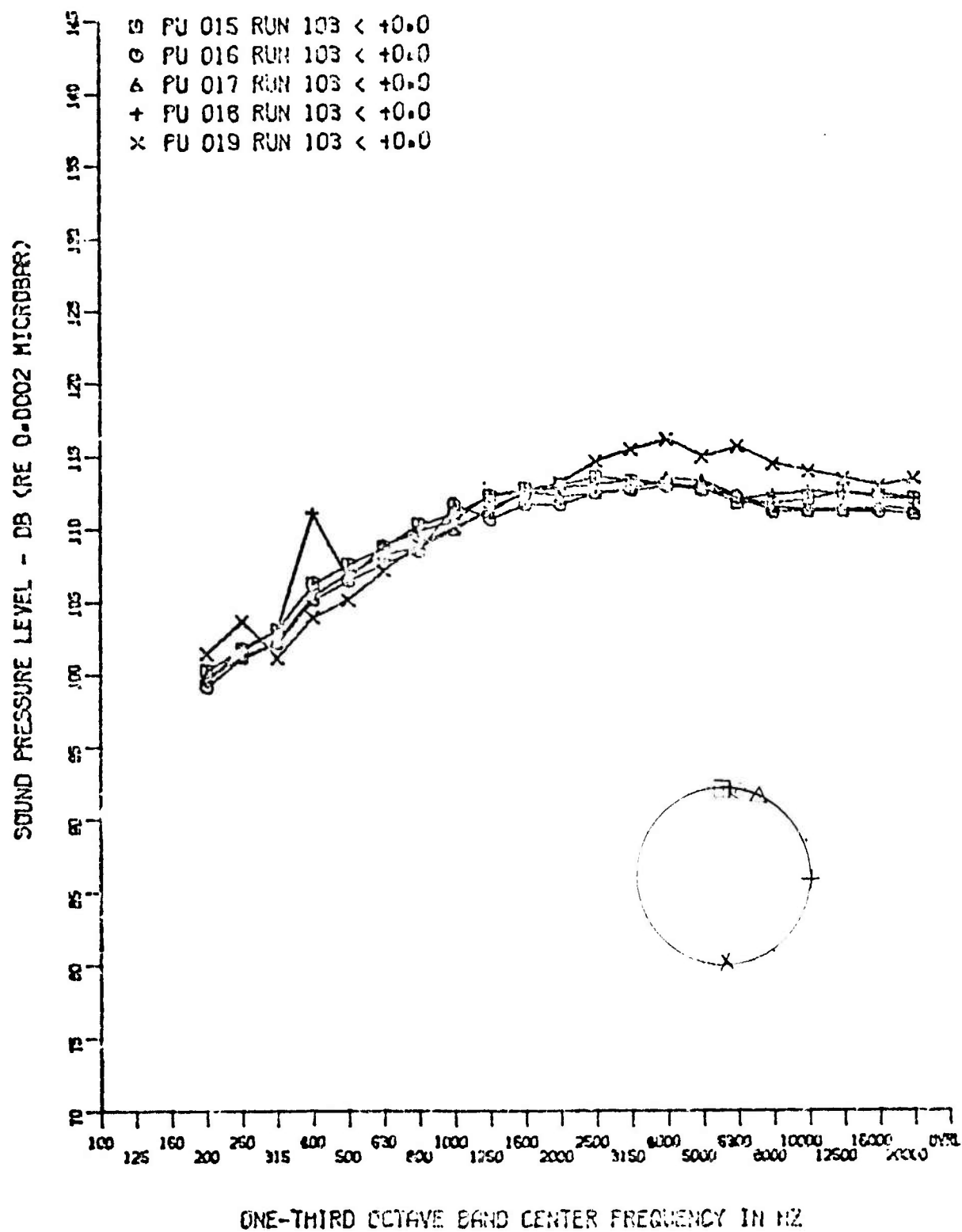
Figure 143. Turbulent Flow Spectra, Circumferential ($M_\infty = 8$, $Re_\infty = 2.8 \times 10^6$, $R_N = 0$)
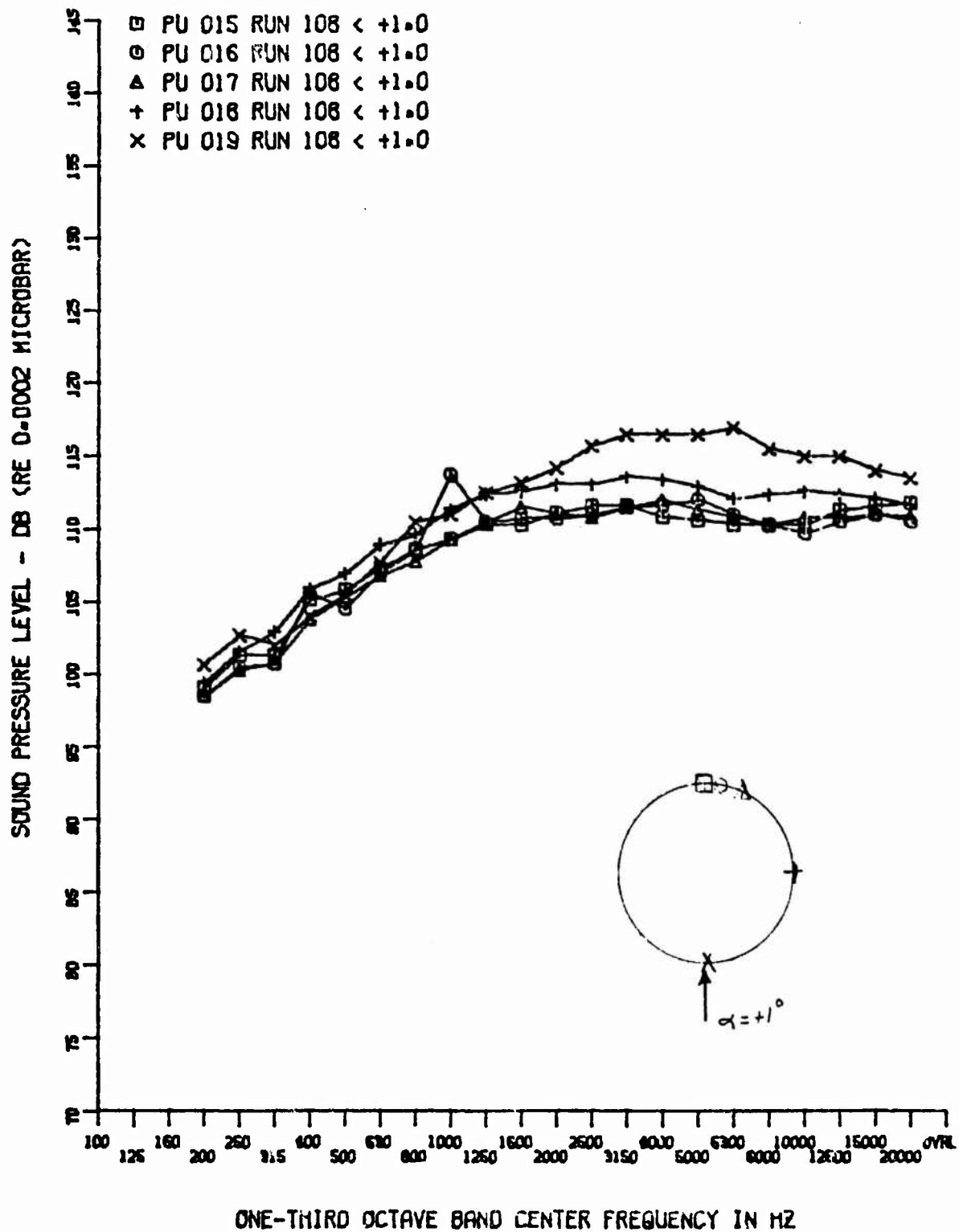
Figure 144. Turbulent Flow Spectra, Circumferential ($M_\infty = 8$, $Re_\infty = 2.8 \times 10^6$, $R_N = 0$)

Figure 145. Turbulent Flow Spectra, (M∞ = 8) Re∞ = 2.8 x 10^6, R_N = 0)
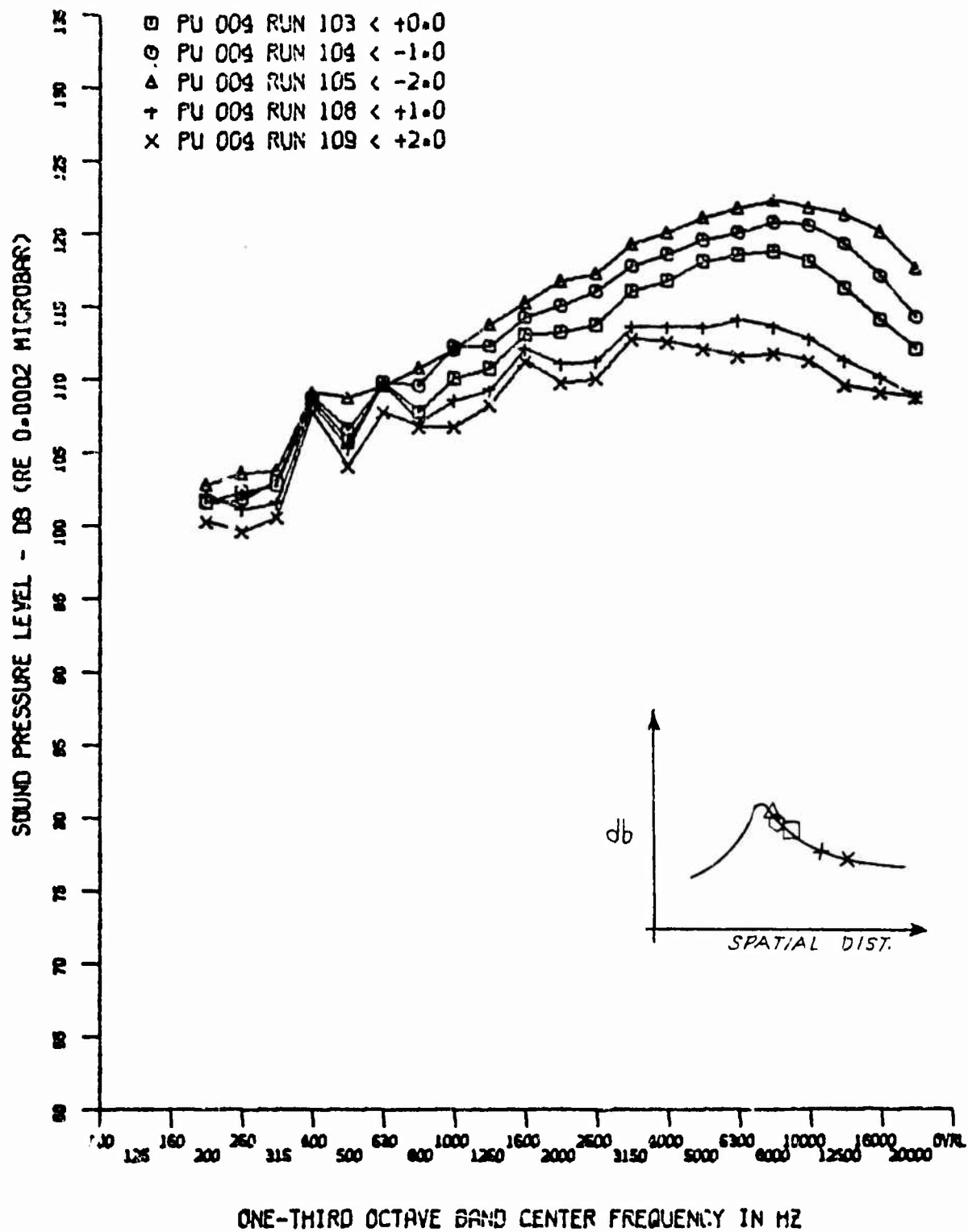
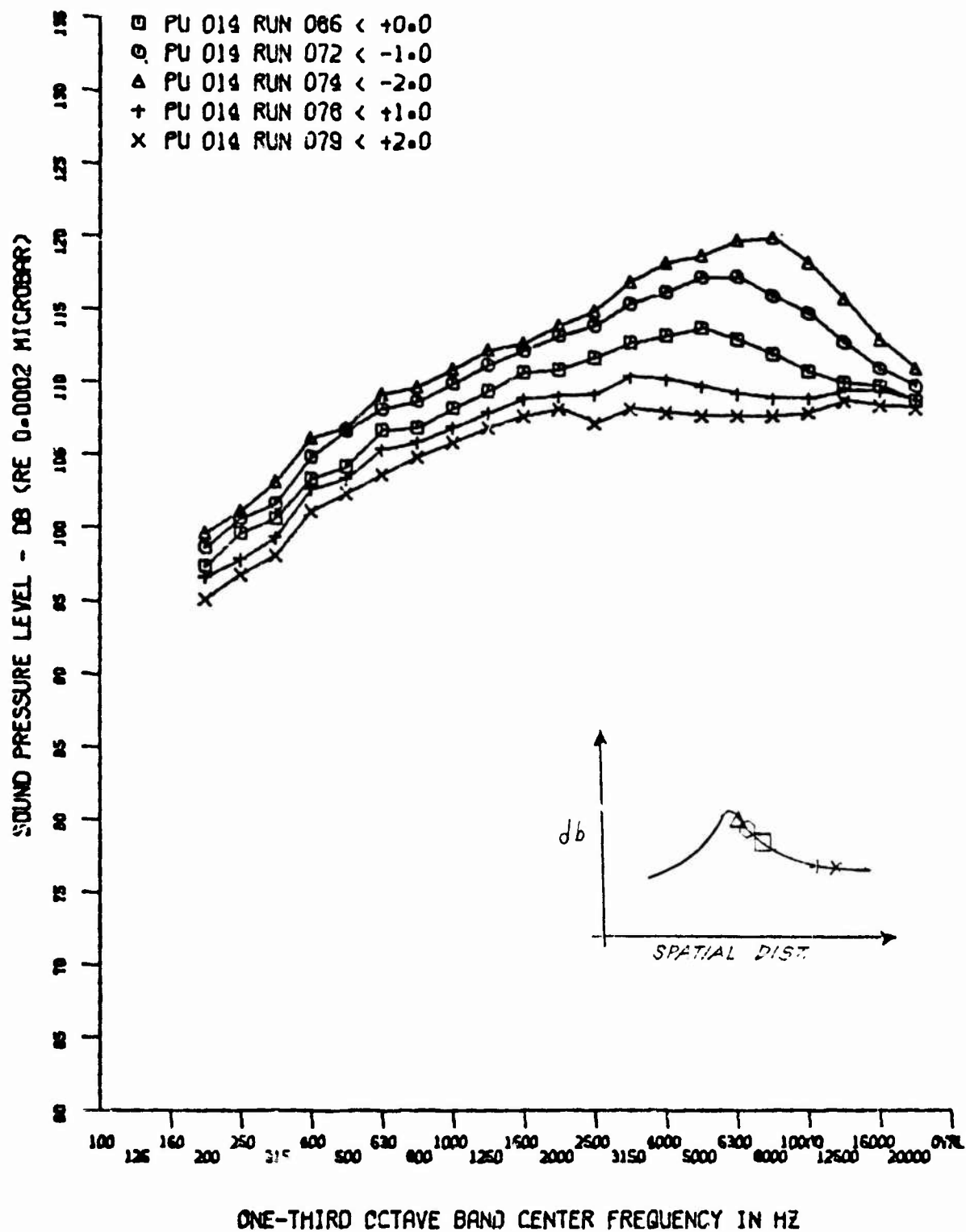Figure 146. Comparison of Spectra in Transition Zone ($M_\infty = 8$, $Re_\infty = 2.8 \times 10^6$, $R_N = 0$)

171
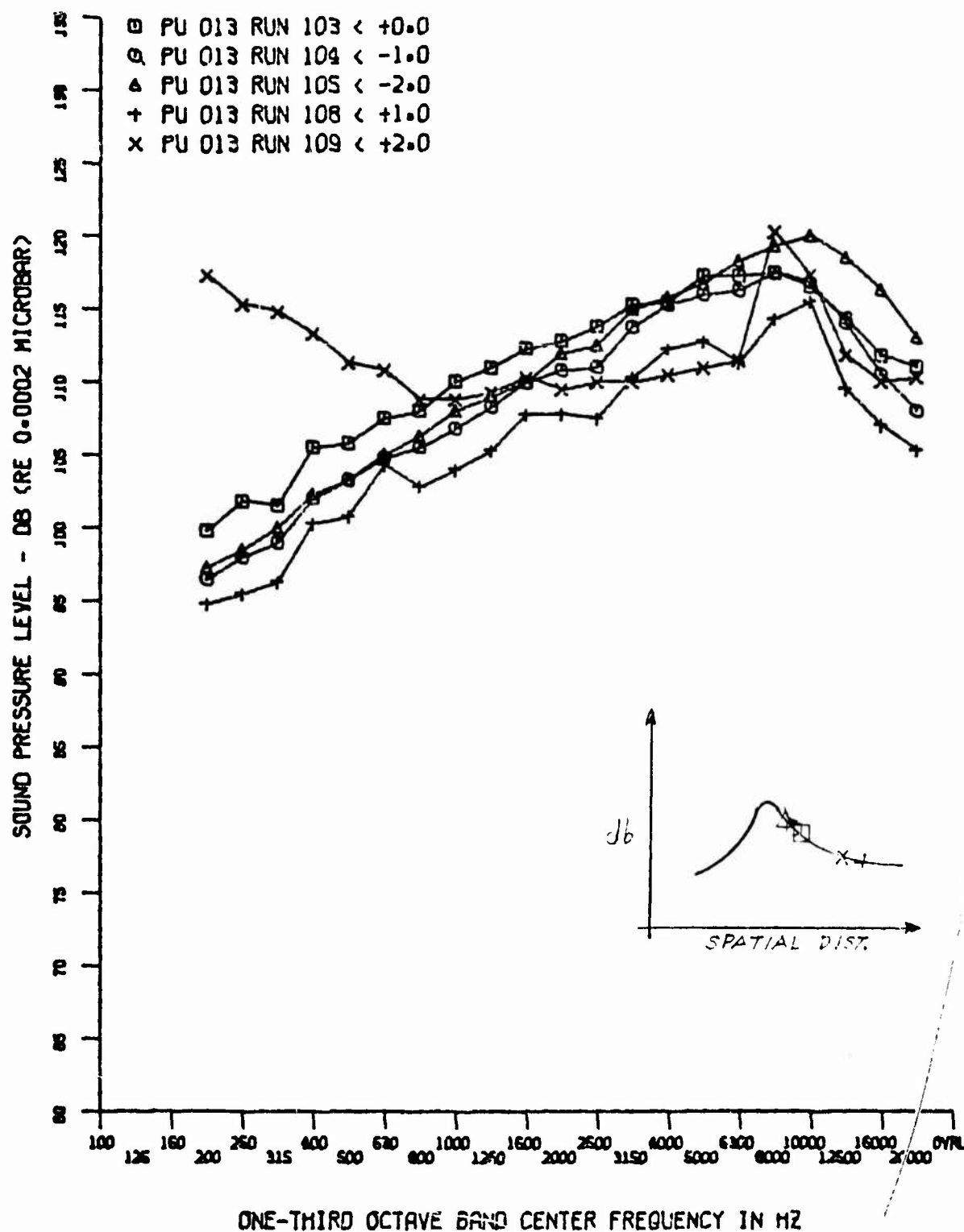
Figure 147. Comparison of Spectra in Transition Zone ($M_\infty = 8$, $Re_\infty = 2.8 \times 10^6$, $R_N = 0$)

172
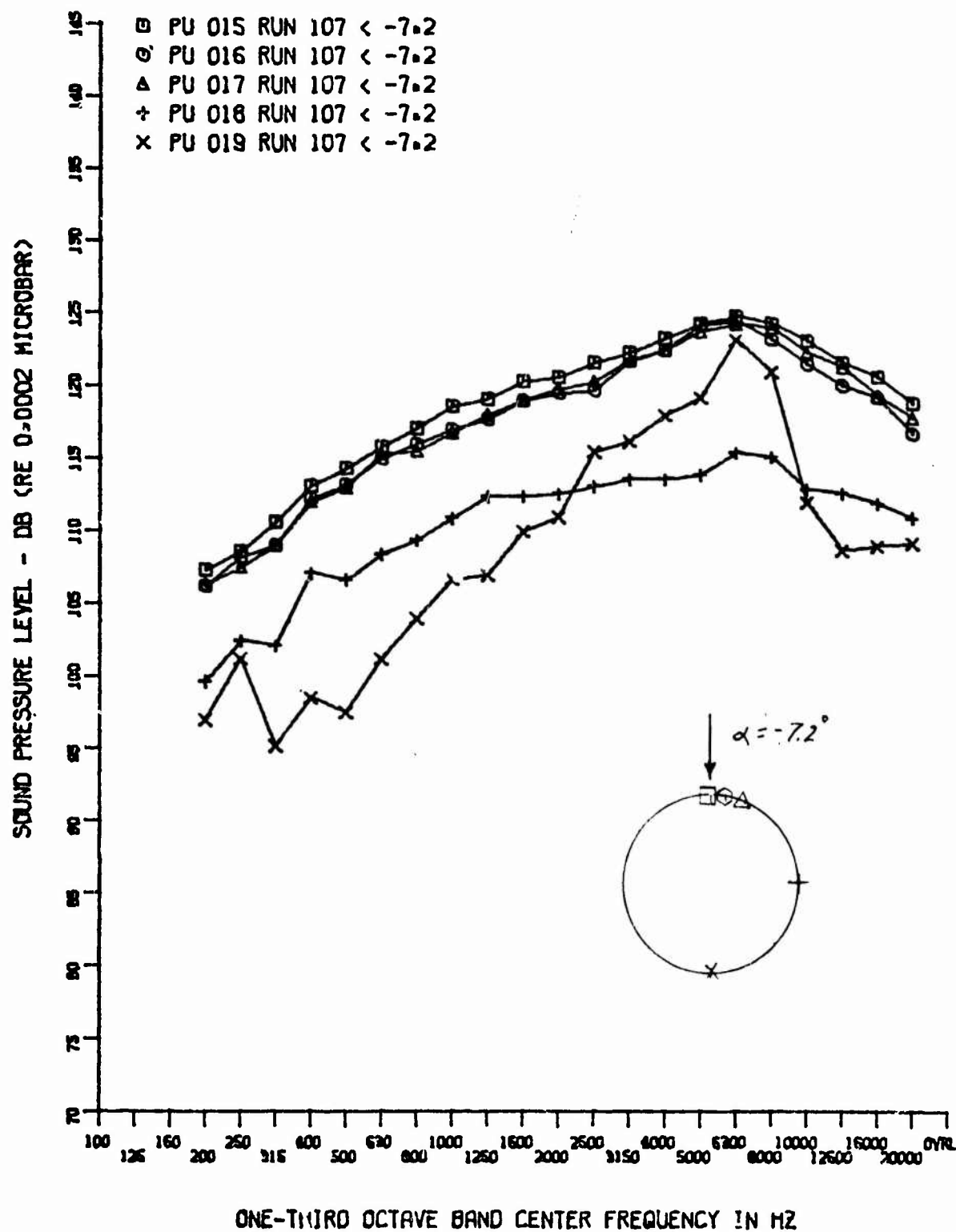
Figure 148. Comparison of Spectra, Circumferential, $\alpha = -7.2$ ($M_\infty = 8$, $Re_\infty = 2.8 \times 10^6$, $R_N = 0$)
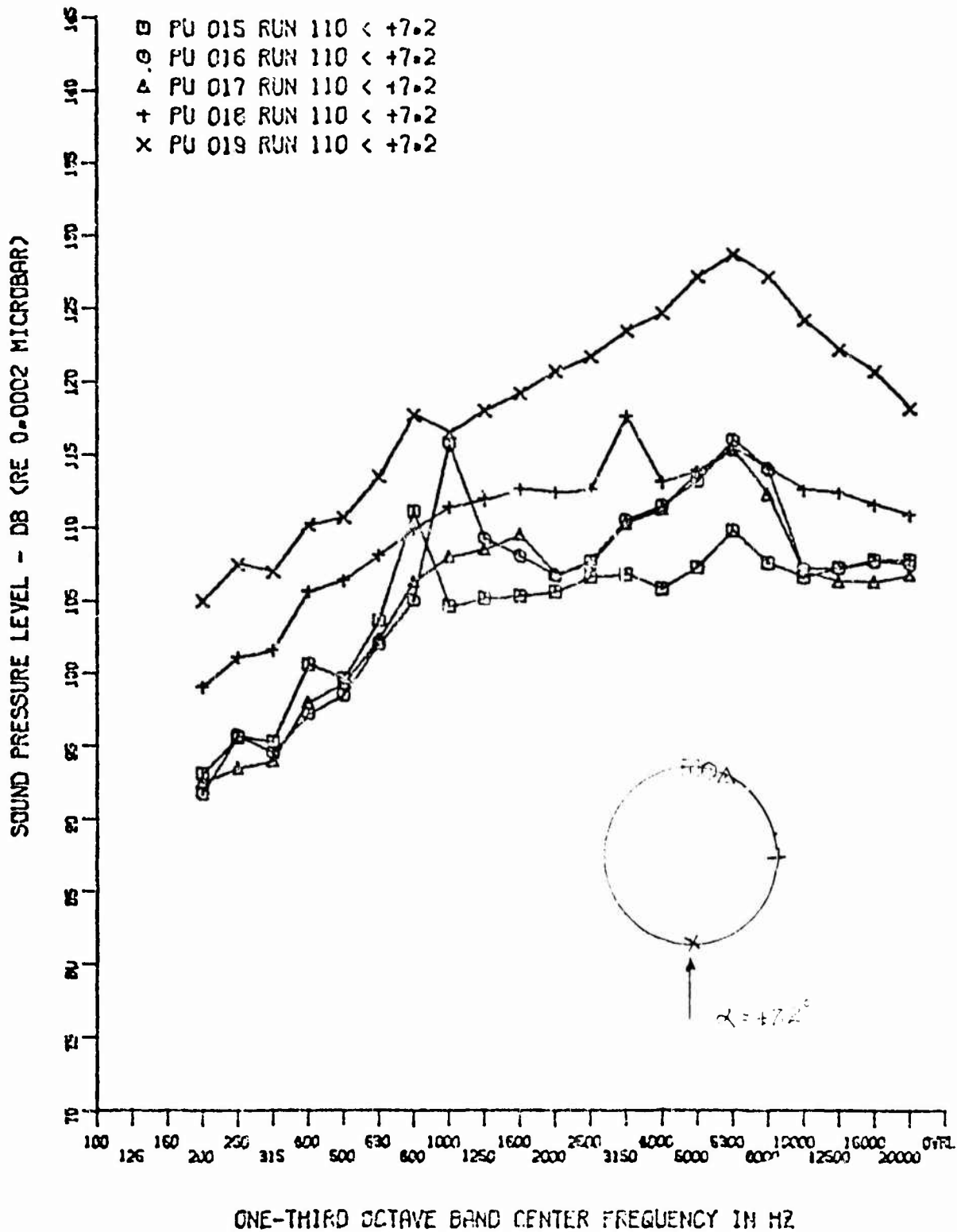
Figure 149. Comparison of Spectra, Circumferential, $\alpha = +7.2$ ($M_\infty = 8$, $Re_\infty = 2.8 \times 10^6$, $R_N = 0$)

174
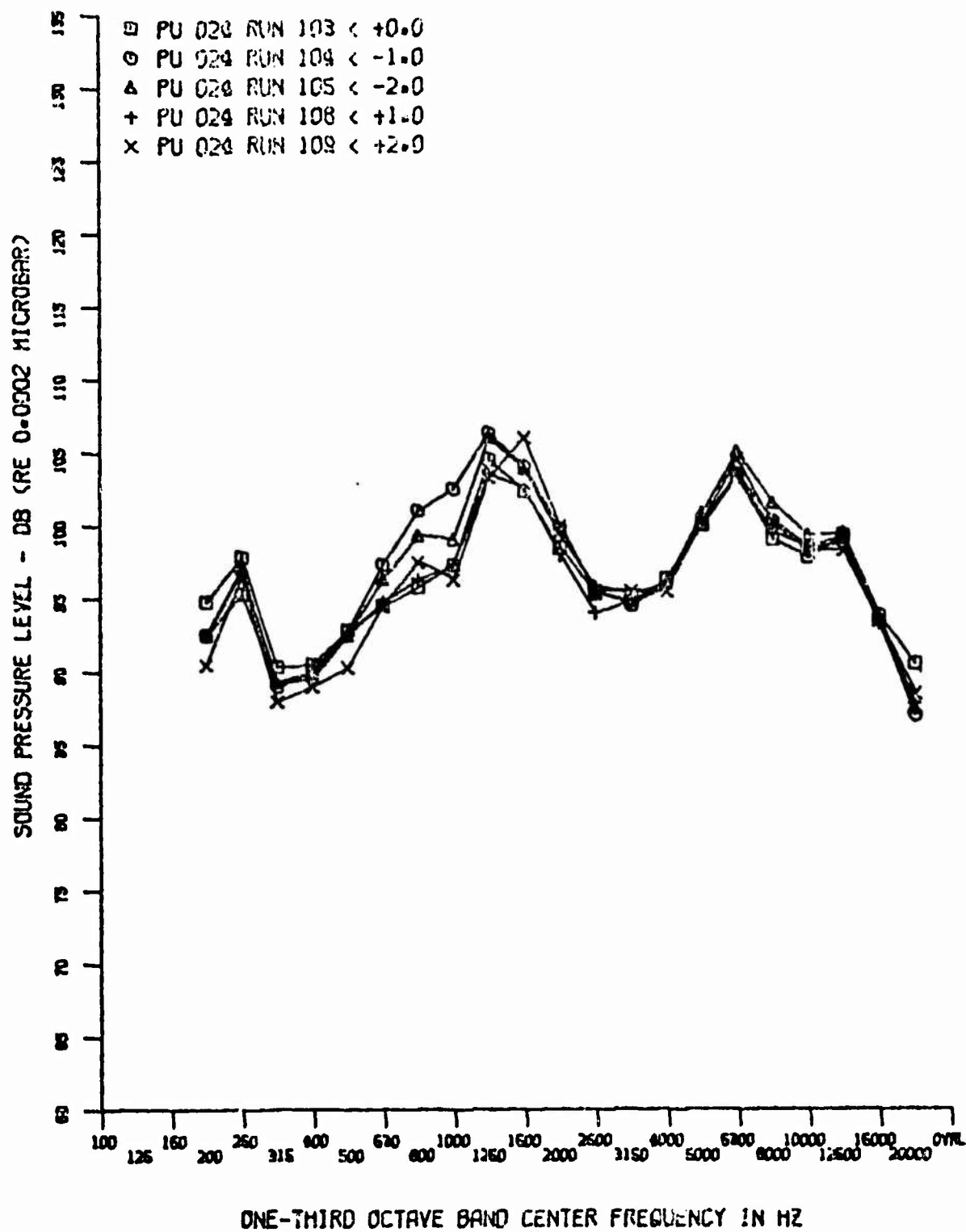
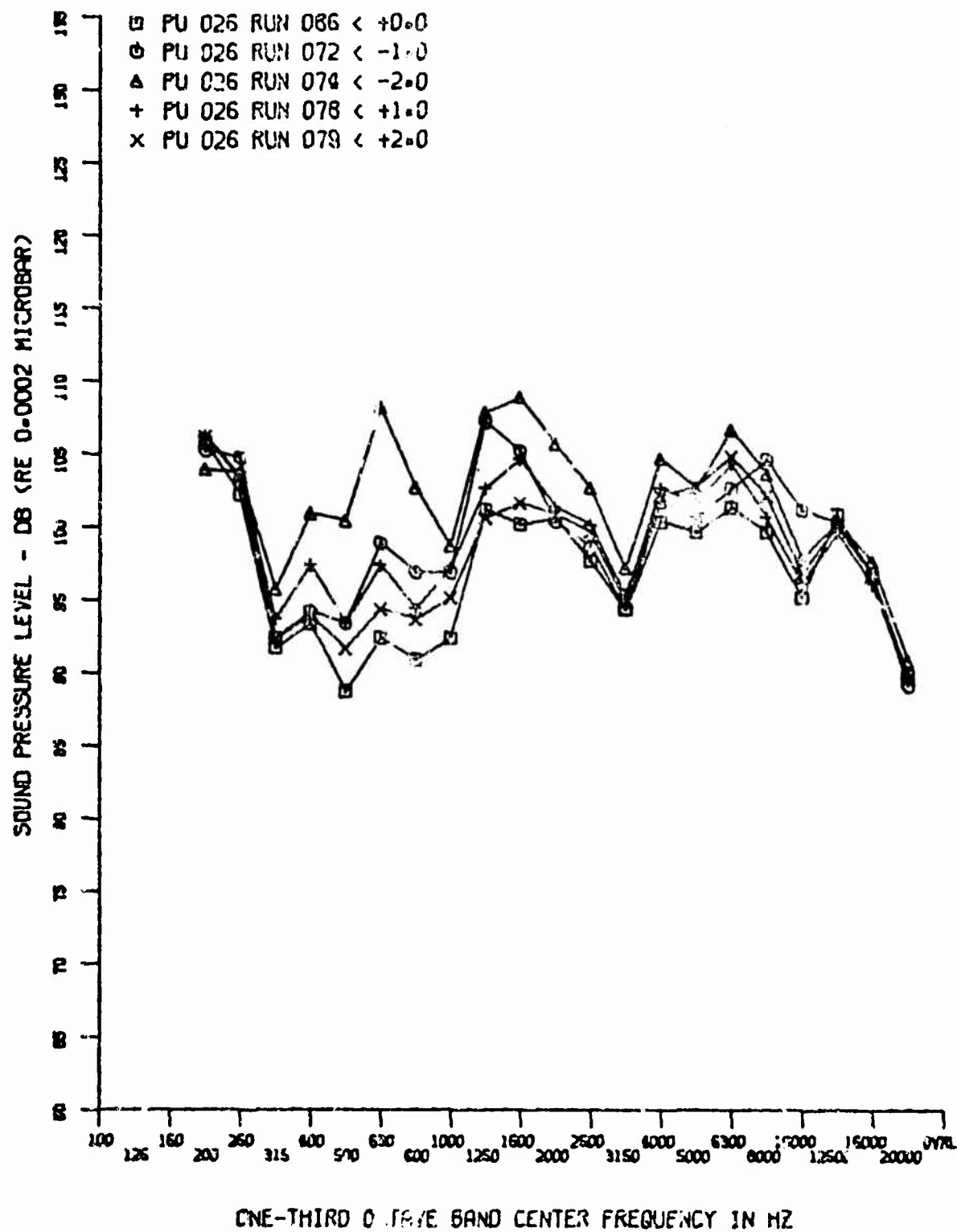Figure 150. Base Spectra at Various ($M_\infty = 8$, $Re_\infty = 2.8 \times 10^6$, $R_N = 0$)
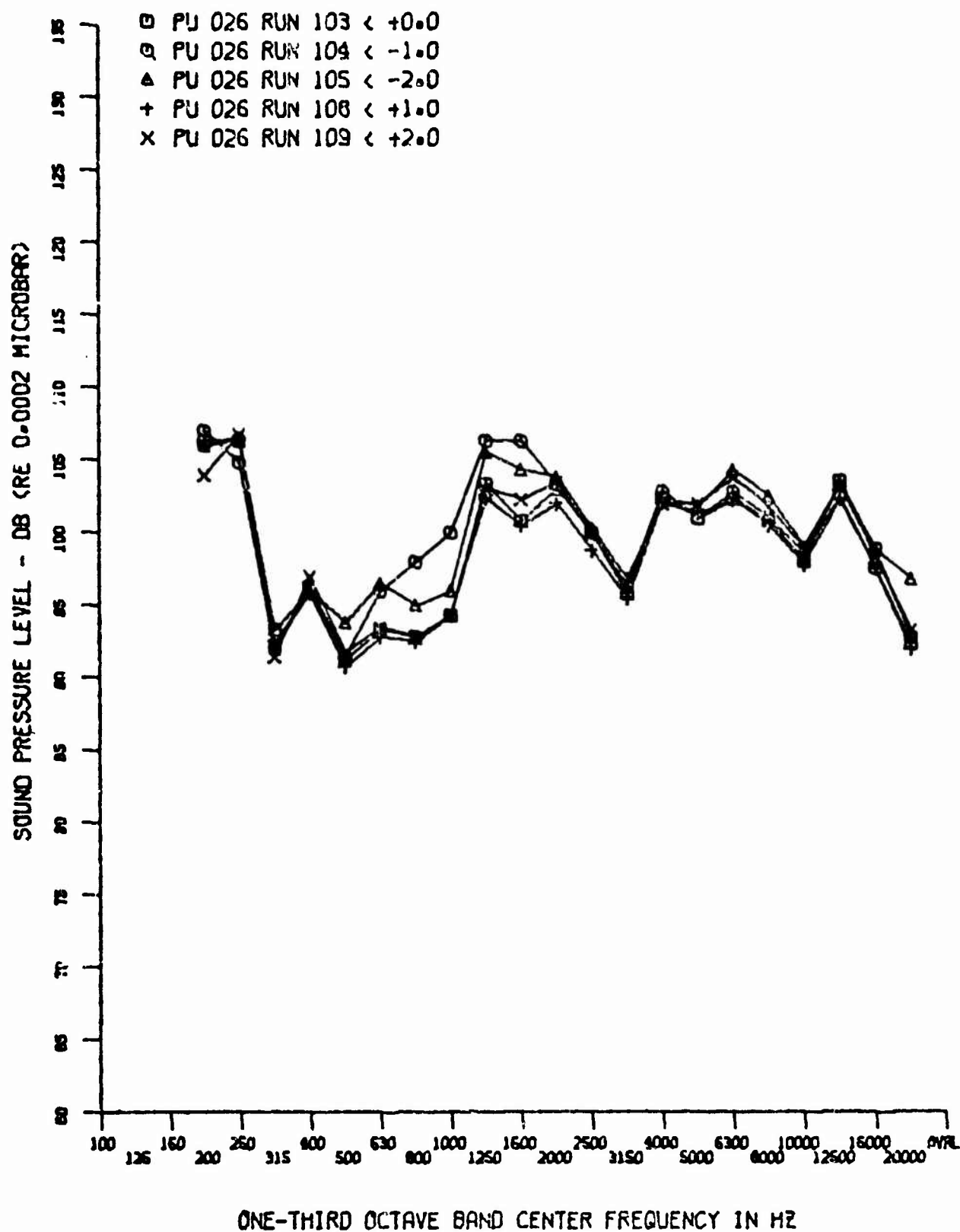
Figure 151. Base Spectra at Various ($M_\infty = 8$, $Re_\infty = 2.8 \times 10^6$, $R_N = 0$)

176
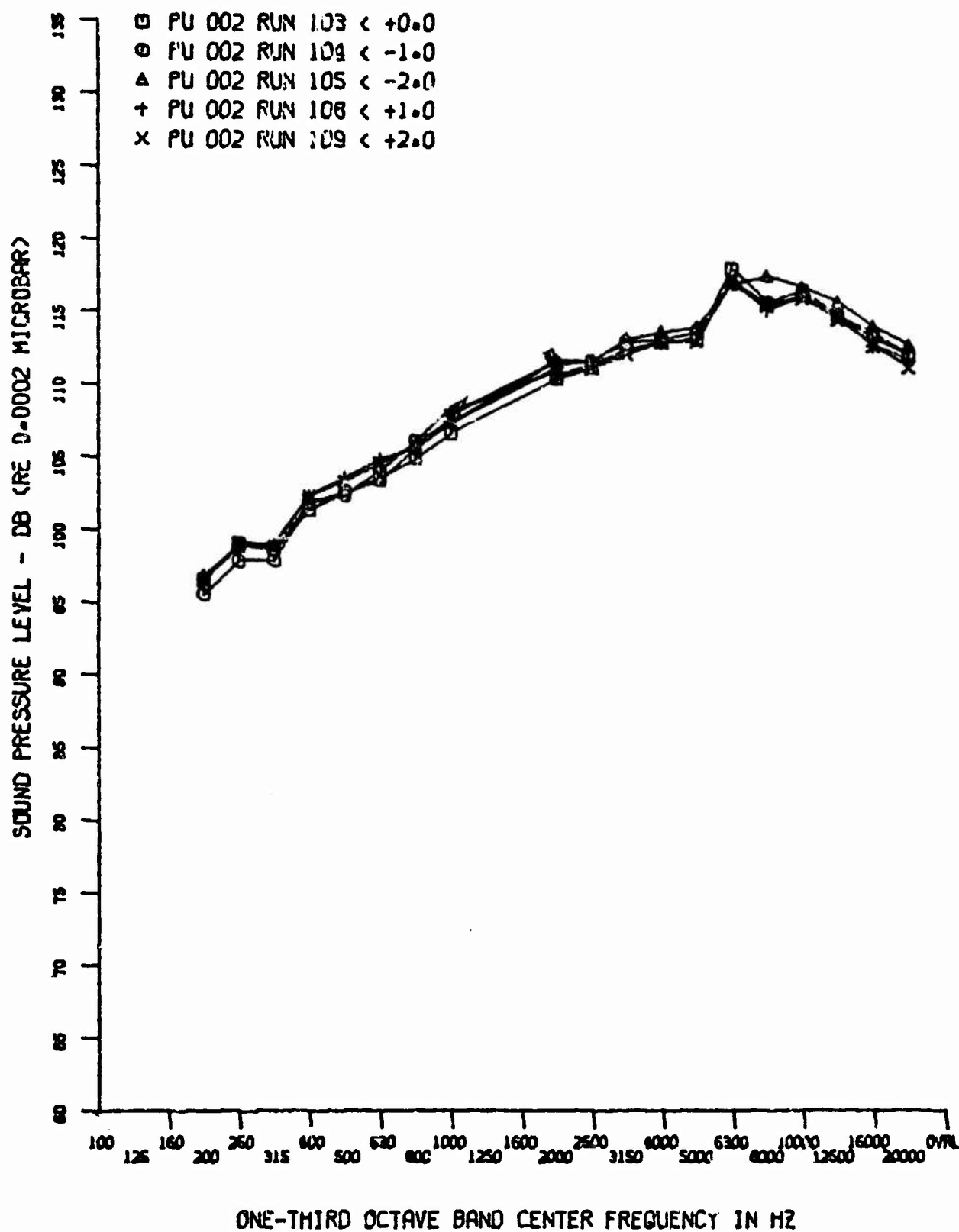
Figure 152. Tunnel Tare Noise ($M_\infty = 8$, $Re_\infty = 2.8 \times 10^6$, $R_N = 0$)

177
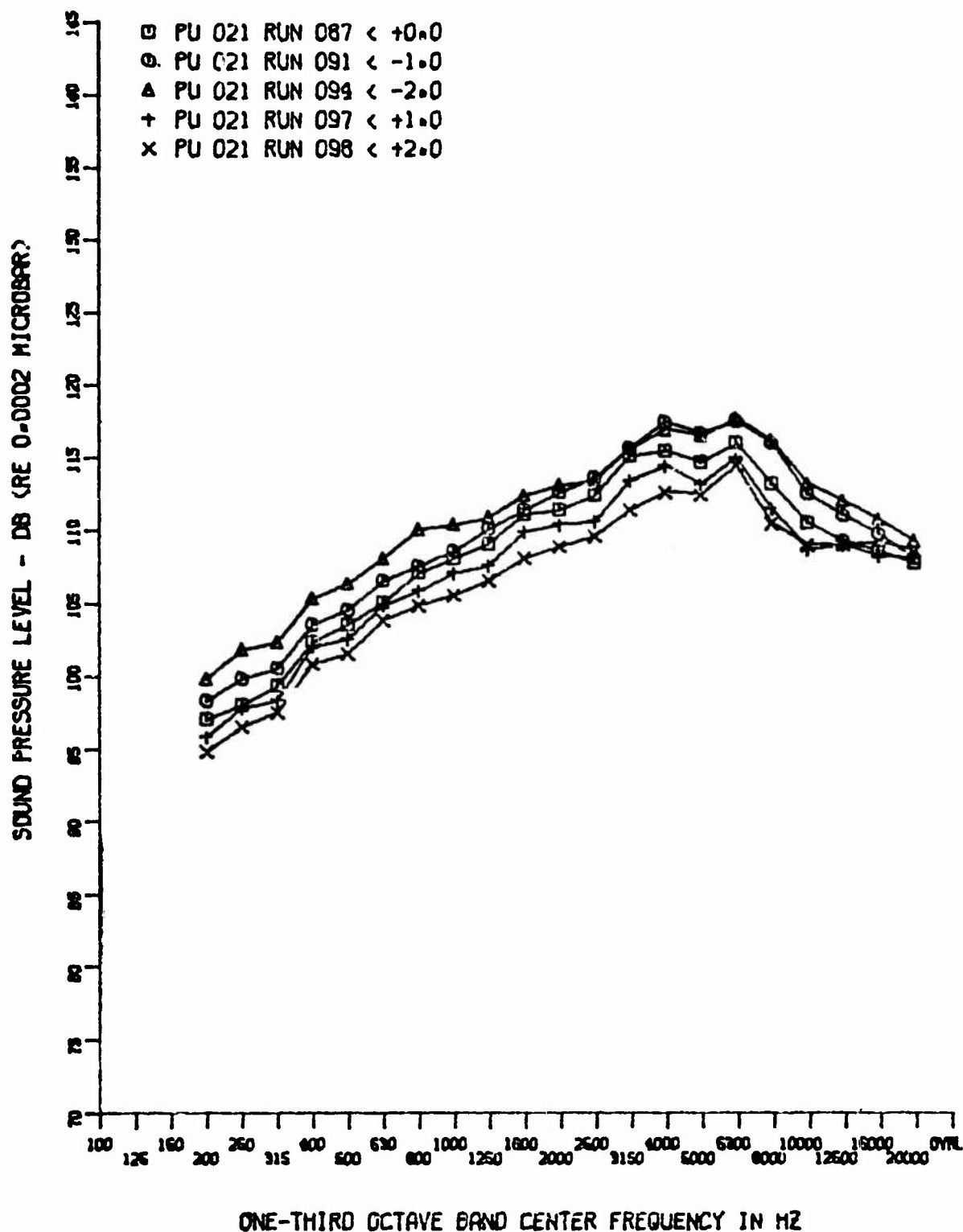
Figure 153. Turbulent Flow Spectra ($M_\infty = 8$, $Re_\infty = 2.2 \times 10^6$, $R_N = 0.055$)

178
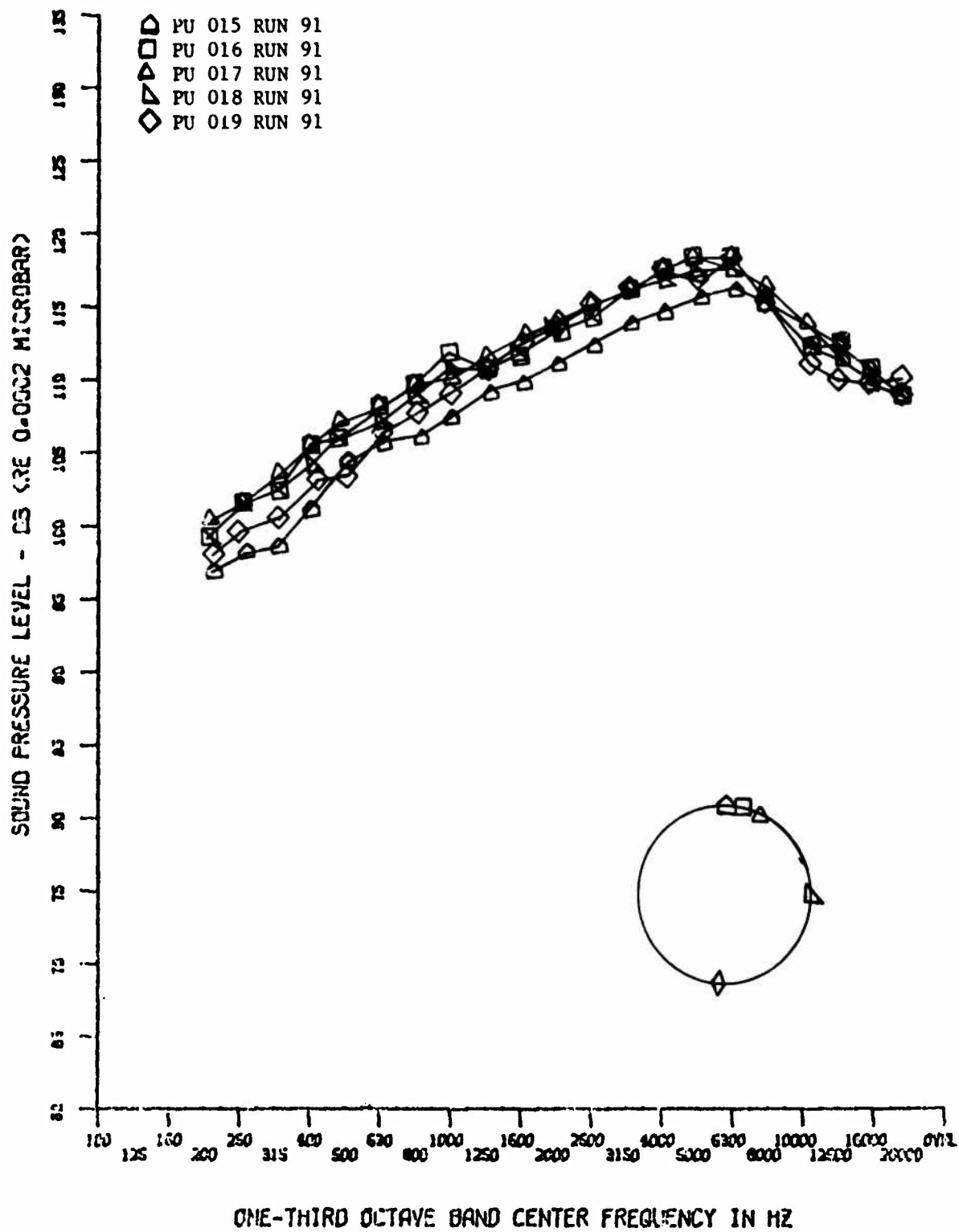
ONE-THIRD OCTAVE BAND CENTER FREQUENCY IN HZ

Figure 154. Turbulent Flow Spectra, Circumferential ($M_\infty = 8$, $Re_\infty = 2.2 \times 10^6$, $R_N = 0.055$)

179
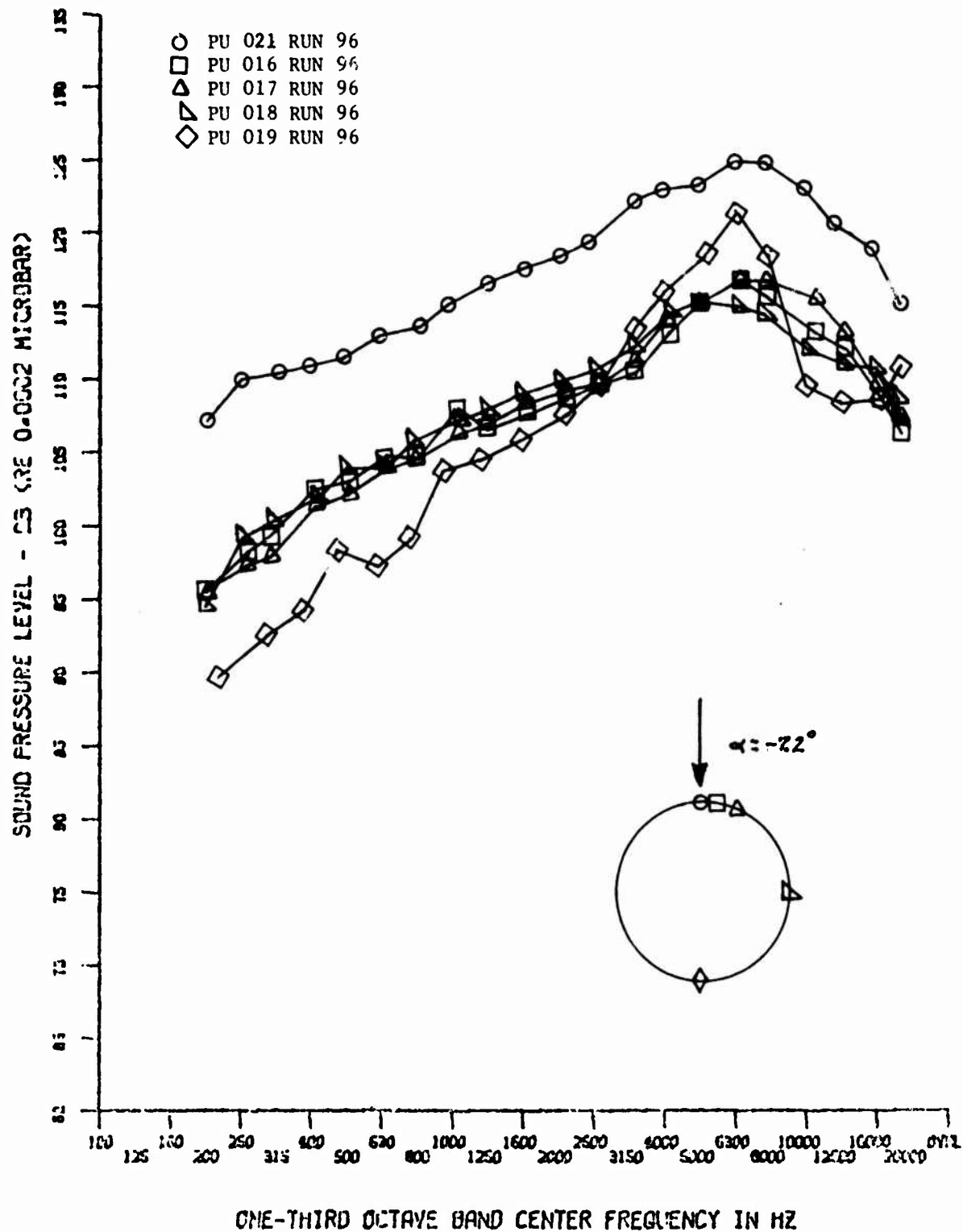
Figure 155. Comparison of Spectra, Circumferential, $\alpha = -7.2$ ($M_\infty = 8$, $Re_\infty = 2.2 \times 10^6$, $R_N = 0.055$)

180
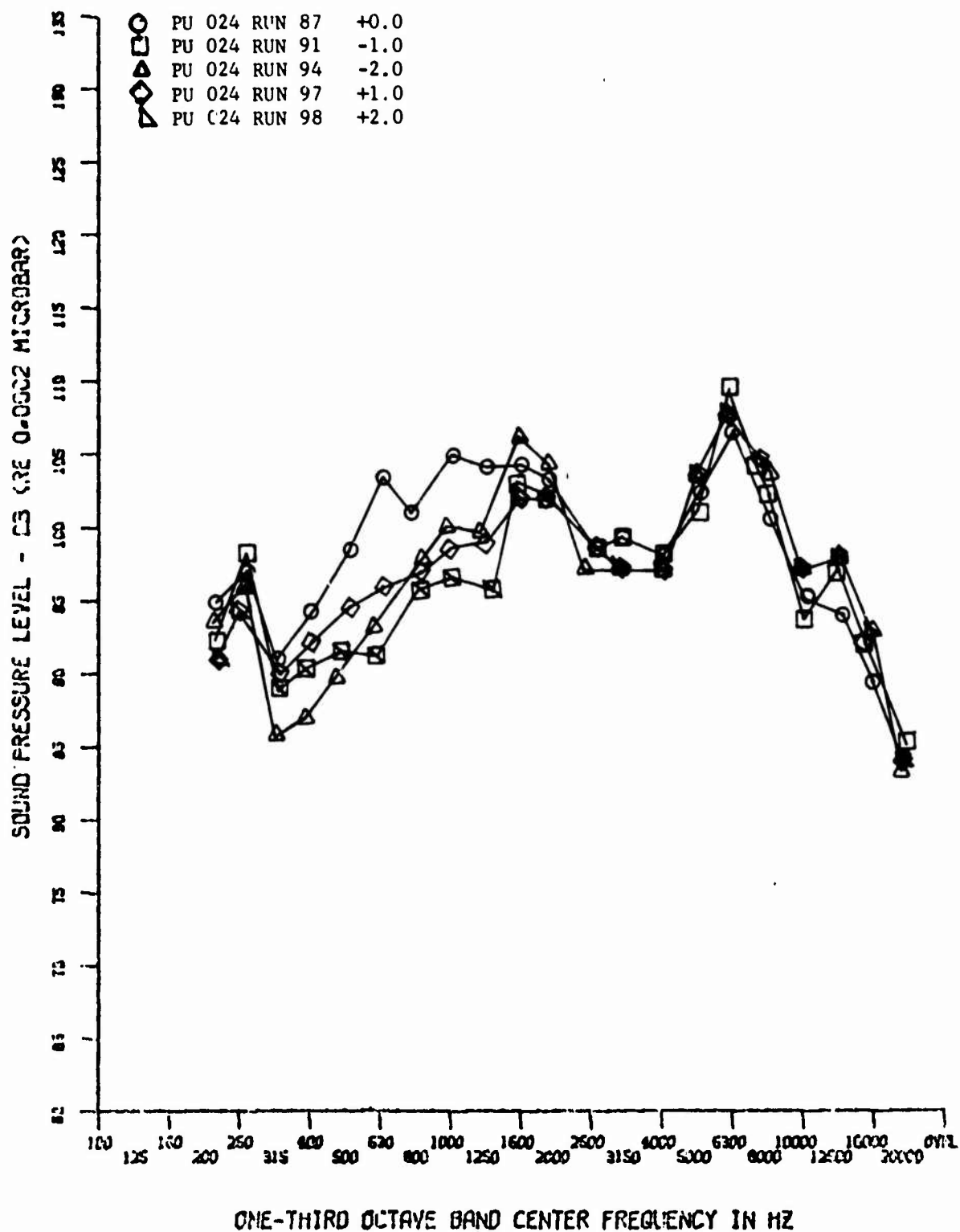
Figure 156.   Base Spectra at Various ($M_\infty = 8$, $Re_\infty = 2.2 \times 10^6$, $R_N = 0.055$)
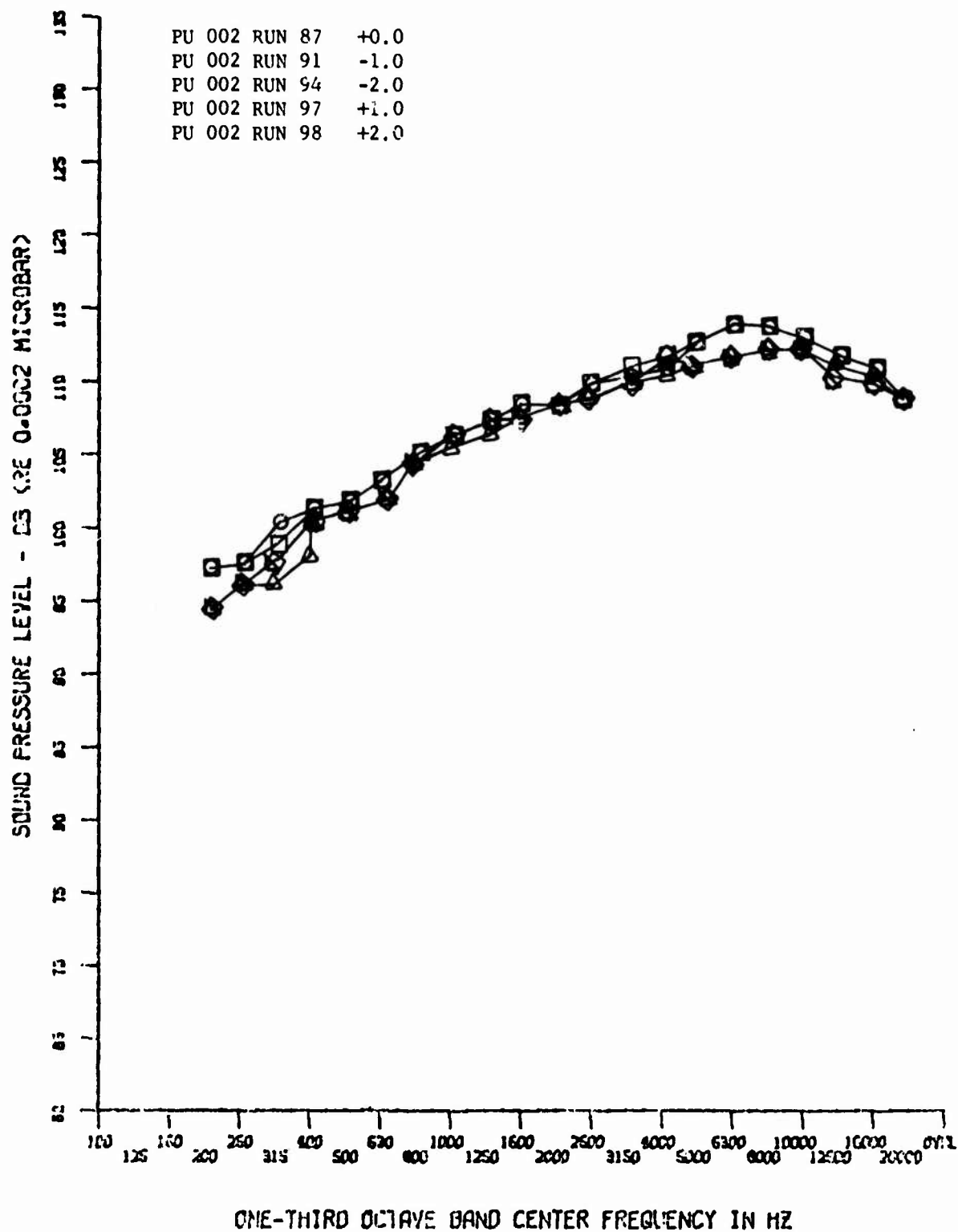
Figure 157. Tunnel Tare Noise ($M_\infty = 8$, $Re_\infty = 2.2 \times 10^6$, $R_N = 0.055$)
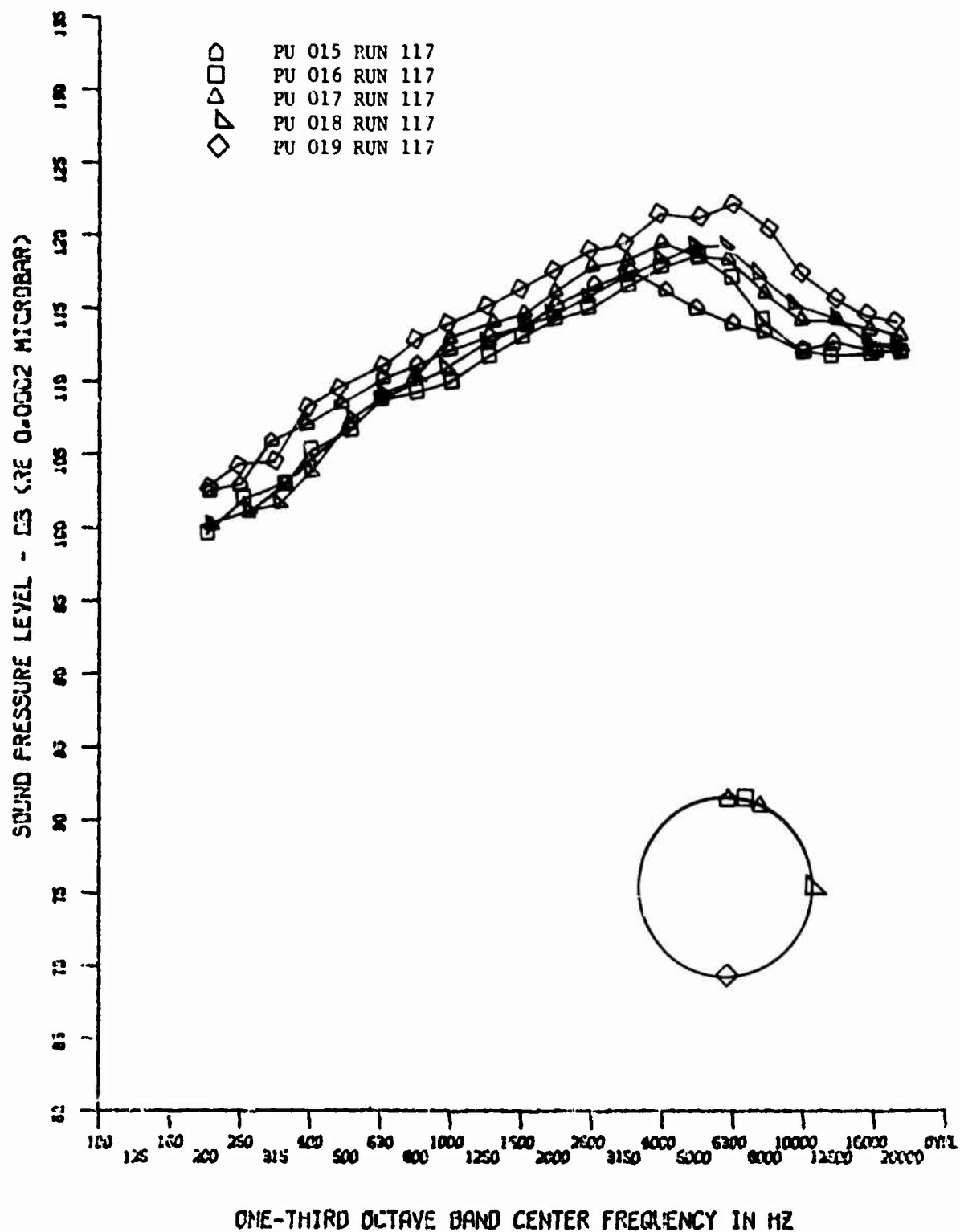
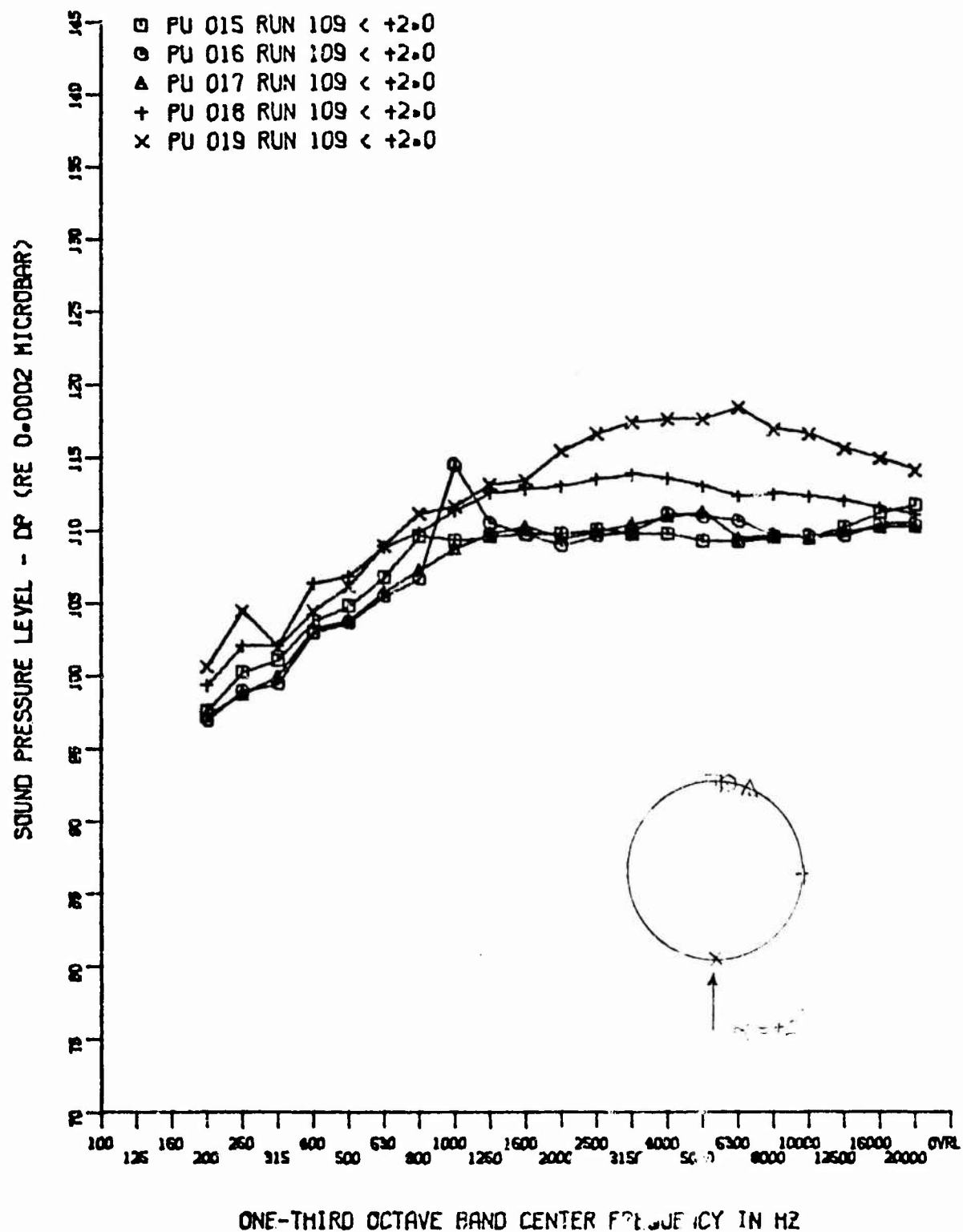Figure 158. Turbulent Flow Spectra, Circumferential ($M_\infty = 8$, $Re_\infty = 3.25 \times 10^6$, $R_N = 0.11$)

Figure 159. Comparison of Spectra, Circumferential, α = -7.2 (M_∞ = 8, Re_∞ = 3.25 x 10^6, R_N = 0.11)
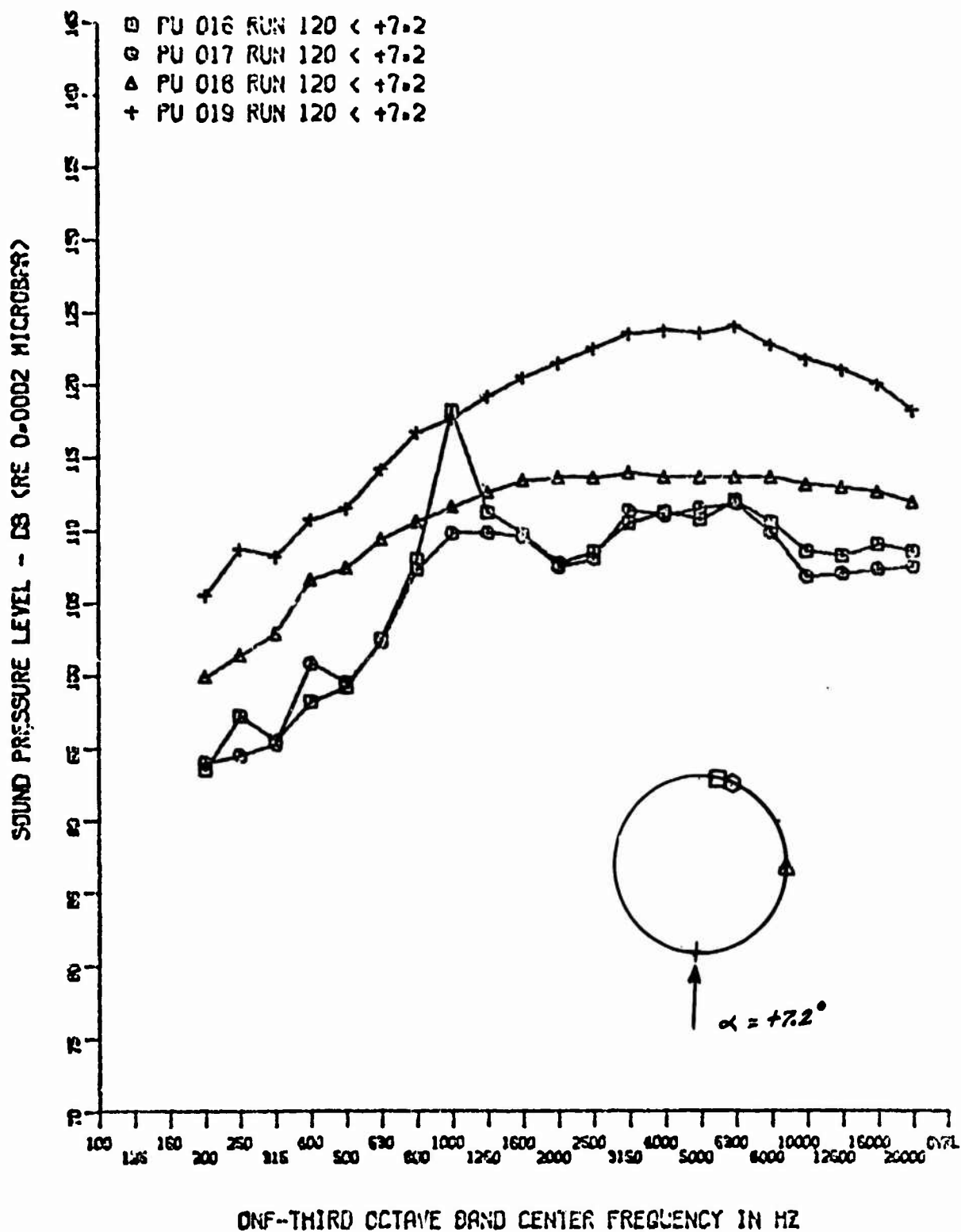
Figure 160. Comparison of Spectra, Circumferential, = +7.2 ($M_\infty = 8$, $Re_\infty = 3.25 \times 10^6$, $R_N = 0.11$)

Figure 161. Base Spectra at Various ($M_\infty = 8$, $Re_\infty = 3.25 \times 10^6$, $R_N = 0.11$)

186

Figure 162. Tunnel Tare Noise ($M_\infty = 8$, $Re_\infty = 3.25 \times 10^6$, $R_N = 0.11$)

187

Figure 163. Comparison of Spectra in Transition Zone ($M_\infty = 10$, $Re_\infty = 1.4 \times 10^6$, $R_N = 0$)

Figure 164. Comparison of Spectra in Transition Zone ($M_\infty = 10$, $Re_\infty = 1.4 \times 10^6$, $R_N = 0$)

189

Figure 165. Base Spectra at Various ($M_\infty = 10$, $Re_\infty = 1.4 \times 10^6$, $R_N = 0$)

Figure 166. Tunnel Tare Noise ($M_\infty = 10$, $Re_\infty = 1.4 \times 10^6$, $R_N = 0$)

191
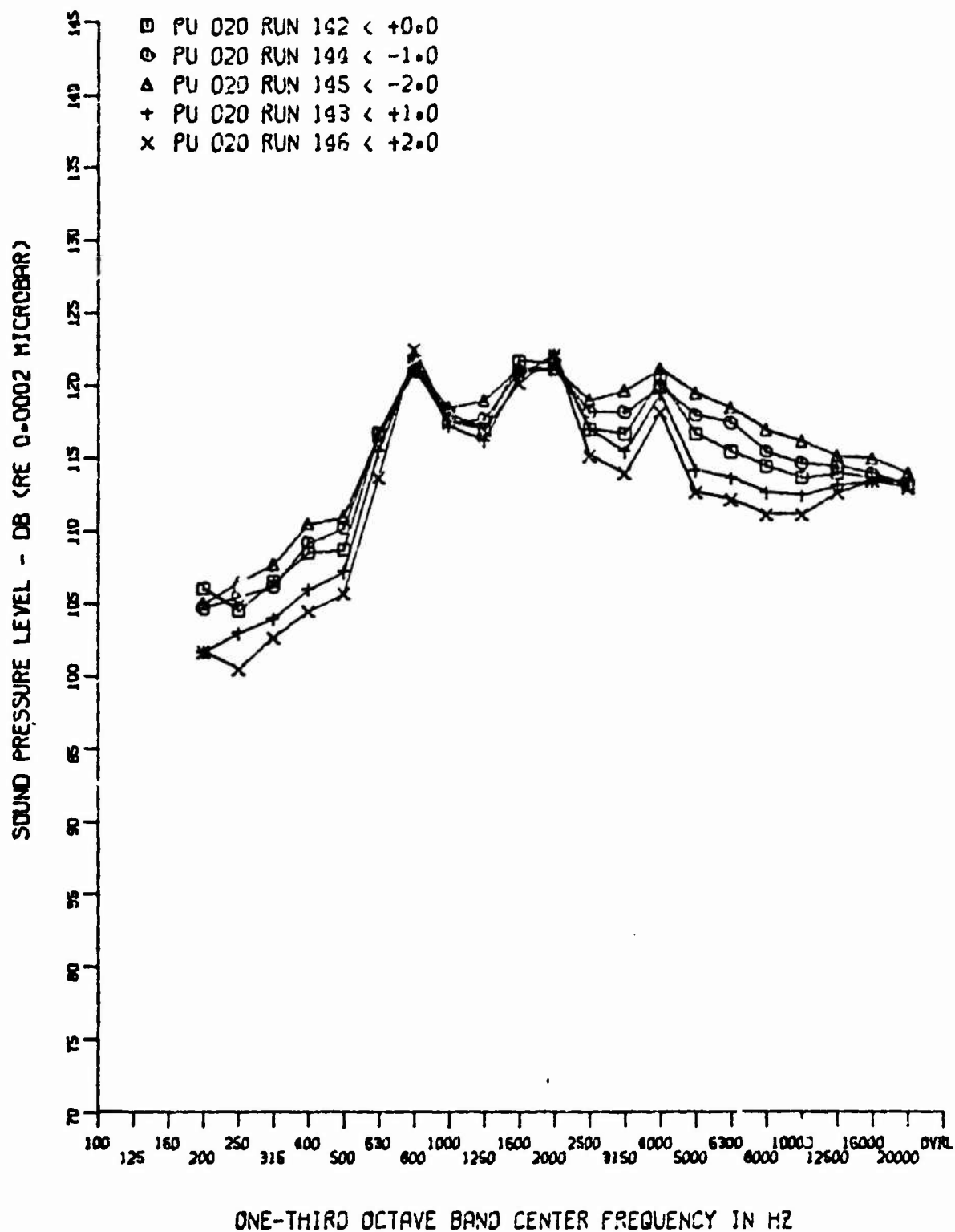
Figure 167. Turbulent Flow Spectra ($M_\infty = 10$, $Re_\infty = 2.2 \times 10^6$, $R_N = 0$)

192
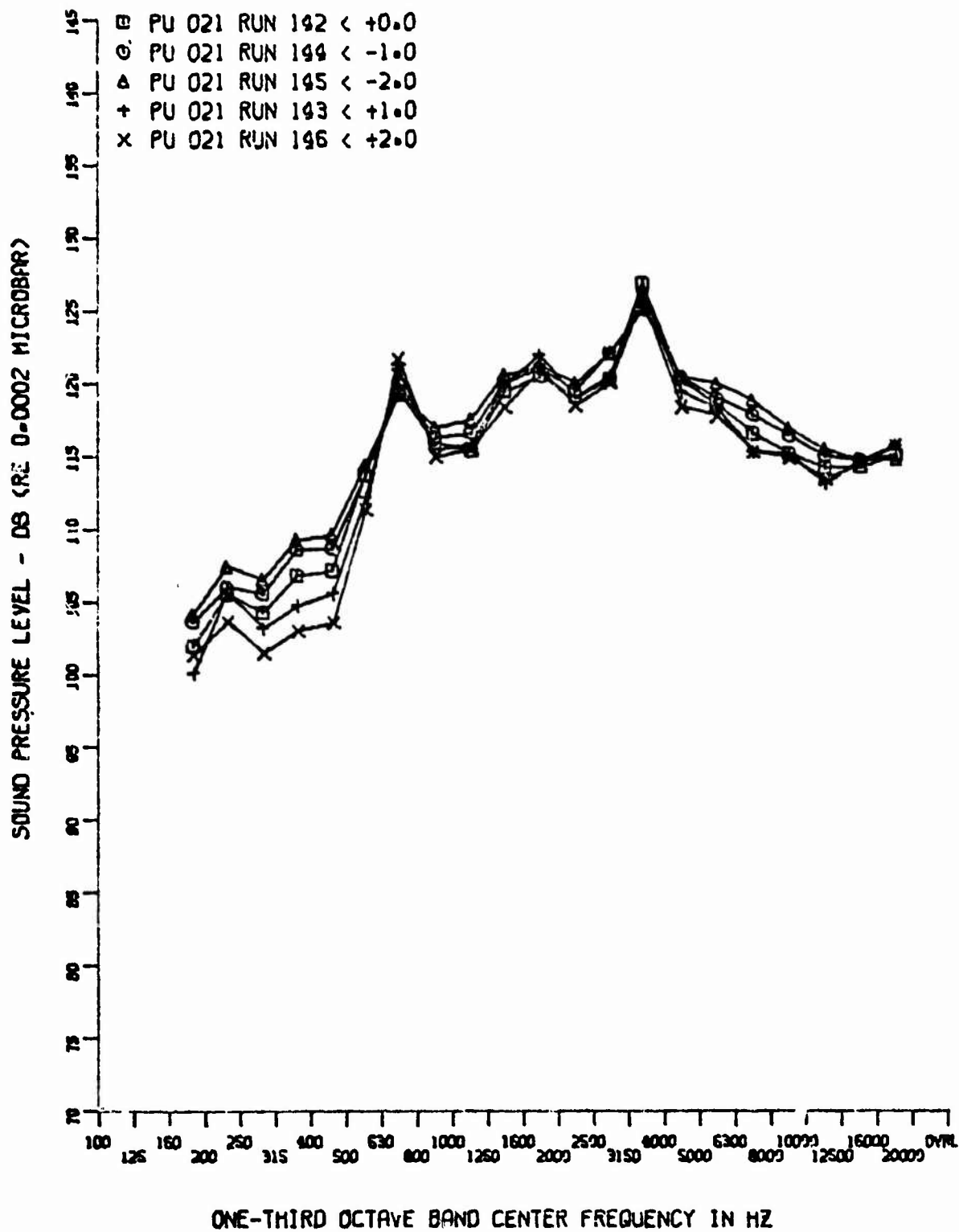
Figure 168. Turbulent Flow Spectra ($M_\infty = 10$, $Re_\infty = 2.2 \times 10^6$, $R_N = 0$)
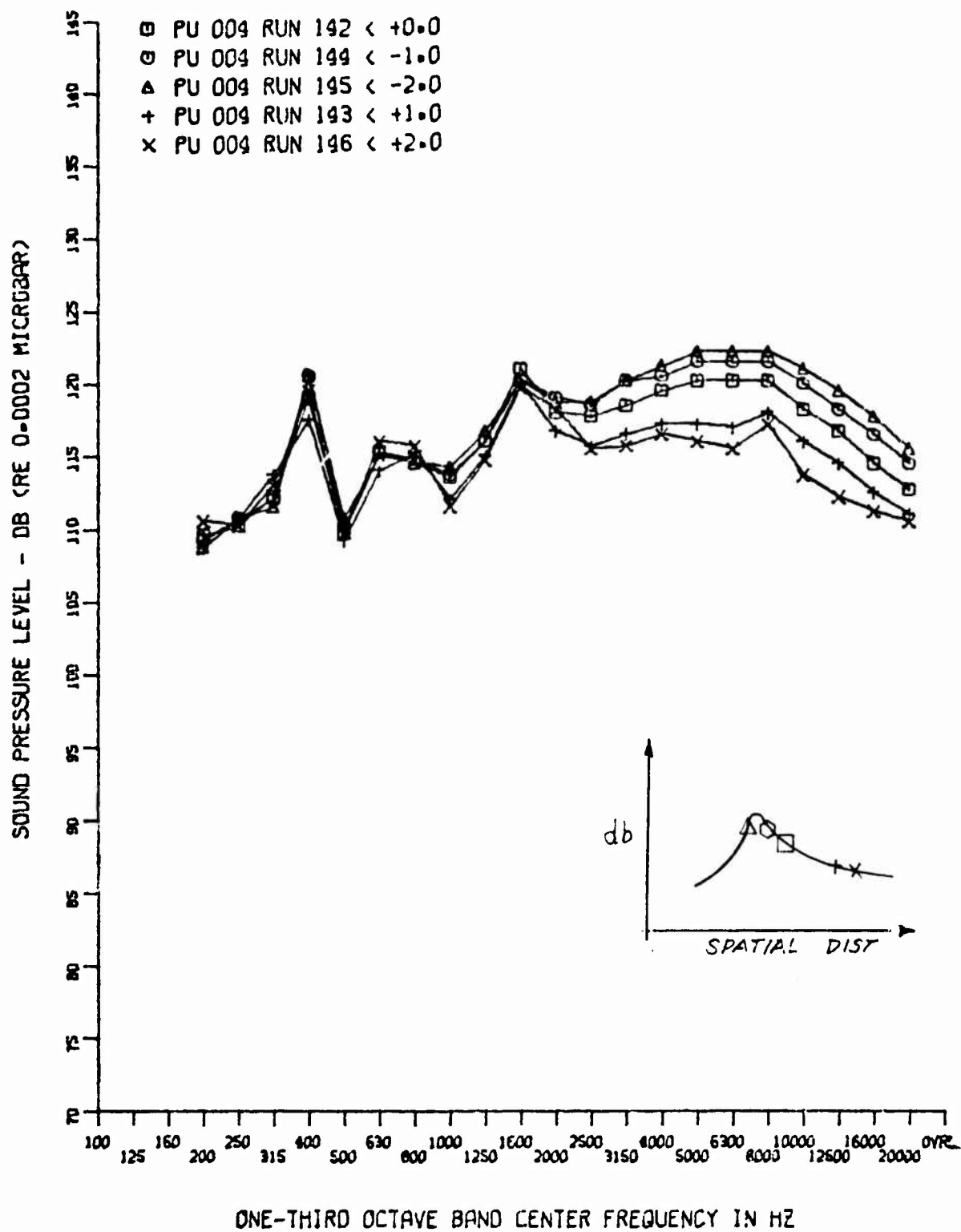
Figure 169. Comparison of Spectra in Transition Zone ($M_\infty = 10$, $Re_\infty = 2.2 \times 10^6$, $R_N = 0$)

194
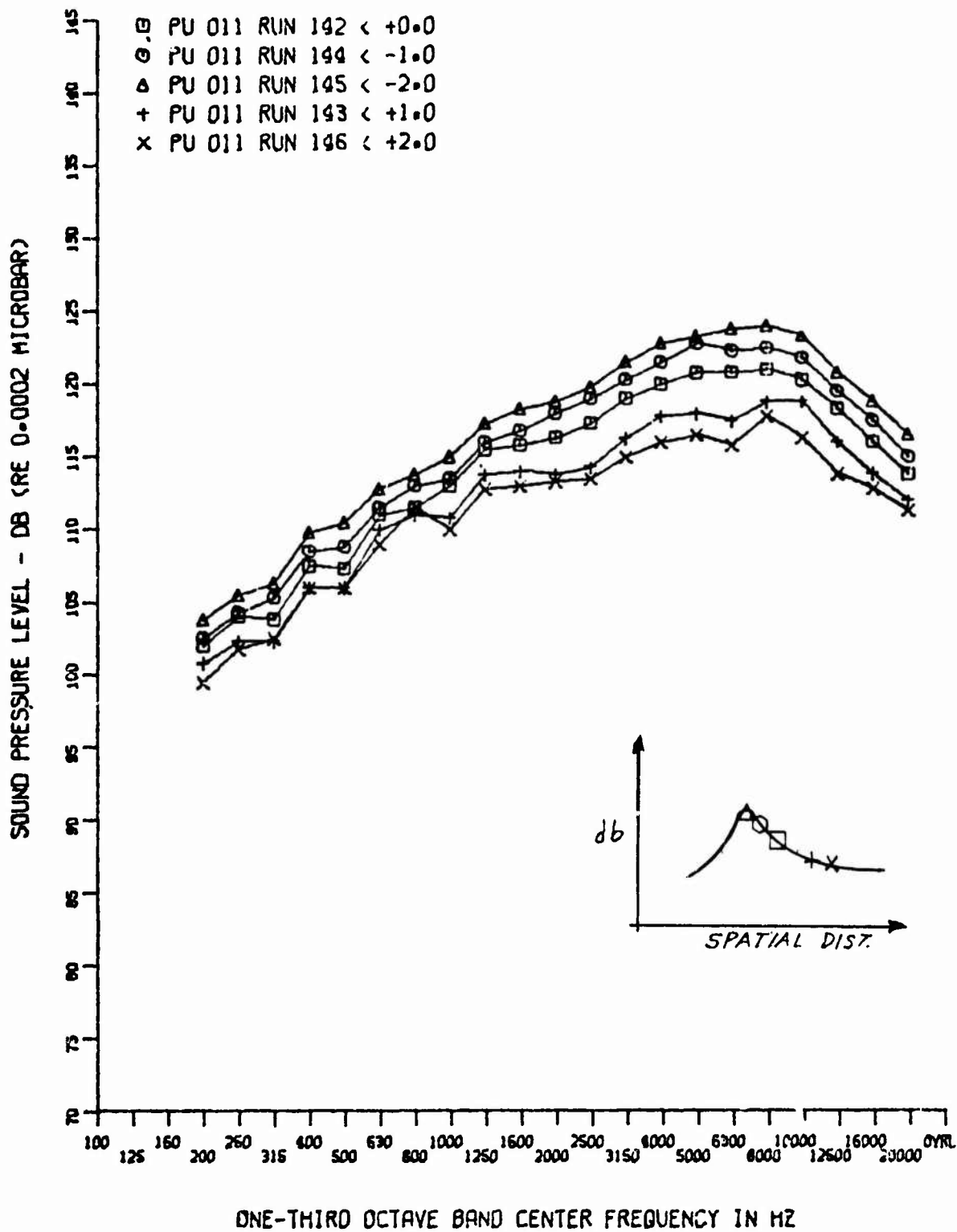
Figure 170. Comparison of Spectra in Transition Zone ($M_\infty = 10$, $Re_\infty = 2.2 \times 10^6$, $R_N = 0$)

195

Figure 171. Comparison of Spectra in Transition Zone ($M_\infty = 10$, $Re_\infty = 2.2 \times 10^6$, $R_N = 0$)

196

Figure 172. Comparison of Spectra at Transition Peak, Circumferential,
($M_\infty = 10$, $Re_\infty = 2.2 \times 10^6$, $R_N = 0$)

197

Figure 173. Base Spectra at Various ($M_\infty = 10$, $Re_\infty = 2.2 \times 10^6$, $R_N = 0$)

198
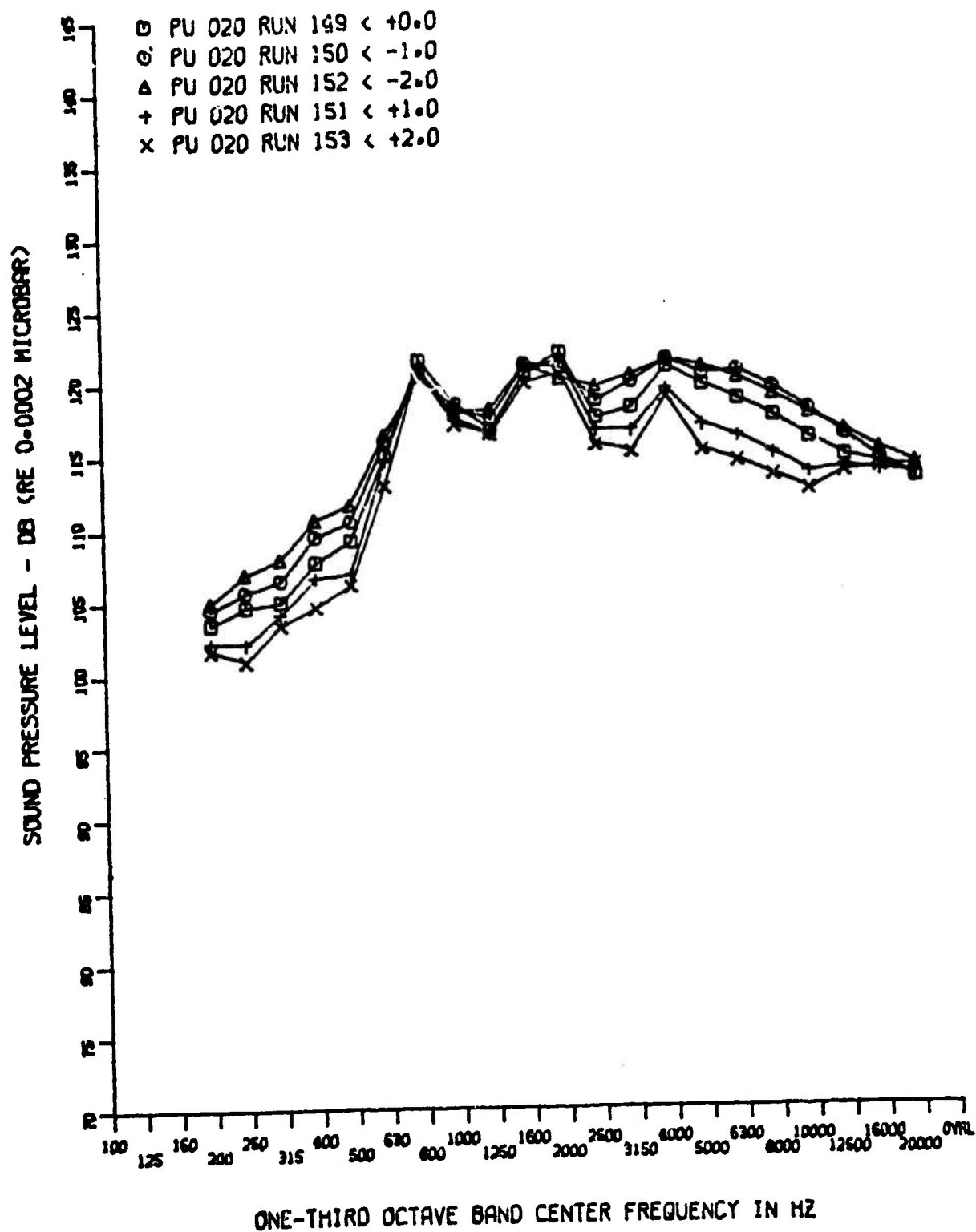
Figure 174. Turbulent Flow Spectra ($M_\infty = 10$, $Re_\infty = 2.2 \times 10^6$, $R_N = 0.055$)
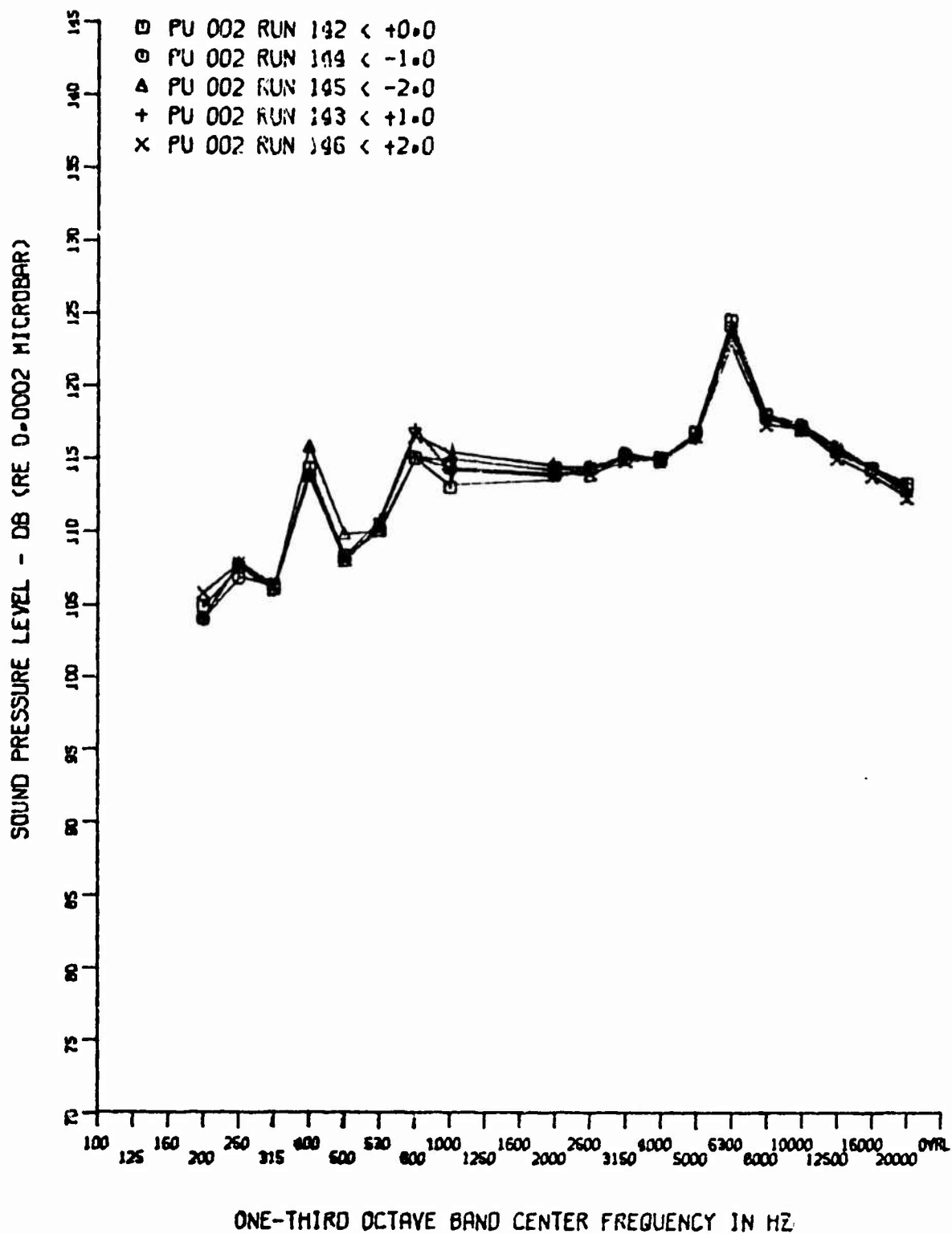
Figure 175. Tunnel Tare Noise ($M_\infty = 10$, $Re_\infty = 2.2 \times 10^6$, $R_N = 0$)
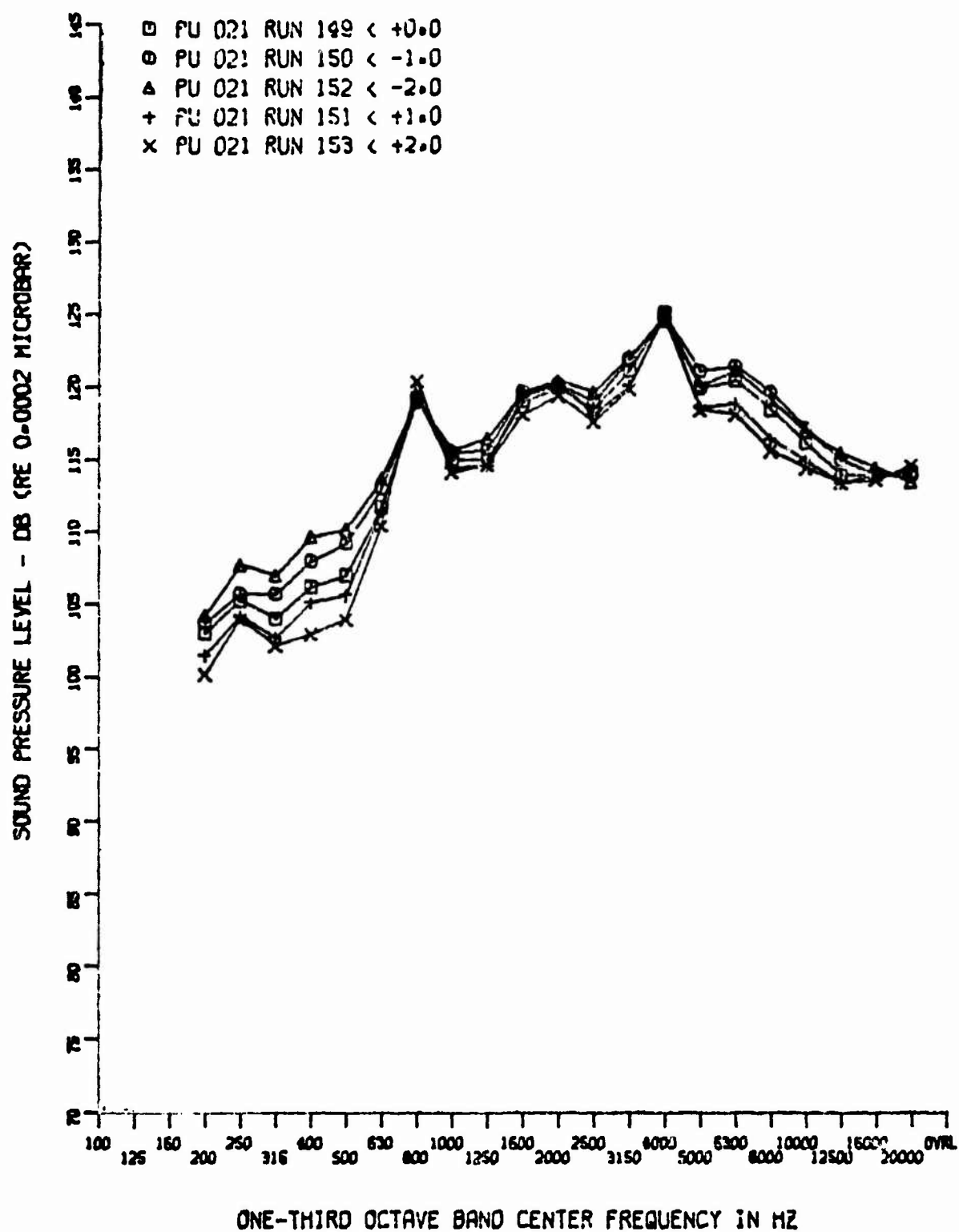
Figure 176. Turbulent Flow Spectra ($M_\infty = 10$, $Re_\infty = 2.2 \times 10^6$, $R_N = 0.055$)

SOUND PRESSURE LEVEL - DB (RE 0.0002 MICROBAR)

□ PU 011 RUN 149 < +0.0
⊙ PU 011 RUN 150 < -1.0
△ PU 011 RUN 152 < -2.0
+ PU 011 RUN 151 < +1.0
× PU 011 RUN 153 < +2.0

db

SPATIAL DIST.-

ONE-THIRD OCTAVE BAND CENTER FREQUENCY IN HZ
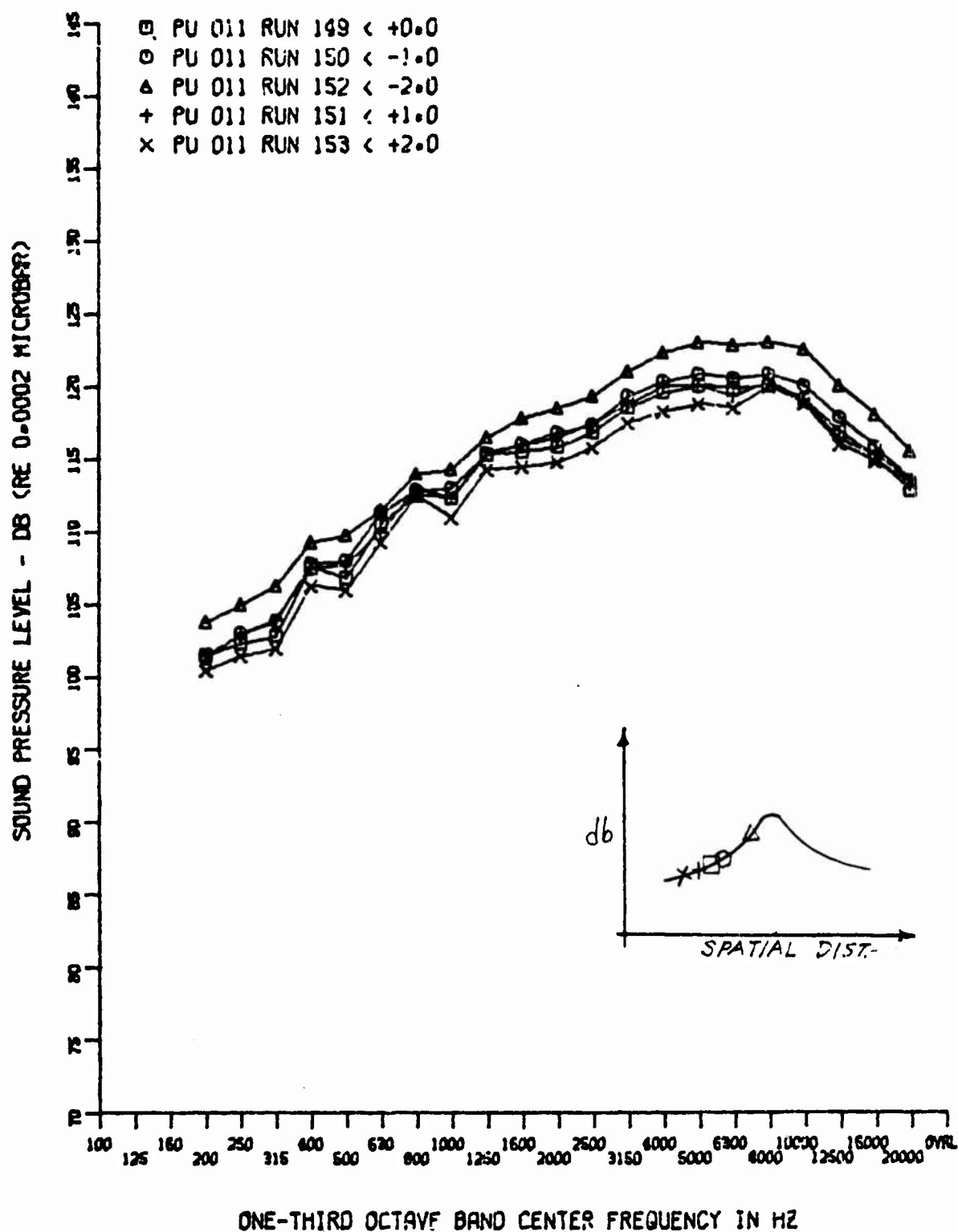
Figure 177. Comparison of Spectra in Transition Zone ($M_\infty = 10$,
$Re_\infty = 2.2 \times 10^6$, $R_N = 0.055$)

Figure 178. Comparison of Spectra in Transition Zone ($M_\infty = 10$, $Re_\infty = 2.2 \times 10^6$, $R_N = 0.055$)
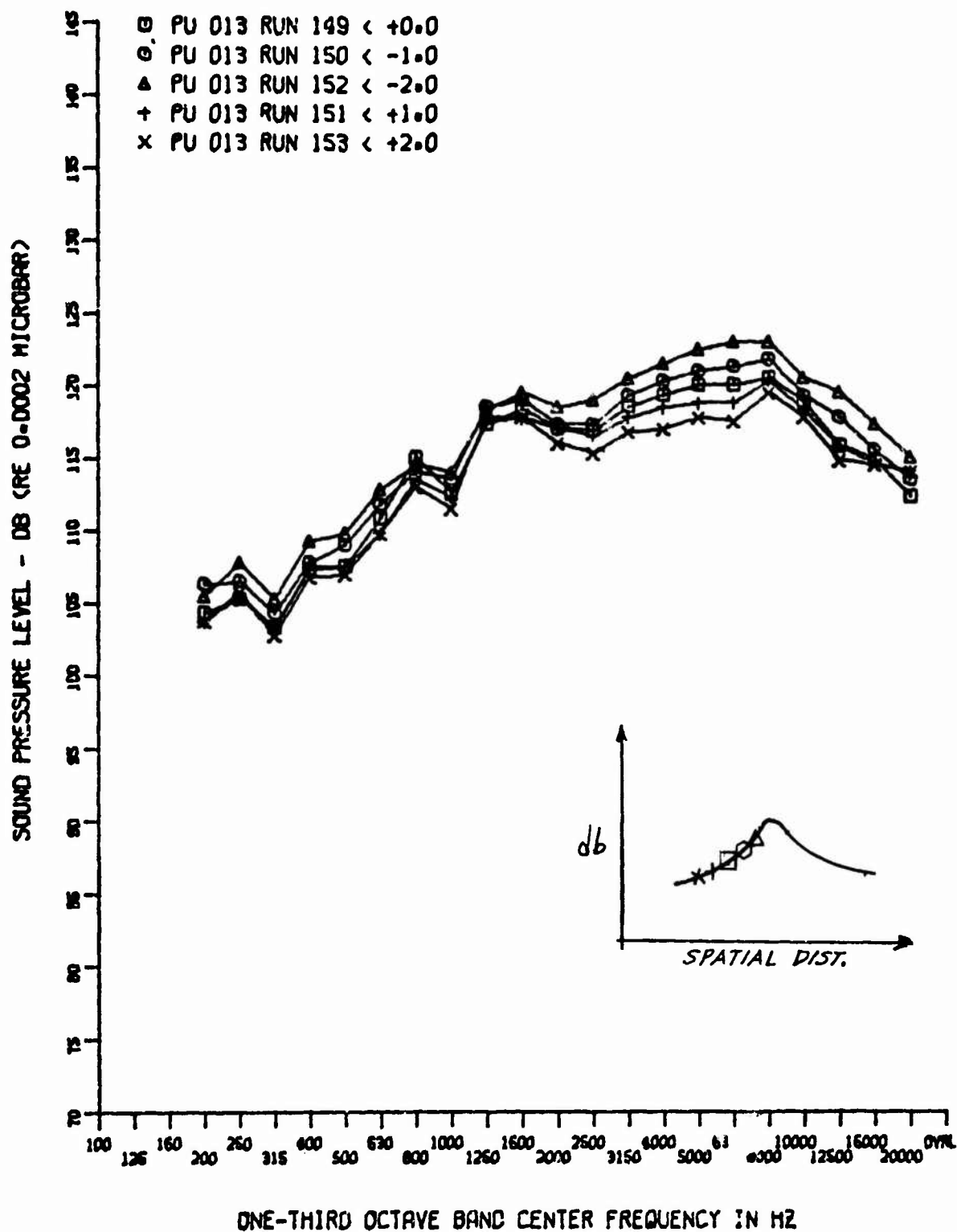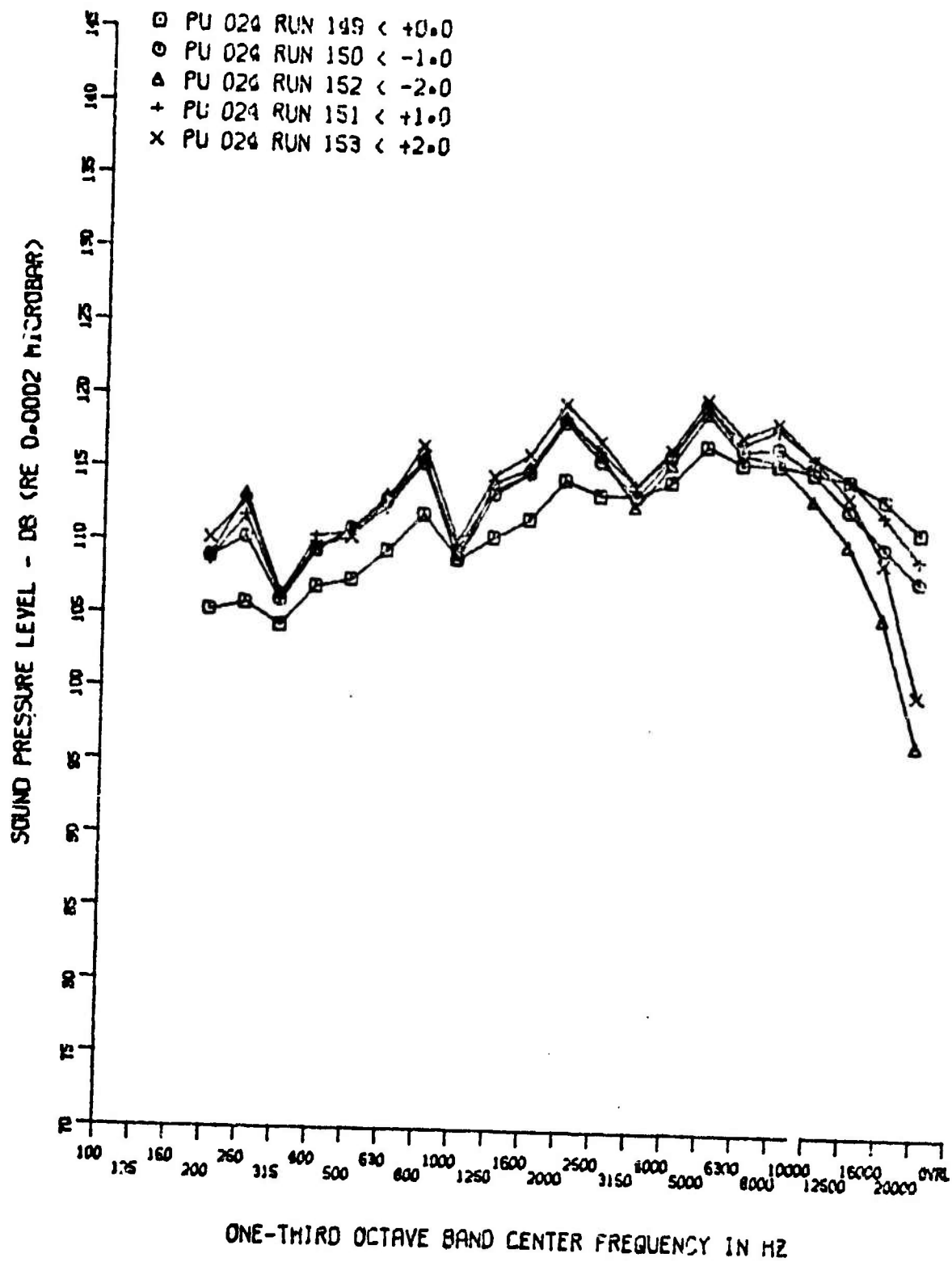
Figure 179. Base Spectra at Various ($M_\infty = 10$, $Re_\infty = 2.2 \times 10^6$, $R_N = 0.055$)

204

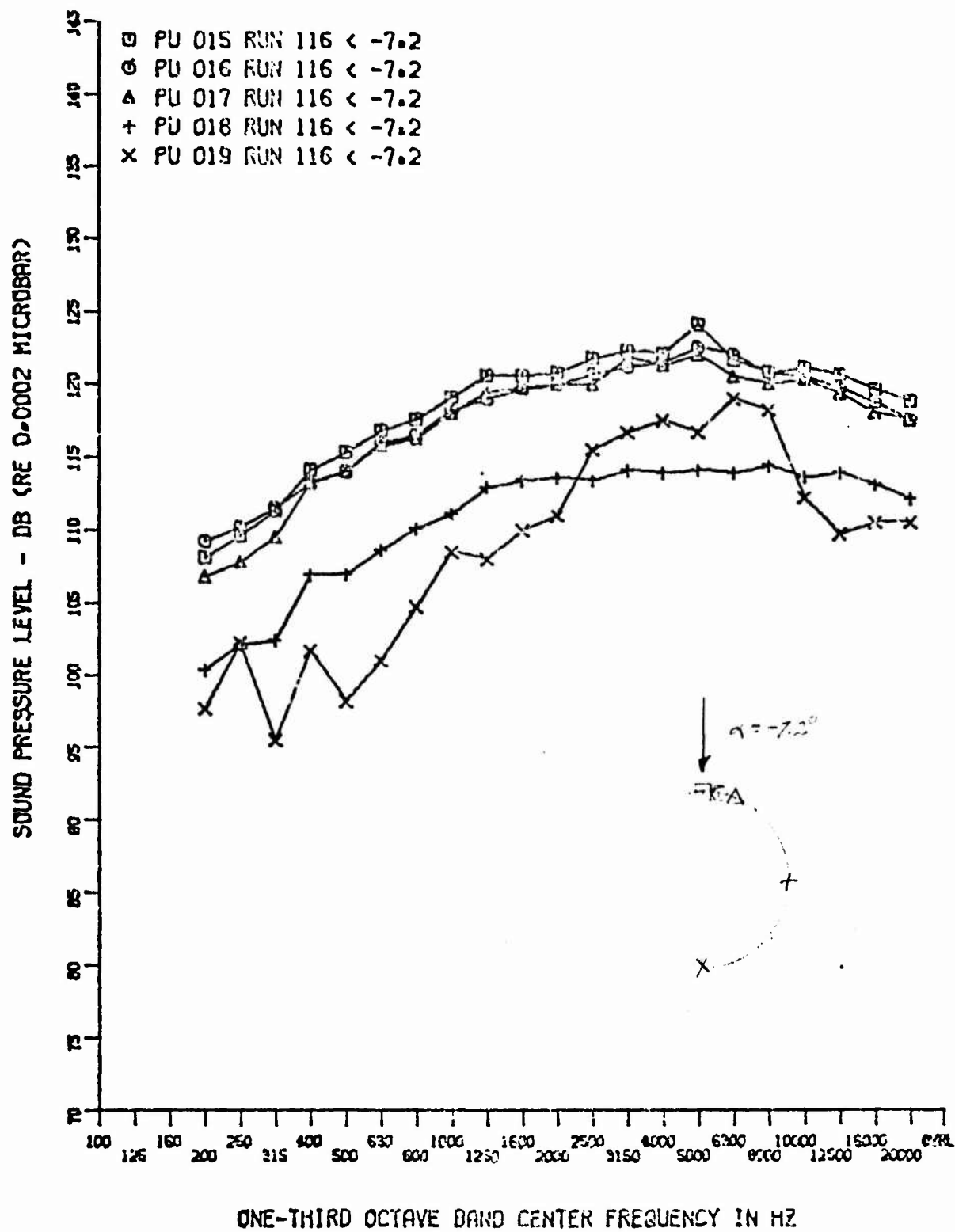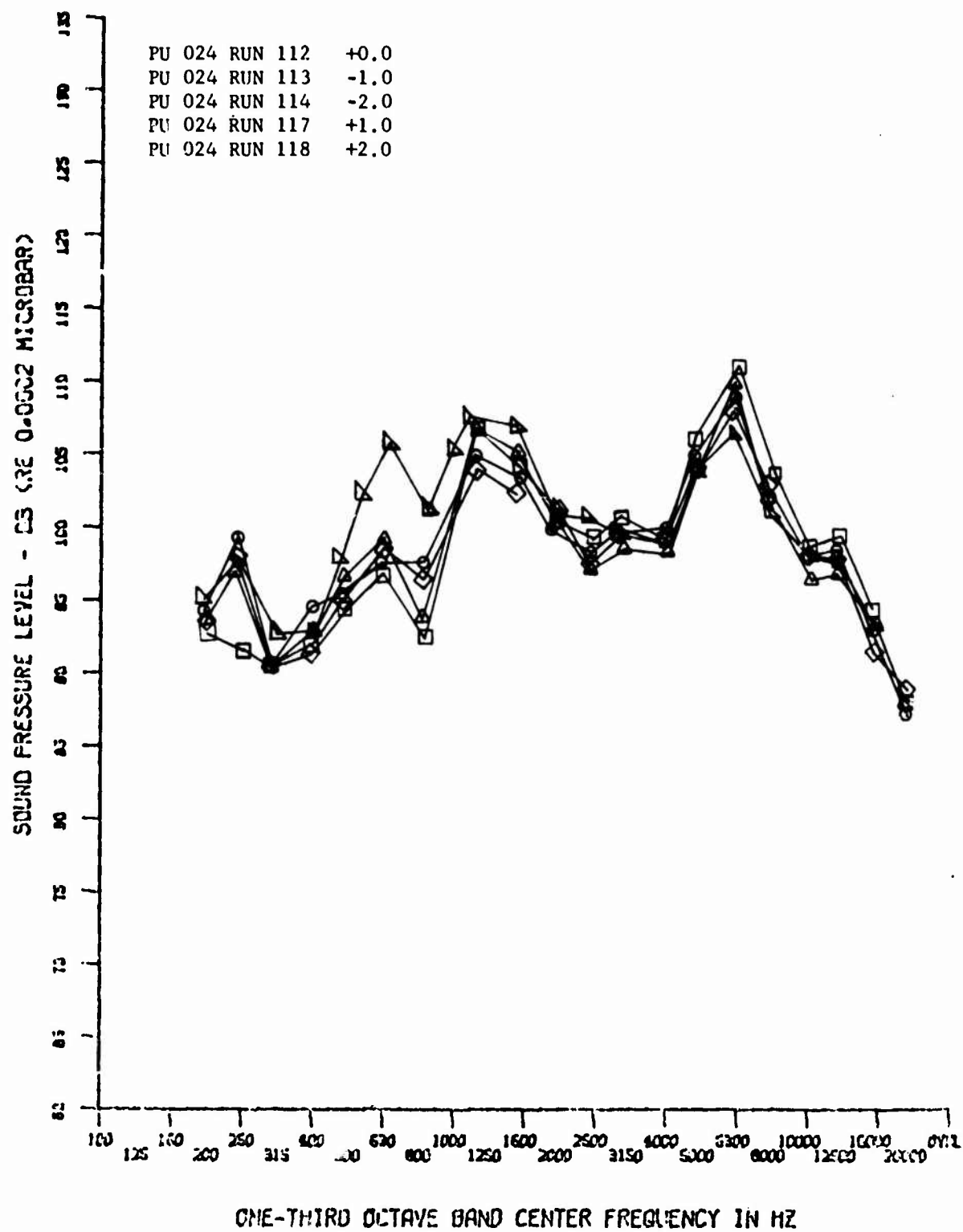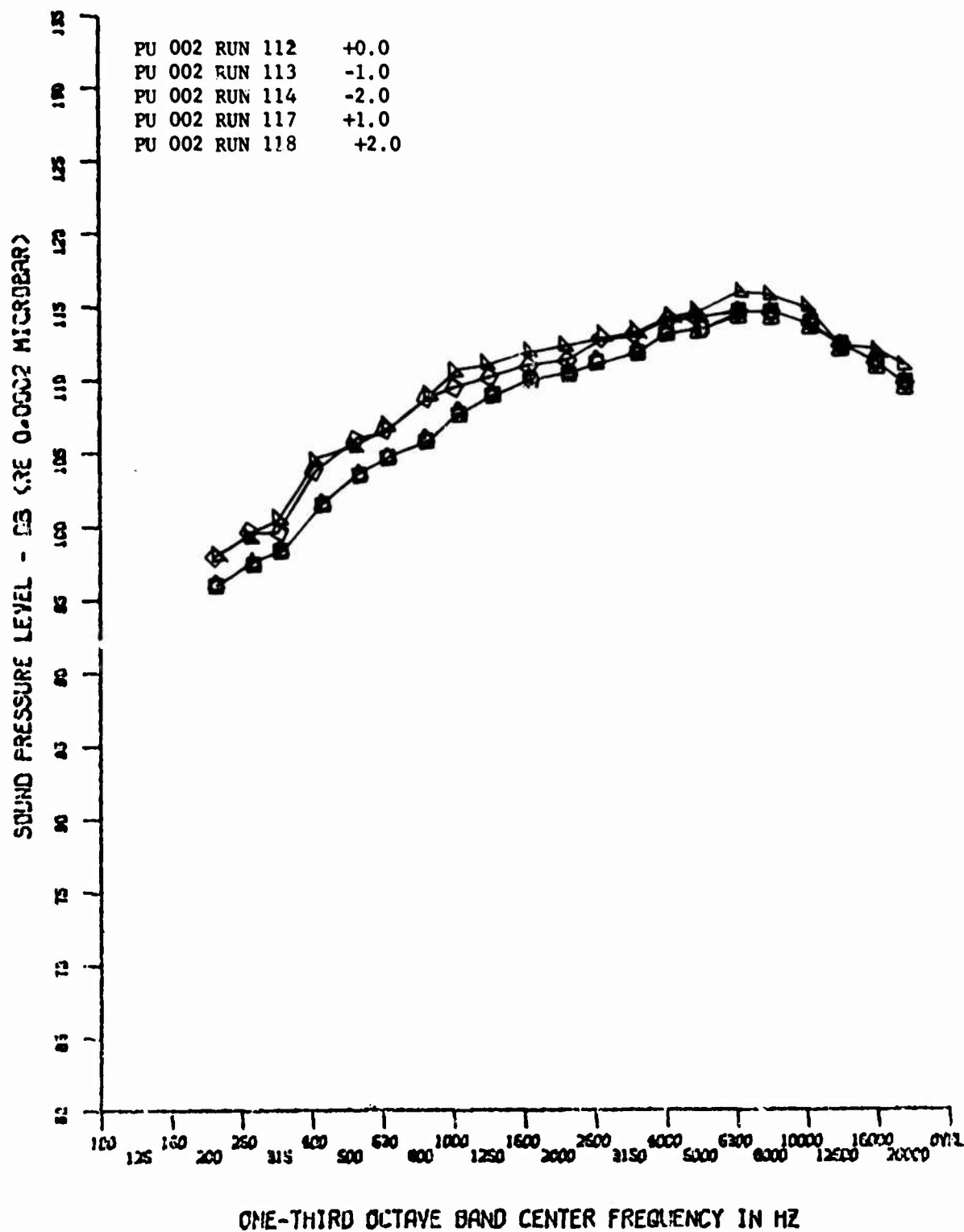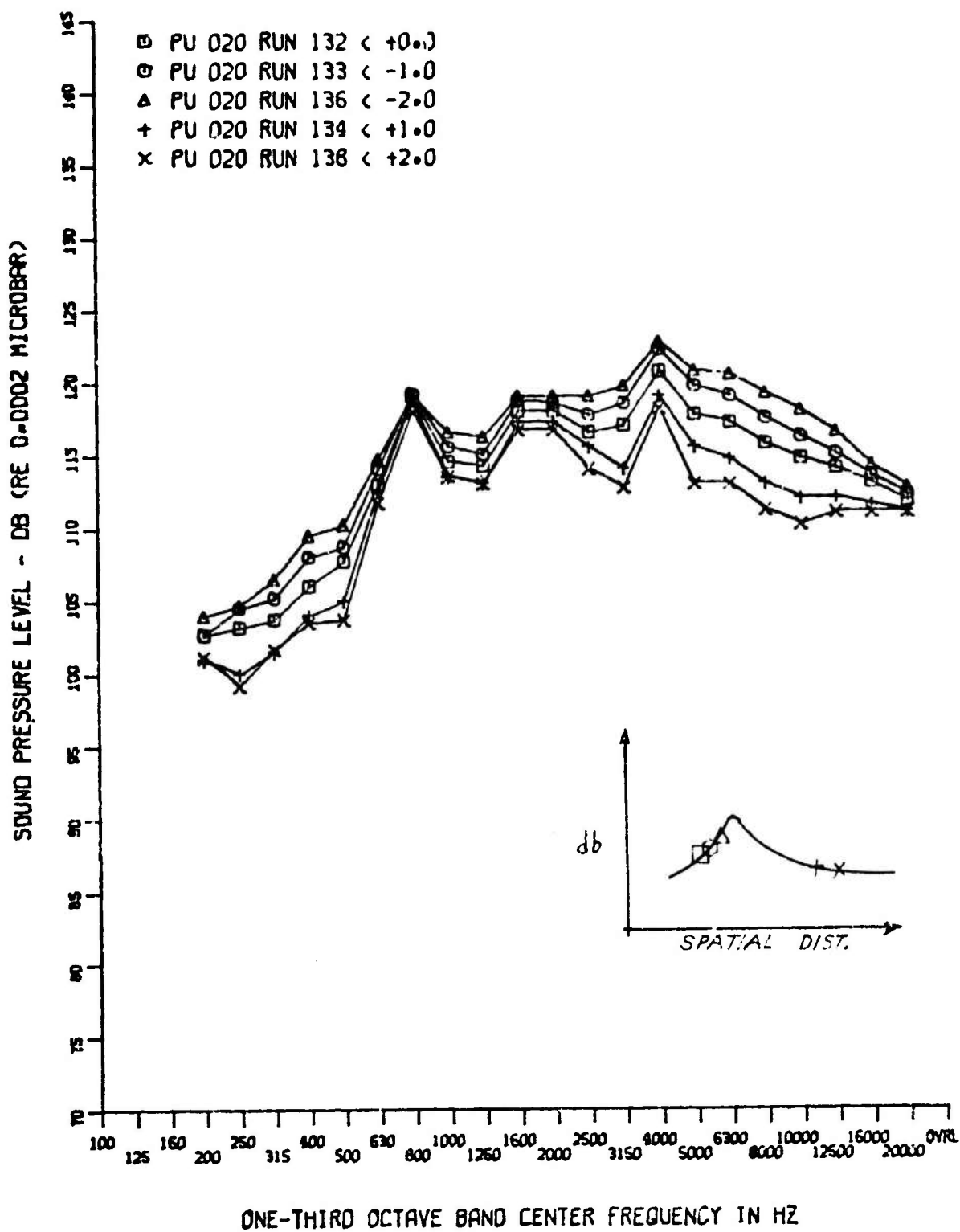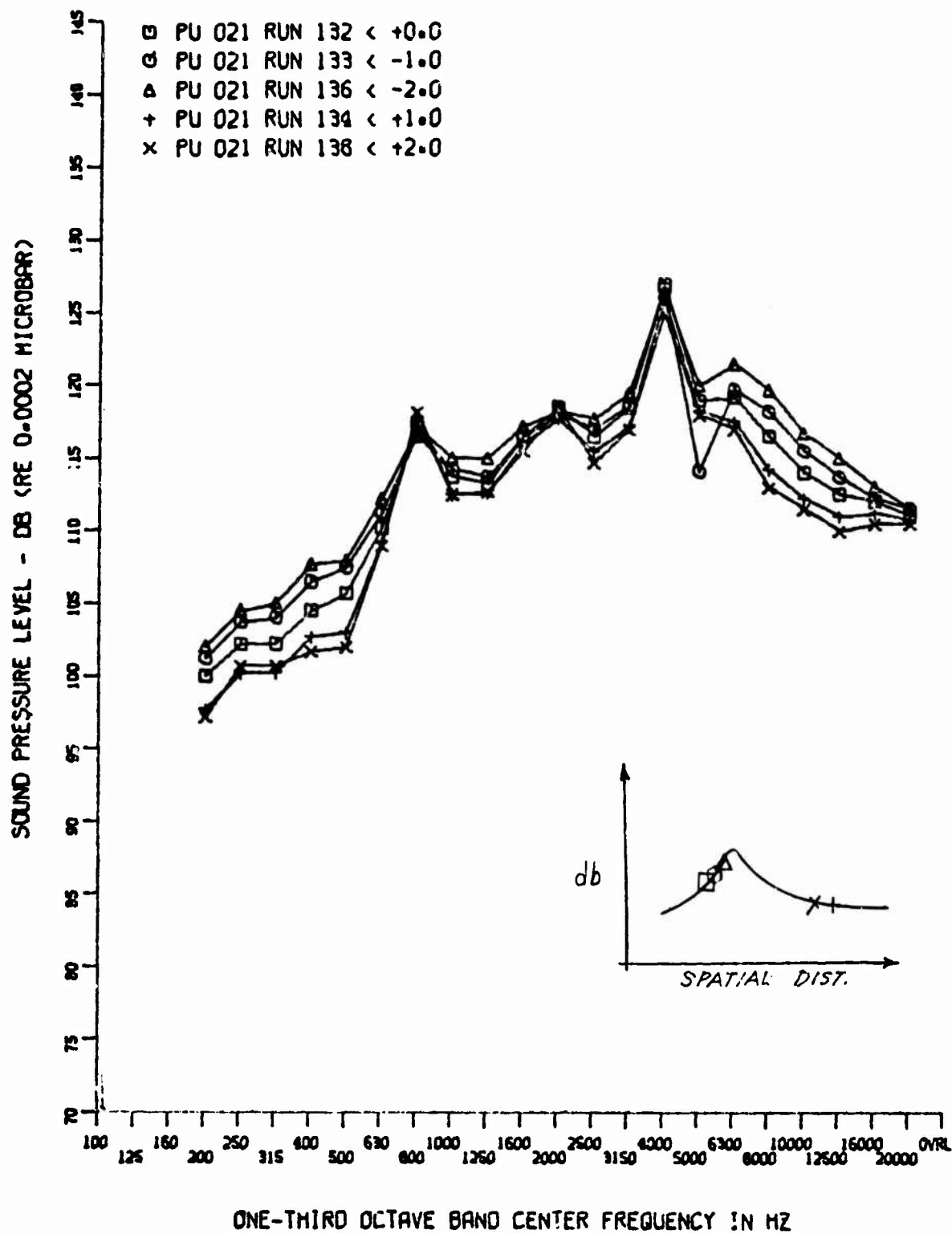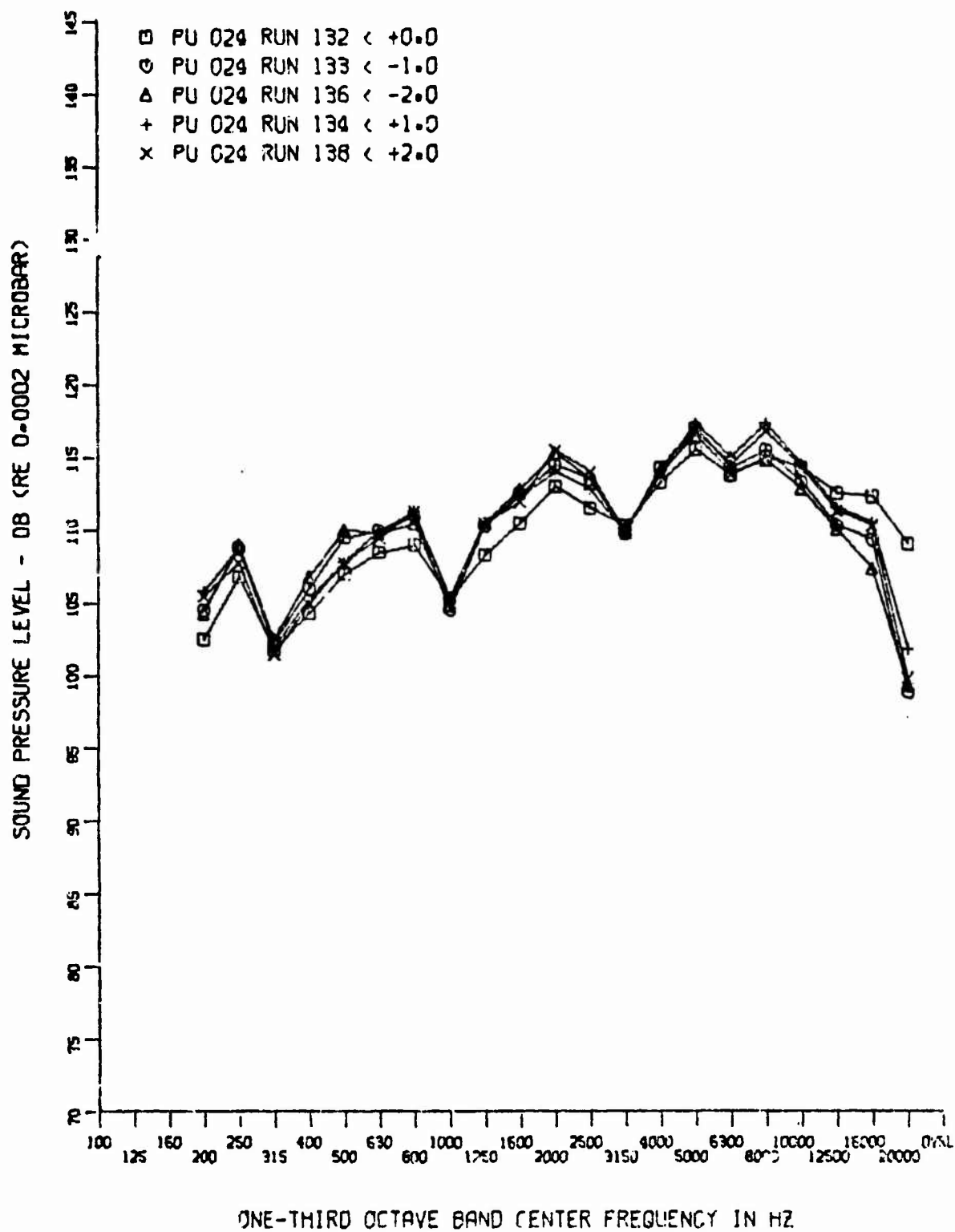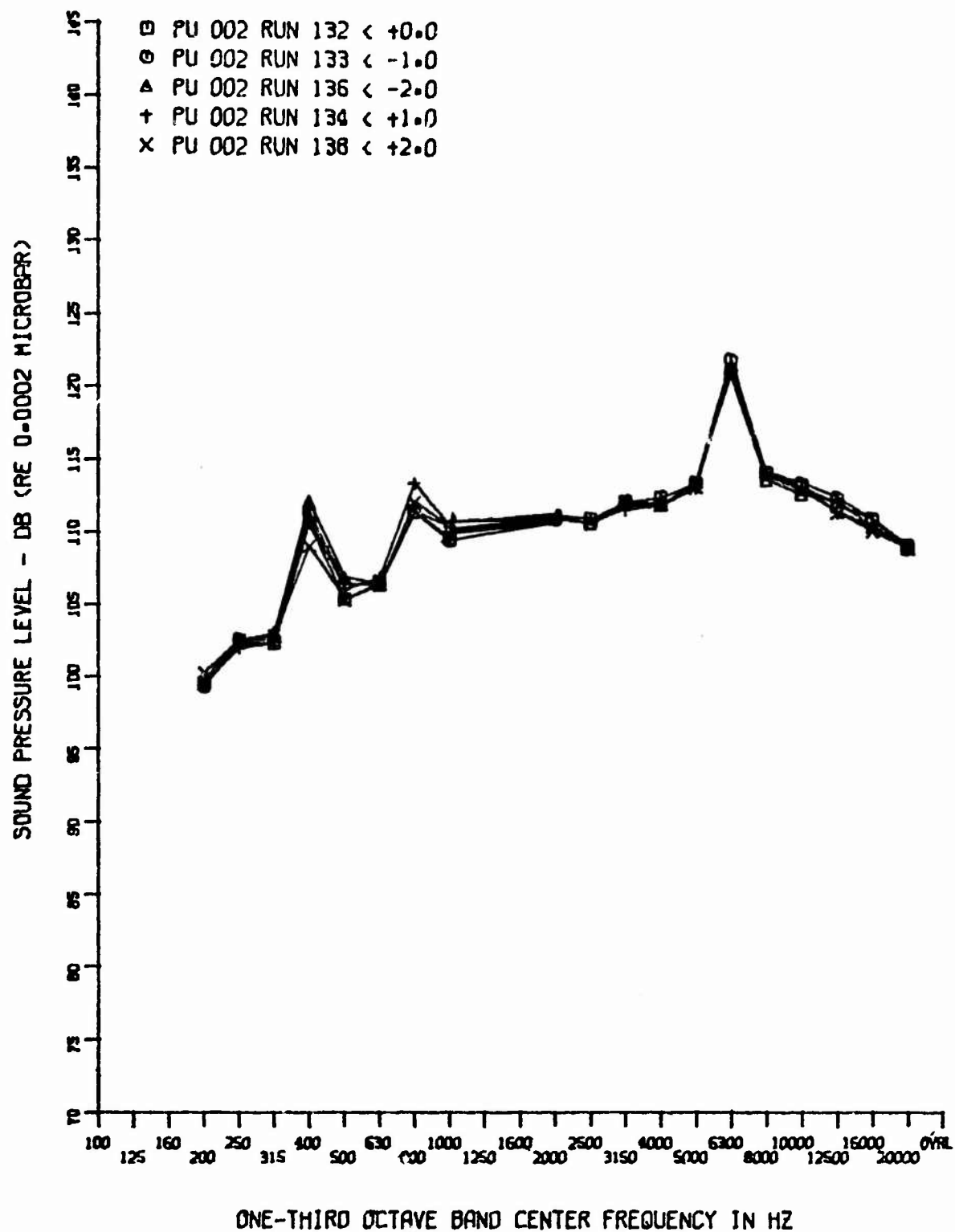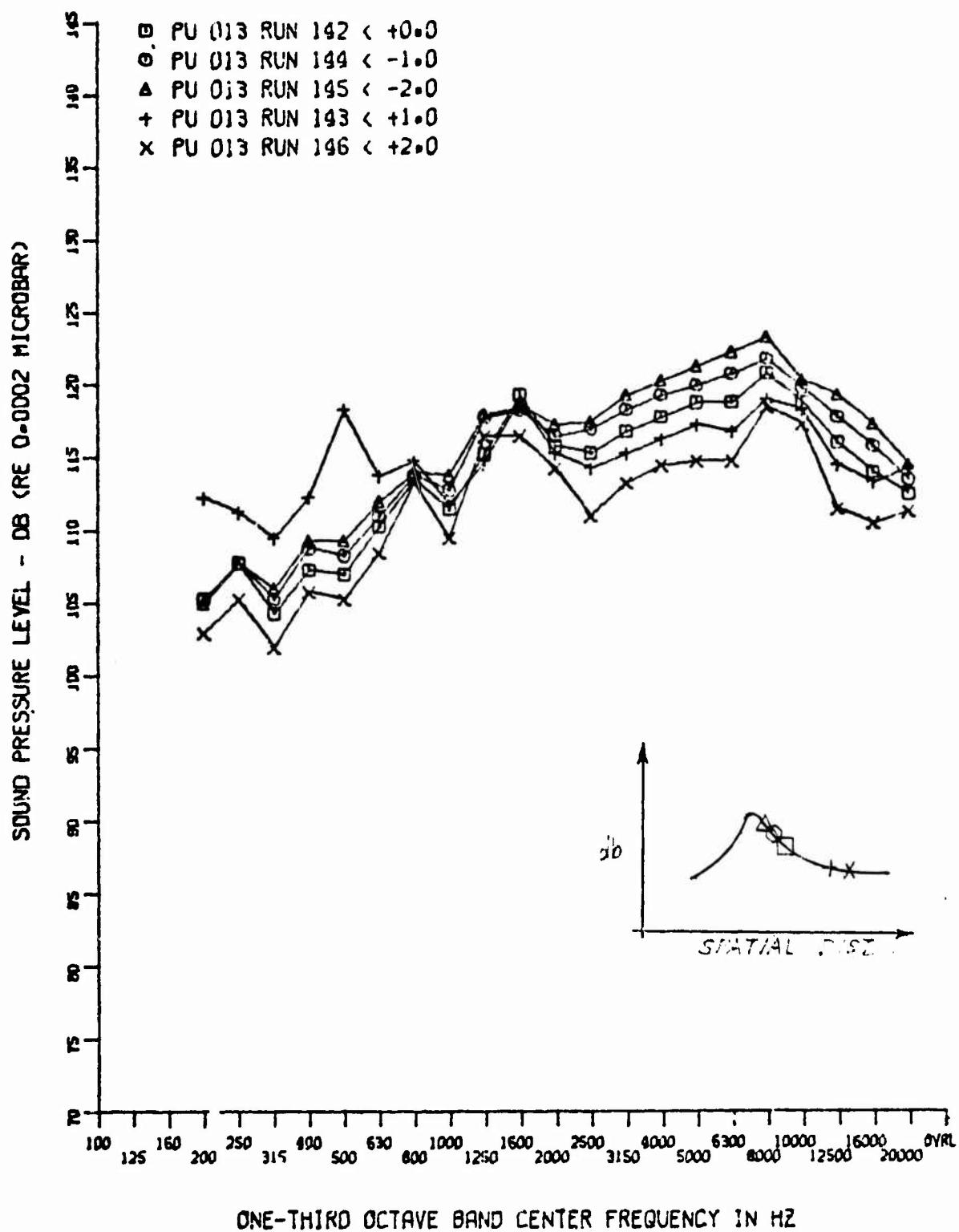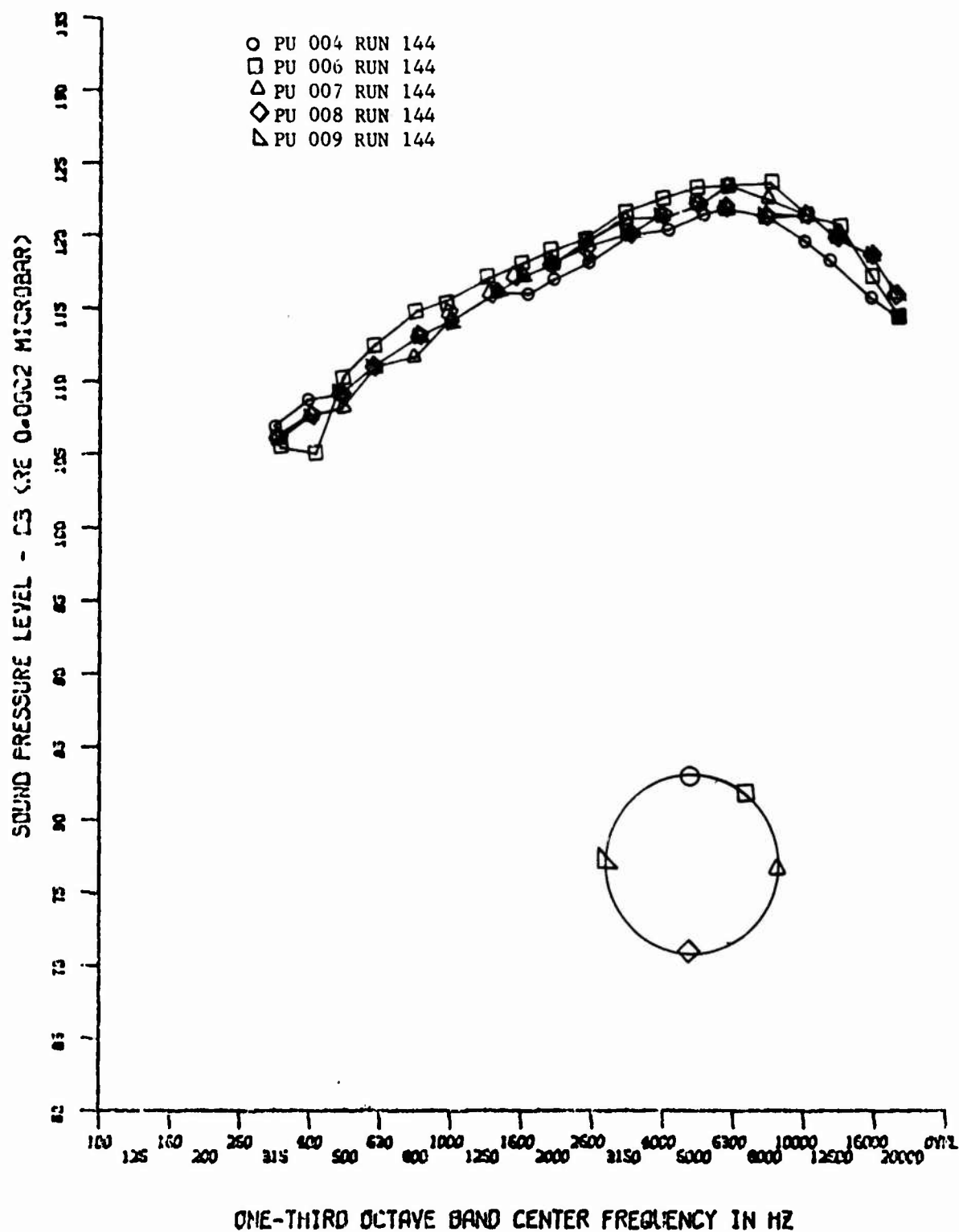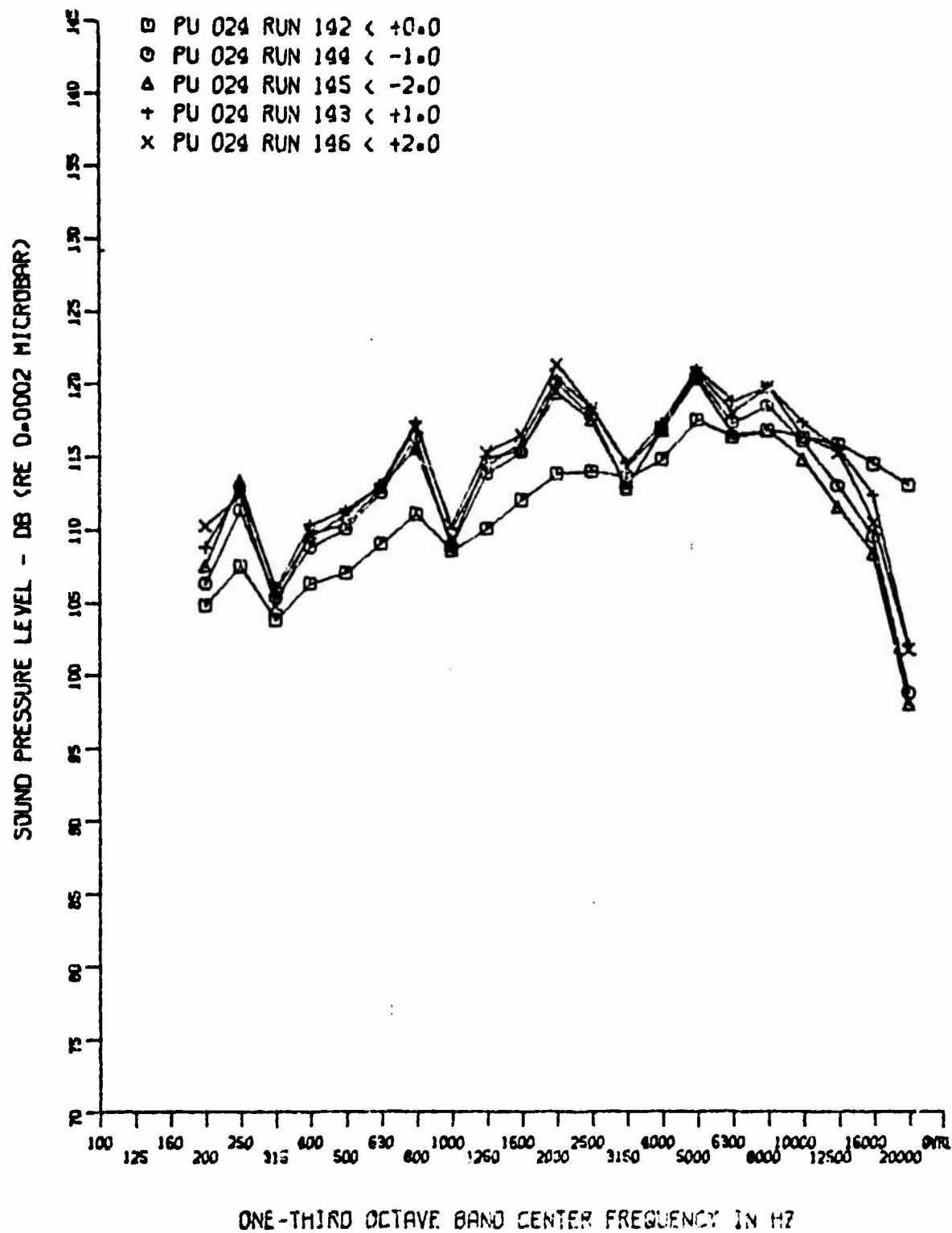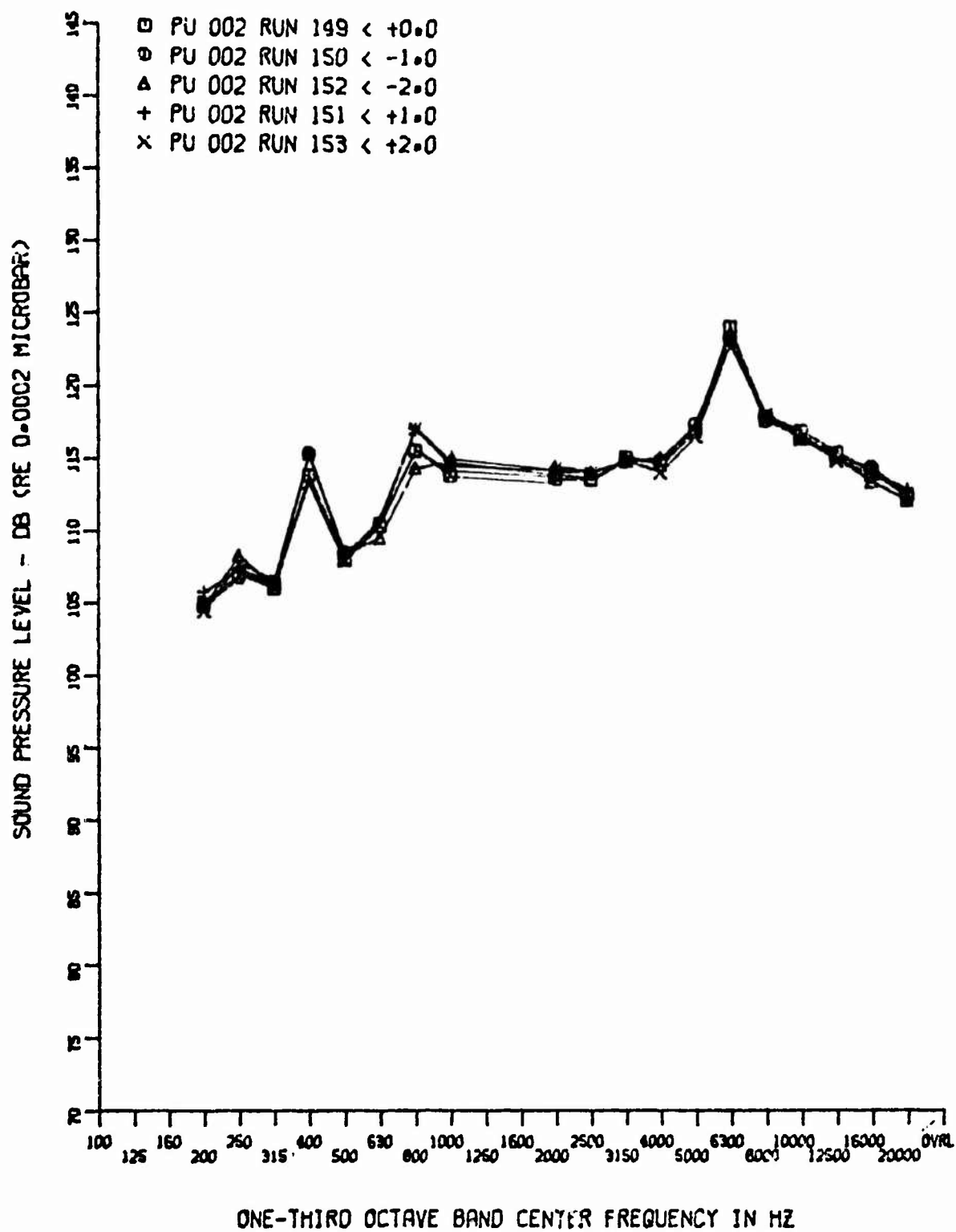Figure 180. Tunnel Tare Noise ($M_\infty = 10$, $Re_\infty = 2.2 \times 10^6$, $R_N = 0.055$)

SECTION IV

REFERENCES

1. Test Facilities Handbook - Arnold Engineering Development Center Arnold Air Force Station, Tennessee, July, 1971.

2. Martellucci, A., "Asymmetric Transition Effects on the Static Stability and Motion History of a Slender Vehicle", SAMSO-TR-70-141, January 1970. Also published in Journal of Spacecraft and Rockets Vol. 8, No. 5, pgs. 476-482, May 1971.

3. Martellucci, A., Ranlet, J. D., "Experimental Study of Near Wakes-Including Base Injection Effects", AMRAC Proceedings, April 1968.

4. Cassanto, J. M., Rasmussen, N. S., and Coats, J. D., "Correlation of Measured Free Flight Base Pressure Data for M = 4 to M = 19 in Laminar and Turbulent Flow", GE-RESD TIS 68SD256, April 1968, Also see AIAA Journal, Vol. 7, No. 6, June 1969, pp. 1154-1157.

5. Ward, L. K., Choate, R. H., "A Model Drop Technique for Free Flight Measurements in Hypersonic Wind Tunnels Using Telemetry, AEDC-TR-66-77, May 1966.

6. Softley, E. J., Graber, B. C., and Zempel, R. E., "Experimental Observation of Transition of the Hypersonic Boundary Layer, AIAA Journal, Vol. 7, No. 2, February 1969.

7. Thomas, K. M., etal, "Some Shock/Wind Tunnel Observations of Interference Effects in Hypersonic Wakes", AEDC TR-69-172, December 1969.

8. Pate, S. R., "Measurements and Correlations of Transition Reynolds Numbers on Sharp Cones at High Speeds", AEDC TR-69-172, December 1968.

9. McCauley, W. D., Saydah, A., and Bueche, J., "The Effect of Controlled Three Dimensional Roughness on Hypersonic Laminar Boundary Layer Transition", AIAA Paper 66-26, January 1966.

10. DiCristina, V., "Three-Dimensional Laminar Boundary Layer Transition on a Sharp 8° Cone at Mach No. 10, AIAA Paper 69-12, January 1969.

11. Private Communication with E. Knox, ARO, Inc.

12. Gravelos, F. G., Edelfelt, I. H. and Emmons, H. W., "The Supersonic Flow About a Blunt Body of Revolution for Gases at Chemical Equilibrium", Proceedings of the 9th Annual Congress of the IAF, Amsterdam, 1958.

13. Kyriss, C. L., "Three Dimensional Inviscid Flow About Blunted Cones (GE Report to be published).

14. Studerus, C. J. and Dienna, E. A., "Viscous Interaction Zero Angle of Attack Drag (VIZAAD) Program, TIS 64SD292, General Electric Co., Philadelphia, Pa. (November 1964).

15. Studerus, C. J., "Sphere Cone Angle of Attack (SCAAT) Program", GE-RS Report 63SD744, December, 1964.

16. Rie, H., "The GE-RESD Equilibrium Non-Similar Boundary Layer Program (ENSBL)", TIE 71SD212, General Electric Co., Philadelphia, Pa., February, 1971.

17. Martellucci, A., "Effects of Mass Transfer on Hypersonic Turbulent Boundary Layer Properties, AIAA Journal Vol. 10, No. 2, February 1972, pp 181-187.

18. Martellucci, A., "Laminar Base Pressure Correlation", GE-RESD DM 67-13, March 1967.

19. Cassanto, J. M., Stover, E. M., "A Revised Technique for Predicting the Base Pressure of Sphere Cone Configurations in Turbulent Flow Including Mass Addition Effects", GE-RESD FM-68-41, October 1968.

20. Fisher, M. C., Weinstein, L. M., "Cone Transitional Boundary Layer Structure at $M_e = 14$, AIAA Journal, Vol. 10, Nov. 5, May 1972, pp 694, 700.

21. Chyu, W. J., Hanly, R. D., "Power-and-cross Spectra and Space-Time correlations of Surface Fluctuations Pressures at Mach Numbers Between 1.6 and 2.5," NASA TN D-5440, September 1969.

DOCUMENT CONTROL DATA · R&D

(Security classification of title, body of abstract and indexing annotation must be entered when the overall report is classified.)

1 ORIGINATING ACTIVITY (Corporate author)	2a. REPORT SECURITY CLASSIFICATION
General Electric - RESD 32nd and Chestnut Streets Philadelphia, Penna. 19101	Unclassified
	2b GROUP

3 REPORT TITLE

AERO ACOUSTIC LOADS ASSOCIATED WITH HIGH-BETA RE-ENTRY VEHICLES

4 DESCRIPTIVE NOTES (Type of report and inclusive dates)

Final - February 1971 to October 1972

5 AUTHOR(S) (Last name, first name, initial)

Chaump, Louis E., Martellucci, Anthony, Monfort, Alan

6 REPORT DATE	7a TOTAL NO. OF PAGES	7b NO OF REFS
May 1973	226	21

8a CONTRACT OR GRANT NO F33615-71-C-1245	9a ORIGINATOR'S REPORT NUMBER(S)
b PROJECT NO. 1471	
c Task 147102	9b OTHER REPORT NO(S) (Any other numbers that may be assigned this report)
d.	AFFDL-TR-72-138, Vol. II

10 AVAILABILITY/LIMITATION NOTICES

Distribution limited to U.S. Government agencies only; test and evaluation; statement applied 28 November 1972. Other requests for this document must be referred to AF Flight Dynamics Laboratory, (FY), Wright-Patterson AFB, Ohio 45433.

11 SUPPLEMENTARY NOTES	12 SPONSORING MILITARY ACTIVITY Air Force Flight Dynamic Laboratory Wright-Patterson AFB, Ohio 45433

13 ABSTRACT

A detailed description is presented defining the wind tunnel test facility, test model and associated instrumentation and recording system. Wind tunnel conditions including test model local flow properties are defined along with a discussion of acoustic data obtained for the various flow regimes of interest (transition, fully turbulent, base and separated flow). Finally, test data in the form of acoustic intensity distributions along the vehicle and third octave pressure spectrums are presented.

DD FORM 1473 (1 JAN 64)

KEY WORDS	LINK A		LINK B		LINK C	
	ROLE	WT	ROLE	WT	ROLE	WT
Aeroacoustic Environments						
Re-entry Vehicle						
Turbulent Flow						
Base Flow						
Transitional Flow						

INSTRUCTIONS

1. ORIGINATING ACTIVITY: Enter the name and address of the contractor, subcontractor, grantee, Department of Defense activity or other organization (corporate author) issuing the report.

2a. REPORT SECURITY CLASSIFICATION: Enter the overall security classification of the report. Indicate whether "Restricted Data" is included. Marking is to be in accordance with appropriate security regulations.

2b. GROUP: Automatic downgrading is specified in DoD Directive 5200.10 and Armed Forces Industrial Manual. Enter the group number. Also, when applicable, show that optional markings have been used for Group 3 and Group 4 as authorized.

3. REPORT TITLE: Enter the complete report title in all capital letters. Titles in all cases should be unclassified. If a meaningful title cannot be selected without classification, show title classification in all capitals in parenthesis immediately following the title.

4. DESCRIPTIVE NOTES: If appropriate, enter the type of report, e.g., interim, progress, summary, annual, or final. Give the inclusive dates when a specific reporting period is covered.

5. AUTHOR(S): Enter the name(s) of author(s) as shown on or in the report. Enter last name, first name, middle initial. If military, show rank and branch of service. The name of the principal author is an absolute minimum requirement.

6. REPORT DATE: Enter the date of the report as day, month, year, or month, year. If more than one date appears on the report, use date of publication.

7a. TOTAL NUMBER OF PAGES: The total page count should follow normal pagination procedures, i.e., enter the number of pages containing information.

7b. NUMBER OF REFERENCES: Enter the total number of references cited in the report.

8a. CONTRACT OR GRANT NUMBER: If appropriate, enter the applicable number of the contract or grant under which the report was written.

8b, 8c, & 8d. PROJECT NUMBER: Enter the appropriate military department identification, such as project number, subproject number, system numbers, task number, etc.

9a. ORIGINATOR'S REPORT NUMBER(S): Enter the official report number by which the document will be identified and controlled by the originating activity. This number must be unique to this report.

9b. OTHER REPORT NUMBER(S): If the report has been assigned any other report numbers (either by the originator or by the sponsor), also enter this number(s).

10. AVAILABILITY/LIMITATION NOTICES: Enter any limitations on further dissemination of the report, other than those imposed by security classification, using standard statements such as:

(1) "Qualified requesters may obtain copies of this report from DDC."

(2) "Foreign announcement and dissemination of this report by DDC is not authorized."

(3) "U. S. Government agencies may obtain copies of this report directly from DDC. Other qualified DDC users shall request through

.''

(4) "U. S. military agencies may obtain copies of this report directly from DDC. Other qualified users shall request through

.''

(5) "All distribution of this report is controlled. Qualified DDC users shall request through

.''

If the report has been furnished to the Office of Technical Services, Department of Commerce, for sale to the public, indicate this fact and enter the price, if known.

11. SUPPLEMENTARY NOTES: Use for additional explanatory notes.

12. SPONSORING MILITARY ACTIVITY: Enter the name of the departmental project office or laboratory sponsoring (paying for) the research and development. Include address.

13. ABSTRACT: Enter an abstract giving a brief and factual summary of the document indicative of the report, even though it may also appear elsewhere in the body of the technical report. If additional space is required, a continuation sheet shall be attached.

It is highly desirable that the abstract of classified reports be unclassified. Each paragraph of the abstract shall end with an indication of the military security classification of the information in the paragraph, represented as (TS), (S), (C), or (U).

There is no limitation on the length of the abstract. However, the suggested length is from 150 to 225 words.

14. KEY WORDS: Key words are technically meaningful terms or short phrases that characterize a report and may be used as index entries for cataloging the report. Key words must be selected so that no security classification is required. Identifiers, such as equipment model designation, trade name, military project code name, geographic location, may be used as key words but will be followed by an indication of technical context. The assignment of links, rules, and weights is optional.